UNIVERSITY OF LIVERPOOL

Characterization of the Reverberation Chamber for Over-the-Air Tests

by

Tianyuan Jia

B.Eng.

A thesis submitted in accordance with the requirements for the award of the degree of *Doctor of Philosophy* of the University of Liverpool

June 2021

Copyright Declaration

I hereby declare that except where specific reference is made to the work of others, the contents of this dissertation are original and have not been submitted in whole or in part for consideration for any other degree or qualification in this, or any other University. This dissertation is the result of my own work and includes nothing which is the outcome of work done in collaboration, except where specifically indicated in the text.

Tianyuan Jia

2021

To my parents: Thank you for your constant encouragement, support, and love.

Acknowledgments

First and foremost, it is a genuine pleasure to express my deep and sincere gratitude to my primary supervisor Prof. Yi Huang for giving me the opportunity to do research and providing invaluable guidance throughout this research. It is his dynamism, enthusiasm, motivation, vision, sincerity, patience, and immense knowledge that deeply inspires me. I could not have imagined having a better advisor and mentor for my Ph.D. research. Secondly, I am extremely grateful to Dr. Qian Xu and Dr. Jiafeng Zhou for their constant academic guidance and useful suggestions.

I would also like to express my special gratitude and thanks to Dr. Chaoyun Song, Mr. Qiang Hua, Dr. Zhihao Tian, and Dr. Zhouxiang Fei for their contributions in editing the published papers of this research and for their academic support.

I would also like to thank my colleagues and friends, in particular, Dr. Manoj Stanley, Dr. Ahmed Alieldin, Mr. Lyuwei Chen, Mr. Chen Xu, Dr. Xuanming Zhang, Mr. Jingyuan Jiang, Mr. Yansong Wang, Mr. Sumin Joseph, Miss. Jiayou Wang, Dr. Yuan Zhuang, Dr. Anqi Chen, Miss. Wenzhang Zhang, Mr. Kai Jiang, Mr. Xiantao Yang, Mr. Jinyao Zhang, Dr. Abed Pour Sohrab, Dr. Muaad Hussein, Dr. Umniyyah Ulfa, Prof. Dajun Lei, Dr. Zhenghua Tang, Dr. Jingchen Wang, Mr. Rui Pei, Miss. Zhenzhen Jiang and Dr. Saqer S. Alja'afreh for their kind help. I truly enjoyed working in such a research environment that stimulates original thinking and initiative.

Last but not the least, the support from the Electrical Engineering and Electronics Department of the University of Liverpool is gratefully acknowledged.

Table of Contents

Acronyms and Abbreviations

2D	Two-Dimensional
3D	Three-Dimensional
3GPP	3rd Generation Partnership Project
5G	Fifth-generation Mobile Communication Networks
AC	Anechoic Chamber
ACF	Autocorrelation Function
ACLR	Adjacent Channel Leakage Ratio
ACS	Absorption Cross Section
ANOVA	Analysis of Variance
AoA	Angle of Arrival
AoD	Angle of Departure
AWGN	Additive Wight Gaussian Noise
BPF	Bandpass Filter
BS	Base Station
CDF	Cumulative Distribution Function
CI	Confidence Interval
CLT	Central Limit Theorem
CTIA	Cellular Telecommunication and Internet Association

CTS	Conducted Two-Stage
DoF	Degree of Freedom
DUT	Device under Test
EIRP	Effective Isotropic Radiated Power
EM	Electromagnetic
FD-ACF	Frequency Domain Autocorrelation Function
FD-ACFUS	Unstirred Frequency Domain Autocorrelation Function
FoM	Figure of Merit
FR1	Frequency Range 1
HUF	Highest Usable Frequency
IFT	Inverse Fourier Transform
i.i.d	Independent and Identically Distributed
LoS	Line-of-Sight
LUF	Lowest Usable Frequency
M2M	Machine-to-Machine
Massive MIMO	Massive Multi-Input Multi-Output
mm-wave	Millimeter-wave
MLE	Maximum Likelihood Estimator
MPAC	Multi-Probe Anechoic Chamber
NLoS	Non-Line-of-Sight
OBUE	Operating Band Unwanted Emissions

OTA	Over-The-Air
OUT	Object under Test
PDF	Probability Density Function
PDP	Power Delay Profile
PWP	Power Wavevector Profile
PEC	Perfect Electrical Conductor
RC	Reverberation Chamber
RF	Radio Frequency
RIMP	Rich Isotropic Multipath
RMS	Root Mean Square
RP	Reference Plane
RTS	Radiated Two-Stage
SA	Signal Analyzer
SEM	Spectrum Emission Mask
SG	Signal Generator
SISO	Single-Input-Single-Output
SNR	Signal to Noise Ratio
SSB	Sum of Squares Between
SSE	Sum of Square Error
SSW	Sum of Squares Within
TCS	Transmission Cross Section

TE	Transverse Electric
TIS	Total Isotropic Sensitivity
TM	Transverse Magnetic
TRP	Total Radiated Power
TSCS	Total Scattering Cross Section
UE	User Equipment
VNA	Vector Network Analyzer

List of Publications

Journal Publications

[1] **T. Jia**, Y. Huang, Q. Xu, Z. Tian, J. Jiang, and Q. Hua, "Frequency Domain Method for Scattering Damping Time Extraction of a Reverberation Chamber Based on Autocorrelation Functions," *IEEE Trans. Electromagn. Compat.*, vol. 62, no. 6, pp. 2349-2357, Dec. 2020.

[2] **T. Jia**, Y. Huang, Q. Xu, Q. Hua, and L. Chen, "Average Rician K-Factor Based Analytical Uncertainty Model for Total Radiated Power Measurement in a Reverberation Chamber," *IEEE Access*, vol. 8, pp. 198078-198090, Oct. 2020.

[3] **T. Jia**, Y. Huang, Q. Xu, and Q. Hua, "Highest Usable Frequency Model for a Reverberation Chamber," *IEEE Antennas Wireless Propag. Lett.*, to be submitted.

[4] Q. Xu, W. Qi, C. Liu, L. Xing, D. Yan, Y. Zhao, **T. Jia,** and Y. Huang, "Measuring the Total Radiated Power of Wideband Signals in a Reverberation Chamber," *IEEE Antennas Wireless Propag. Lett.*, vol. 19, no. 12, pp. 2260-2264, Dec. 2020.

[5] Q. Xu, L. Xing, D. Yan, Y. Zhao, **T. Jia,** and Y. Huang, "A General Method to Calculate the Source-Stirred Correlations in a Well-Stirred Reverberation Chamber," *IEEE Lett. Electromagn. Compat. Practice Appl.*, vol. 2, no. 4, pp. 169-173, Dec. 2020.

[6] L. Li, X. Zhang, C. Song, W. Zhang, **T. Jia,** and Y. Huang, "Compact Dual-Band, Wide-Angle, Polarization-Angle-Independent Rectifying Metasurface for Ambient Energy Harvesting and Wireless Power Transfer," *IEEE Trans. Microw. Theory Techn.*, vol. 69, no. 3, pp. 1518-1528, Mar. 2021.

[7] Q. Hua, Y. Huang, A. Alieldin, C. Song, **T. Jia,** and X. Zhu, "A Dual-Band Dual-Polarized Base Station Antenna Using a Novel Feeding Structure for 5G Communications," *IEEE Access*, vol. 8, pp. 63710-63717, Mar. 2020.

[8] Q. Xu, L. Xing, Y. Zhao, **T. Jia,** and Y. Huang, "Identifying the Circular Polarization Handedness of an Antenna in a Reverberation Chamber," *IEEE Trans. Antennas Propag.*, vol. 68, no. 10, pp. 7228-7233, Oct. 2020.

[9] C. Song, E. L. Bennett, J. Xiao, **T. Jia**, R. Pei, K. Luk, and Y. Huang, "Passive Beam-Steering Gravitational Liquid Antennas," *IEEE Trans. Antennas Propag.*, vol. 68, no. 4, pp. 3207-3212, Apr. 2020.

[10] Q. Xu, L. Xing, Y. Zhao, **T. Jia,** and Y. Huang, "A Source Stirred Reverberation Chamber Using a Robotic Arm," *IEEE Trans. Electromagn. Compat.*, vol. 62, no. 2, pp. 631-634, Apr. 2020.

[11] Q. Hua, Y. Huang, C. Song, M. O. Akinsolu, B. Liu, **T. Jia**, Q. Xu, and A. Alieldin, "A Novel Compact Quadruple-Band Indoor Base Station Antenna for 2G/3G/4G/5G Systems," *IEEE Access*, vol. 7, pp. 151350-151358, Oct. 2019.

[12] Q. Xu, L. Xing, Y. Zhao, T. Loh, **T. Jia** and Y. Huang, "The Noise Level of Total Scattering Cross Section Measurement in a Reverberation Chamber," *IEEE Antennas Wireless Propag. Lett.*, vol. 17, no. 10, pp. 1842-1846, Oct. 2018.

[13] Q. Xu, L. Xing, Y. Zhao, **T. Jia,** and Y. Huang, "Use one-bit technique to measure the coherence in the time, frequency and space domain in a reverberation chamber," *IET Microw. Antennas Propag.*, vol. 13, no. 15, pp. 2632-2635, Apr. 2019.

Conference Publications

[1] **T. Jia**, Y. Huang, Q. Xu, Q. Hua, and L. Chen, "Fast and Accurate TRP Measurements Using a Reverberation Chamber," *Proc. Eur. Conf. Antennas Propag. (EuCAP)*, Düsseldorf, Germany, Mar. 2021.

[2] **T. Jia**, Y. Huang, and Q. Xu, "Investigation of Enhanced Backscatter Coefficient in a Reverberation Chamber in Frequency, Spatial and Power Domains," *Proc. Eur. Conf. Antennas Propag. (EuCAP)*, Krakow, Poland, Apr. 2019.

[3] Q. Xu, L. Xing, Y. Zhao, **T. Jia,** and Y. Huang, "The Measurable Range Issue in the Measurement of Enhanced Backscatter Coefficient in a Reverberation Chamber," *Proc. IEEE Int. Conf. Microw. Millim. Wave Technol. (ICMMT)*, Shanghai, China, Sep. 2020.

[4] M. Stanley, Y. Huang, H. Wang, H. Zhou, A. Alieldin, S. Joseph, C. Song, and **T. Jia**, "A Dual-Band Dual-Polarised Stacked Patch Antenna for 28 GHz and 39 GHz

5G Millimetre-Wave Communication," *Proc. Eur. Conf. Antennas Propag. (EuCAP)*, Krakow, Poland, Apr. 2019.

[5] A. Alieldin, Y. Huang, M. Stanley, S. Joseph, **T. Jia**, F. Elhouni and Q. Xu "A Camouflage Antenna Array Integrated with a Street Lamp for 5G Picocell Base Stations," *Proc. Eur. Conf. Antennas Propag. (EuCAP)*, Krakow, Poland, Apr. 2019.

[6] Q. Xu, L. Xing, D. Yan, Y. Zhao, **T. Jia**, and Y. Huang, "Experimental verification of stirrer angular correlation with different definitions in a reverberation chamber," *Proc. Int. Symp. Antennas, Propag. EM Theory*, Hangzhou, China, Dec. 2018.

[7] Q. Xu, L. Xing, J. Zhu, Y. Zhao, **T. Jia,** and Y. Huang, "Mixing Music Using Electromagnetic Reverberation Chamber," *Proc. Int. Symp. Antennas, Propag. EM Theory*, Hangzhou, China, Dec. 2018.

[8] Z. Fei, Y. Huang, J. Zhou, C. Song, and **T. Jia**, "Efficient stochastic analysis of transmission signal integrity for remote sensing applications," *Proc. IEEE Int. Symp. Electromagn. Compat. IEEE Asia Pac. Symp. Electromagn. Compat. (EMC/APEMC)*, Suntec City, Singapore, 2018.

Abstract

With the advent of the fifth-generation (5G) mobile communication systems, the rapid evolution of new wireless technologies makes the relevant measurement tasks unprecedently challenging. Although a perfect testing solution has not been developed yet, an agreement has been reached by both industry and academia that it is necessary to have the paradigm shift from conducted to over-the-air (OTA) in terms of measurement methodology.

Currently, there are primarily three eligible candidates for OTA testing, namely multi-probe anechoic chamber (MPAC), radiated two-stage (RTS), and reverberation chamber (RC). Each has its own advantages and disadvantages. The MPAC and RTS methods can be well modeled and analyzed by deterministic theories, and quantities of interest can typically be measured directly. In contrast, statistical theories are applied in the RC method, and post-processing is usually required. By utilizing multiple stirring techniques, an RC can statistically reproduce a uniform, isotropic, and polarization balanced electromagnetic (EM) environment, making it ideal for OTA measurement of non-directional parameters.

The ultimate objective of the RC in the category of OTA testing is to fulfill the industrial requirements and get fully standardized. RC characterization is pivotal to its standardization process since it is closely related to the RC performance evaluation, the optimum design of an RC, and the uncertain quantification of RC-based measurements. Therefore, this thesis aims at overcoming the limitations and problems that remain unsolved in the traditional RC characterization method, in particular: 1) the reliable characterization of the stirrer performance of an RC; 2) the accurate characterization of the statistical nonuniformity and anisotropy of an RC, and the analytical quantification of the RC-based OTA total radiated power (TRP) measurement uncertainty; 3) the study of the highest usable frequency (HUF) of an RC, and the fast characterization of the RC-based measurement system in terms of the frequency of operation and the output power level. It is believed that this thesis further improves and optimizes the traditional RC characterization methodology, which contributes to the standardization process of the RC for OTA testing.

For the first aspect, the scattering damping time can provide a reliable and repeatable evaluation of an RC's stirrer performance, which is independent of the amount of extra loading or the position of the measurement antennas. By constructing two frequency domain autocorrelation functions (ACFs), the scattering damping time can be directly extracted from measured S-parameters without the need to perform the inverse Fourier transform (IFT). Compared with the conventional IFT-based method, this novel method has a wider dynamic range and does not involve selecting the fitting range manually. As a result, the data post-processing can be significantly simplified. Meanwhile, it retains several advantages of the IFT-based method, such as independent of the radiation efficiency and input impedance of the measurement antennas.

For the second aspect, the statistical anisotropy of an RC can be accurately quantified by the average Rician *K*-factor, which is only sensitive to the loading conditions. In order to accurately estimate the value of the average Rician *K*-factor, an unbiased maximum likelihood estimator (MLE) is given. Based on the statistical properties of the average Rician *K*-factor, an improved analytical uncertainty model for the RC-based TRP measurement is derived. Compared with the traditional uncertainty model, the proposed model is more accurate. Besides, it allows different experimental configurations in the calibration stage and the measurement stage, which sheds light on the best practice for RC-based TRP measurement. Furthermore, the proposed analytical model enables fast characterization of the measurement uncertainty without tedious and inefficient empirical estimation processes.

For the third aspect, the enhanced backscattering phenomenon inside an RC is first investigated in the frequency domain, spatial domain, and power domain. Then, based on the investigation findings, a theoretical HUF model of an RC is given. Detailed analysis, as well as the physical meaning of the proposed HUF model, are provided. An iterative algorithm is also developed for efficient calculation. It is the first comprehensive study of the HUF of an RC. With the help of the proposed HUF model, the RC-based measurement system can be fast characterized in terms of the frequency of operation and the output power level. Besides, it also provides guidance on how to optimize the existing system setup for improved HUF.

Chapter 1 Introduction

1.1 Research Background

The past few years have seen the prosperity of the emerging fifth-generation (5G) wireless communication networks. Generally speaking, 5G improves the performance of the existing broadband cellular networks to an unforeseen level by accommodating a much higher data rate, greater capacity, lower latency, and higher connection density. These advancements open up the potential for many ground-breaking services and applications like virtual reality, Autonomous driving, remote surgery, *etc*. That is why 5G is not called "4G+". While incessantly reshaping our way of life, 5G also introduce numerous challenges to the instrumentation and measurement community [1] – [4].

Over-the-air (OTA) testing, as its name indicates, is defined as the radiated method to test the performance of the device under test (DUT) without the requirement of the transmission line connection. Traditionally, tests for wireless devices are usually done using conducted approach, which combines separate tests of modem chipsets and radio frequency (RF) components. However, this is no longer the case in the 5G era. Among various enabling technologies for 5G, three of them are representative: millimeter-wave (mm-wave), massive multi-input multi-output (massive MIMO), and adaptive beamforming (as illustrated in Figure 1.1) [5]. Massive MIMO is composed of a large number of antenna elements, which focus the radiated energy towards the desired directions of propagation and serve multiple users simultaneously using the entire frequency spectra resources. Nevertheless, due to its high degree of integration, an individual antenna port in a typical massive MIMO system is no longer accessible. The use of adaptive antenna technology for beamforming renders the system level radiation performance considerably different from the simple combination of the test results of individual components. Consequently, the paradigm shift in terms of testing methodology from conducted to OTA becomes necessary. In addition, moving towards the mm-wave

spectrum for increased carrier bandwidth also leads to unforeseen issues for OTA testing, such as the unrealistic requirement for far-field conditions, increased insertion loss, *etc.*

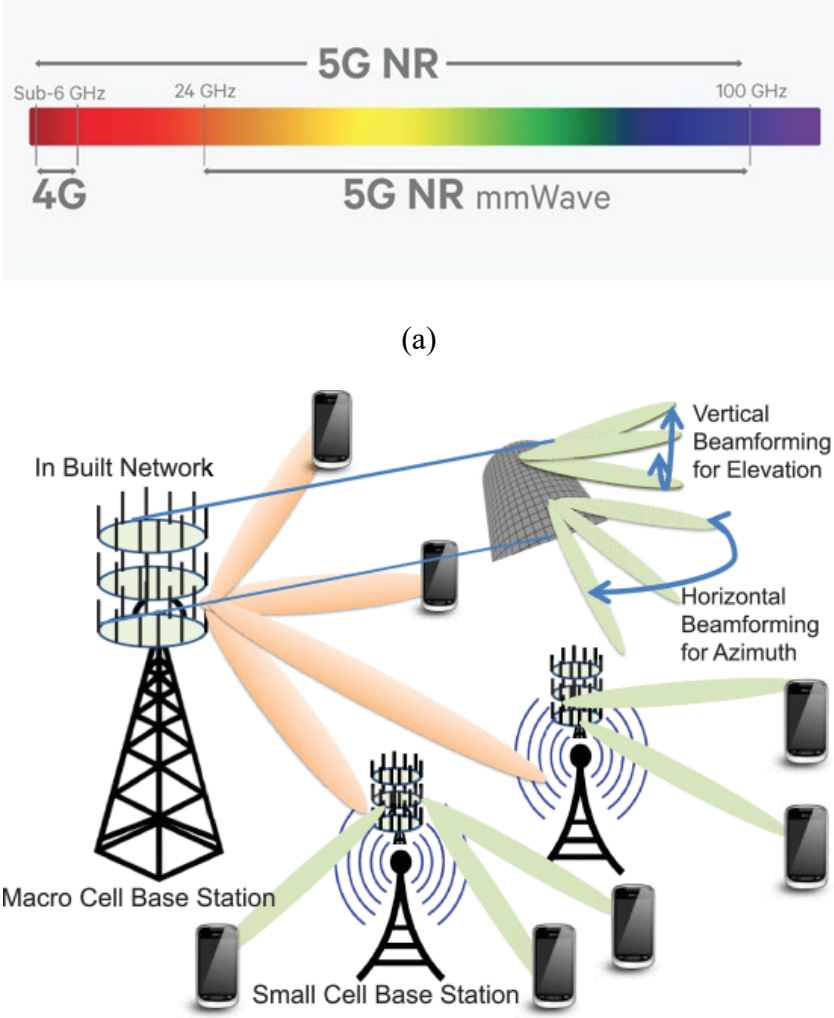

Figure 1.1: Key enabling technologies for 5G: (a) 5G new radio (NR) including mm-wave. (b) Massive MIMO and adaptive beamforming [5].

Hitherto, multi-probe anechoic chamber (MPAC) [6] – [12], radiated two-stage (RTS) [13] – [18], and reverberation chamber (RC) [19] – [38] are the three most promising candidate facilities for OTA testing of 5G enabled wireless devices. They will be introduced in Section 1.1.1, Section 1.1.2, and Section 1.1.2, respectively.

1.1.1 Multi-Probe Anechoic Chamber Method

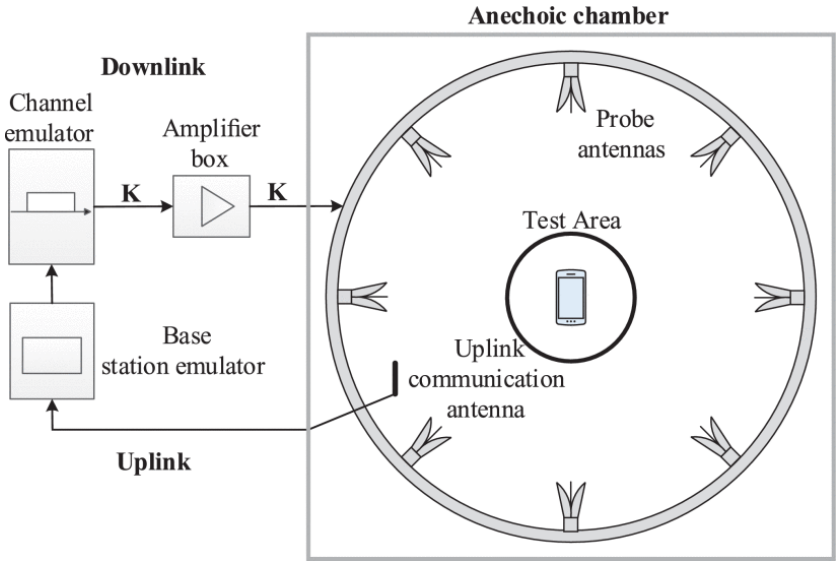

(a)

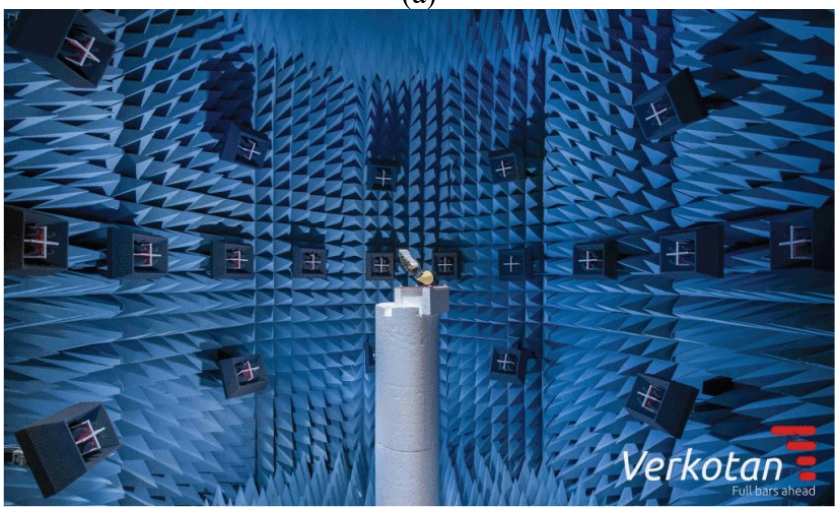

(b)

Figure 1.2: (a) Schematic diagram of the MPAC system. (b) Photo of the 3D MPAC OTA setup [8].

A typical MPAC system primarily comprises the following components [6] – [8]: a communication tester, one or multiple channel emulators, power amplifiers, an anechoic chamber (AC), and a number of dual-polarized probe antennas (as illustrated in Figure 1.2 (a)). There is a geometric zone (usually in a spherical shape) at the center of the MPAC, named the test area. Standard spatial channel models and intended channel impairments such as Doppler and fading can be accurately emulated within the

test area [9]. The core idea of the MPAC based test method is to arrange multiple probe antennas around the DUT either in two-dimensional (2D) or three-dimensional (3D) for field synthesis [10]. A photograph of a 3D MPAC OTA setup is available in Figure 1.2 (b). The outputs of the probe antennas are generated and controlled by the channel emulator.

MPAC has been standardized by Cellular Telecommunication and Internet Association (CTIA) and 3rd Generation Partnership Project (3GPP) for OTA testing of MIMO enabled user equipment (UE) [9]. Since the test environment is based on pure line-of-sight (LoS), the characterization and measurement processes of the MPAC approach are straightforward. It also has the highest potential for generating arbitrary practical wireless channels with specified temporal, angular, and polarization characteristics in a reliable, repeatable, and feasible manner [11], [12]. However, there are also several major concerns for this method:1) extremely high system cost; 2) complex and time-consuming calibration and alignment procedures; 3) the available test area is relatively small and limited by the number of probe antennas.

1.1.2 Radiated Two-Stage Method

The conducted two-stage (CTS) approach (as shown in Figure 1.3 (a)) has also been adopted by standard organizations for MIMO OTA tests [13], [14]. As its name indicates, implementation of this method requires two separate stages. In the first stage, the full 3D radiation patterns of the DUT with two orthogonal polarizations are measured in a single-input-single-output (SISO) AC. In the second stage, the transmitting signal generated by the communication tester, the wireless channel emulated by the channel emulator, and the radiation patterns measured in the first stage are combined and then fed into the DUT through RF cables. The CTS method only requires a SISO AC equipped with a dual-polarized probe antenna and a rotating platform, which is less expensive than the MPAC method. Moreover, it is capable of reproducing realistic 3D channels with a much simpler configuration and setup. Nonetheless, the second stage of CTS requires conducted access to individual antenna ports, which is intrusive and might be impractical for the commercialized DUT with integrated MIMO antennas. Besides, the CTS method cannot evaluate the mutual coupling of the antenna elements

on the DUT, which might be a potential issue causing the degradation of the overall MIMO performance [14].

The RTS approach (as illustrated in Figure 1.3 (b)) improves the CTS method by implementing the second stage OTA in an AC [14] – [16]. The core idea is to derive the static calibration matrix between the MIMO antennas on the DUT and the probe antennas, and then invert it to obtain the desired signals to be fed into the probe antennas. Both stages of the RTS method utilize the pure LoS environment created by the AC so that the characterization processes can be directly performed based on deterministic theories. Given the same chamber size, the available test area of the RTS method is usually larger than that of the MPAC method. The main concerns of the RTS method are: 1) the number of probe antennas should be equal to that of the antenna elements on the DUT [14]; 2) 3D radiation patterns of both the DUT and the probe antenna array are required, and the DUT should support both amplitude and relative phase measurements; 3) in some cases it is not easy to invert the static calibration matrix [17], [18]; 4) it is not suitable for measuring adaptive antenna systems whose radiation patterns are continuously changing.

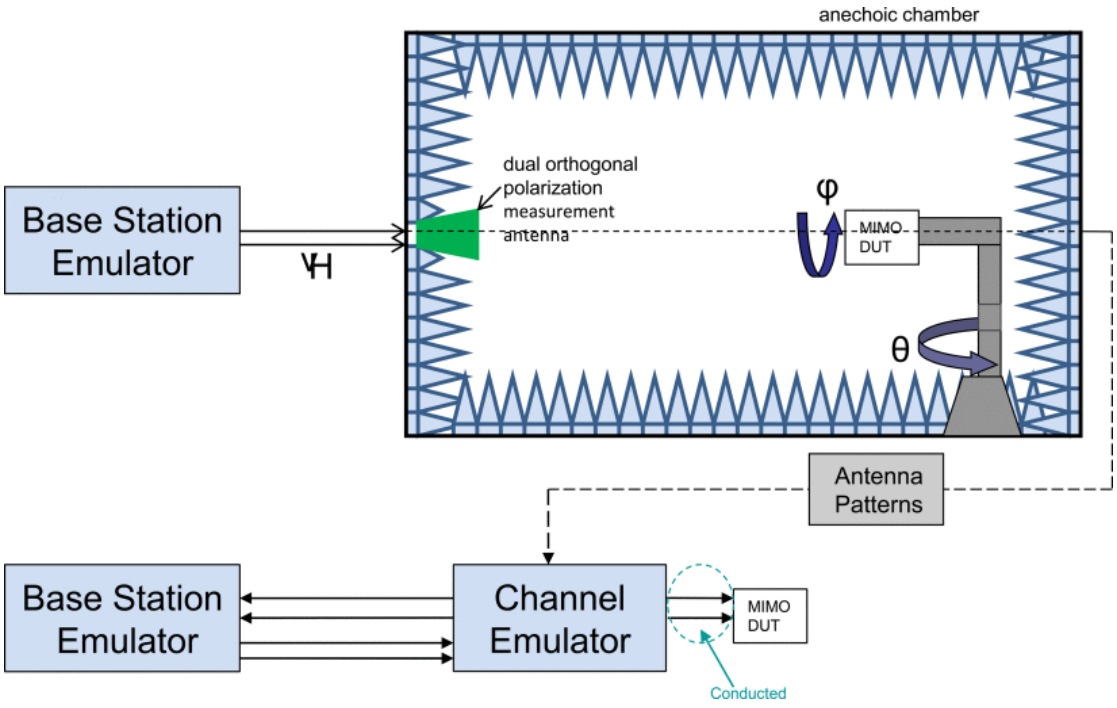

(a)

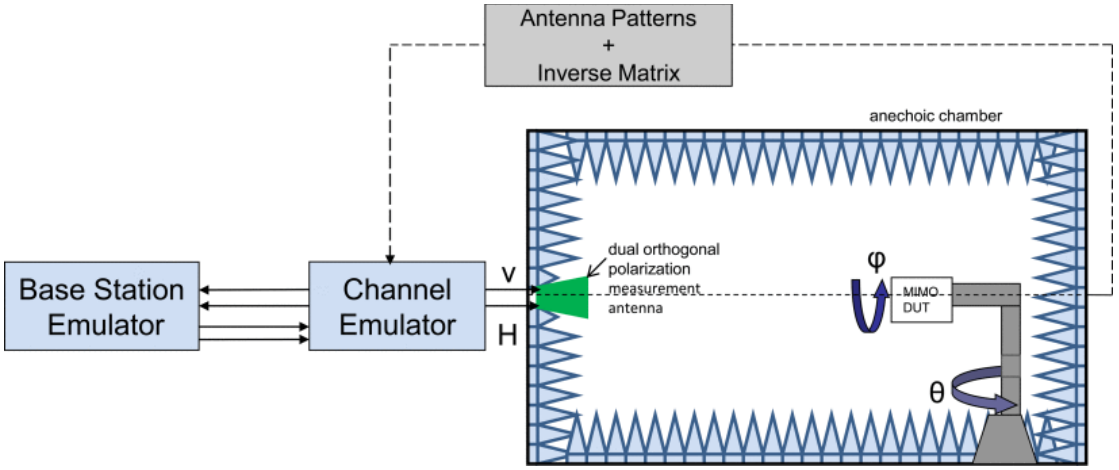

(b)

Figure 1.3: (a) Schematic diagram of the CTS system. (b) Schematic diagram of the RTS system [14].

1.1.3 Reverberation Chamber Method

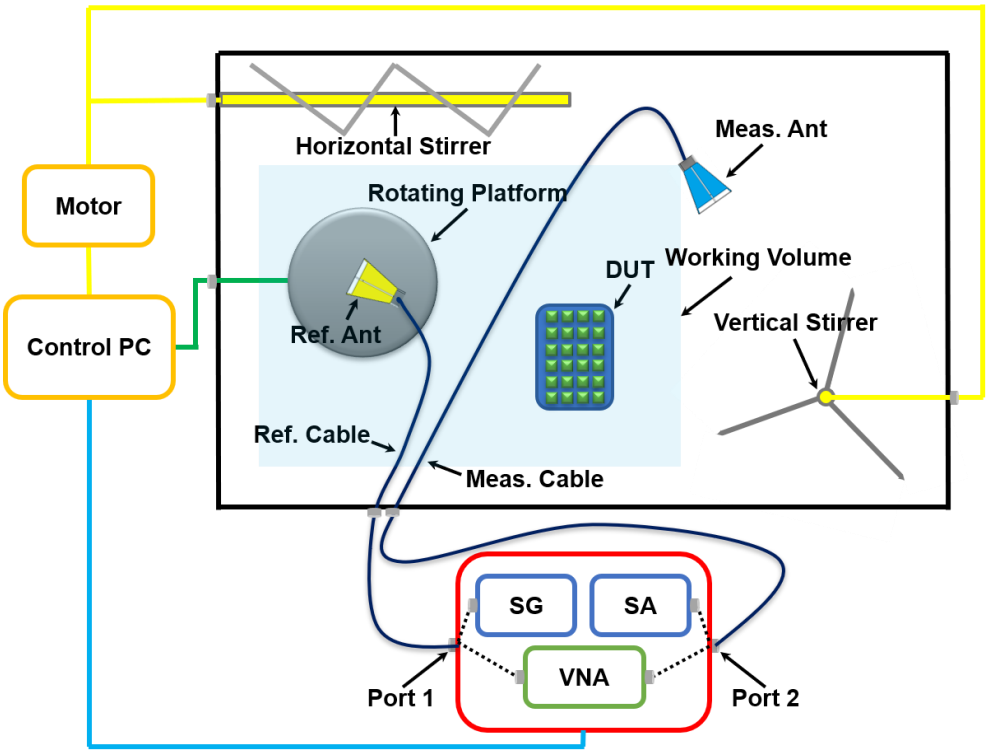

(a)

(b) (c)

Figure 1.4: (a) Schematic diagram of the RC system. (b) The RC at the Nanjing University of Aeronautics and Astronautics. (c) The RC at the University of Liverpool.

Essentially, an RC is an electrically large shielded cavity, where the electromagnetic (EM) signal emitted by a single source is reflected and diffused multiple times by metallic walls before it is received by the probe antenna [19] – [21]. Inside an RC, stirring facilities like mechanical stirrers and rotating platforms are installed so that the EM boundary conditions can be effectively altered to provide a stochastic environment [22]. The schematic diagram of an RC system with all necessary components is shown in Figure 1.4 (a). RCs are usually designed to be rectangular-shaped, but they come in various sizes and configurations for different application scenarios. Figure 1.4 (b) and Figure 1.4 (c) show the RC at the Nanjing University of Aeronautics and Astronautics and the RC at the University of Liverpool, respectively, for comparison. Different from the MPAC and RTS methods, which are based on the LoS environment and the channel emulator, the RC method utilizes the non-line-of-sight (NLoS) environment to statistically reproduce a spatially homogeneous, isotropic, and polarization balanced wireless channel. This unique property makes the RC method a fast and cost-effective candidate in the wireless community for OTA tests, especially on non-directional parameters such as antenna efficiency, diversity gain, antenna correlation, MIMO

capacity, total radiated power (TRP), and total isotropic sensitivity (TIS) [23] – [28]. Important channel characteristics including the delay spread/coherence bandwidth [29], Doppler effect/coherence time [30], Rician *K*-factor [31] of the wireless channel created by the RC can also be controlled and adjusted.

Compared with the MPAC and RTS methods, the RC method can be much more cost-effective since it does not require the radio absorbing material and the channel emulator. Given the same chamber size, the available test area of the RC method is the largest among the three. The RC method's measurement setup and calibration process are also much more straightforward without any requirement for precise probe alignment and rotation of the DUT. Besides, it has been proved in [32] that there is no need to fulfill the far-field condition for the RC-based measurements, which makes it an attractive solution for testing wireless devices working at mm-wave bands. To date, the RC has already been standardized for OTA measurements of UE [33] and large-form-factor machine-to-machine (M2M) devices [34], and its certification in terms of the base station (BS) tests [35] is ongoing. Worldwide, there are many institutions and universities that are engaged in RC-related research. To name a few, the National Institute of Standards and Technology (NIST) in the United States of America, the University of Liverpool and the National Physical Laboratory (NPL) in the United Kingdom, the Institute of Electronics and Telecommunications of Rennes in France, the Chalmers University of Technology in Sweden, the Nanjing University of Aeronautics and Astronautics and the National Institute of Metrology (NIM) in China, *etc*. Meanwhile, there are key manufactures like ETS-Lindgren, Bluetest, and Emite that can provide either standalone RC or the complete RC-based measurement system.

However, the RC method also has its limitations: 1) the RC method has limited control in its reproduced wireless channel, especially the spatial domain profiles; 2) due to its statistical environment, the RC characterization process is much more complicated than that of the MPAC and RTS.

A table of comparison for the MPAC method, the RTS method, and the RC method is shown below:

Table 1-I: Comparison of the 3 candidate OTA testing methods

Method	Advantages	Disadvantages
MPAC	☑ Can emulate wireless channels with different angular domain distributions ☑ The implementation is straightforward ☑ Simple characterization ☑ Easy post-processing procedures	☒ Extremely high cost due to the use of channel emulator and multiple probes ☒ Even higher cost if the MPAC updated to emulate 3D wireless channels ☒ Complex calibration procedures and rigorous probe alignment requirement ☒ The available test area is small compared to its physical dimension
RTS	☑ Can reproduce arbitrary 2D or 3D spatial channels ☑ The traditional SISO AC can be reused ☑ Less expensive ☑ Simple characterization	☒ Radiation pattern information is required for the DUT antenna ☒ Complex calibration procedures ☒ Slow test speed ☒ In some cases, inverting the static calibration matrix can be impractical
RC	☑ Ideal for measurement of non-direction parameters like TRP and TIS without using the channel emulator ☑ Cost effective ☑ There is no need to fulfill the far field condition requirement ☑ Large available test area ☑ Easy setup, simple calibration	☒ Limited control over the spatial profiles ☒ Complex, inaccurate, and incomplete characterization process ☒ Have problems like the double-Rayleigh effect when the channel emulator is combined with the RC

1.2 Research Motivation and Objective

Although the RC method has attracted increasingly widespread attention from both industry and academia over the past few years, its standardization process for OTA testing on wireless devices is still slower than the MPAC method and RTS method [3],

[4], [9], [21], [33] – [35]. One primary limiting factor is the complicated, experience-dependent, and yet incomplete research and practice for RC characterization.

Owing to its complex and unpredictable EM environment, studying and applying an RC from the statistical perspective is much more suitable and feasible [19], [20]. Besides, some well-known parameters and quantities, *e.g.*, average Rician *K*-factor, enhanced backscatter coefficient, in the context of the RC only have statistical meanings. This potentially makes the characterization processes for an RC much more complicated than MPAC and RTS, which can be well characterized based on deterministic theories.

Conventionally, one fundamental assumption for the RC-based OTA testing is that individual measurement results are random-like. More precisely, rectangular components of the EM field generated within the working volume of the RC should be independent and identically distributed (*i.i.d*) circular Gaussian random variables centered at 0 [19]. Ideally, it can be mathematically proved using the Central Limit Theorem (CLT). However, whether and to what extent this assumption could differ in practice is to date challenging to answer, especially in measurement scenarios where the RC extends its usage by changing the stirrer configuration, experimental setup, and frequency of operation. This discrepancy, if not correctly characterized and compensated, would introduce non-negligible error on measurement results.

The anticipation of accurate, reliable, and repeatable processes for RC characterization has led researchers to three main questions:

1. How to reliably characterize and evaluate the stirrer performance of an RC for arbitrary stirrer configurations so that people can tell whether the RC is working at "well-stirred" conditions?
2. How to accurately characterize the RC's statistical anisotropy generated either unintentionally (*e.g.*, the loading effect or proximity effect of the DUT itself) or on purpose (*e.g.*, strategically load the RC for desired channel properties)? How to analytically quantify the influence of statistical anisotropy on the uncertainty of RC-based OTA TRP measurement?
3. How to characterize an RC at a specific frequency of operation and output power level? Is there a highest usable frequency (HUF) for an RC in addition to its well-known lowest usable frequency (LUF)? If yes, what are the influencing factors for

it? Is there an explicit expression for the HUF?

For **Question 1**, many efforts have been made for quantifying the stirrer efficiency [36] – [39]. In [36], the stirrer efficiency is defined based on the Rician *K*-factor, which could change drastically with different loading conditions or antenna orientations. [37] defines the stirrer efficiency as a function of the independent sample number, but it is still sensitive to the loading conditions. A similar problem also can be found in [38], which tries to define it in the time domain. In [39], the stirrer efficiency is defined based on the scattering damping time, and it is robust against loadings or the positions of the measurement antenna. In order to extract the scattering damping time, a time domain method using the inverse Fourier transform (IFT) is adopted in [39]. However, this method has several drawbacks: 1) the range of the time domain response used for the least square fitting is selected empirically, which introduces non-negligible error; 2) the signal to noise ratio (SNR) of the unstirred power envelope is relatively low, which significantly reduces the available measurement range; 3) in order to perform the IFT, a digital filter is usually needed, and the number of samples required is the same as that of the initial frequency response obtained from the VNA, regardless of the desired resolution bandwidth. Therefore, an improved method for calculating the scattering damping time is crucial to ensure reliable stirrer performance characterization [40].

For **Question 2**, to accurately characterize the uncertainty of an RC, both the sample correlation and the statistical anisotropy should be quantified and corrected. So far, numerous studies have been conducted in this field [21], [22], [25], [41] – [43]. Conventionally, the Rician *K*-factor is used to measure this statistical anisotropy effect. Nevertheless, there are several concerns: 1) the value of the Rician *K*-factor actually varies when using source stir and frequency stir; 2) it is hard, if not impossible, to acquire the accurate value of the Rician *K*-factor when measuring the DUT; 3) the reference measurement of the Rician *K*-factor is meaningless since it is sensitive to antenna position and orientation. Consequently, the average Rician *K*-factor, which is only sensitive to the loading conditions, should be used instead. The average Rician *K*-factor is first adopted by [22] for RC uncertainty characterization, but the corresponding model is based on empirical assumptions. The model in [41] is based on the components-of-variance model, and the Rician *K*-factor that appeared in the expression is equivalent to the average Rician *K*-factor when source stirring is utilized. However, there is no information about the statistical property of the average Rician *K*-factor and

how to estimate it. [42] directly pooled multiple single-case Rician *K*-factor values, which is mathematically viable but lacks physical meaning and explanation. Furthermore, the RC-based OTA TRP measurement actually consists of two stages: the calibration stage and the measurement stage. The reference transfer function is estimated between the reference antenna and the measurement antenna in the calibration stage. In the measurement stage, the signal radiated by the DUT is measured by the measurement antenna. The uncertainty of each stage should be characterized so as to derive an accurate overall uncertainty model [25]. The model in [42] is the only one that takes both stages into consideration, but it is not purely analytical.

For **Question 3**, the signal measured by the RC-based measurement system can be divided into two components: the desired signal and the undesired noise. They can be modeled as two independent random variables, which jointly determine the statistical property of the measured signal [44]. It is commonly assumed that the desired component dominates the measured signal [25], [26], [43]. However, with the increased frequency of operation or the decreased output power, the influence of the noise gradually becomes more significant. Eventually, the statistical property of the measured signal could be completely altered by the noise, which makes the RC virtually unusable. This implies that in addition to the well-known LUF, there exists a HUF for an RC, which is determined by the system SNR. To analytically quantify the HUF, an explicit theoretical model which includes all influencing factors is desired. If such a model could be derived, fast characterization and evaluation of the RC-based measurement system at a particular frequency of operation and output power level could become possible, and the system setup could be optimized accordingly for improved HUF [44]. Statistical analysis of the noise in an RC-based system can be found in various researches [22], [41], [42]. However, in these researches, the effect of the noise on the RC characterization is only qualitative, and no in-depth study is available. Furthermore, no one has linked the noise or SNR to the HUF of an RC, and no explicit analytical expression of the HUF has been given.

The objective of this thesis is to deal with the above three aspects [25], [40], [44] for more comprehensive and reliable RC characterization processes, thereby laying a solid foundation for promoting the RC as a fully standardized facility for OTA testing.

1.3 Thesis Organization

The contents of this thesis are organized in the following manner:

Chapter 2 is to review the fundamental theories for the RC characterization so that a solid foundation can be built for the novel characterization techniques elaborated in subsequent chapters, which are more specific and orientated.

To characterize the stirrer performance of an RC more reliably and efficiently, in **Chapter 3,** a novel frequency domain method is proposed for calculating the scattering damping time [40]. By utilizing the frequency domain autocorrelation function (FD-ACF) and the unstirred frequency domain autocorrelation function (FD-ACFUS), the scattering damping time can be directly calculated from measured S-parameters without the need of performing the IFT. Mathematical derivation is given based on the Wiener-Khinchin theorem, and experimental measurements are conducted with different frequency bands and different stirrer configurations to verify the proposed approach. Compared with the conventional IFT-based method, the proposed method has a wider dynamic range and does not involve the procedure of manually selecting the fitting range. As a result, the data post-processing can be greatly simplified. Meanwhile, it retains several advantages of the IFT-based method, such as independent of the radiation efficiency and input impedance of the measurement antennas.

In **Chapter 4**, it is shown in the first place that the statistical property of the average Rician *K*-factor plays a pivotal role in the accurate characterization of the statistical anisotropy in an RC. Estimators of the average Rician *K*-factor are modeled and analyzed based on different assumptions. Specifically, the maximum likelihood estimator (MLE) of the average Rician *K*-factor is formulated and validated by the Monte Carlo simulation, and its unbiased correction is derived accordingly [25]. Then the RC is applied to the OTA TRP measurement, and an improved analytical uncertainty model is established based on the average Rician *K*-factor and the number of independent samples [25]. Compared with the conventional uncertainty model, the proposed model is more accurate, and it allows different experimental configurations in the calibration stage and the measurement stage. This makes it possible to characterize the measurement dispersion without tedious and inefficient empirical estimation processes. Extensive 9-Point estimation measurements are also conducted to

evaluate the performance of the proposed analytical model.

Engineering practices indicate that in addition to the well-known LUF, there exists a HUF for the RC-based measurement system. In **Chapter 5**, a thorough investigation of the enhanced backscatter coefficient in terms of the frequency, power, and spatial domains is first conducted for the RC characterization. An explicit HUF model is then derived based on the statistical distributions of the average power of the desired received signal and the corresponding average noise power [44]. The physical explanation of the HUF model proves that it essentially reflects the system SNR. More precisely, the HUF should be a function of the chamber volume, chamber decay constant, cable losses, the power level of the transmitting signal, sensitivity of the measurement equipment, *etc*. Nonetheless, the HUF should be insensitive to the spatial domain parameters such as location, orientation, and polarization within the working volume of the RC. Detailed analysis and discussion of each term in the HUF expression are also given. An iterative algorithm is developed to address the problem that frequency-dependent terms are included in the HUF expression. Experimental validation in terms of different output power levels demonstrates that good agreement between the experimental estimation and the proposed HUF model is achieved.

Chapter 6 summarizes the key contributions and highlighted the importance and impact of this thesis. Suggestions for future research directions are also given.

1.4 References

[1] M. D. Foegelle, "The future of MIMO over-the-air testing," *IEEE Commun. Mag.*, vol. 52, no. 9, pp. 134–142, Sep. 2014.

[2] Y. Qi *et al*., "5G over-the-air measurement challenges: Overview," *IEEE Trans. Electromagn. Compat.*, vol. 59, no. 6, pp. 1661–1670, Dec. 2017.

[3] K. A. Remley *et al*., "Measurement challenges for 5G and beyond: An update from the National Institute of Standards and Technology," *IEEE Microw. Mag.*, vol. 18, no. 5, pp. 41–56, Jul./Aug. 2017.

[4] P. Zhang, X. Yang, J. Chen, and Y. Huang, "A survey of testing for 5g: Solutions, opportunities, and challenges," *China Communications.*, vol. 16, no. 1, pp. 69–85, Jan 2019.

[5] M. Agiwal, A. Roy, and N. Saxena, "Next generation 5G wireless networks: A comprehensive survey," *IEEE Commun. Surveys Tut.*, vol. 18, no. 3, pp. 1617–1655, 3rd Quart., 2016.

[6] P. Kyösti, T. Jämsä, and J. P. Nuutinen, "Channel modelling for multiprobe over-the-air MIMO testing," *Int. J. Antennas Propag.*, vol. 2012, Mar. 2012.

[7] W. Fan, X. de Lisbona, F. Sun, J. Nielsen, M. Knudsen, and G. Pedersen, "Emulating spatial characteristics of MIMO channels for OTA testing," *IEEE Trans. Antennas Propag.*, vol. 61, no. 8, pp. 4306–4314, Aug. 2013.

[8] W. Fan, I. Carton, P. Kyosti, and G. F. Pedersen, "Emulating ray-tracing channels in multiprobe anechoic chamber setups for virtual drive testing," *IEEE Trans. Antennas Propag.*, vol. 64, no. 2, pp. 730–739, Feb. 2016.

[9] *Study on radiated metrics and test methodology for the verification of multi-antenna reception performance of NR User Equipment (UE)*, 3GPP Std. TR 38.827, Rev. V16.1.0, Jan. 2021.

[10] W. Fan, X. Carreno, P. Kyosti, J. Nielsen, and G. Pedersen, "Over the-air testing of MIMO-capable terminals: Evaluation of multiple antenna systems in realistic multipath propagation environments using an OTA method," *IEEE Veh. Technol. Mag.*, vol. 10, no. 2, pp. 38–46, Jun. 2015.

[11] P. Kysti, L. Hentil, W. Fan, J. Lehtomki, and M. Latva-Aho, "On radiated performance evaluation of massive MIMO devices in multiprobe anechoic chamber OTA setups," *IEEE Trans. Antennas Propag.*, vol. 66, no. 10, pp. 5485–5497, Oct. 2018.

[12] W. Fan, F. Zhang, and Z. Wang, "Over-the-Air Testing of 5G Communication Systems: Validation of the Test Environment in Simple-Sectored Multiprobe Anechoic Chamber Setups," *IEEE Antennas Propag. Mag.*, vol. 63, no. 1, pp. 40-50, Feb. 2021.

[13] Y. Jing, X. Zhao, H. Kong, S. Duffy, and M. Rumney, "Two-stage over the air (OTA) test method for LTE MIMO device performance evaluation," *Int. J. Antennas Propag.*, vol. 2012, art. Mar. 2012.

[14] W. Yu, Y. Qi, K. Liu, Y. Xu, and J. Fan, "Radiated two-stage method for LTE MIMO user equipment performance evaluation," *IEEE Trans. Electromagn. Compat.*, vol. 56, no. 6, pp. 1691–1696, Dec. 2014.

[15] W. Fan, P. Kysti, L. Hentil, and G. F. Pedersen, "MIMO terminal performance evaluation with a novel wireless cable method," *IEEE Trans. Antennas Propag.*, vol. 65, no. 9, pp. 4803–4814, Sep. 2017.

[16] P. Shen, Y. Qi, W. Yu, and F. Li, "Eliminating RSARP reporting errors in the RTS method for MIMO OTA test," *IEEE Trans. Electromagn. Compat.*, vol. 59, no. 6, pp. 1708–1715, Dec. 2017.

[17] P. Shen, Y. Qi, W. Yu, and F. Li, "Inverse matrix auto-search technique for the RTS MIMO OTA test—Part 1: Theory," *IEEE Trans. Electromagn. Compat.*, vol. 59, no. 6, pp. 1716–1723, Dec. 2017.

[18] P. Shen, Y. Qi, W. Yu, and F. Li, "Inverse matrix auto-search technique for the RTS MIMO OTA test—Part II: Validations," *IEEE Trans. Electromagn. Compat.*, vol. 60, no. 5, pp. 1288–1295, Oct. 2018.

[19] D. A. Hill, Electromagnetic Fields in Cavities, Piscataway, NJ, USA: IEEE Press, 2009.

[20] Q. Xu and Y. Huang, Anechoic and Reverberation Chambers: Theory, Design and Measurements, Wiley-IEEE, UK, 2019.

[21] X. Chen, J. Tang, T. Li, S. Zhu, Y. Ren, Z. Zhang, and A. Zhang, "Reverberation Chambers for Over-the-Air Tests: An Overview of Two Decades of Research," *IEEE Access.*, vol. 6, pp. 49129–49143, Aug. 2018.

[22] P.-S. Kildal, X. Chen, C. Orlenius, M. Franzén, and C. S. L. Patané, "Characterization of reverberation chambers for OTA measurements of wireless devices: Physical formulations of channel matrix and new uncertainty formula," *IEEE Trans. Antennas Propag.*, vol. 60, no. 8, pp. 3875–3891, Aug. 2012.

[23] C. L. Holloway, H. Shah, R. J. Pirkl, W. Young, J. Ladbury, and D. A. Hill, "Reverberation chamber techniques for determining the radiation and total efficiency of antennas," *IEEE Trans. Antennas Propag.*, vol. 60, no. 4, pp. 1758–1770, Apr. 2012.

[24] K. Rosengren and P.-S. Kildal, "Radiation efficiency, correlation, diversity gain, and capacity of a six monopole antenna array for a MIMO system: Theory simulation and measurement in reverberation chamber," *Proc. Inst. Elect. Eng. Microwave Antennas Propag.*, vol. 152, no. 1, pp. 7-16, Feb. 2005.

[25] T. Jia, Y. Huang, Q. Xu, Q. Hua, and L. Chen, "Average Rician K-Factor Based Analytical Uncertainty Model for Total Radiated Power Measurement in a Reverberation Chamber," *IEEE Access*, vol. 8, pp. 198078-198090, Oct. 2020.

[26] Q. Xu, W. Qi, C. Liu, L. Xing, D. Yan, Y. Zhao, T. Jia, and Y. Huang, "Measuring the Total Radiated Power of Wideband Signals in a Reverberation Chamber," *IEEE Antennas Wireless Propag. Lett.*, vol. 19, no. 12, pp. 2260-2264, Dec. 2020.

[27] R. D. Horansky, T. B. Meurs, M. V. North, C.-M. Wang, M. G. Becker, and K. A. Remley, "Statistical considerations for total isotropic sensitivity of wireless devices measured in reverberation chambers," in Proc. *Int. Symp. Electromagn. Compat. (EMC EUROPE),* pp. 398–403, Aug. 2018.

[28] W. Xue, F. Li, X. Chen, S. Zhu, A. Zhang, and T. Svensson, "A Unified Approach for Uncertainty Analyses for Total Radiated Power and Total Isotropic Sensitivity Measurements in Reverberation Chamber," *IEEE Trans. Instrum. Meas.*, vol. 70, pp. 1-12, Nov. 2021.

[29] E. Genender, C. L. Holloway, K. A. Remley, J. M. Ladbury, G. Koepke, and H. Garbe, "Simulating the multipath channel with a reverberation chamber: Application to bit error rate measurements," *IEEE Trans. Electromagn. Compat.*, vol. 52, no. 4, pp. 766–777, Nov. 2010.

[30] C. L. Holloway, D. A. Hill, J. M. Ladbury, P. F. Wilson, G. Koepke, and J. Coder, "On the use of reverberation chambers to simulate a Rician radio environment for the testing of wireless devices," *IEEE Trans. Antennas Propag.*, vol. 54, no. 11, pp. 3167–3177, Nov. 2006.

[31] K. Karlsson, X. Chen, J. Carlsson, and A. Skarbratt, "On OTA test in the presence of Doppler spreads in a reverberation chamber," *IEEE Antennas Wireless Propag. Lett.*, vol. 12, pp. 886–889, Jul. 2013.

[32] X. Chen, "On near-field and far-field correlations in reverberation chambers," *IEEE Microw. Wireless Compon. Lett.*, vol. 29, no. 1, pp. 74–76, Jan. 2019.

[33] *User Equipment (UE) / Mobile Station (MS) Over The Air (OTA) antenna performance; Conformance testing*, 3GPP Std. TS 34.114, Rev. V12.2.0, Sep. 2016.

[34] *Test Plan for Wireless Large-Form-Factor Device Over-the-Air Performance*, CTIA, ver. 1.2.1, Feb. 2019.

[35] *Radio Frequency (RF) conformance testing background for radiated Base Station (BS) requirements*, 3GPP Std. TR 37.941, Rev. V16.0.1, Jun. 2020.

[36] C. Lemoine, E. Amador, and P. Besnier, "Mode-stirring efficiency of reverberation chambers based on Rician K-factor," *Electron. Lett.*, vol. 47, no. 20, pp. 1114–1115, Sep. 2011.

[37] F. Moglie and V. M. Primiani, "Analysis of the independent positions of reverberation chamber stirrers as a function of their operating conditions," *IEEE Trans. Electromagn. Compat.*, vol. 53, no. 2, pp. 288–295, May 2011.

[38] G. Esposito, G. Gradoni, F. Moglie, and V. M. Primiani, "Stirrer performance of reverberation chambers evaluated by time domain fidelity," *in Proc. IEEE Int. Symp. Electromagn. Compat.*, Denver, CO, USA, pp. 207–216, 2013.

[39] Q. Xu, Y. Huang, L. Xing, Z. Tian, M. Stanley, and S. Yuan, "B-scan in a reverberation chamber," *IEEE Trans. Antennas Propag.*, vol. 64, no. 5, pp. 1740–1750, May 2016.

[40] T. Jia, Y. Huang, Q. Xu, Z. Tian, J. Jiang, and Q. Hua, "Frequency Domain Method for Scattering Damping Time Extraction of a Reverberation Chamber Based on Autocorrelation Functions," *IEEE Trans. Electromagn. Compat.*, vol. 62, no. 6, pp. 2349-2357, Dec. 2020.

[41] K. A Remley, R. J Pirkl, H. A Shah, and C.-M. Wang, "Uncertainty from choice of mode-stirring technique in reverberation-chamber measurements," *IEEE Trans. Electromagn. Compat.*, vol. 55, no. 6, pp. 1022– 1030, Dec. 2013.

[42] K. A. Remley, C.-M. J. Wang, D. F. Williams, J. J. aan den Toorn, and C. L. Holloway, "A significance test for reverberation-chamber measurement uncertainty in total radiated power of wireless devices," *IEEE Trans. Electromagn. Compat.*, vol. 58, no. 1, pp. 207–219, Feb. 2016.

[43] D. Senic *et al*., "Estimating and reducing uncertainty in reverberation chamber characterization at millimeter-wave frequencies," *IEEE Trans. Antennas Propag.*, vol. 64, no. 7, pp. 3130–3140, Jul. 2016.

[44] T. Jia, Y. Huang, Q. Xu, and Q. Hua, "Highest Usable Frequency Model for a Reverberation Chamber," *IEEE Antennas Wireless Propag. Lett.*, to be submitted.

Chapter 2 Fundamental Theories for the Reverberation Chamber Characterization

2.1 Introduction

Figure 2.1: A photograph showing the RC at the University of Liverpool with dimensions 3.60 m (*a*) × 5.80 m (*d*) × 4.00 m (*b*).

As already elaborated in Section 1.1.3, an RC is an electrically large cavity resonator equipped with stirrers so that the distribution of excited modes inside it can be changed continuously or in a stepwise manner [3], [5]. A photograph of the RC at the University

of Liverpool with dimensions 3.60 m (a) × 5.80 m (d) × 4.00 m (b) is demonstrated in Figure 2.1.

The characterization of an RC is critical to the RC performance evaluation, the optimum RC design, and the measurement uncertainty quantification. The purpose of this chapter is to present a review of the classical theories for the RC characterization from both physical and mathematical points of view. Consequently, a solid foundation can be built for the novel characterization techniques elaborated in subsequent chapters, which are more specific and orientated. Most of the concepts introduced in this chapter are theoretically or experimentally validated using the RC at the University of Liverpool (shown in Figure 2.1). Note that this chapter is by no means exhaustive, and the author does not claim any credit for any concept or work introduced in this chapter.

Table 2-I: Dependency table of subsequent chapters on each section in Chapter 2

	Chapter 3	Chapter 4	Chapter 5
2.2: Resonant Cavity Model	●	●	●
2.3: Quality Factor and Loss Mechanism	●	●	●
2.4: Time Domain Characterization	●		●
2.5: Wiener-Khinchin Theorem	●	●	
2.6: Statistical Electromagnetics	●	●	●

To characterize an RC, the first step is to determine its LUF. The LUF is defined as the frequency above which a specific field uniformity requirement can be satisfied within the working volume of the RC [23]. It can be determined using the first resonant frequency, mode number, mode density, *etc*. In **Section 2.2**, the resonant cavity model is presented [3], [5]. In particular, analytical expressions for modal resonant frequencies and mode number/mode density are given for an arbitrary rectangular-shaped cavity. The LUF can then be determined accordingly. Prior to all subsequent works in this thesis, dedicated theoretical or experimental validation should be performed to ensure

the frequency of operation is above the LUF of the RC. In addition, the resonant cavity model can be used for deterministically explaining the working principle of an RC.

Section 2.3 introduces the quality factor (Q factor), which measures the ability of an RC to store energy under the steady-state condition [3], [12] – [14]. The Q factor is an important parameter for the RC characterization. A high Q value is often desired for an RC (typically tens of thousands) at its frequency of operation. The Q factor is closely related to the RC's transfer function through the well-known Hill's equation [3]. One assumption for the TRP measurement in Chapter 4 is that the Q factor (thus the transfer function) is kept unchanged throughout the entire measurement procedure. The loss mechanism of the RC can be explained by decomposing the Q factor [14]. In Chapter 5, the HUF model is established based on the loss of the RC-based system. Moreover, the Q factor can be defined in the time domain, which links it to the chamber decay time (Chapter 3 and Chapter 5) [16], [17].

In **Section 2.4,** it is shown that the RC can be characterized using time domain parameters. The chamber decay time describes how fast the stored energy in an RC damps after the excitation source is instantaneously turned off [16], [17], [25], and it is usually used to characterize the RC's loading effect (Chapter 3 and Chapter 5). In contrast, the scattering damping time indicates how fast the mechanical stirrers can scatter the energy excited by a source [30] – [32], and it is used to characterize the stirrer performance of an RC (Chapter 3).

The Wiener-Khinnchin Theorem states that, for a well-behaved stationary random process, the power spectrum is equal to the Fourier transform of its autocorrelation function (ACF) [36]. In the context of an RC, channel characterization is of crucial importance for measurement uncertainty evaluation and channel emulation with desired properties. **Section 2.5** demonstrates that the channel characterization of an RC in different domains can be unified using Wiener-Khinnchin Theorem [37] – [39]. Specifically, in this thesis: I) the mathematical relationship between the FD-ACFUS and the scattering damping time is established (Chapter 3); II) corresponding ACFs are formulated to calculate the number of independent stirrer positions and independent frequency points (Chapter 4).

Due to its complex EM environment, the RC is usually applied from a statistical point of view in practice. Consequently, the measurement uncertainty largely depends on the

number of independent samples. In **Section 2.6**, the statistical model of an RC is introduced based on the plane wave spectrum theory [3], [58]. For an ideal RC, the in-phase and quadrature parts of an arbitrary rectangular component of the received complex signal are *i.i.d* Gaussian distributed with 0 mean [58], [59]. Statistical theories are extensively used throughout the thesis, in particular: I) the uncertainty analysis of the scattering damping time (Chapter 3); II) MLE formulation of the average Rician *K*-factor (Chapter 4); III) the analytical uncertainty model for the RC-based TRP measurement (Chapter 4); IV) derivation of statistical distributions of the average power of the desired received signal and the corresponding average noise power (Chapter 5).

The dependencies of subsequent chapters on each section in Chapter 2 are summarized in Table 2-I.

2.2 Resonant Cavity Model

To gain an in-depth understanding of the working principle of an RC, the first step is to deterministically analyze and obtain its standing wave patterns with fixed boundary conditions. To this end, the RC is simplified as a metallic cavity that is made of the perfect electrical conductor (PEC) with a source-free, linear, isotropic, and homogeneous interior region (for most cases, free space).

For a cavity resonator with a certain regular shape, *e.g.,* rectangular, cylindrical, and spherical, the analytical expressions of its resonant modes can be obtained by solving the Helmholtz equation which is derived from the well-known Maxwell's equations [1], [2]. To solve the partial differential equations, the separation of variables method [3] – [5] is utilized, and the relevant boundary conditions should be considered. This section will mainly focus on rectangular-shaped cavities, as it is adopted by the majority of RC designs. A typical rectangular cavity with dimensions $a \times b \times d$ and corresponding Cartesian coordinates is illustrated in Figure 2.2.

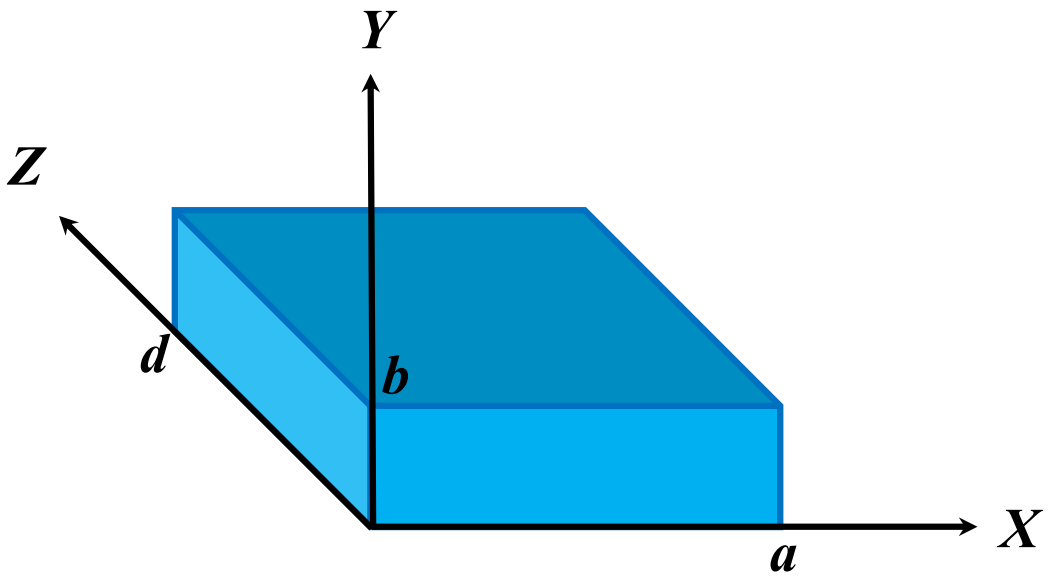

Figure 2.2: Rectangular metallic cavity geometry with principal axes.

2.2.1 Maxwell's Equations

Maxwell's equations of the time-varying electric and magnetic fields in the differential form [1] consist of two curl equations and two divergence equations, which are listed below

$$\nabla \times \mathbf{E} = -\frac{\partial \mathbf{B}}{\partial t} - \mathbf{M} \tag{2.1}$$

$$\nabla \times \mathbf{H} = -\frac{\partial \mathbf{D}}{\partial t} + \mathbf{J} \tag{2.2}$$

$$\nabla \cdot \mathbf{D} = \rho \tag{2.3}$$

$$\nabla \cdot \mathbf{B} = 0 \tag{2.4}$$

where

E is the electric field with the unit of volts per meter (V/m);

H is the magnetic field with the unit of amperes per meter (A/m);

D is the electric flux density with the unit of coulombs per meter squared (C/m^2);

B is the magnetic flux density with the unit of webers per meter squared (Wb/m^2);

M is the magnetic current density with the unit of volts per meter squared (V/m^2);

$\mathbf{J}$ is the electric current density with the unit of amperes per meter squared (A/m^2);

ρ is the electric charge density with the unit of coulombs per meter cubed (C/m^3).

It should be pointed out that the quantities denoted in bold represent the vector fields which are time-varying and are essentially real functions of spatial coordinates *X, Y, Z*, and the time variable *t*.

2.2.2 Helmholtz Equation

According to equations (2.1) – (2.4), the possible sources of the EM fields are the magnetic current density $\mathbf{M}$, the electric current density $\mathbf{J}$, and the electric charge density ρ. Note that $\mathbf{M}$ is only a fictitious source since magnetic monopole charges are so far considered non-existent. Inside a source-free volume ($\mathbf{M}=\mathbf{0}$, $\mathbf{J}=\mathbf{0}$, and $\rho=0$) with linear, isotropic, and homogeneous dielectric material (which is usually the case within an empty metallic rectangular cavity), the following relationships hold [1], [4]:

$$\mathbf{D}=\varepsilon\mathbf{E} \tag{2.5}$$

$$\mathbf{B}=\mu\mathbf{H} \tag{2.6}$$

where

$\varepsilon=\varepsilon_r\varepsilon_0$ is the dielectric permittivity with the unit of farad per meter (F/m) which is the product of the free space permittivity $\varepsilon_0=8.854\times10^{-12}$ F/m and the relative permittivity ε_r;

$\mu=\mu_r\mu_0$ is the magnetic permeability with the unit of henry per meter (H/m) which is the product of the free space permeability $\mu_0=4\pi\times10^{-7}$ H/m and the relative permeability μ_r.

Assuming that all field quantities are time-harmonic complex vectors with steady-state conditions [2], based on (2.1) – (2.6) and adopting the phasor notation (by suppressing the time dependence) gives

$$\nabla\times\mathbf{E}=-j\omega\mu\mathbf{H} \tag{2.7}$$

$$\nabla \times \mathbf{H} = j\omega\mu\mathbf{E} \tag{2.8}$$

$$\nabla \cdot \mathbf{E} = 0 \tag{2.9}$$

$$\nabla \cdot \mathbf{H} = 0 \tag{2.10}$$

where j is the imaginary notation, and ω is the radian frequency.

Here we use the electric field $\mathbf{E}$ as an example. Taking the curl of (2.7) and substituting (2.8) into it gives

$$\nabla \times \nabla \times \mathbf{E} = -j\omega\mu\left(\nabla \times \mathbf{H}\right) = \omega^2\mu\varepsilon\mathbf{E} \tag{2.11}$$

Then we use the following vector identity [1]

$$\nabla \times \nabla \times \mathbf{E} = \nabla\left(\nabla \cdot \mathbf{E}\right) - \nabla^2\mathbf{E} \tag{2.12}$$

Combining (2.9), (2.11), and (2.12), we have

$$\nabla^2\mathbf{E} + \omega^2\mu\varepsilon\mathbf{E} = 0 \tag{2.13}$$

The same applies to the magnetic field $\mathbf{H}$:

$$\nabla^2\mathbf{H} + \omega^2\mu\varepsilon\mathbf{H} = 0 \tag{2.14}$$

If we define the propagation constant (also known as wave number, or eigenvalue) of the medium as

$$k = \frac{2\pi}{\lambda} = \omega\sqrt{\mu\varepsilon} \tag{2.15}$$

where λ is the wavelength, then (2.13), (2.14) can be rewritten as

$$\left(\nabla^2 + k^2\right)\mathbf{E} = 0 \tag{2.16}$$

$$\left(\nabla^2 + k^2\right)\mathbf{H} = 0 \tag{2.17}$$

Equations (2.16), (2.17) are called the wave equation, or Helmholtz equation [1], [2]. The Helmholtz equation can be solved by using the separation of variables method [3] – [5] with corresponding boundary conditions.

2.2.3 Boundary Conditions

At the interface of two media, the boundary conditions involving the normal and tangential fields can be obtained by Maxwell's equations in the integral form [1]. For the normal components, by applying the Gaussian divergence theorem, we have the

following

$$\hat{\mathbf{n}} \cdot \left(\mathbf{D}_2 - \mathbf{D}_1 \right) = \rho_s \tag{2.18}$$

$$\hat{\mathbf{n}} \cdot \left(\mathbf{B}_2 - \mathbf{B}_1 \right) = 0 \tag{2.19}$$

where $\hat{\mathbf{n}}$ is the unit normal vector which points from material 1 to material 2, and ρ_s is the surface charge density on the interface. For the tangential components, by applying the Stokes' theorem, we can get

$$\hat{\mathbf{n}} \times \left(\mathbf{E}_2 - \mathbf{E}_1 \right) = \mathbf{M}_s \tag{2.20}$$

$$\hat{\mathbf{n}} \times \left(\mathbf{H}_2 - \mathbf{H}_1 \right) = \mathbf{J}_s \tag{2.21}$$

where $\mathbf{M}_s$ is the magnetic surface current density, and $\mathbf{J}_s$ is the electric surface current density. $\mathbf{J}_s$ might occur on the surface of the interface, while $\mathbf{M}_s$ is fictitious. Specifically, at the interface between the PEC (note that no electric field or magnetic field can exist inside the PEC) and the free space, equations (2.18) – (2.21) are reduced to:

$$\hat{\mathbf{n}} \cdot \mathbf{D} = \rho_s \tag{2.22}$$

$$\hat{\mathbf{n}} \cdot \mathbf{B} = 0 \tag{2.23}$$

$$\hat{\mathbf{n}} \times \mathbf{E} = 0 \tag{2.24}$$

$$\hat{\mathbf{n}} \times \mathbf{H} = \mathbf{J}_s \tag{2.25}$$

Equation (2.23) states that the normal component of the magnetic field $\mathbf{H}$ should be zero, and equation (2.24) shows that the tangential component of the electric field $\mathbf{E}$ should be zero.

Regular-shaped cavities are usually adopted in RC design. For a rectangular shaped metallic cavity with geometry and corresponding Cartesian coordinates shown in Figure 2.2, the boundary conditions for its six plane surfaces are summarized below:

$$\begin{cases} E_y = 0 \\ E_z = 0 \\ H_x = 0 \end{cases} \quad \text{for} \quad x = 0 \quad \text{and} \quad x = a \tag{2.26}$$

$$\begin{cases} E_x = 0 \\ E_z = 0 \\ H_y = 0 \end{cases} \quad \text{for} \quad y = 0 \quad \text{and} \quad y = b \tag{2.27}$$

$$\begin{cases} E_x = 0 \\ E_y = 0 \quad \text{for} \quad z = 0 \quad \text{and} \quad z = d \\ H_z = 0 \end{cases} \tag{2.28}$$

2.2.4 Resonant Modes for a Metallic Rectangular Cavity

Without loss of generality, we assume that the transverse electric (TE) modes and the transverse magnetic (TM) modes to be derived are with respect to the *Z*-axis shown in Figure 2.2. Therefore, for the TE modes we have $E_z = 0$, while for the TM modes we have $H_z = 0$. Another thing worth mentioning is that resonances only occur discretely at frequencies satisfying the following condition [3], [5]:

$$f_{mnp} = \frac{ck_{mnp}}{2\pi} = \frac{1}{2\sqrt{\varepsilon\mu}}\sqrt{\left(\frac{m}{a}\right)^2 + \left(\frac{n}{b}\right)^2 + \left(\frac{p}{d}\right)^2} \tag{2.29}$$

where

$$k_{mnp} = \sqrt{k_x^2 + k_y^2 + k_z^2} = \sqrt{\left(\frac{m\pi}{a}\right)^2 + \left(\frac{n\pi}{b}\right)^2 + \left(\frac{p\pi}{d}\right)^2} \tag{2.30}$$

is the wave number which has the same definition as (2.15), k_x, k_y and k_z are its projections onto the corresponding axes, $c = \frac{c_0}{\sqrt{\varepsilon_r \mu_r}}$ is the propagation speed of the EM wave in the medium inside the cavity with $c_0 = 3.0 \times 10^8 \quad m/s$ the speed of the EM wave in free space, *m*, *n,* and *p* are the mode coefficients which are non-negative integer numbers, and *a*, *b* and *d* are the dimensions of the rectangular cavity. Equation (2.29) is the analytical expression for the modal resonant frequencies.

Analytical solutions of the resonant modes of the metallic rectangular cavity can be derived by solving (2.16), (2.17) under constraints (2.26) – (2.28). The normal (Z-axis) component of the magnetic field for the TE modes can be analytically expressed as:

$$H_{z,mnp}^{TE} = H_0 \cos\left(\frac{m\pi}{a}x\right)\cos\left(\frac{n\pi}{b}y\right)\sin\left(\frac{p\pi}{d}z\right) \tag{2.31}$$

where H_0 is a constant indicating the amplitude of $H_{z,mnp}^{TE}$ with unit of A/m. The transverse components (X-axis and Y-axis) of the magnetic field for the TE modes are given as:

$$H_{x,mnp}^{TE} = -\frac{k_x k_y H_0}{k_{mnp}^2 - k_z^2} \sin\left(\frac{m\pi}{a}x\right)\cos\left(\frac{n\pi}{b}y\right)\cos\left(\frac{p\pi}{d}z\right) \tag{2.32}$$

$$H_{y,mnp}^{TE} = \frac{k_y k_z H_0}{k_{mnp}^2 - k_z^2} \cos\left(\frac{m\pi}{a}x\right)\sin\left(\frac{n\pi}{b}y\right)\sin\left(\frac{p\pi}{d}z\right) \tag{2.33}$$

It is straightforward to obtain that the normal component of the electric field for the TE modes is

$$E_{z,mnp}^{TE} = 0 \tag{2.34}$$

The transverse components of the electric field for the TE modes are:

$$E_{x,mnp}^{TE} = -\frac{j\omega_{mnp}\mu k_y H_0}{k_{mnp}^2 - k_z^2} \cos\left(\frac{m\pi}{a}x\right)\sin\left(\frac{n\pi}{b}y\right)\sin\left(\frac{p\pi}{d}z\right) \tag{2.35}$$

$$E_{y,mnp}^{TE} = \frac{j\omega_{mnp}\mu k_x H_0}{k_{mnp}^2 - k_z^2} \sin\left(\frac{m\pi}{a}x\right)\cos\left(\frac{n\pi}{b}y\right)\sin\left(\frac{p\pi}{d}z\right) \tag{2.36}$$

It should be stressed that *m* and *n* cannot be 0 simultaneously, while *p* should always be larger than 0.

Similarly, for the TM modes, the normal component of the electric field is issued as:

$$E_{z,mnp}^{TM} = E_0 \sin\left(\frac{m\pi}{a}x\right)\sin\left(\frac{n\pi}{b}y\right)\cos\left(\frac{p\pi}{d}z\right) \tag{2.37}$$

where E_0 is a constant indicating the amplitude of $E_{z,mnp}^{TM}$ with unit of V/m. The transverse components of the electric field are:

$$E_{x,mnp}^{TM} = -\frac{k_x k_z E_0}{k_{mnp}^2 - k_z^2} \cos\left(\frac{m\pi}{a}x\right)\sin\left(\frac{n\pi}{b}y\right)\sin\left(\frac{p\pi}{d}z\right) \tag{2.38}$$

$$E_{y,mnp}^{TM} = \frac{k_y k_z E_0}{k_{mnp}^2 - k_z^2} \sin\left(\frac{m\pi}{a}x\right)\cos\left(\frac{n\pi}{b}y\right)\sin\left(\frac{p\pi}{d}z\right) \tag{2.39}$$

As for the magnetic field, there is no normal component, that is

$$H_{z,mnp}^{TM} = 0 \tag{2.40}$$

We can also obtain the transverse components of the magnetic field as:

$$H_{x,mnp}^{TM} = -\frac{j\omega_{mnp}\varepsilon k_y E_0}{k_{mnp}^2 - k_z^2}\sin\left(\frac{m\pi}{a}x\right)\cos\left(\frac{n\pi}{b}y\right)\cos\left(\frac{p\pi}{d}z\right) \tag{2.41}$$

$$H_{y,mnp}^{TM} = \frac{j\omega_{mnp}\varepsilon k_x E_0}{k_{mnp}^2 - k_z^2}\cos\left(\frac{m\pi}{a}x\right)\sin\left(\frac{n\pi}{b}y\right)\cos\left(\frac{p\pi}{d}z\right) \tag{2.42}$$

Concerning the TM modes, *m* and *n* should always be larger than 0.

Table 2-II: The first 12 resonant modes of the RC at the University of Liverpool

Number	Mode	Resonant Frequency (MHz)
1	TE_{011}	45.55
2	TE_{101}	49.04
3	TM_{110}	56.06
4	TE_{111}	61.73
4	TM_{111}	61.73
6	TE_{012}	63.89
7	TE_{102}	66.42
8	TE_{112}	76.27
8	TM_{112}	76.27
10	TE_{021}	79.33
11	TM_{120}	85.80
12	TE_{013}	86.17

Essentially, a rectangular-shaped cavity resonator has the property of "high-pass". If we assume that the dimensions of the cavity satisfy $a<b<d$, then its first (lowest) resonant frequency is f_{011} (see (2.29)), and the relevant mode excited is the TE_{011} mode. Taking the RC at the University of Liverpool (as illustrated in Figure 2.1) with dimensions a = 3.6 *m*, b = 4.0 *m*, and d=5.8 *m* as an example, its first 12 allowable resonant modes are listed in Table 2-II. It can be found that some modes share the same resonant frequencies (such as mode number 4 and mode number 8). Actually, this happens when *m*, *n,* and *p* are all nonzero so that the corresponding TE and TM modes establish identical cut-offs. This is called the mode degeneracy [3], [4], [6]. Another possible situation for the occurrence of degeneration of modes is when the ratio $a^2 : b^2 : d^2$ is rational [7]. Since mode degeneracy has an adverse effect on the mode uniformity regarding frequency, it should be suppressed when designing an RC. On the other hand, since mode degeneracy can focus power on the corresponding frequencies and increase the overall magnitude fluctuation, this effect can be intentionally

strengthened in some application scenarios where high power and wide signal dynamic range are desired, such as the shielding effectiveness measurement.

Mode distribution theoretically calculated using (2.29) for the RC at the University of Liverpool up to 200 MHz is illustrated in Figure 2.3, with the TE modes represented by green solid lines, and the TM modes indicated by blue dashed lines. It can be seen that mode degeneracies exist at frequencies where lines of different types coincide with each other. In addition, as frequency increases, the distribution of modes becomes denser and more uniform, implying better statistical performance.

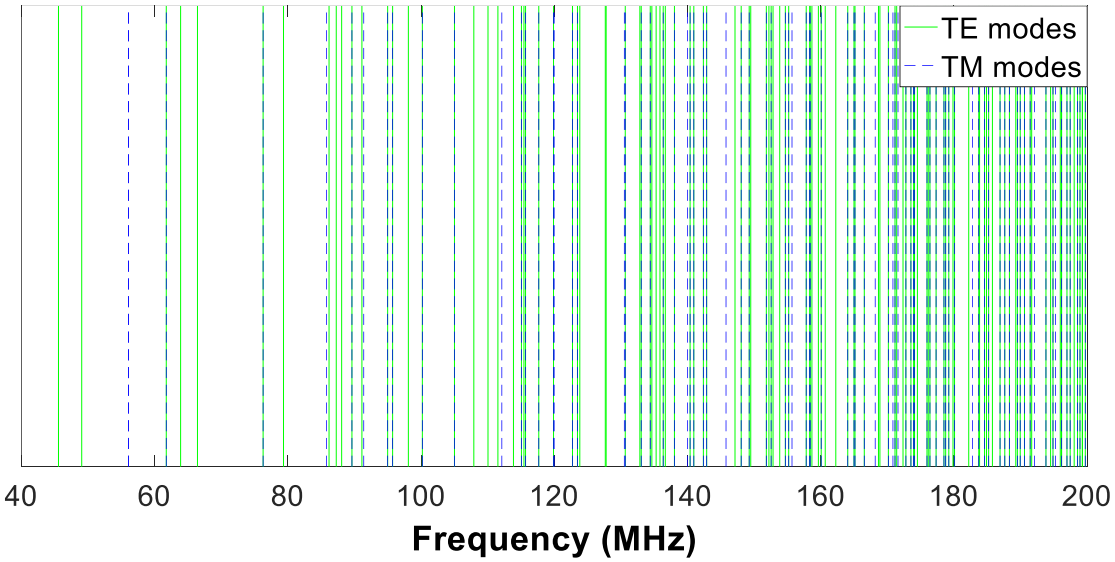

Figure 2.3: Mode distribution with respect to frequency up to 200 MHz for the RC at the University of Liverpool.

2.2.5 Mode Orthogonality and Mode Decomposition

The total field generated by an excitation source inside a cavity resonator can be represented by the superposition of (or equivalently, can be decomposed into) all the excited TE and TM modes with relevant weight coefficients [8] – [10]. Taking the total electric field $\mathbf{E}$ as an example, we can obtain [5]

$$\mathbf{E} = \sum_{m,n,p} A_{mnp}\mathbf{E}_{mnp}^{TE} + \sum_{m,n,p} B_{mnp}\mathbf{E}_{mnp}^{TM} \tag{2.43}$$

Altering boundary conditions using a certain stirring mechanism is equivalent to

changing the weighting coefficients A_{mnp} and B_{mnp}. Due to the property of mode orthogonality, we have

$$\iiint_V \mathbf{E}_{mnp}^{TE} \cdot \mathbf{E}_{m'n'p'}^{TE*} dV = 0 \tag{2.44}$$

$$\iiint_V \mathbf{E}_{mnp}^{TE} \cdot \mathbf{E}_{m'n'p'}^{TM*} dV = 0 \tag{2.45}$$

$$\iiint_V \mathbf{E}_{mnp}^{TM} \cdot \mathbf{E}_{m'n'p'}^{TM*} dV = 0 \tag{2.46}$$

for $m \neq m'$, $n \neq n'$, and $p \neq p'$. * denotes the complex conjugate operation, and V is the volume of the cavity. Based on (2.43) – (2.46), A_{mnp} and B_{mnp} can be derived in the following manner:

$$A_{mnp} = \iiint_V \mathbf{E} \cdot \mathbf{E}_{mnp}^{TE*} dV \tag{2.47}$$

$$B_{mnp} = \iiint_V \mathbf{E} \cdot \mathbf{E}_{mnp}^{TM*} dV \tag{2.48}$$

The same applies to the magnetic field $\mathbf{H}$.

2.2.6 Cavity Mode Number & Lowest Usable Frequency

Since the total EM field distributed in an RC is complicated, the statistical method is preferred in practice for RC-based measurements. Therefore, it is more meaningful to use the mode number/mode density to evaluate the statistical performance of the RC at a given working frequency (or frequency range). For a metallic cavity with arbitrary shape, according to Weyl's law [3], [11], the accumulated mode number N_w and the mode density D_w with respect to f are given as:

$$N_w(f) = \frac{8\pi V}{3} \frac{f^3}{c^3} \tag{2.49}$$

$$D_w(f) = \frac{dN_w(f)}{df} = \frac{8\pi V f^2}{c^3} \tag{2.50}$$

where V is the volume of the cavity. It can be seen that N_w (as well as D_w)

increases with increasing f. At a fixed working frequency, the RC with a larger volume has higher N_w and D_w values. If the frequency is downscaled by a factor of α ($\alpha > 1$), to keep the mode number/mode density unchanged, V should be upscaled by a factor of α^3 (α^2).

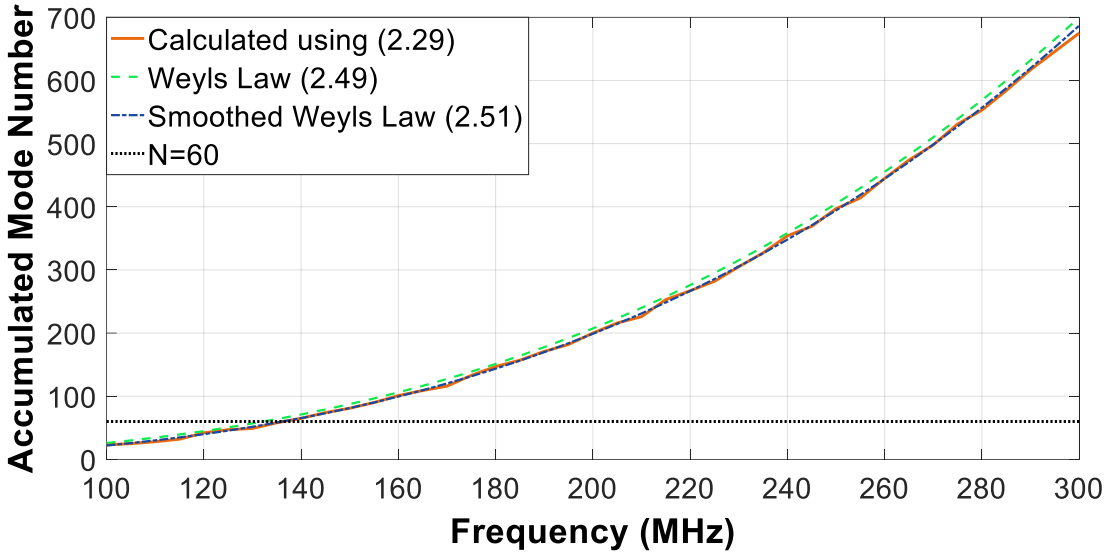

Figure 2.4: Mode number derived using different approaches for the RC at the University of Liverpool between 100 MHz and 300 MHz.

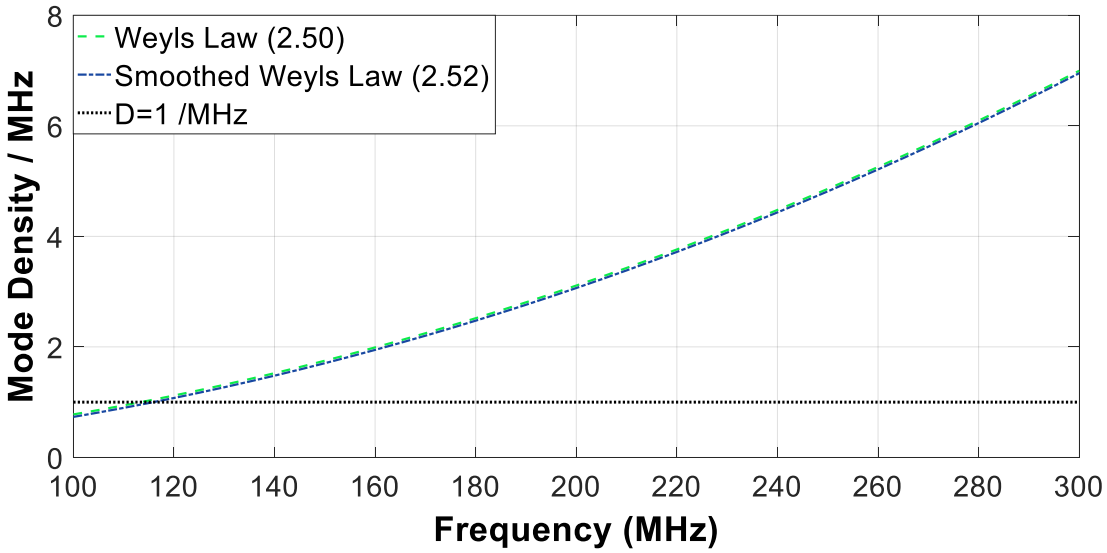

Figure 2.5: Mode density derived using different approaches for the RC at the University of Liverpool between 100 MHz and 300 MHz.

Specifically, for a rectangular-shaped resonant cavity, $V = a \times b \times d$, and (2.49), (2.50) can be further smoothed for better approximation [3], [7]:

$$N_s(f) = \frac{8\pi}{3}(a \times b \times d)\frac{f^3}{c^3} - (a + b + d)\frac{f}{c} + \frac{1}{2} \tag{2.51}$$

$$D_s(f) = 8\pi(a \times b \times d)\frac{f^2}{c^3} - \frac{a + b + d}{c} \tag{2.52}$$

The number of modes calculated by repeatedly solving (2.29) for different valid *m, n, p* combinations, and approximated by analytical expressions (2.49) and (2.51) for the RC at the University of Liverpool between 100 MHz and 300 MHz is illustrated in Figure 2.4. It can be found that the original Weyl's law (2.49) tends to overestimate the result, while the smoothed formula (2.51) provides better agreement with that calculated using (2.29). Similarly, the mode density per MHz as a function of frequency using the original (2.50) and smoothed (2.52) formulas for the RC at the University of Liverpool is shown in Figure 2.5.

There is no unique mathematical equation for determining the LUF: it is usually defined as the frequency above which an RC can fulfill the stipulated operational requirements *e.g.*, specified in [23]. Common practice is to define the LUF based on quantities such as the first resonant frequency, number of modes, mode density, *etc*. Several definitions of LUF given in the literature are summarized below:

1. LUF is defined as three times the first resonant frequency f_{011} of the RC [23];
2. LUF falls somewhere between $5f_{011}$ and $6f_{011}$ [24];
3. LUF is defined as the frequency above which the cavity has at least 60 modes according to (2.49) [23];
4. LUF is defined as the frequency above which the mode density is larger than 1 mode/MHz according to (2.50) [3].

For instance, the LUF of the RC at the University of Liverpool is around 135 MHz according to Definition 3, and around 120 MHz according to Definition 4.

2.3 Quality Factor and Loss Mechanism of an RC

The Q factor is an essential parameter for the RC characterization, which measures the ability of an RC to store energy. The Q factor can be related to the RC's transfer function using Hill's equation. The Q factor can also be defined in the time domain, linking it to the chamber decay time. Moreover, the loss mechanism of the RC can be explained by decomposing the Q factor.

2.3.1 Quality Factor and Hill's Equation

By definition, the Q factor in the context of an RC is the ratio between the energy stored in the chamber and the energy dissipated during an entire cycle [3], [12] – [14]:

$$Q = \omega \frac{\bar{U}_s}{P_d} \tag{2.53}$$

where $\bar{U}_s$ is the average total energy stored in an RC, and P_d is the power dissipated. Specifically, for rectangular shaped resonators, the Q factor can be analytically derived based on TE modes and TM modes discussed in Section 2.2.4:

$$Q_{mnp}^{TE} = \omega \frac{\mu \iiint_V \mathbf{H}_{mnp}^{TE} \cdot \mathbf{H}_{mnp}^{TE*} dV}{R_s \oiint_S \mathbf{H}_{mnp}^{TE} \cdot \mathbf{H}_{mnp}^{TE*} dS} \tag{2.54}$$

$$Q_{mnp}^{TM} = \omega \frac{\mu \iiint_V \mathbf{H}_{mnp}^{TM} \cdot \mathbf{H}_{mnp}^{TM*} dV}{R_s \oiint_S \mathbf{H}_{mnp}^{TM} \cdot \mathbf{H}_{mnp}^{TM*} dS} \tag{2.55}$$

where S is the total surface area of the chamber, and R_s is the surface resistance which is defined as:

$$R_s = \sqrt{\frac{\omega \mu_0}{2\sigma}} \tag{2.56}$$

where σ is the conductivity (in Siemens per meter, S/m) of the wall material of the chamber. In the situation where the RC is electrically large, it is more meaningful to use the composite Q factor which is averaged over a small range of frequency [7].

Under steady-state conditions, due to the conservation of power, the dissipated power P_d should be equal to the transmitted power P_t. Substituting into (2.53) gives:

$$Q = \omega \frac{\bar{U}_s}{P_t} \tag{2.57}$$

$\bar{U}_s$ can be written as

$$\bar{U}_s = \bar{W} V \tag{2.58}$$

herein $\bar{W}$ is the average energy density, which is obtained in [3] based on the electric/magnetic field as

$$\bar{W} = \frac{1}{2}\left[\varepsilon_0 \left\langle |\mathbf{E}|^2 \right\rangle + \mu_0 \left\langle |\mathbf{H}|^2 \right\rangle \right] = \varepsilon_0 \left\langle |\mathbf{E}|^2 \right\rangle = \mu_0 \left\langle |\mathbf{H}|^2 \right\rangle \tag{2.59}$$

By combing (2.57) – (2.59) at the transmitting side, we have

$$P_t = \frac{\omega \varepsilon_0 V \left\langle |\mathbf{E}|^2 \right\rangle}{Q} \tag{2.60}$$

At the receiving side, the first important parameter is the power density S_c (or Poynting vector in the vector form), which is defined as follows:

$$S_c = |\mathbf{E} \times \mathbf{H}| = \frac{\left\langle |\mathbf{E}|^2 \right\rangle}{\eta_0} = c_0 \bar{W} \tag{2.61}$$

where η_0 is the characteristic impedance in free space with the definition

$$\eta_0 = \sqrt{\frac{\mu_0}{\varepsilon_0}} \approx 377 \quad Ohm \tag{2.62}$$

Then the ensembled received power can be expressed as

$$\left\langle P_r \right\rangle = \frac{1}{2} \cdot S_c \cdot \frac{\lambda^2}{4\pi} = \frac{\lambda^2 \left\langle |\mathbf{E}|^2 \right\rangle}{8\pi\eta_0} \tag{2.63}$$

where the correction factor $\frac{1}{2}$ is used for compensating the 50% chance of polarization mismatch, and the term $\frac{\lambda^2}{4\pi}$ is the effective aperture of an isotropic antenna [15] (which is equivalent to a non-isotropic antenna in an isotropic multipath environment). Combining (2.60) with (2.63) by canceling $\left\langle |\mathbf{E}|^2 \right\rangle$ gives

$$\langle P_r \rangle = \frac{\lambda^2 Q}{8\pi\omega\eta_0\varepsilon_0 V} P_t = \frac{\lambda^3 Q}{16\pi^2 V} P_t \tag{2.64}$$

Equation (2.64) is Hill's equation [3] in rich isotropic multipath (RIMP) environment, and the ratio $T = \frac{\langle P_r \rangle}{P_t}$ is defined as the transfer function (or insertion loss, coupling coefficient) for an RC. In essence, Hill's equation can be treated as the counterpart of the Friis equation [4], [15] in free space. By rearranging (2.64), it can be obtained that

$$Q = \frac{8\pi\omega\eta_0\varepsilon_0 V}{\lambda^2} \frac{\langle P_r \rangle}{P_t} = \frac{16\pi^2 V}{\lambda^3} \frac{\langle P_r \rangle}{P_t} \tag{2.65}$$

Equation (2.65) is called the Q factor in the frequency domain [3]. In practice, for extracting Q, the effect of antenna efficiencies should be considered and calibrated out [16]. It can be found that Q is frequency-dependent (included in λ). For higher working frequency or larger chamber volume, Q tends to be larger.

The Q factor can also be derived in terms of the time domain response [16], [17]. Consider the situation in which the state inside the RC is transformed from the initial steady-state by instantaneously turning off the energy source. Then the change rate of energy ($d\bar{U}_s$) can be described with respect to a short time interval dt by the following differential equation:

$$d\bar{U}_s = -P_d dt \tag{2.66}$$

the minus sign indicates that the energy is continuously decaying. Combining (2.53) with (2.66) by canceling P_d, we have

$$d\bar{U}_s = -\frac{\omega}{Q}\bar{U}_s dt \tag{2.67}$$

Given the initial condition $\bar{U}_s|_{t=0} = \bar{U}_0$, equation (2.67) has the following analytical solution:

$$\bar{U}_s = \bar{U}_0 \exp\left(-\frac{\omega t}{Q}\right) \tag{2.68}$$

As expected, the energy will decrease exponentially. Conventionally, a time constant can be defined for the convenience of representation in (2.68) based on the following:

$$Q = \omega\tau_{RC} \tag{2.69}$$

this time constant τ_{RC} is called the chamber decay time [16], [17] which will be explained in detail in Section 2.4.1. Equation (2.69) is actually the definition of the Q factor in the time domain. We can see that Q is proportional to both ω and τ_{RC}. At the same frequency, the RC with a larger τ_{RC} gives a higher Q.

In addition, the Q factor can be defined based on the average mode bandwidth Δf [3], [18] – [20] as:

$$Q = \frac{f}{\Delta f} \tag{2.70}$$

Modes that fall outside of the $\pm\frac{\Delta f}{2}$ region from the relevant resonant frequency can be considered negligible for constructing the total field. According to (2.70), Q is inversely proportional to Δf. For the ideal case in which the RC is completely lossless, $\Delta f \to 0$, which is equivalent to $Q \to \infty$.

2.3.2 Loss Mechanism

According to the law of conservation of power, the total dissipated power P_d can be expressed as the sum of the following four types of losses [3], [14]:

$$P_d = P_{d1} + P_{d2} + P_{d3} + P_{d4} \tag{2.71}$$

where P_{d1} is the power consumed by the metallic walls inside the cavity. P_{d2} is the power absorbed by the loading objects inside the cavity, which is defined as:

$$P_{d2} = S_c \cdot \langle \sigma_a \rangle \tag{2.72}$$

where $\langle \sigma_a \rangle$ is the absorption cross section (ACS) [14], [21], [22] of the loading objects averaged over all incident angles and polarizations for both TE and TM modes. $\langle \sigma_a \rangle$ should be minimized if we want to minimize the contribution of P_{d2}.

P_{d3} is the power leaked through apertures on the cavity:

$$P_{d3} = S_c \cdot \frac{1}{2} \langle \sigma_t \rangle \tag{2.73}$$

where $\langle \sigma_t \rangle$ is the transmission cross section (TCS) [3], [14] of the apertures. Note that a scaling factor $\frac{1}{2}$ is introduced since only the energy leaked out of the cavity (with a 50% chance for the isotropic case) is considered. Similarly, $\langle \sigma_t \rangle$ should be minimized if we want to minimize the contribution of P_{d3}.

P_{d4} is the power dissipated in the load impedance of receiving antennas. Based on (2.63) and taking the total efficiency of the receiving antenna $\eta_{r,tot}$ into consideration, we have

$$P_{d4} = \frac{1}{2} \cdot S_c \cdot \frac{\lambda^2}{4\pi} \cdot \eta_{r,tot} \tag{2.74}$$

According to (2.53), Q is inversely proportional to P_d. So equivalently we have

$$Q^{-1} = Q_1^{-1} + Q_2^{-1} + Q_3^{-1} + Q_4^{-1} \tag{2.75}$$

Q_1 is defined as [12]

$$Q_1 = \frac{\omega \bar{U}_s}{P_{d1}} = \frac{3V}{2\mu_r \delta A} \tag{2.76}$$

where $\delta = \sqrt{\frac{2}{\omega\mu\sigma}}$ is the skin depth of the wall material, and A is the total inner surface area of the RC. Based on (2.72) – (2.74), Q_2, Q_3, and Q_4 can be expressed as

$$Q_2 = \frac{\omega \bar{U}_s}{P_{d2}} = \frac{2\pi V}{\lambda \langle \sigma_a \rangle} \tag{2.77}$$

$$Q_3 = \frac{\omega \bar{U}_s}{P_{d3}} = \frac{4\pi V}{\lambda \langle \sigma_t \rangle} \tag{2.78}$$

$$Q_4 = \frac{\omega \bar{U}_s}{P_{d4}} = \frac{16\pi^2 V}{\eta_{r,tot} \lambda^3} \tag{2.79}$$

(a)

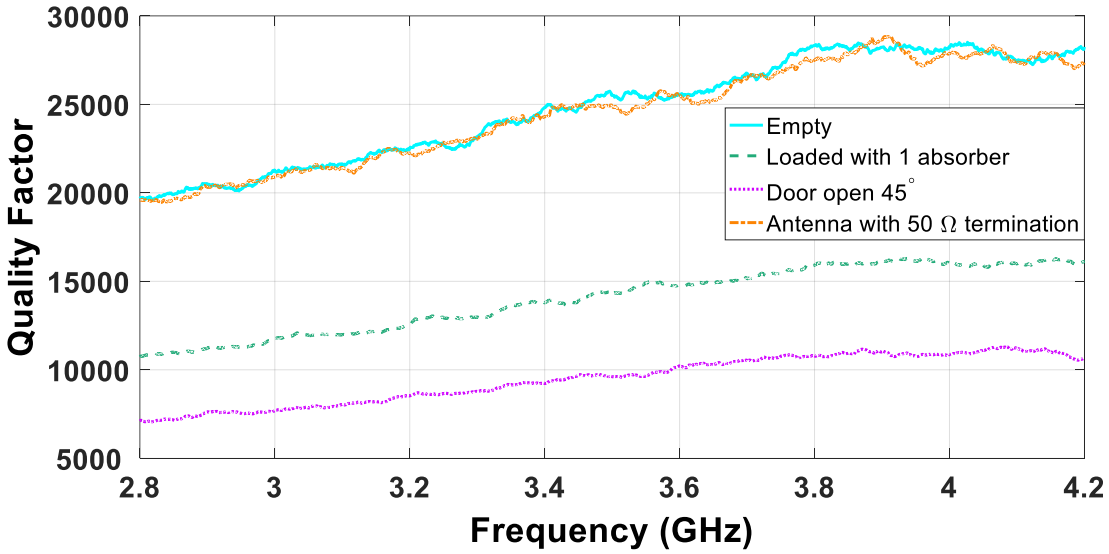

(b)

Figure 2.6: Quality factor values for the RC at the University of Liverpool between 2.8 GHz and 4.2 GHz: (a) Different types of loss. (b) Measurement Results.

To verify the loss mechanism, the effect of different types of loss on the Q factor of the RC at the University of Liverpool is shown in Figure 2.6. All curves are smoothed by a 50 MHz running averaging window. It can be found that for an empty chamber, Q increases from 20000 to around 28000 as frequency increases from 2.8 GHz to 4.2 GHz. Increasing the TCS (open the chamber door by 45^{o}) or increasing the ACS (load the chamber with one absorber) can significantly reduce Q. In contrast, loading the RC with a horn antenna (with bandwidth 1 GHz – 18 GHz) seems to have a negligible effect at

the frequency of interest.

2.4 Time Domain Characterization of an RC

The RC can also be characterized using time domain parameters. In this section, two important time domain parameters are introduced. The chamber decay time describes how fast the stored energy dissipates, and it is usually used to characterize the RC's loading effect. In contrast, the scattering damping time indicates how fast the mechanical stirrers can scatter the energy, and it is used to characterize the stirrer performance of an RC.

2.4.1 Chamber Decay Time

As already appeared in equation (2.69), the chamber decay time (τ_{RC})is defined as the characteristic time that the energy stored in an RC is reduced by a factor of *e* (the mathematical constant) after the excitation source is instantaneously turned off [16], [17], [25]. Traditionally, τ_{RC} can be extracted from the power delay profile (PDP):

$$PDP = \left\langle \left| E_a(t) \right|^2 \right\rangle = P_0 \exp\left(-\frac{t}{\tau_{RC}} \right) \tag{2.80}$$

where P_0 is the initial power (usually normalized in practice), and the subscript *a* denotes the direction of the antenna, usually assigned to an arbitrary axis of the Cartesian coordinate. For the RIMP environment (averaged over all stirrer positions), we have

$$\left\langle \left| E_a(t) \right|^2 \right\rangle = \frac{\left\langle \left| \mathbf{E}(t) \right|^2 \right\rangle}{3} \tag{2.81}$$

Actually, (2.81) implies the isotropy property in a well-stirred RC, which will be explained in Section 2.6.2. An example of PDP (in logarithm scale) measurement in the RC at the University of Liverpool in the frequency range 2.3 GHz – 2.5 GHz is shown in Figure 2.7. The least-square method is used to fit the slope of the curve (denoted by

k_1) by neglecting the early-time region and the noise floor [17]. Then we have

$$\tau_{RC} = -\frac{10}{k_1 \ln 10} \tag{2.82}$$

τ_{RC} is closely related to important wireless channel parameters like the RMS delay spread for the time dispersiveness characterization, and the coherence bandwidth for the frequency selectivity evaluation [26], [27]. Therefore, it is usually desired to measure τ_{RC} accurately and to further control its value by intentionally loading the RC in order to emulate different propagation scenarios [28], [29].

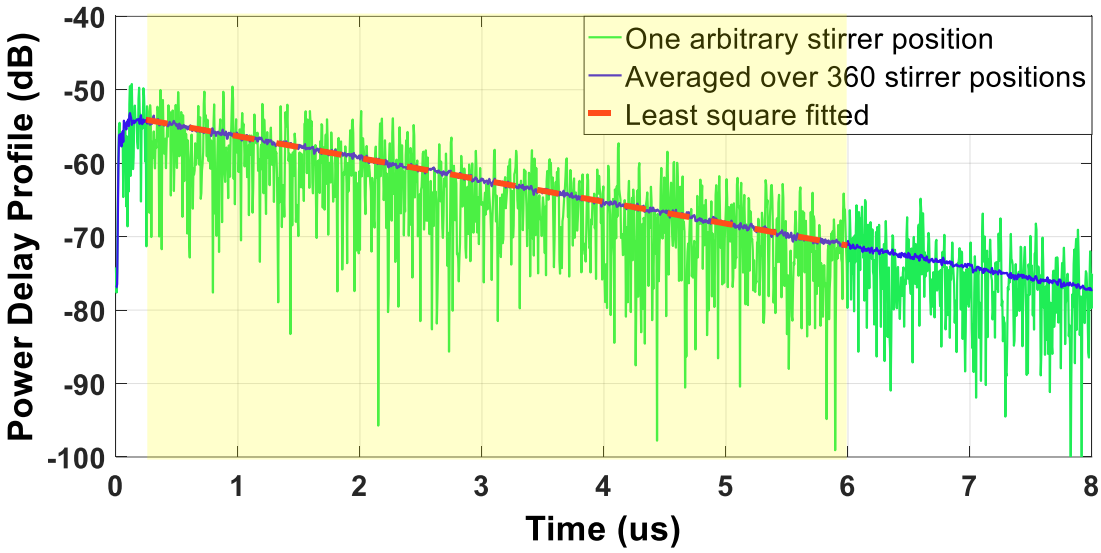

Figure 2.7: PDP measured in the RC at the University of Liverpool for extraction of chamber decay time.

2.4.2 Scattering Damping Time

The scattering damping time is defined as the characteristic time for the targets to scatter the wave at least once [30] – [32]. According to [25], [30], the unstirred power envelope $\left|\langle E_a(t)\rangle\right|^2$ also decays exponentially with time:

$$\left|\langle E_a(t)\rangle\right|^2 = P_0 \exp\left(-t\left(\frac{1}{\tau_{RC}} + \frac{1}{\tau_s}\right)\right) \tag{2.83}$$

where τ_s is the scattering damping time [30] – [32]. It can be seen from (2.83) that there are two reasons that cause the damping of $\left|\langle E_a(t)\rangle\right|^2$: 1) losses due to loadings inside the RC (which is reflected by τ_{RC}); 2) scattering of the EM field by the stirrers (which is reflected by τ_s). For an RC that meets operational requirements, energy (or power) should be effectively stirred before it decays and reaches the noise floor of the measurement instrumentation. Therefore, τ_s should be much smaller than τ_{RC} in value. Besides, τ_s is considered to be independent of the loading effect since it is already included in τ_{RC}. Combining (2.80) and (2.83), we have

$$\frac{\left|\langle E_a(t)\rangle\right|^2}{\left\langle\left|E_a(t)\right|^2\right\rangle} = P_0 \exp\left(-\frac{t}{\tau_s}\right) \tag{2.84}$$

Now it is clear that τ_s describes how fast the unstirred power decays compared with the total power.

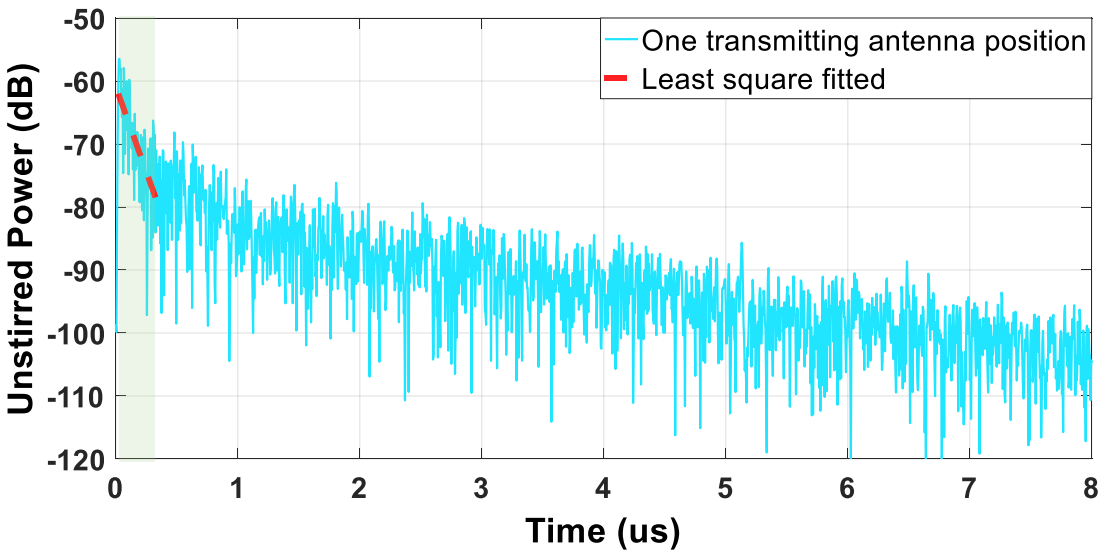

Figure 2.8: Unstirred power envelope measured in the RC at the University of Liverpool for extraction of scattering damping time.

An example of unstirred power envelope (in logarithm scale) measurement in the RC at the University of Liverpool in the frequency range 2.3 GHz – 2.5 GHz is illustrated in Figure 2.8. The least-square method is used to fit the slope of the curve (denoted by

k_2) by neglecting the early-time region and the noise floor. Then we have

$$\frac{\tau_{RC}\tau_s}{\tau_{RC}+\tau_s} = -\frac{10}{k_2 \ln 10} \tag{2.85}$$

Combining (2.82) with (2.85), τ_s can be obtained as

$$\tau_s = \frac{10}{(k_1 - k_2)\ln 10} \tag{2.86}$$

As can be viewed in Figure 2.7 and Figure 2.8, $|k_1| \ll |k_2|$. The time interval available for extracting k_2 is much shorter than that for k_1 (comparing the shaded regions in the two figures). In practice, this might introduce extra uncertainty, which causes the measurement result inaccurate. An alternative approach implemented in the frequency domain is introduced in [33], which can be used with the conventional time domain method for cross-validation.

τ_s can be used for quantifying the total scattering cross section (TSCS) of the mechanical stirrers [30] – [32], [34], [35]. Furthermore, it can be used for characterizing the stirrer performance [25], [33] since it is independent of the chamber loading effect.

2.5 Wiener-Khinchin Theorem for Channel Characterization in an RC

In the field of signal processing, the well-known Wiener-Khinchin theorem (also known as the Wiener-Khinchin-Einstein theorem or the Khinchin-Kolmogorov theorem) describes that the ACF and the power spectrum of a wide sense stationary signal form a Fourier pair [36]. The Wiener-Khinchin theorem is valid provided that the Fourier transform exists. Essentially, the wireless channel is a function of time, delay, frequency, and spatial parameters such as angle of departure (AoD) and angle of arrival (AoA). Based on the Wiener-Khinchin theorem, several important quantities for characterizing the radio channel emulated in an RC can be interlinked [37] – [39].

2.5.1 Frequency Domain & Delay Domain

(a)

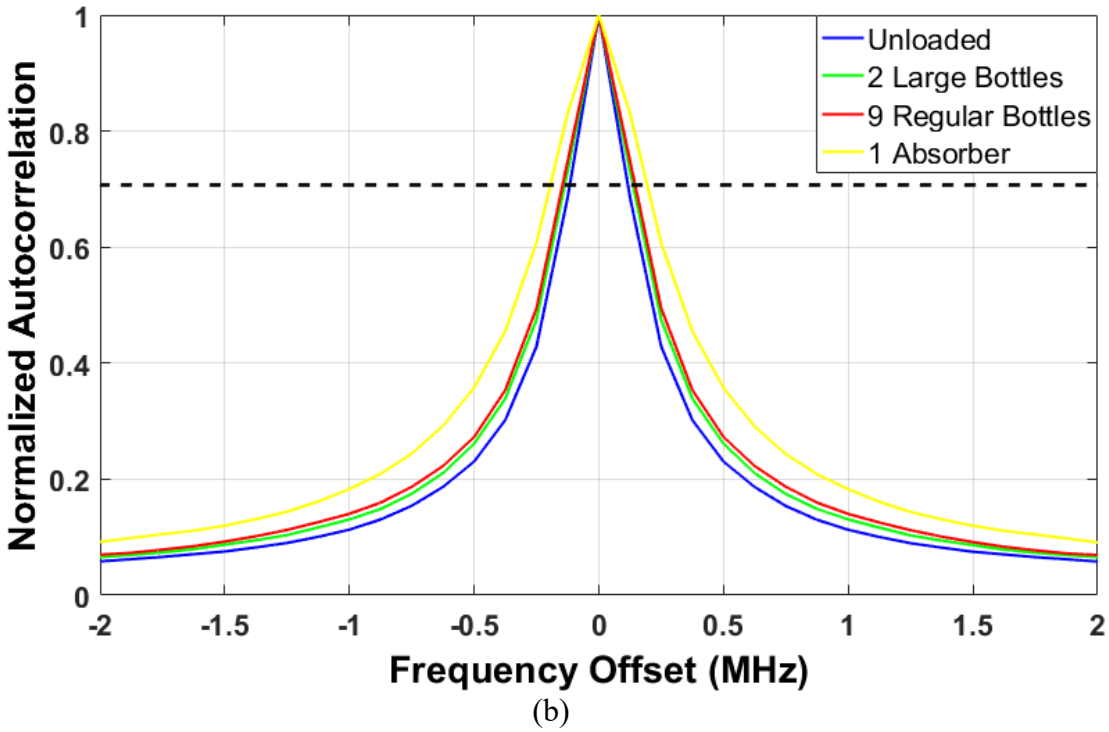

(b)

Figure 2.9: Magnitude of the normalized ACF measured in the RC at the University of Liverpool with different loading conditions: (a) Different loadings. (b) Measurement results.

For fixed transmitter-receiver pair, the channel impulse response of the RC is denoted

as $h(t,\tau)$, where t is the time domain indicating that the response is time-varying (*e.g.,* rotate the mechanical stirrers to change the boundary conditions), and τ stands for the delay domain. The corresponding frequency domain response is $H(t,f)=\mathcal{F}\left[h(t,\tau)\right]$. Then the frequency domain ACF can be written as:

$$R(t,\partial f)=\int_{-\infty}^{+\infty}H(t,f)H^{*}(t,f+\partial f)\,df \tag{2.87}$$

where ∂f is the frequency offset, and the superscript * is the complex conjugate operation. According to [26], [40], the ACF is closely related to the mode bandwidth and the coherence bandwidth which is used to evaluate the channel's frequency domain selectivity.

An example of ACF (in normalized magnitude) measurement in the RC at the University of Liverpool with different loading conditions in the frequency range of 3.3 GHz – 3.5 GHz is shown in Figure 2.9. The result is averaged over 360 stirrer positions (so we denote it as $\left|\left\langle R(t,\partial f)\right\rangle_{T}\right|_{norm}$). When the value of $\left|\left\langle R(t,\partial f)\right\rangle_{T}\right|_{norm}$ falls below a certain threshold [26], [37], the relevant reading of ∂f is the mode bandwidth/coherence bandwidth. It can be found in Figure 2.9 that different loadings result in different coherence bandwidths. Not surprisingly, the heavier the loading, the wider the coherence bandwidth. Hence, if the flat fading condition is required for a measurement task, the common practice is to strategically load the RC [28].

By applying the Wiener-Khinchin theorem, we have

$$R(t,\partial f)=\mathcal{F}\left[\left|h(t,\tau)\right|^{2}\right]=\mathcal{F}\left[PDP(t,\tau)\right] \tag{2.88}$$

The PDP (in logarithm scale) corresponding to the ACF plots in Figure 2.9 is illustrated in Figure 2.10. The result is averaged over 360 stirrer positions. We can see that the heavier the loading, the sharper the slope of the profile, and the smaller the value of τ_{RC} (as well as the RMS delay spread) according to (2.82). More detailed explanations can be found in Section 2.4.1. Equation (2.88) establishes the important link between the frequency domain parameters like coherence bandwidth and the delay domain parameters like RMS delay spread [26], [37].

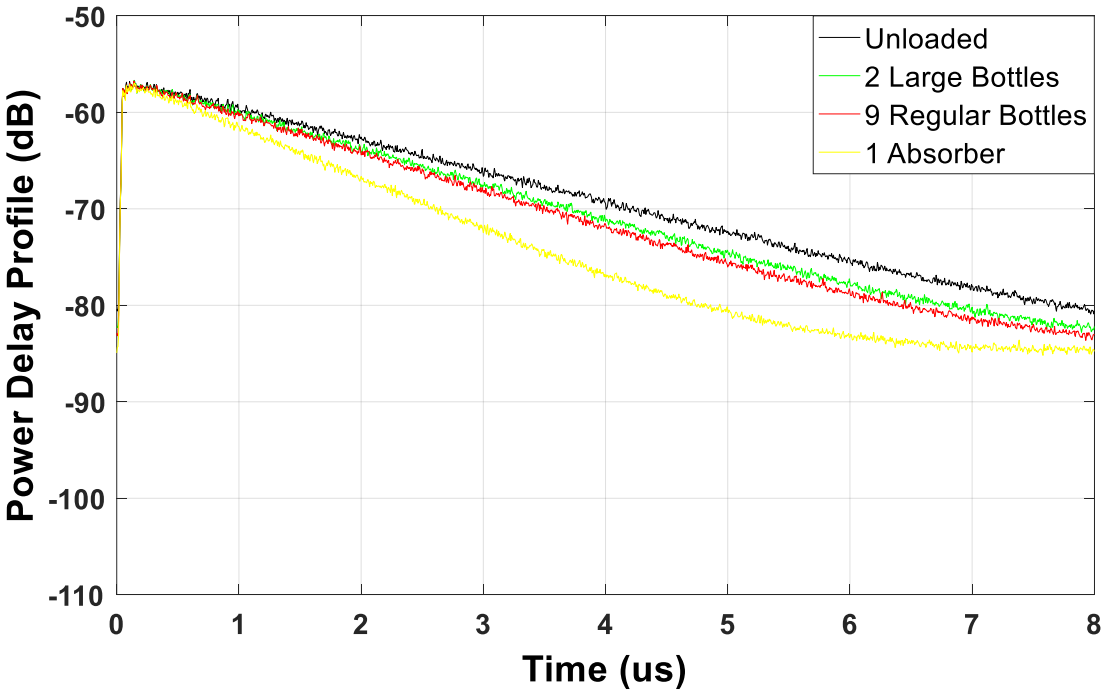

Figure 2.10: PDP measured in the RC at the University of Liverpool with different loading conditions.

2.5.2 Time Domain & Doppler Domain

(a)

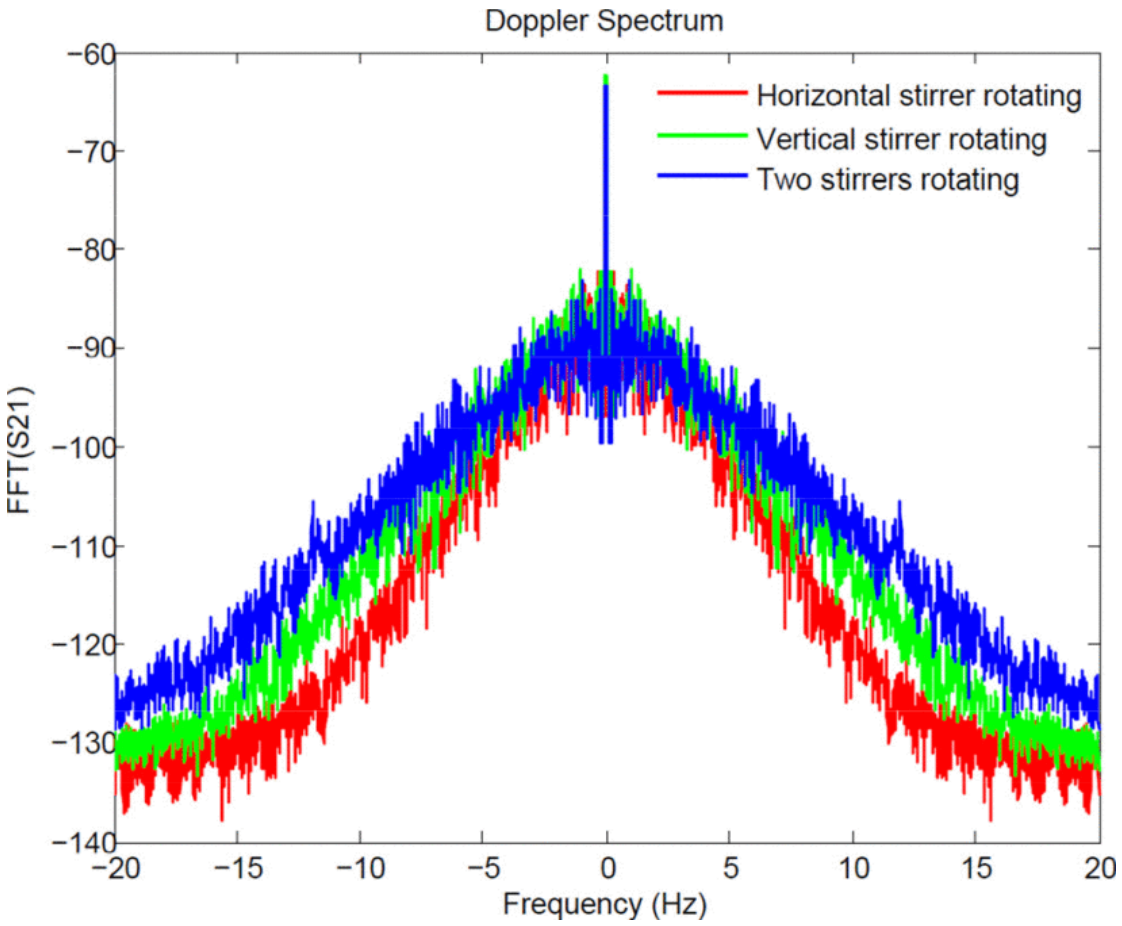

(b)

Figure 2.11: Doppler spectrum measured in the RC at the University of Liverpool with different stirring scenarios: (a) The horizontal and vertical stirrer. (b) Measurement results [44].

In terms of the time domain, the ACF is defined as [41] – [44]:

$$R(\partial t, f) = \int_{-\infty}^{+\infty} H(t, f) H^{*}(t + \partial t, f)\, dt \tag{2.89}$$

where ∂t is the time offset. It should be pointed out that the channel frequency response $H(t, f)$ rather than the channel impulse response $h(t, f)$ is used for calculating $R(\partial t, f)$. The coherence time is defined as the time over which a propagating wave can be considered coherent (so that it can be predicted). Similar to the procedure of deriving the coherence bandwidth in Section 2.5.1, the coherence time can be determined by reading the corresponding ∂t value when the magnitude of $R(\partial t, f)$ falls below a certain threshold. In practice, the change of the channel response is usually realized by implementing multiple stirring techniques, *e.g.,* rotating

the mechanical stirrers continuously or stepwise. In this case, it could be of more interest to characterize the coherence angle of the stirrers rather than the coherence time. If we define $G(\rho,f)=\mathcal{F}\left[H(t,f)\right]$, where ρ denotes the Doppler frequency domain, then according to the Wiener-Khinchin theorem,

$$R(\partial t,f)=\mathcal{F}^{-1}\left[\left|G(\rho,f)\right|^2\right]=\mathcal{F}^{-1}\left[D(\rho,f)\right] \tag{2.90}$$

where $D(\rho,f)=\left|G(\rho,f)\right|^2$ is the Doppler spectrum at frequency *f*.

An example Doppler spectrum measured in the RC at the University of Liverpool with three different stirrer scenarios at 2 GHz is shown in Figure 2.11 [44]. The stirrers are rotating continuously with a speed of 6 degrees per second. We can see that the larger the stirring volume, the broader the shape of the Doppler spectrum, and the larger the RMS Doppler spread which can be calculated using the following formula:

$$\rho_{rms}=\sqrt{\frac{\int_{-\infty}^{+\infty}\rho^2 D(\rho,f)\,d\rho}{\int_{-\infty}^{+\infty}D(\rho,f)\,d\rho}} \tag{2.91}$$

As described above, the coherence time and the Doppler spread are inter-linked through equations (2.89) – (2.91). According to the property of the Fourier transform, since $R(\partial t,f)$ and $D(\rho,f)$ form a Fourier pair, the higher the relative velocity between the source and the probe (in the context of the RC, this is equivalent to a higher angular speed of the mechanical stirrers), the wider the doppler spectrum, and the narrower the ACF in the time domain (thus the shorter the coherent time). By setting the stirrers (rotating speed, step size, stirring volume, *etc.*), the desired Doppler effect can be emulated in the RC, and the coherence time can be quantified accordingly to control whether it is fast fading or slow fading. In addition, the coherence time/coherence angle can also be used for determining the independent sample number [23], [45] – [48], which is important for estimating the measurement uncertainty.

2.5.3 Spatial Domain & Angular Domain

Statistically homogeneous, isotropic, and polarization balanced multipath channel is usually assumed inside the working volume of an RC [49]. However, a certain degree

of anisotropy is inevitable in practice due to the imperfect stirring process and unbalanced loading, especially when the operating frequency is low [50]. Besides, this anisotropy property can be further enhanced and utilized (*e.g.*, strategically place the absorbers in the RC) to emulate more realistic multipath environments. In this case, it is of crucial importance to characterize the angular domain distribution (usually versus the azimuth) of the received power at a given frequency *f*. According to [51] – [56], the angular domain information can be derived from the spatial domain by using the Wiener-Khinchin theorem. The synthetic aperture measurement is usually used for improved angular resolution [53] – [56].

Assume that the channel frequency response measured by the virtual array element at the position $\mathbf{r}$ with fixed orientation and polarization is denoted as $H(\mathbf{r}, f)$. The spatial domain ACF is given as [53]:

$$R(\partial\mathbf{r}, f) = \int H(\mathbf{r}, f) H^*(\mathbf{r} + \partial\mathbf{r}, f)\, d\mathbf{r} \tag{2.92}$$

herein $\partial\mathbf{r}$ is the length offset which is a vector. The coherence length can be quantified based on $R(\partial\mathbf{r}, f)$. The Fourier transform of $H(\mathbf{r}, f)$ from the spatial domain ($\mathbf{r}$) to the wave vector domain ($\mathbf{k}$) is defined as:

$$P(\mathbf{k}, f) = \int H(\mathbf{r}, f) \exp(-j\mathbf{k}\cdot\mathbf{r})\, d\mathbf{r} \tag{2.93}$$

Note that the wave vector domain is equivalent to the angular domain since the wave vector $\mathbf{k}$ can be expressed based on the azimuth AoA φ and the elevation AoA θ:

$$\mathbf{k} = -k\sin\theta\cos\varphi\hat{\mathbf{x}} - k\sin\theta\sin\varphi\hat{\mathbf{y}} - k\cos\theta\hat{\mathbf{z}} \tag{2.94}$$

Then according to the Wiener-Khinchin theorem, we have

$$R(\partial\mathbf{r}, f) = \mathcal{F}^{-1}\left[\left|P(\mathbf{k}, f)\right|^2\right] = \mathcal{F}^{-1}\left[PWP(\mathbf{k}, f)\right] \tag{2.95}$$

where $PWP(\mathbf{k}, f) = \left|P(\mathbf{k}, f)\right|^2$ is called the power wavevector profile (PWP). If a 2-D case is assumed (only the azimuth component is explicitly expressed, while the elevation component is included in the projected magnitude k), the PWP can be rewritten as $PWP(k, \varphi+\pi, f)$ with $\mathbf{k} = -k\cos\varphi\hat{\mathbf{x}} - k\sin\varphi\hat{\mathbf{y}}$. Adding π to φ is to map the arrival angle to the departure angle. Then the 2-D azimuth power angular profile (PAP) is defined as [53]:

$$PAP(f,\varphi)=\int_0^{k_0} PWP(k,\varphi+\pi,f)kdk \tag{2.96}$$

where k_0 is the wavenumber in the free space. As can be seen from equation (2.96), the physical meaning of the integration with regard to k is to average out the elevation components. Therefore, the instantaneous distribution of the received power against the azimuth AoA can be fully described by $PAP(f,\varphi)$.

An example of PAP measurement is shown in Figure 2.12 [53]. The experiment is performed within an RC with dimensions 3.60 m × 4.27 m × 2.90 m. Synthetic-aperture measurement is adopted and the experimental setup is illustrated in Figure 2.12 (a). Measurement results are depicted in Figure 2.12 (b) at 2 GHz with six different stirrer positions (traces with different colors). Since each trace is for only one stirrer position, the anisotropy property can be clearly viewed, especially at lower frequencies.

Essentially, the spatial domain corresponds to the distribution of EM modes (near field concept), while the angular domain corresponds to the plane waves (far-field concept). Therefore, the Wiener-Khinchin theorem also gives hints to the link between the near field and the far-field.

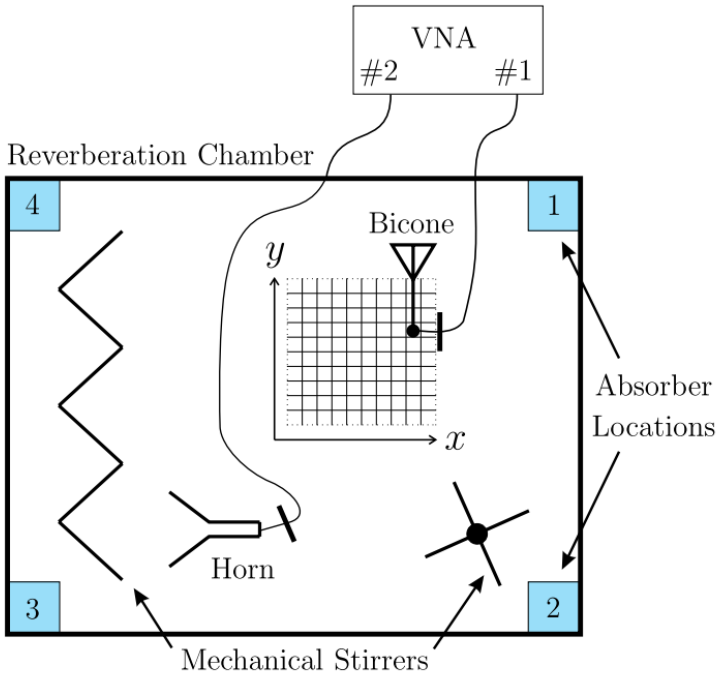

(a)

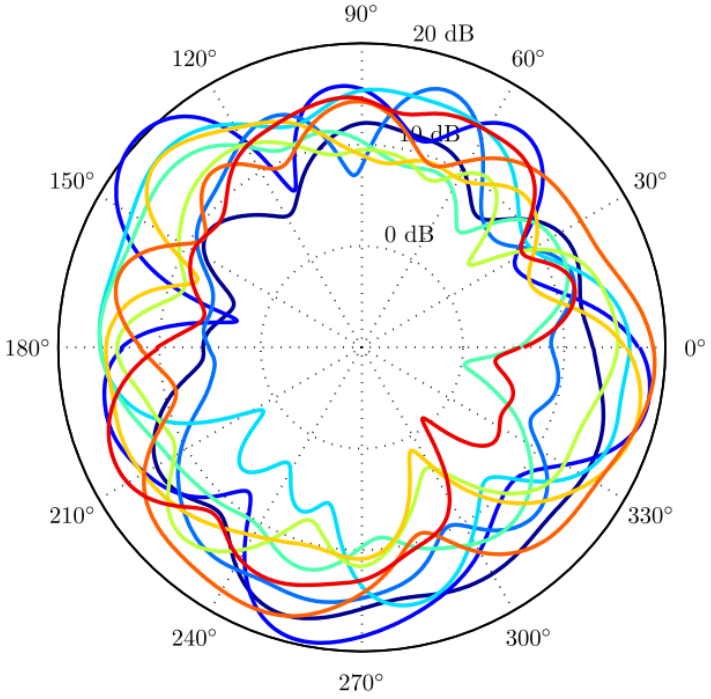

(b)

Figure 2.12: Power angular profiles measured at 2 GHz with different stirrer positions: (a) Schematic diagram of the measurement setup. (b) Measurement results [53].

2.6 Statistical Electromagnetics in an RC

As aforementioned, an RC is based on an electrically large metallic cavity with a regular shape (usually rectangular). However, in practice, the assembly of mechanical stirrers with asymmetric geometry and other facilities with unknown scattering and absorbing properties inside the RC make the EM environment much more complex. Thus, it is too complicated and laborious to deterministically solve the mode distribution for every boundary condition, if not impossible. Besides, some well-known quantities in the context of the RC only have the statistical meaning [3], [5], [8]. Therefore, the statistical theory is not only important for the RC characterization but also for the RC-based measurement applications.

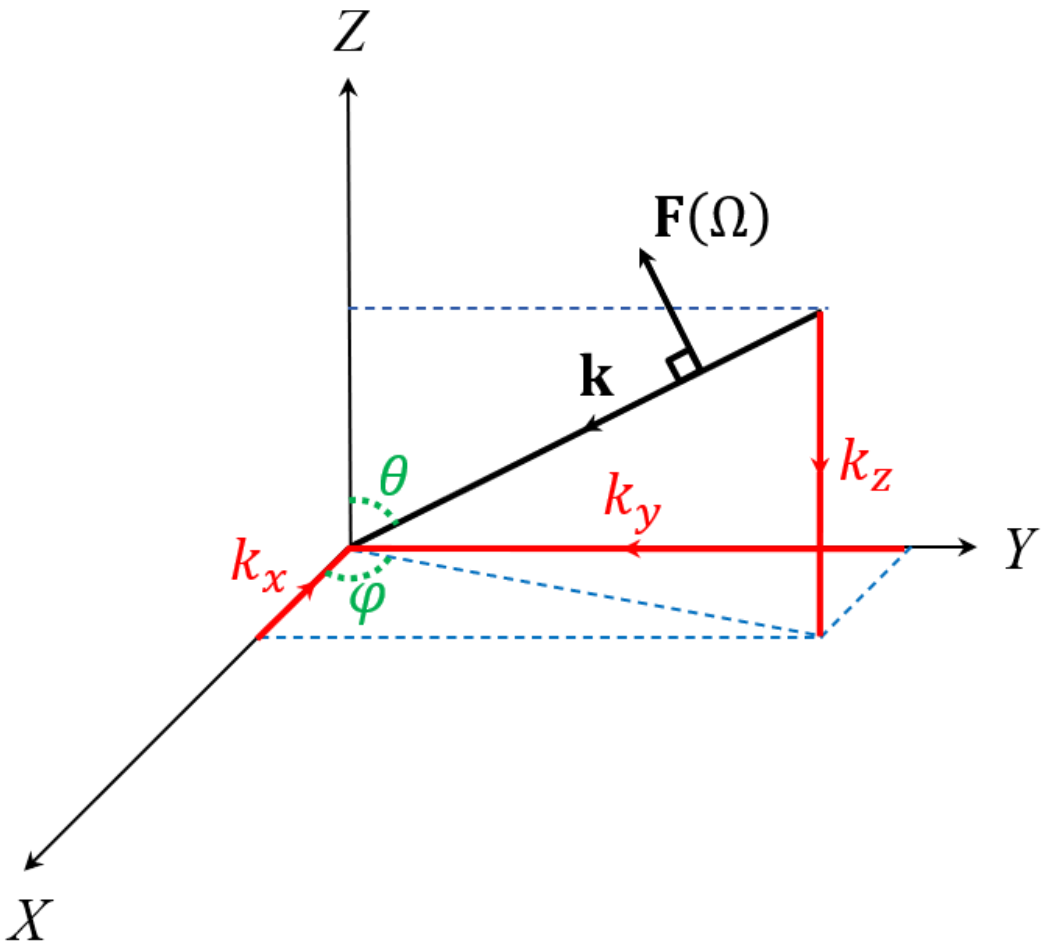

Figure 2.13: Geometry and Cartesian coordinates for modeling the plane wave spectrum.

2.6.1 Plane Wave Spectrum Theory

Within the operating frequency bands of the RC, it is assumed that the ergodic-mode case is statistically fulfilled. Equivalently, as for the angular domain, the number of plane waves generated inside the RC tends to approach infinite. The electric field $\mathbf{E}$ at the position $\mathbf{r} = x\hat{\mathbf{x}} + y\hat{\mathbf{y}} + z\hat{\mathbf{z}}$ can be decomposed into plane wave components with random amplitude, phase, polarization, and coming from arbitrary azimuth angle φ and elevation angle θ with equal probability [3], [49], [57], [58]:

$$\mathbf{E}(\mathbf{r}) = \iint_{4\pi} \mathbf{F}(\Omega) \exp(j\mathbf{k}\cdot\mathbf{r})\, d\Omega \tag{2.97}$$

Again, the phasor form is adopted and the $\exp(-j\omega t)$ dependence is suppressed for notational convenience. Ω is the solid angle which ranges from 0 to 4π, and in the differential form it can be linked to φ and θ as $d\Omega = \sin\theta d\theta d\varphi$. The definition of the wave vector $\mathbf{k}$ has already been given in (2.94). $\mathbf{F}(\Omega)$ is called the angular spectrum which is used for representing the individual plane wave component (see Figure 2.13). In terms of the angular domain, $\mathbf{F}(\Omega)$ can be represented as:

$$\mathbf{F}(\Omega) = F_{\varphi}(\Omega)\hat{\boldsymbol{\varphi}} + F_{\theta}(\Omega)\hat{\boldsymbol{\theta}} \tag{2.98}$$

The polarization components $\hat{\boldsymbol{\theta}}$ and $\hat{\boldsymbol{\varphi}}$ are perpendicular to each other as well as to $\mathbf{k}$. Both $F_{\varphi}(\Omega)$ and $F_{\theta}(\Omega)$ are complex quantities that can be decomposed into two quadrature parts (*i.e.*, real and imaginary):

$$F_{\varphi}(\Omega) = F_{\varphi r}(\Omega) + jF_{\varphi i}(\Omega) \tag{2.99}$$

$$F_{\theta}(\Omega) = F_{\theta r}(\Omega) + jF_{\theta i}(\Omega) \tag{2.100}$$

When the RC is used to generate the statistical EM field, $\mathbf{F}(\Omega)$ is regarded as a random variable. Independent random samples of $\mathbf{F}(\Omega)$ can be obtained by multiple stirring techniques (*e.g.*, rotating the mechanical stirrers). According to [3], [58], the following statistical properties are valid if the RC is well stirred:

$$\langle F_{\varphi}(\Omega)\rangle = \langle F_{\theta}(\Omega)\rangle = 0 \tag{2.101}$$

$$\langle F_{\varphi r}(\Omega_1)F_{\varphi i}(\Omega_2)\rangle = \langle F_{\theta r}(\Omega_1)F_{\theta i}(\Omega_2)\rangle = 0 \tag{2.102}$$

$$\begin{aligned}\langle F_{\varphi r}(\Omega_1)F_{\theta r}(\Omega_2)\rangle &= \langle F_{\varphi i}(\Omega_1)F_{\theta i}(\Omega_2)\rangle \\ \langle F_{\varphi r}(\Omega_1)F_{\theta i}(\Omega_2)\rangle &= \langle F_{\varphi i}(\Omega_1)F_{\theta r}(\Omega_2)\rangle = 0\end{aligned} \tag{2.103}$$

$$\begin{aligned}\langle F_{\varphi r}(\Omega_1)F_{\varphi r}(\Omega_2)\rangle &= \langle F_{\varphi i}(\Omega_1)F_{\varphi i}(\Omega_2)\rangle \\ \langle F_{\theta r}(\Omega_1)F_{\theta r}(\Omega_2)\rangle &= \langle F_{\theta i}(\Omega_1)F_{\theta i}(\Omega_2)\rangle = C_E\delta(\Omega_1 - \Omega_2)\end{aligned} \tag{2.104}$$

where $\langle\ \rangle$ denotes the ensemble average over all individual samples, C_E is a constant with the unit of V^2/m^2 which is proportional to the square of the electric field strength, and $\delta(\ )$ represents the Dirac delta function. (2.101) shows that each polarization component of the angular spectrum is of zero mean due to the superposition of rays arriving with random phases. Hence, the mean value of $\mathbf{F}(\Omega)$ should also be

zero. (2.102) indicates that the two quadrature parts of the same polarization component are uncorrelated, which is straightforward. (2.103) describes that the two polarization components are uncorrelated due to orthogonality. (2.104) tells us that angular spectrum components with different AoAs are uncorrelated since they have experienced different multiple random scattering paths. Based on (2.102) – (2.104), we can further deduce the following properties [3], [58]:

$$\left\langle F_{\varphi}\left(\Omega_1\right)F_{\theta}^{*}\left(\Omega_2\right)\right\rangle = 0 \tag{2.105}$$

$$\left\langle F_{\varphi}\left(\Omega_1\right)F_{\varphi}^{*}\left(\Omega_2\right)\right\rangle = \left\langle F_{\theta}\left(\Omega_1\right)F_{\theta}^{*}\left(\Omega_2\right)\right\rangle = 2C_E\delta\left(\Omega_1-\Omega_2\right) \tag{2.106}$$

2.6.2 Statistical Spatial Uniformity and Isotropy Properties in an RC

Taking the ensemble average on both sides of equation (2.97) and applying (2.101) gives [3], [58]

$$\left\langle \mathbf{E}\left(\mathbf{r}\right)\right\rangle = \iint_{4\pi}\left\langle \mathbf{F}\left(\Omega\right)\right\rangle \exp\left(j\mathbf{k}\cdot\mathbf{r}\right)d\Omega = 0 \tag{2.107}$$

which means ideally the mean of the total electric field $\mathbf{E}\left(\mathbf{r}\right)$ is 0. The square magnitude of the total electric field $\left|\mathbf{E}\left(\mathbf{r}\right)\right|^2$ (which is a measure of the power or energy as shown in (2.59), (2.61)) can be expanded based on (2.97) as

$$\left|\mathbf{E}\left(\mathbf{r}\right)\right|^2 = \mathbf{E}\left(\mathbf{r}\right)\mathbf{E}^{*}\left(\mathbf{r}\right) = \iint_{4\pi}\iint_{4\pi}\mathbf{F}\left(\Omega_1\right)\mathbf{F}^{*}\left(\Omega_2\right)\exp\left(j\left(\mathbf{k}_1-\mathbf{k}_2\right)\cdot\mathbf{r}\right)d\Omega_1 d\Omega_2 \tag{2.108}$$

Similarly, taking the ensemble average on both sides of (2.108) and applying (2.105), (2.106) gives [3], [58]

$$\begin{aligned}\left\langle\left|\mathbf{E}\left(\mathbf{r}\right)\right|^2\right\rangle &= \iint_{4\pi}\iint_{4\pi}\left\langle\mathbf{F}\left(\Omega_1\right)\mathbf{F}^{*}\left(\Omega_2\right)\right\rangle\exp\left(j\left(\mathbf{k}_1-\mathbf{k}_2\right)\cdot\mathbf{r}\right)d\Omega_1 d\Omega_2 \\ &= \iint_{4\pi}\iint_{4\pi}4C_E\delta\left(\Omega_1-\Omega_2\right)\exp\left(j\left(\mathbf{k}_1-\mathbf{k}_2\right)\cdot\mathbf{r}\right)d\Omega_1 d\Omega_2 \\ &= \iint_{4\pi}4C_E d\Omega_2 = 16\pi C_E \equiv E_0^2\end{aligned} \tag{2.109}$$

According to (2.109), for the ideal case in which the RC is well stirred, the mean-square magnitude of the electric field is a fixed value E_0^2, which is independent of the position

$\mathbf{r}$. This proves the spatial uniformity property of the RC.

In terms of the Cartesian coordinate, the total electric field can be expressed as

$$\mathbf{E} = E_x\hat{\mathbf{x}} + E_y\hat{\mathbf{y}} + E_z\hat{\mathbf{z}} = \left(E_{xr} + jE_{xi}\right)\hat{\mathbf{x}} + \left(E_{yr} + jE_{yi}\right)\hat{\mathbf{y}} + \left(E_{zr} + jE_{zi}\right)\hat{\mathbf{z}} \tag{2.110}$$

Each rectangular component of $\mathbf{E}$ is a complex value that consists of two quadrature parts. The $\mathbf{r}$ dependence is suppressed hereafter for notational convenience. Again, based on (2.101) – (2.104), the following statistical properties can be derived [3]

$$\langle E_x \rangle = \langle E_y \rangle = \langle E_z \rangle = 0 \tag{2.111}$$

$$\langle E_{xr} \rangle = \langle E_{xi} \rangle = \langle E_{yr} \rangle = \langle E_{yi} \rangle = \langle E_{zr} \rangle = \langle E_{zi} \rangle = 0 \tag{2.112}$$

Accordingly, the square magnitude of the total electric field is

$$|\mathbf{E}|^2 = |E_x|^2 + |E_y|^2 + |E_z|^2 = |E_{xr}|^2 + |E_{xi}|^2 + |E_{yr}|^2 + |E_{yi}|^2 + |E_{zr}|^2 + |E_{zi}|^2 \tag{2.113}$$

and we can obtain the following statistical properties [3]

$$\left\langle |E_x|^2 \right\rangle = \left\langle |E_y|^2 \right\rangle = \left\langle |E_z|^2 \right\rangle = \frac{E_0^2}{3} \tag{2.114}$$

$$\left\langle |E_{xr}|^2 \right\rangle = \left\langle |E_{xi}|^2 \right\rangle = \left\langle |E_{yr}|^2 \right\rangle = \left\langle |E_{yi}|^2 \right\rangle = \left\langle |E_{zr}|^2 \right\rangle = \left\langle |E_{zi}|^2 \right\rangle = \frac{E_0^2}{6} \tag{2.115}$$

(2.114) and (2.115) indicate that the mean-square values of the rectangular components of the electric field are identical and do not change with the direction of the axes, which proves the isotropy property of the RC. The statistical spatial uniformity and isotropy properties of the magnetic field are similar to that of the electric field and are omitted here. By combining (2.59), (2.61), and (2.109), the energy density and the power density can be represented in terms of E_0^2 as

$$\bar{W} = \varepsilon E_0^2 \tag{2.116}$$

$$S_c = \frac{E_0^2}{\eta} \tag{2.117}$$

2.6.3 Statistical Distributions of the Field and Power

For the rectangular components of the electric field, since the waves are superimposed with random amplitude, phase, polarization, and AOAs, the CLT [59] can be applied to

obtain the Gaussian distribution for each quadrature part. With the knowledge of (2.112) and (2.115), the corresponding probability density function (PDF) can be derived as [58] – [60]

$$PDF\left(E_{*_r}\right)=PDF\left(E_{*_i}\right)=\frac{1}{\sqrt{2\pi}\sigma}\exp\left(-\frac{x^2}{2\sigma^2}\right),\quad x=E_{*_r}\ \text{ or }\ E_{*_i} \tag{2.118}$$

where $*$ can be x, y, or z, and

$$\sigma^2=\left\langle\left|E_{*_r}-\left\langle E_{*_r}\right\rangle\right|^2\right\rangle=\left\langle\left|E_{*_i}-\left\langle E_{*_i}\right\rangle\right|^2\right\rangle=\left\langle\left|E_{*_r}\right|^2\right\rangle=\left\langle\left|E_{*_i}\right|^2\right\rangle=\frac{E_0^2}{6} \tag{2.119}$$

That is, E_{*_r} and E_{*_i} are *i.i.d* random variables following a Gaussian distribution with 0 mean and standard deviation σ.

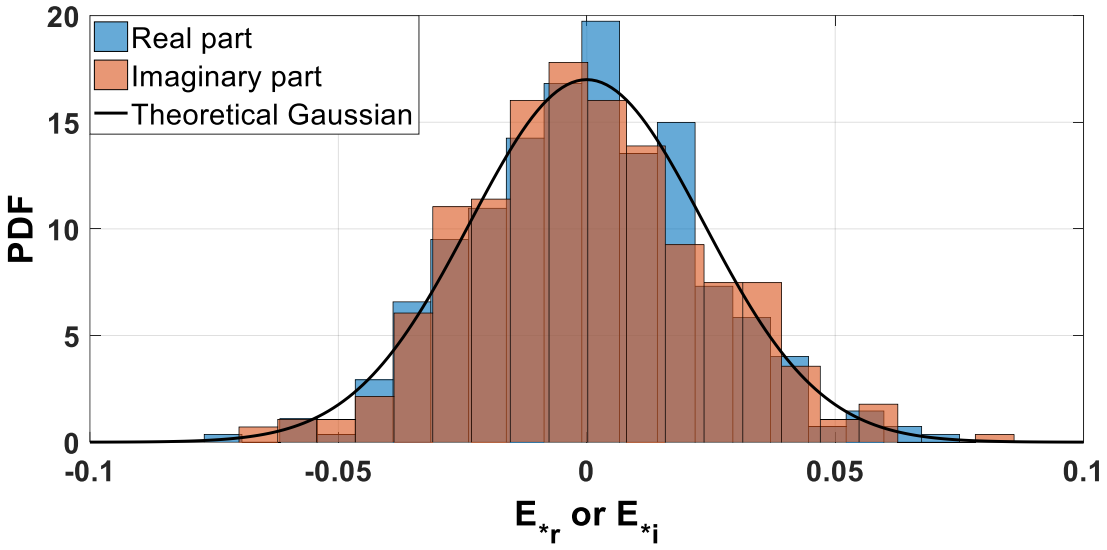

Figure 2.14: Distributions of the real and imaginary parts of the measured electric field component and the corresponding theoretical Gaussian PDF at 3.5 GHz.

An example of the electric field component measurement is conducted in the RC at the University of Liverpool using a vector network analyzer (VNA). The operating frequency is 3.5 GHz. Note that the transmission coefficient (S_{21}) measured by the VNA is equivalent to an arbitrary component of the electric field (but is normalized by its output). In total, 360 field samples are collected using mechanical stirring. The histograms of the real and imaginary parts of the measured samples and the theoretical Gaussian PDF directly calculated by (2.118) are illustrated in Figure 2.14. Relevant

parameters in (2.118) are estimated by the MLE. It can be found that the real and imaginary parts follow identical distribution, and there is a good agreement between the measured data and the theoretical Gaussian PDF curve.

The magnitude of an arbitrary rectangular component of the electric field $|E_*|$ is Chi distributed with 2 degrees of freedom (or equivalently, Rayleigh distributed). The PDF is shown below [59]:

$$PDF\left(|E_*|\right)=\frac{x}{\sigma^2}\exp\left(-\frac{x^2}{2\sigma^2}\right),\quad x=|E_*| \tag{2.120}$$

with mean $\sqrt{\frac{\pi}{2}}\sigma$ and standard deviation $\sqrt{\frac{2-\pi}{2}}\sigma$. An example of the distribution of $|E_*|$ measured in the RC at the University of Liverpool at 3.5 GHz and the corresponding theoretical Rayleigh PDF (2.120) is shown in Figure 2.15. Again, good agreement between the measured samples and the theoretical PDF can be obtained. Thus, $|E_*|$ follows a Rayleigh distribution.

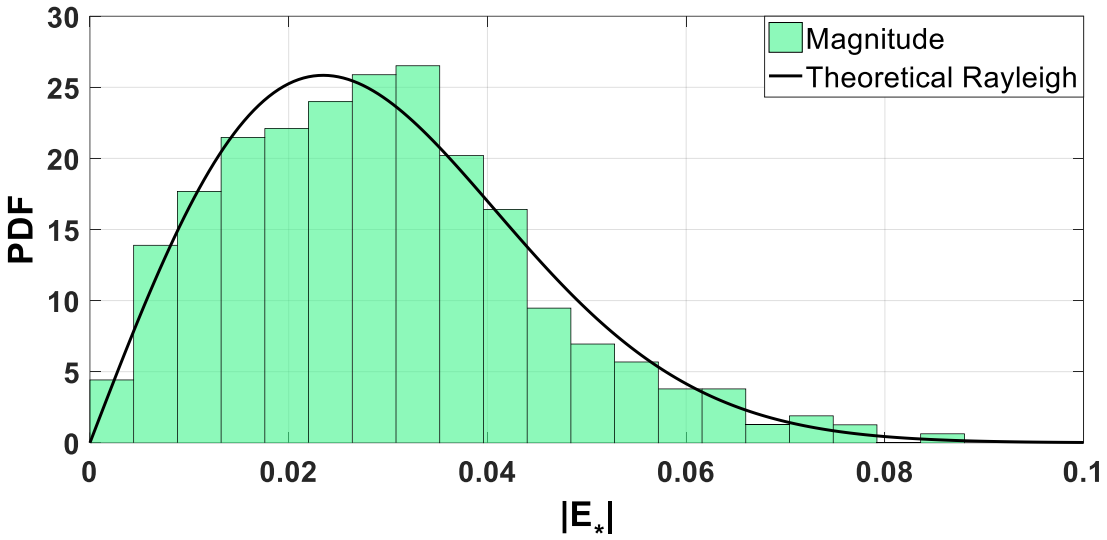

Figure 2.15: Distribution of the magnitude of the measured electric field component and the corresponding theoretical Rayleigh PDF at 3.5 GHz.

The phase of the rectangular component of the electric field $\angle E_*$ follows a uniform distribution from $-\pi$ to π with the following PDF:

$$PDF\left(\angle E_*\right)=\begin{cases}\dfrac{1}{2\pi}, -\pi \le x \le \pi \\ 0, x<-\pi \,||\, x>\pi\end{cases}, \quad x=\angle E_* \tag{2.121}$$

The magnitude of the total electric field $|\mathbf{E}|$ follows a Chi distribution with 6 degrees of freedom [61]:

$$PDF\left(|\mathbf{E}|\right)=\frac{x^5}{8\sigma^6}\exp\left(-\frac{x^2}{2\sigma^2}\right), \quad x=|\mathbf{E}| \tag{2.122}$$

with mean $\dfrac{15\sqrt{2\pi}}{16}\sigma$ and standard deviation $\sqrt{\dfrac{768-225\pi}{128}}\sigma$.

The square magnitude of an arbitrary rectangular component of the electric field $|E_*|^2$ is related to the power (or energy) of the signal, and follows a Chi-square distribution with 2 degrees of freedom (or equivalently, Exponential distribution) which has the following PDF:

$$PDF\left(|E_*|^2\right)=\frac{1}{2\sigma^2}\exp\left(-\frac{x}{2\sigma^2}\right), \quad x=|E_*|^2 \tag{2.123}$$

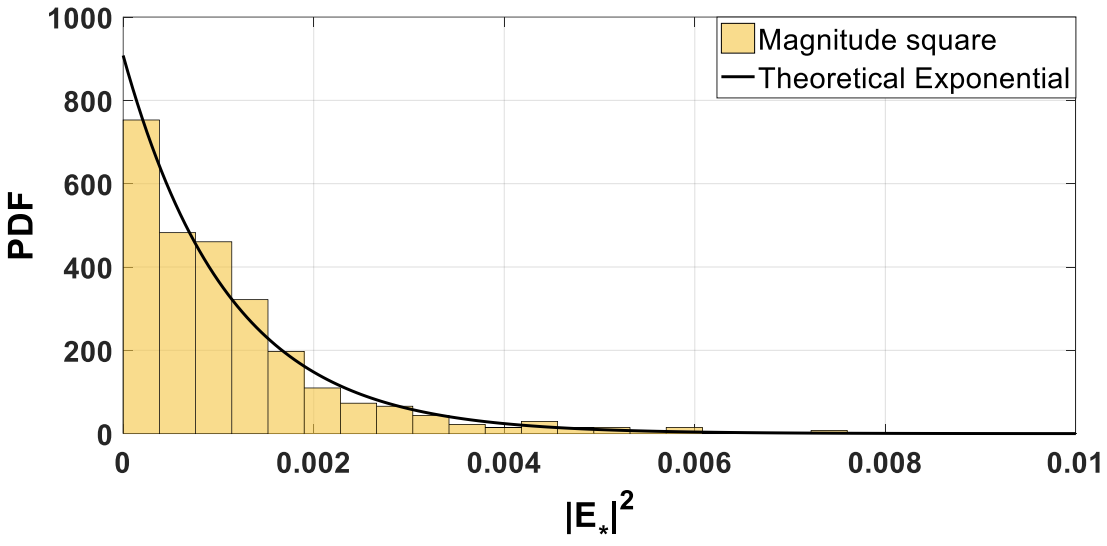

Figure 2.16: Distribution of the square magnitude of the measured electric field component and the corresponding theoretical Exponential PDF at 3.5 GHz.

with mean $2\sigma^2$ and standard deviation $2\sigma^2$. An example of the distribution of $|E_*|^2$

measured in the RC at the University of Liverpool at 3.5 GHz and the corresponding theoretical Exponential PDF (2.123) are shown in Figure 2.16. Experimental evidence proves that $|E_*|^2$ follows an Exponential distribution.

Based on (2.123) and the additive property of the Chi-square distributed random variable, the square magnitude of the total electric field $|\mathbf{E}|^2$ also follows a Chi-square distribution with 6 degrees of freedom [61]:

$$PDF\left(|\mathbf{E}|^2\right) = \frac{x^2}{16\sigma^6}\exp\left(-\frac{x^2}{2\sigma^2}\right), \quad x = |\mathbf{E}|^2 \tag{2.124}$$

with mean $6\sigma^2$ and standard deviation $\frac{\sigma^2}{\sqrt{12}}$.

2.7 Summary

In this chapter, fundamental theories for the basic characterization process of an RC were introduced from both physical and mathematical points of view. Specifically, in Section 2.2, the resonant cavity model for an arbitrary rectangular-shaped cavity was presented, and the LUF of the RC with the same dimensions was determined accordingly. For all experimental validations of the novel works in Chapter 3 – 5, the frequencies of operation were chosen to be well above the LUF of the RC to ensure that the results are rigorous and convincing. In Section 2.3, the *Q* factor, which is an important parameter for RC characterization, was introduced. In Chapter 3, the time domain method for calculating the chamber decay constant is essentially based on the finite *Q* of the RC. The reference substitution method for TRP measurement and the corresponding analytical uncertainty model proposed in Chapter 4 is only valid if *Q* is kept unchanged. In Chapter 5, the change of the insertion loss as a function of the frequency can be clearly explained by decomposing *Q*. In section 2.4, two time domain parameters were introduced. Losses due to loadings inside the RC (Chapter 3 and Chapter 5), and scattering of the EM field by the stirrers (Chapter 3) can be well characterized in the time domain. In section 2.5, channel characterization in the RC in different domains were interlinked by using the Wiener-Khinchin theorem. In Chapter 3, the proposed frequency domain method for calculating the scattering damping time

is derived from the relationship from the unstirred power envelope and the FD-ACFUS. In Chapter 4, the number of independent stirrer positions and independent frequency points can be determined based on the corresponding ACFs or power profiles. In section 2.6, the statistical model of an RC was elaborated based on the plane wave spectrum theory. In Chapter 3, the statistical model is used for the uncertainty analysis of the scattering damping time. In Chapter 4, the MLE of the average Rician *K*-factor is derived based on the ratio of two Chi-square distributions. In Chapter 5, the theoretical HUF model is based on the statistical distributions of the average power of the desired received signal and the corresponding average noise power.

2.8 References

[1] David M. Pozar, Microwave Engineering. Singapore: Wiley, 4th ed., 2011.

[2] R. F. Harrington, Time-Harmonic Electromagnetic Fields. New York: McGraw-Hill, 1961.

[3] D. A. Hill, Electromagnetic Fields in Cavities: Deterministic and Statistical Theories. New York: Wiley-IEEE Press, 2009.

[4] C.A. Balanis, Advanced Engineering Electromagnetics. Wiley, 2nd ed., 2012.

[5] Q. Xu and Y. Huang, Anechoic and Reverberation Chambers: Theory, Design and Measurements, Wiley-IEEE, UK, 2019.

[6] Y. Huang, "Conducting triangular chambers for EMC measurements," *Measurement Science and Technology*, vol. 10, pp. 121-124, 1999.

[7] B. H. Liu, D. C. Chang, and M. T. Ma, "Eigenmodes and the composite quality factor of a reverberating chamber," US National Bureau of Standards, Tech. Rep., 1983.

[8] S. J. Boyes, and Y. Huang, Reverberation Chambers: Theories and Applications to EMC and Antenna Measurements, West Sussex, WS, UK: Wiley, 2016.

[9] Y. Huang, "The investigation of chamber for electromagnetic systems," Ph.D. thesis, Dept. of Eng. Sci., Univ. of Oxford, Oxford, U.K., 1993.

[10] U. Carlberg, P. S. Kildal and J. Carlsson, "Numerical study of position stirring and frequency stirring in a loaded reverberation chamber," *IEEE Trans. Electromagn. Compat.*, vol. 51, pp. 12-17, 2009.

[11] W. A. Strauss, Partial Differential Equations: An Introduction. New York: Wiley, 2nd ed., 2008.

[12] D. A. Hill, "A reflection coefficient derivation for the Q of a reverberation chamber," *IEEE Trans. Electromagn. Compat.*, vol. 38, pp. 591-592, 1996.

[13] P. Corona, G. Latmiral, and E. Paolini, "Performance and Analysis of a Reverberating Enclosure with Variable Geometry," *IEEE Trans. Electromagn. Compat.*, vol. 22, pp. 2-5, 1980.

[14] D. A. Hill, M. T. Ma, A. R. Ondrejka, B. F. Riddle, M. L. Crawford, and R. T. Johnk, "Aperture excitation of electrically large, lossy cavities," *IEEE Trans. Electromagn. Compat.*, vol. 36, pp. 169-178, 1994.

[15] Y. Huang, and K. Boyle, Antennas: from Theory to Practice. West Sussex, UK: Wiley, 1st ed. 2008.

[16] C. L. Holloway, H. A. Shah, R. J. Pirkl, W. F. Young, D. A. Hill, and J. Ladbury, "Reverberation chamber techniques for determining the radiation and total efficiency of antennas," *IEEE Trans. Antennas Propag.*, vol. 60, no. 4, pp. 1758–1770, Apr. 2012.

[17] C. L. Holloway, H. A. Shah, R. J. Pirkl, K. A. Remley, D. A. Hill, and J. Ladbury, "Early time behavior in reverberation chambers and its effect on the relationships between coherence bandwidth, chamber decay time, RMS delay spread, and the chamber build-up time," *IEEE Trans. Electromagn. Compat.*, vol. 54, no. 4, pp. 714-725, Aug. 2012.

[18] K. Rosengren, and P.S. Kildal, "Study of distributions of modes and plane waves in reverberation chambers for the characterization of antennas in a multipath environment," *Microw. Opt. Technol. Lett.*, vol. 30, pp. 386-391, 2001.

[19] P.-S. Kildal, X. Chen, C. Orlenius, M. Franzén, and C. S. L. Patané, "Characterization of reverberation chambers for OTA measurements of wireless devices: Physical formulations of channel matrix and new uncertainty formula," *IEEE Trans. Antennas Propag.*, vol. 60, no. 8, pp. 3875–3891, Aug. 2012.

[20] P.-S. Kildal, Foundations of Antenna Engineering: A Unified Approach for Line-of-Sight and Multipath. Artech House, 2015.

[21] U. Carlberg, P. S. Kildal, A. Wolfgang, O. Sotoudeh, and C. Orlenius, "Calculated and measured absorption cross sections of lossy objects in reverberation chamber," *IEEE Trans. Electromagn. Compat.*, vol. 46, no. 2, pp. 146-154, May. 2004.

[22] Z. Tian, Y. Huang, Y. Shen, and Q. Xu, "Efficient and accurate measurement of absorption cross section of a lossy object in reverberation chamber using two one-antenna methods," *IEEE Trans. Electromagn. Compat.*, vol. 58, no. 3, pp. 686-693, Jun. 2016.

[23] *Electromagnetic Compatibility (EMC)—Part 4–21: Testing and Measurement Techniques – Reverberation Chamber Test Methods*, IEC 61000-421, IEC Standard, Ed 2.0, Jan. 2011.

[24] B. Demoulin, and P. Besnier, Electromagnetic Reverberation Chambers. Wiley, 1st ed. 2011.

[25] Q. Xu, Y. Huang, L. Xing, Z. Tian, M. Stanley, and S. Yuan, "B-scan in a reverberation chamber," *IEEE Trans. Antennas Propag.*, vol. 64, no. 5, pp. 1740–1750, May 2016.

[26] X. Chen, P.-S. Kildal, C. Orlenius, and J. Carlsson, "Channel sounding of loaded reverberation chamber for over-the-air testing of wireless devices: Coherence bandwidth versus average mode bandwidth and delay spread," *IEEE Antennas Wireless Propag. Lett.*, vol. 8, pp. 678–681, 2009.

[27] G. B. Tait and R. E. Richardson, "Wireless channel modelling of multiply connected reverberant spaces: Application to electromagnetic compatibility assessment," *IEEE Trans. Electromagn. Compat.*, vol. 55, no. 6, pp. 1320–1327, Dec. 2013.

[28] E. Genender, C. L. Holloway, K. A. Remley, J. M. Ladbury, G. Koepke, and H. Garbe, "Simulating the multipath channel with a reverberation chamber: Application to bit error rate measurements," *IEEE Trans. Electromagn. Compat.*, vol. 52, no. 4, pp. 766–777, Nov. 2010.

[29] Test Plan for Wireless Large-Form-Factor Device Over-the-Air Performance, CTIA Certification, Washington, DC, USA, 2016.

[30] G. Lerosey and J. de. Rosny, "Scattering cross section measurement in reverberation chamber," *IEEE Trans. Electromagn. Compat.*, vol. 49, no. 2, pp. 280–284, May 2007.

[31] Q. Xu, L. Xing, Y. Zhao, T. Loh, T. Jia and Y. Huang, "The Noise Level of Total Scattering Cross Section Measurement in a Reverberation Chamber," *IEEE Antennas Wireless Propag. Lett.*, vol. 17, no. 10, pp. 1842-1846, Oct. 2018.

[32] Q. Xu, Y. Huang, L. Xing, Z. Tian, C. Song, and M. Stanley, "The limit of the total scattering cross section of electrically large stirrers in a reverberation chamber," *IEEE Trans. Electromagn. Compat.*, vol. 58, no. 2, pp. 623–626, Apr. 2016.

[33] T. Jia, Y. Huang, Q. Xu, Z. Tian, J. Jiang, and Q. Hua, "Frequency Domain Method for Scattering Damping Time Extraction of a Reverberation Chamber Based on Autocorrelation Functions," *IEEE Trans. Electromagn. Compat.*, vol. 62, no. 6, pp. 2349-2357, Dec. 2020.

[34] S. Lallechere, I. E. Baba, P. Bonnet, and F. Paladian, "Total scattering cross section improvements from electromagnetic reverberation chambers modelling and stochastic formalism," *in Proc. 5th European Conf. Antennas Propag.*, Rome, Italy, pp. 81–85, Apr. 2011.

[35] I. E. Baba, S. Lallechere, P. Bonnet, J. Benoit, and F. Paladian, "Computing total scattering cross section from 3-D reverberation chambers time modelling," *in Proc. Asia-Pacific Symp. Electromagn. Compat.*, Singapore, May 2012.

[36] E. W. Weisstein, "Wiener–Khinchin Theorem." From MathWorld— A Wolfram Web Resource. [Online]. Available: https://mathworld.wolfram.com/Wiener-KhinchinTheorem.html

[37] Q. Xu, L. Xing, Y. Zhao, Z. Tian, and Y. Huang, "Wiener–Khinchin theorem in a reverberation chamber," *IEEE Trans. Electromagn. Compat.*, vol. 61, no. 5, pp. 1399-1407, Oct. 2019.

[38] Q. Xu L. Xing Y. Zhao T. Loh M. Wang and Y. Huang, "Approximate analytical equations for the stirrer angular correlation in a reverberation chamber," *IEEE Trans. Electromagn. Compat.*, vol. 61, no. 6, pp. 1707-1713, Dec. 2019.

[39] X. Chen, J. Tang, T. Li, S. Zhu, Y. Ren, Z. Zhang, and A. Zhang, "Reverberation Chambers for Over-the-Air Tests: An Overview of Two Decades of Research," *IEEE Access.*, vol. 6, pp. 49129–49143, Aug. 2018.

[40] G. B. Tait and R. E. Richardson, "Wireless channel modelling of multiply connected reverberant spaces: Application to electromagnetic compatibility assessment," *IEEE Trans. Electromagn. Compat.*, vol. 55, no. 6, pp. 1320–1327, Dec. 2013.

[41] K. Karlsson, X. Chen, P.-S. Kildal, and J. Carlsson, "Doppler spread in reverberation chamber predicted from measurements during step-wise stationary stirring," *IEEE Antennas Wireless Propag. Lett.*, vol. 9, pp. 497– 500, May 2010.

[42] J.-H. Choi, J.-H. Lee, and S.-O. Park, "Characterizing the impact of moving mode-stirrers on the Doppler spread spectrum in a reverberation chamber," *IEEE Antennas Wireless Propag. Lett.*, vol. 9, pp. 375–378, Apr. 2010.

[43] X. Chen, P.-S. Kildal, and J. Carlsson, "Determination of maximum Doppler shift in reverberation chamber using level crossing rate," *in Proc. 5th Eur. Conf. Antennas Propag.*, Rome, Italy, pp. 62–65, 2011.

[44] Z. Tian, Y. Huang, and Q. Xu, "Stirring effectiveness characterization based on Doppler spread in a reverberation chamber," *in Proc. 10th Eur. Conf. Antennas Propag.*, Davos, Switzerland, pp. 1–3, 2016.

[45] N. Wellander, O. Lunden, and M. Bäckström, "Experimental investigation and mathematical modeling of design parameters for efficient stirrers in mode stirred reverberation chambers," *IEEE Trans. Electromagn. Compat.*, vol. 49, no. 1, pp. 94–103, 2007.

[46] C. Lemoine, P. Besnier, and M. Drissi, "Estimating the effective sample size to select independent measurements in a reverberation chamber," *IEEE Trans. Electromagn. Compat.*, vol. 50, no. 2, pp. 227–236, 2008.

[47] O. Delangre, P.D. Doncker, M. Lienard, *et al.*, "Analytical angular correlation function in mode-stirred reverberation chamber," *Electron. Lett.*, vol. 45, no. 2, pp. 90–91, 2009.

[48] F. Moglie, and V.M. Primiani, "Analysis of the independent positions of reverberation chamber stirrers as a function of their operating conditions," *IEEE Trans. Electromagn. Compat.*, vol. 53, no. 2, pp. 288–295, 2011.

[49] K. Rosengren and P.-S. Kildal, "Study of distributions of modes and plane waves in reverberation chambers for the characterization of antennas in a multipath environment," *Microw. Opt. Technol. Lett.*, vol. 30, no. 6, pp. 386–391, Aug. 2001.

[50] L. R. Arnaut, R. Serra, and P. D. West, "Statistical anisotropy in imperfect electromagnetic reverberation," *IEEE Trans. Electromagn. Compat.*, vol. 59, no. 1, pp. 3–13, Feb. 2017.

[51] M. Otterskog and K. Madsen, "On creating a nonisotropic propagation environment inside a scattered field chamber," *Microw. Opt. Technol. Lett.*, vol. 43, no. 3, pp. 192–195, Nov. 2004.

[52] J. F. Valenzuela-Valdes, A. M. Martinez-Gonzalez, and D. A. Sanchez-Hernandez, "Emulation of MIMO nonisotropic fading environments with reverberation chambers," *IEEE Antennas Wireless Propag. Lett.*, vol. 7, pp. 325–328, 2008.

[53] R. J. Pirkl, and K. A. Remley, "Experimental evaluation of the statistical isotropy of a reverberation chamber's plane-wave spectrum," *IEEE Trans. Electromagn. Compat.*, vol. 46, no. 3, pp. 498–509, Jun. 2014.

[54] M. G. Becker *et al*., "Spatial channels for wireless over-the-air measurements in reverberation chambers," *in Proc. 12th Eur. Conf. Antennas Propag.*, London, U.K., pp. 1–5, Apr. 2018.

[55] X. Chen, M. Zhang, S. Zhu, and A. Zhang, "Empirical Study of Angular–Temporal Spectra in a Reverberation Chamber," *IEEE Trans. Antennas Propag.*, vol. 66, no. 11, pp. 6452-6456, Nov. 2018.

[56] X. Chen, T. Li, M. Zhang, S. Zhu, and A. Zhang, "On Power Angular Spectrum Estimation in a Reverberation Chamber," *in Proc. 13th Eur. Conf. Antennas Propag.*, Krakow, Poland, pp. 1-5, 2019.

[57] R. H. Price, H. T. Davis, and E.P. Wenaas, "Determination of the statistical distribution of electromagnetic-field amplitudes in complex cavities," *Phys. Rev. E*, vol. 48, pp. 4716-4729, 1993.

[58] D. A. Hill, "Plane wave integral representation for fields in reverberation chambers," *IEEE Trans. Electromagn. Compat.*, Vol. 40, pp. 209-217, 1998.

[59] A. Papoulis, *Probability, Random Variables, and Stochastic Processes*. New York: McGraw-Hill, 1965.

[60] J. G. Kostas and B. Boverie, "Statistical model for a mode-stirred chamber," *IEEE Trans. Electromagn. Compat.*, vol. 33, no. 4, pp. 366–370, Nov. 1991.

[61] N. L. Johnson and S. Kotz, *Continuous Univariate Distributions, Volume 2 (2nd Edition)*. New York, NY, USA: Wiley, 1995.

Chapter 3 A Novel Method for Scattering Damping Time Extraction and Stirrer Performance Characterization

In this chapter, to characterize the stirrer performance of an RC in a more reliable and efficient way, a novel frequency domain method based on two ACFs is proposed for calculating the scattering damping time.

3.1 Introduction

The scattering damping time (τ_s) is defined as the characteristic time for the targets to scatter the wave at least once [1]. In the context of an RC, τ_s gives an indication about how fast its assembled mechanical stirrers can scatter the EM waves excited by a transmitting antenna [2]. For a well-designed RC, its assembled stirrers usually occupy a significant fraction of the RC dimensions. Consequently, if a signal trace is stirred by the stirrers once, it is more likely that it will interact with the stirrers (not necessarily the same part) multiple times before it finally reaches the receiving antenna. τ_s is closely related to the equivalent TSCS [1], [3] – [6], which is a widely used parameter to quantify the geometry and movement properties of the stirrers assembled in an RC. More importantly, the stirrer efficiency can be defined based on τ_s so that it is independent of the amount of extra loading or the position of the measurement antennas [7]. In this way, the reliable and repeatable stirrer performance characterization of an RC can be achieved. Stirrers with higher stirrer efficiency can provide better field uniformity [8], [9], more independent samples [10], and improved uncertainty [11] for

various RC-based measurement applications [12].

Conventionally, τ_s is extracted based on the slopes of two types of time domain responses, namely the PDP [13] and the unstirred power envelope [1], on a logarithmic scale. Therefore, it is necessary to perform the IFT to convert S-parameters measured from the VNA into the time domain. Feasible as it is, this commonly used method suffers from several limitations, which results in additional sources of errors. Firstly, the ranges of the time domain responses used for the least square fitting are selected empirically [13], and the error that arises from this procedure becomes more prominent for the τ_s measurement in which the stirrer itself is the object under test (OUT). Secondly, the noise level of the late-time response is relatively high during the τ_s measurement (*e.g.,* only about 15 dB dynamic range for the measurement scenario in [6]), which could reduce the available measurement range. Thirdly, the number of samples required is the same as that of the original frequency response obtained from the VNA, regardless of the desired resolution bandwidth [14].

In this chapter, based on two types of ACFs) defined in (3.1) and (3.14) and the Wiener-Khinchin theorem [15], we show that τ_s can be directly extracted from the relevant threshold frequency offset values, and no IFT operation is required. Therefore, the abovementioned limitations and assumptions in the conventional method are eliminated. On the other hand, the main merits of the conventional method, such as independent of the total efficiency of the measurement antennas, are maintained. A more reliable stirrer performance characterization process of an RC can be achieved by applying the proposed ACF-based method.

The rest of this chapter is organized as follows. The mathematical deduction of the proposed ACF-based method for the measurement of τ_s is given in Section 3.2. Section 3.3 elaborates the experimental setup and preparations. Section 3.4 presents comparisons of the measurement results using the IFT-based and ACF-based methods under different scenarios, including two frequency bands and three stirrer configurations. Discussions are also given in Section 3.4. Finally, Section 3.5 summarizes the work done in this chapter.

3.2 Theory

Let $S_{21}(f,n)$ be the complex transmission coefficient measured at a mechanical stirrer position *n* and frequency *f*. By definition, the frequency domain ACF (FD-ACF) $R(\partial f,n)$ can be calculated using

$$R(\partial f,n)=\int_{-\infty}^{+\infty}S_{21}(f,n)S_{21}^{*}(f+\partial f,n)df \tag{3.1}$$

where ∂f stands for the frequency offset of the FD-ACF, and $*$ is the complex conjugate operation. For practical measurement scenarios, the frequency band of interest is limited, and the integration interval in (3.1) is substituted by a finite region.

According to the Wiener-Khinchin theorem [15], the FD-ACF and the time domain PDP essentially constitute a Fourier pair as follows

$$R(\partial f,n)=\int_{-\infty}^{+\infty}PDP(t,n)e^{-j2\pi\partial ft}dt=\int_{-\infty}^{+\infty}\left|s_{21}(t,n)\right|^{2}e^{-j2\pi\partial ft}dt \tag{3.2}$$

where $s_{21}(t,n)$ is the time domain transmission coefficient from Antenna 1 to Antenna 2 at one stirrer position, which is the IFT of $S_{21}(f,n)$

$$s_{21}(t,n)=\int_{-\infty}^{+\infty}S_{21}(f,n)e^{j2\pi ft}df \tag{3.3}$$

and $\left|s_{21}(t,n)\right|^{2}$ is the corresponding PDP. Averaging both sides of (3.2) with all *N* stirrer positions (covering a complete revolution) gives

$$\left\langle R(\partial f,n)\right\rangle_{N}=\int_{-\infty}^{+\infty}\left\langle PDP(t,n)\right\rangle_{N}e^{-j2\pi\partial ft}dt \tag{3.4}$$

Provided that the early-time behavior of the RC is neglected, it is proven in [13] that

$$\left\langle PDP(t,n)\right\rangle_{N}=\left\langle\left|s_{21}(t,n)\right|^{2}\right\rangle_{N}=P_{0}e^{-\frac{t}{\tau_{RC}}}\quad t>0 \tag{3.5}$$

where $\langle\ \rangle$ denotes the ensemble average over multiple stirrer positions, P_0 is the normalized initial power when $t=0$ and τ_{RC} means the chamber (decay) time constant. Simplifying the indefinite integral in (3.4) based on (3.5) and normalizing the magnitude to its peak value (when $\partial f=0$) gives [13]

$$\left|\left\langle R\left(\partial f,n\right)\right\rangle_N\right|_{norm}=\frac{1}{\sqrt{1+\left(2\pi\tau_{RC}\partial f\right)^2}} \tag{3.6}$$

where $|\ |_{norm}$ means taking the absolute value and normalizing to the peak value. If a threshold value $\frac{1}{\sqrt{2}}$ is set in (3.6) [16], we can get

$$\tau_{RC}=\frac{1}{2\pi\partial f_{th}} \tag{3.7}$$

where ∂f_{th} is the reading of the frequency offset when the value of $\left|\left\langle R\left(\partial f,n\right)\right\rangle_N\right|_{norm}$ drops to $\frac{1}{\sqrt{2}}$. Note that (3.7) directly relates τ_{RC} to the FD-ACF.

According to the two definitions (from different perspectives) of the *Q* factor for an RC given in [17]

$$Q=\frac{f}{\Delta f}=\omega\tau_{RC} \tag{3.8}$$

where Δf is the average mode bandwidth due to different sources of power loss leading to finite *Q*, and ω is the angular frequency. By substituting (3.8) into (3.7), we obtain $\partial f_{th}=\Delta f$, which is the actual physical meaning of ∂f_{th} [18].

Further investigation into $\mathrm{S}_{21}\left(f,n\right)$ shows that it consists of two parts [11]

$$S_{21}\left(f,n\right)=S_{21,s}\left(f,n\right)+S_{21,us}\left(f\right) \tag{3.9}$$

where $S_{21,s}\left(f,n\right)$ is the stirred part that efficiently interacts with the stirrer position *n*, and $S_{21,us}\left(f\right)$ is the unstirred part which is defined as [11]

$$S_{21,us}\left(f\right)=\left\langle S_{21}\left(f,n\right)\right\rangle_N \tag{3.10}$$

The following equation can be derived based on (3.3) and (3.10)

$$\left\langle s_{21}\left(t,n\right)\right\rangle_N=\int_{-\infty}^{+\infty}S_{21,us}\left(f\right)e^{j2\pi ft}df \tag{3.11}$$

which indicates that $S_{21,us}\left(f\right)$ and $\left\langle s_{21}\left(t,n\right)\right\rangle_N$ together form a Fourier pair. In [1], it is given that

$$\left|\left\langle s_{21}\left(t,n\right)\right\rangle_N\right|^2=P_o e^{-\frac{t}{\tau_{eq}}}\quad t>0 \tag{3.12}$$

with

$$\frac{1}{\tau_{eq}} = \frac{1}{\tau_{RC}} + \frac{1}{\tau_s} \tag{3.13}$$

where τ_s is the scattering damping time. From (3.5), (3.12), and (3.13), it can be seen that τ_s essentially describes how fast the unstirred power is dissipated relative to that of the total excitation power (for more details, please see Section 2.4.2

).

Similar to equation (3.1), we can define the ACF-based on the unstirred power (or FD-ACFUS for simplicity), which is given as follows

$$R_{us}(\partial f) = \int_{-\infty}^{+\infty} S_{21,us}(f) S_{21,us}^{*}(f+\partial f)\, df \tag{3.14}$$

Again, based on the Wiener-Khinchin theorem, the following Fourier pair can be derived

$$R_{us}(\partial f) = \int_{-\infty}^{+\infty} \left| \langle s_{21}(t,n) \rangle_N \right|^2 e^{-j2\pi\partial f t}\, dt \tag{3.15}$$

Substituting (3.12) into (3.15) and normalizing the magnitude to its peak value gives

$$\left| R_{us}(\partial f) \right|_{norm} = \frac{1}{\sqrt{1+\left(2\pi\tau_{eq}\partial f\right)^2}} \tag{3.16}$$

If we also set a threshold value $\frac{1}{\sqrt{2}}$ to equation (3.16), then we obtain

$$\partial f_{th2} = \frac{1}{2\pi\tau_{eq}} = \frac{1}{2\pi}\left(\frac{1}{\tau_{RC}} + \frac{1}{\tau_s}\right) \tag{3.17}$$

where ∂f_{th2} is the reading of the frequency offset when the value of $\left| R_{us}(\partial f) \right|_{norm}$ reduces to $\frac{1}{\sqrt{2}}$. Combining (3.7) and (3.17) to give

$$\tau_s = \frac{1}{2\pi\left(\partial f_{th2} - \partial f_{th}\right)} \tag{3.18}$$

Thus, τ_s is extracted directly in the frequency domain from the FD-ACF and FD-ACFUS, and no IFT operation is needed. It is worth emphasizing that there is no explicit term related to radiation efficiency or free space impedance in equation (3.18), which indicates that this method does not require prior knowledge for the measurement

antennas.

3.3 Experimental Setup and Preparations

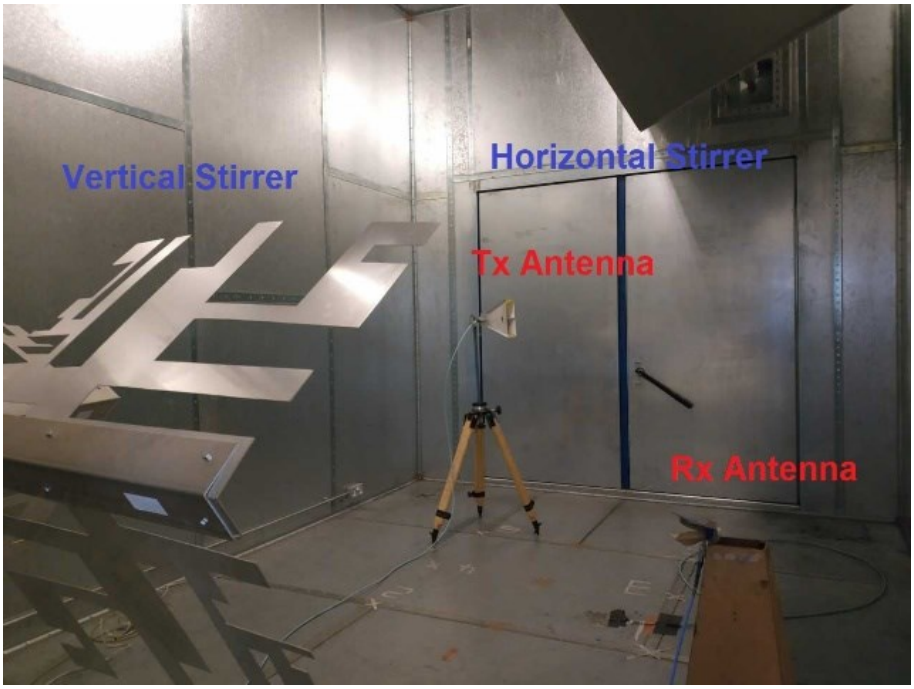

(a)

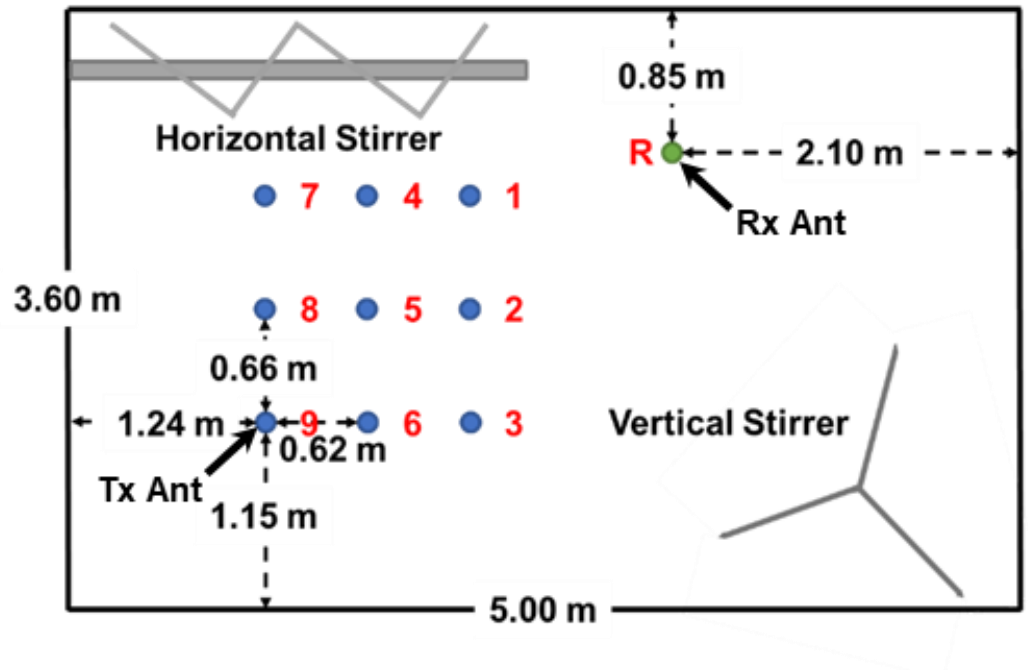

(b)

Figure 3.1: Typical experimental setup: (a) Practical measurement scenario. (b) Schematic diagram showing the two stirrers and two antennas.

The RC at the University of Liverpool (with dimensions 3.60 m (w) × 5.80 m (l) × 4.00 m (h)) was used for measurements [17]. A typical chamber measurement setup is illustrated in Figure 3.1 (a). The chamber is furnished with two computer-controlled mechanical stirrers. The receiving antenna (SATIMO SH 2000) was placed at a fixed location (point "R" in Figure 3.1 (b)) with unchanged orientation (towards the vertical stirrer), polarization (vertical polarization), and height (0.77 m). In contrast, the transmitting antenna (Rohde & Schwarz HF 906), with 1.40 m in height, was fixed at point 9 in Figure 3.1 (b) facing the horizontal stirrer with horizontal polarization. Before each measurement, a standard 2-port calibration was performed to move the reference plane (RP) from the output ports of the VNA to the input ports of Antenna 1 and Antenna 2. Throughout the whole experimental procedure, the intermediate frequency (IF) bandwidth was chosen to be 10 kHz as a compromise between the noise floor level and the measurement time. The output power was set to -3 dBm. During each measurement, the stirrers were moved in mode-tuning mode with 1° step size to 360 positions to cover a complete revolution. At each stirrer position, a 200 MHz frequency band (giving a 5 ns time domain resolution) was swept with 1601 S_{21} samples, which corresponds to a 125 kHz sampling interval or an 8 μs time period, which is long enough to avoid the aliasing effect.

Subsequently, the central 100 MHz was used for τ_{RC} and τ_s extraction. The reason for doing this is to emphasize the function of the frequency domain moving filtering window, which is necessary, especially in wideband measurement scenarios like the 5G mm-wave band characterization, to select narrower sub-bands for improved resolution of the quantity to be measured. For the proposed ACF-based approach, samples outside the moving window can be discarded. In contrast, for the conventional IFT-based method, a relatively complex bandpass filter (BPF) (Elliptic, Gaussian, *etc.*) is generally required, and the number of samples needed is the same as that of the initial frequency response obtained from the VNA despite the actual frequency resolution.

Frequency samples of the stirred (S_{21}) and unstirred ($S_{21,us}$) responses used for the ACF-based and IFT-based methods for 200 MHz bandwidth (2.3 GHz – 2.5 GHz) and 100 MHz (2.35 GHz – 2.45 GHz) resolution are shown in Figure 3.2 for details. It can be seen that the unstirred power is around 15 dB lower than the original power. Figure 3.2

also indicates that for the IFT-based method, although only the frequency range of 2.35 GHz – 2.45 GHz is of interest, all the 1601 points are required in order to perform the IFT correctly. In contrast, the proposed method only needs 961 points (60% of the IFT-based method) by considering a 10 MHz frequency offset band (80 points) on both sides, which saves storage and computational resources. It is also flexible to adjust the width of the offset band to adapt to different situations. However, this offset band is small compared to the whole bandwidth of the frequency response in practical cases.

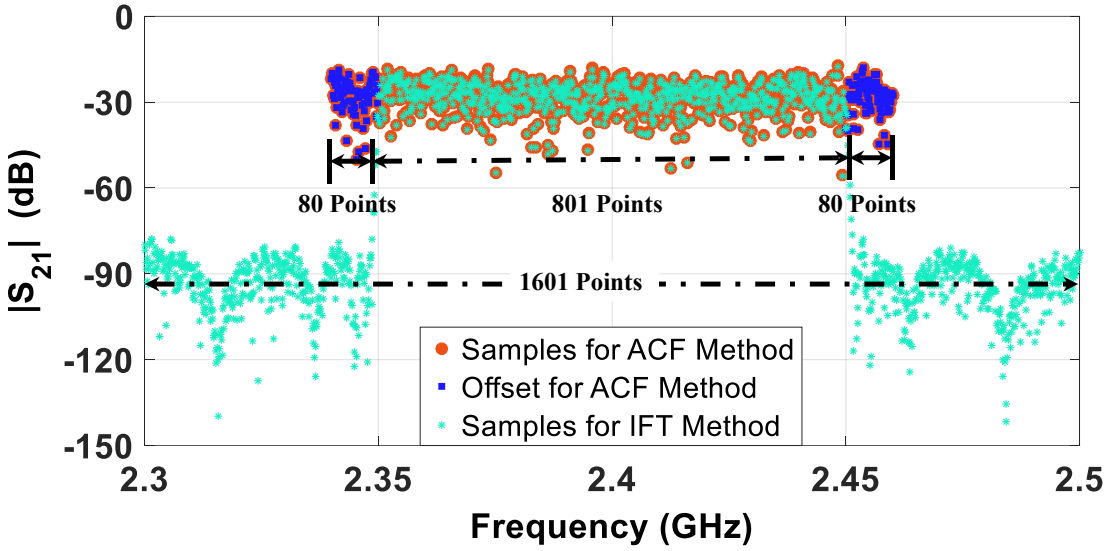

(a)

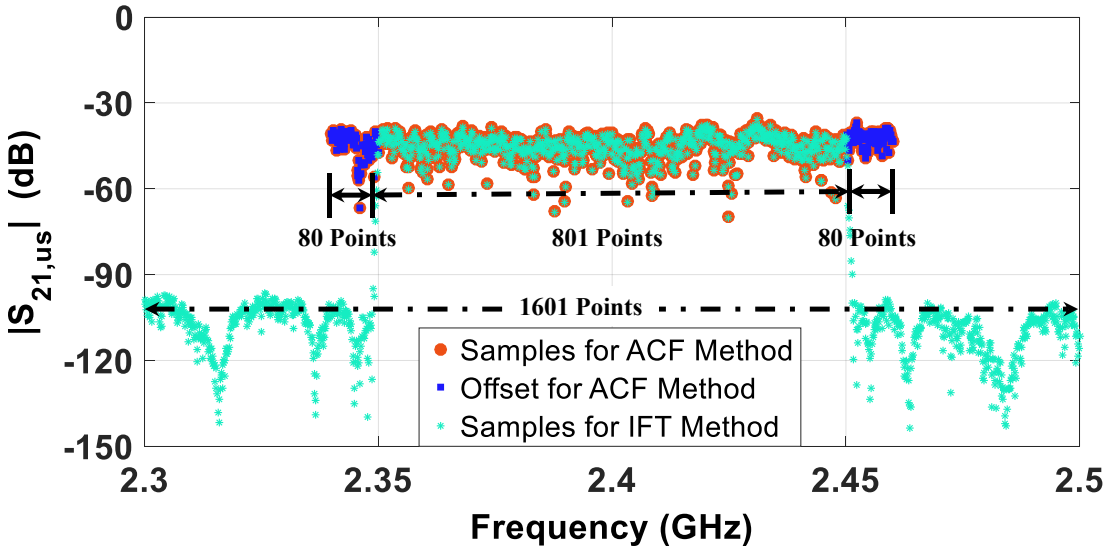

(b)

Figure 3.2: Frequency samples used for ACF-based and IFT-based methods for 200 MHz bandwidth (2.3 GHz – 2.5 GHz) and 100 MHz (2.35 GHz – 2.45 GHz)

resolution: (a) S_{21}. (b) $S_{21,us}$.

Moreover, the scenario mentioned above will be more prominent for wideband measurement with much more frequency samples, while a specific frequency resolution is still required for the parameters to be calculated.

In the next section, two sets of experiments are conducted in order to verify the proposed approach. Firstly, measurements are repeated at two different frequency bands: the lower band (2.3 GHz – 2.5 GHz) and the higher band (5.8 GHz – 6.0 GHz) to check if it is sensitive to the frequency of operation. Secondly, three different stirrer configurations (case 1: with both the horizontal stirrer and the vertical stirrer rotating simultaneously; case 2: with the horizontal stirrer only; case 3: with the vertical stirrer only) are examined to evaluate if it is sensitive to stirrers used. For each measurement, the traditional IFT-based method is also performed for comparison purposes, and a 10th order elliptic BPF with 100 MHz bandwidth, 0.5 dB passband ripple, and 60 dB stopband attenuation is used. As aforementioned, τ_s is closely related to the equivalent TSCS and the stirrer efficiency, and these two quantities can be used to verify the proposed method. The equivalent TSCS is, by definition, linked to τ_s by the following equation [1]:

$$TSCS = \frac{V}{\tau_s c_0} \tag{3.19}$$

where V is the volume of the RC, and c_0 is the speed of the light in free space. The stirrer efficiency is defined based on τ_s in [7] as

$$\eta_s = 1 - \exp\left(-\frac{12\sqrt[3]{V}}{c_0 \tau_s}\right) \tag{3.20}$$

In order to quantify the difference between the parameters obtained using the IFT-based method and the proposed ACF-based method, the following relative discrepancy (described in percentage) is defined

$$D_r(x) = \frac{\left|x_{ACF} - x_{IFT}\right|}{x_{ACF}} \times 100\% \tag{3.21}$$

where x is the measured quantity, *e.g.*, τ_s, $TSCS$, and η_s.

3.4 Measurements and Discussions

3.4.1 Two Different Frequency Bands

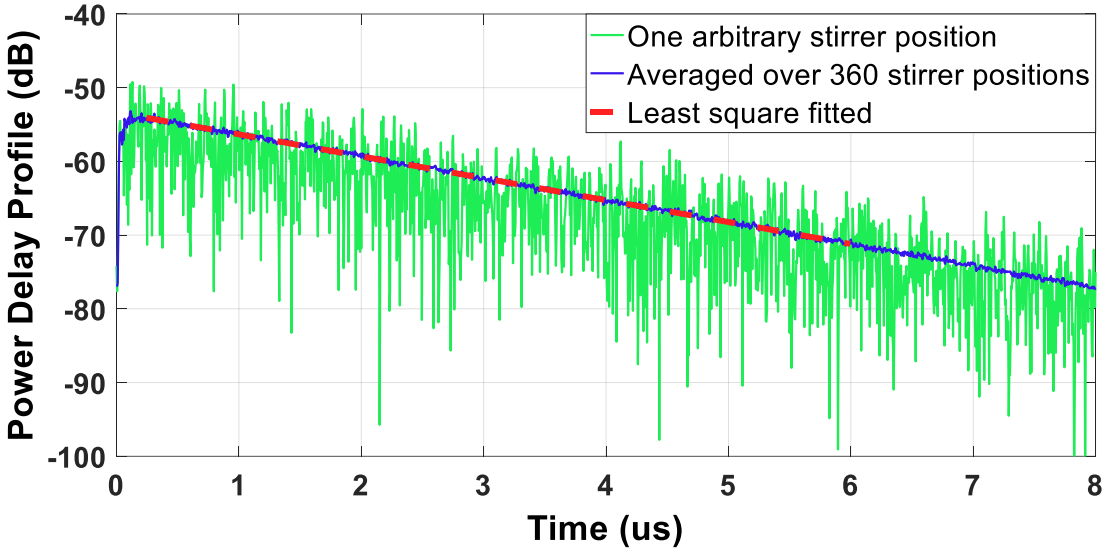

(a)

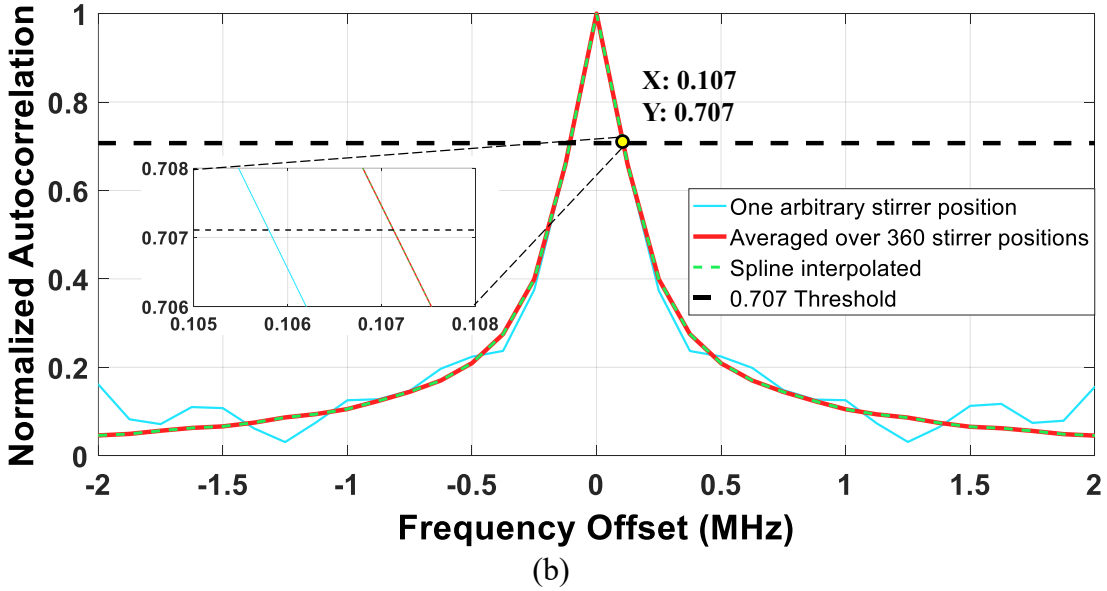

(b)

Figure 3.3: Extracting τ_{RC} in the frequency range 2.3 GHz – 2.5 GHz: (a) IFT-based method. (b) ACF-based method.

In this scenario, the horizontal and vertical stirrers are rotated simultaneously in mode-

tuning mode. τ_{RC} extraction in the 2.3 GHz – 2.5 GHz range is illustrated in Figure 3.3. Figure 3.3 (a) represents the IFT-based approach. The green curve stands for PDP at one arbitrary stirrer position, and the blue curve is the averaged PDP over all 360 stirrer positions. The red dashed line is the least-square fitted result which can be formulated as

$$10\log_{10}\left\langle PDP(t,n)\right\rangle_N = k_1 t + b \tag{3.22}$$

with $k_1 = -10/\left(\tau_{RC}\ln 10\right)$ the slope of the fitted line, and $b = 10\log_{10} P_0$ the initial power condition. The time region 250 ns – 6000 ns is chosen for linear curve fitting. Result gives $k_1 = -2.98\times10^6$, or equivalently, $\tau_{RC,IFT} = 1459$ ns.

The ACF-based method is depicted in Figure 3.3 (b). The blue curve stands for the FD-ACF at one arbitrary stirrer position, and the red curve is the averaged FD-ACF over all 360 stirrer positions. ∂f_{th} defined in (3.7) can be read from the abscissa value of the intersection point between the FD-ACF and the black dashed threshold line. Cubic spline interpolation [19] can be used to increase the density of points (the green dashed line in Figure 3.3 (b)) of the FD-ACF. As can be seen, $\partial f_{th} = 107$ kHz, which corresponds to $\tau_{RC,ACF} = 1487$ ns. Note that using only one arbitrary stirrer position tends to underestimate ∂f_{th}, as can be observed in the zoomed-in subplot in Figure 3.3 (b). Equivalently, this results in a 1.2% overestimation of $\tau_{RC,ACF}$. Not surprisingly, further studies indicate that this relative discrepancy gradually reduces as the number of stirrer positions increases. Specifically, when 20 independent stirrer positions are used, the corresponding relative discrepancy is reduced to less than 0.5%.

Similarly, Figure 3.4 demonstrates the τ_s extraction procedure for the 2.3 GHz – 2.5 GHz band. The IFT-based method is illustrated in Figure 3.4 (a). The blue curve is the unstirred power envelope when the transmitting antenna is fixed at position 9 (as shown in Figure 3.1 (b)). The red dashed line is the least-square fitted result, given by

$$10\log_{10}\left|\left\langle s_{21}(t,n)\right\rangle_N\right|^2 = k_2 t + b \tag{3.23}$$

where $k_2 = -10/\left(\tau_{eq}\ln 10\right)$ is the slope of the fitted line. Comparing Figure 3.4 (a) with Figure 3.3 (a), it can be found that the damping speed of the unstirred power envelope is much faster than that of the PDP. Consequently, a much smaller time

interval (50 ns – 450 ns) should be selected for the least-square fitting process. The slope k_2 can be extracted accordingly (-5.41×10^7), giving $\tau_{eq,IFT}=80$ ns and $\tau_{s,IFT}=85$ ns according to (3.13).

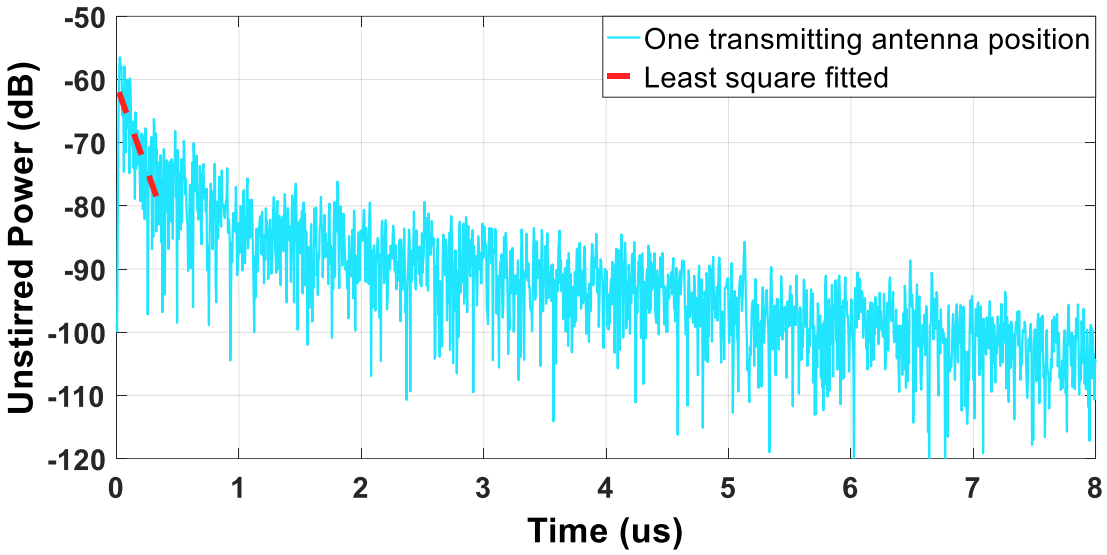

(a)

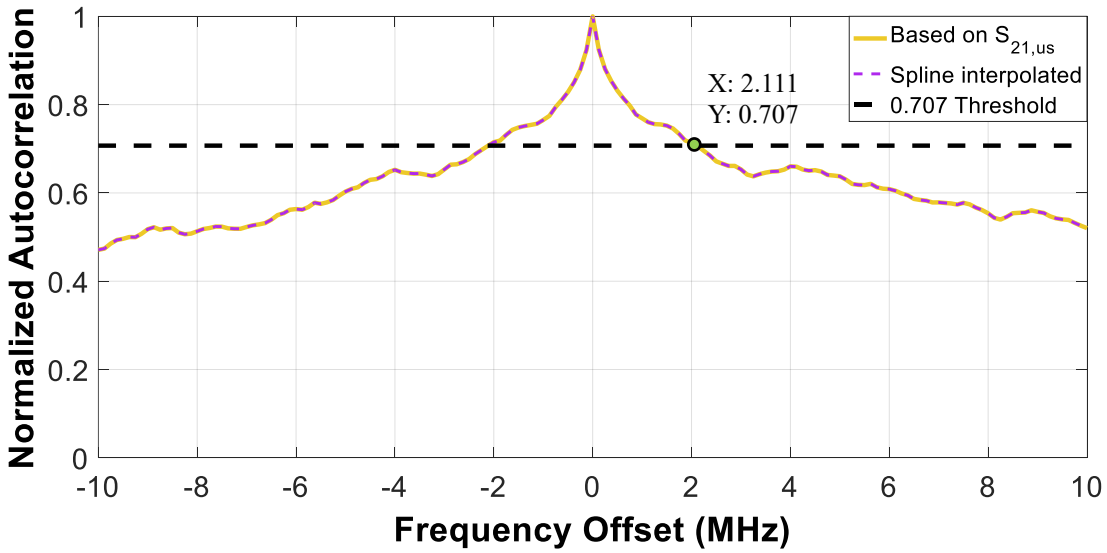

(b)

Figure 3.4: Extracting τ_s in the frequency range 2.3 GHz – 2.5 GHz: (a) IFT-based method. (b) ACF-based method.

Figure 3.4 (b) shows the corresponding ACF-based method. $\partial f_{th2}=2111$ kHz is

directly read from the FD-ACFUS curve, giving $\tau_{s,ACF} = 79$ ns according to (3.18). Note that an asymmetric pattern can be observed when the absolute value of ∂f is greater than 4 MHz.

Table 3-I lists a detailed comparison of τ_s, $TSCS$ and η_s obtained using both the IFT-based and the ACF-based methods. In both cases, more than 3 m^2 $TSCS$ (3.28 m^2 and 3.52 m^2, respectively) can be obtained with nearly 90% stirrer efficiency, indicating satisfactory stirrer performance and field uniformity within the RC. Since the stirrer itself is the OUT during the τ_s measurement, the fluctuation level of the unstirred power envelope is much larger than that of the averaged PDP, which makes the least-square fitting procedure more difficult and prone-to-error. Combining with other stirring techniques such as source stir could reduce the measurement uncertainty, but at the expense of much more data to be measured and much longer measurement time. Another factor that limits the available fitting range for τ_s extraction is its reduced signal dynamic range compared to that of Figure 3.3 (a). This is due to the fact that the unstirred power is usually much smaller than the stirred power for a well-stirred RC. Increasing the excitation power of the source or improving the sensitivity of the measurement system might levitate this problem.

In contrast, for the ACF-based method, ∂f_{th} and ∂f_{th2} can be obtained easily and straightforward. According to the last column of Table 3-I, relative discrepancies of the three measured quantities are acceptably small (no more than 8%), verifying that the proposed approach is an effective alternative to the conventional IFT-based method but with fewer limitations and assumptions.

Table 3-I: Comparison of parameters obtained using IFT and ACF methods in the frequency range 2.3 GHz – 2.5 GHz

Parameter	IFT-based	ACF-based	Relative Discrepancy
τ_s (ns)	85	79	7.6%
$\widehat{TSCS}$ (m^2)	3.28	3.52	6.8%
η_s (%)	87.2	89.1	2.1%

To elaborate the effect of manually selecting the time region *t* on $\tau_{s,IFT}$ extraction, *t* is first characterized by two parameters: the start time (represented by t_1) and the stop time (denoted by t_2). The extracted $\tau_{s,IFT}$ can hence be regarded as a function of t_1 and t_2, as illustrated in Figure 3.5 (a). The 3D surface, rendered by the parula colormap, covers $\tau_{s,IFT}$ values for t_1 ranging from 30 ns to 70 ns and t_2 ranging from 350 ns to 550 ns. The 3D histogram highlights the region that the corresponding $\tau_{s,IFT}$ values are within 10% relative discrepancy compared with $\tau_{s,ACF}$. The red curve is for t_1=50 ns, while the black curve is for t_2=450 ns, and the intersection of the two curves represents the time region adopted in this work for $\tau_{s,IFT}$ calculation. It can be seen that $\tau_{s,IFT}$ is more susceptible to t_1 than t_2 within the time region of interest. Especially when t_1 is smaller than 40 ns, $\tau_{s,IFT}$ will rapidly surge to around 150 ns, nearly twice the original value. This is because that a small t_1 value may include the early time region into slope computation. In contrast, a large t_2 value may include the noise floor region into the slope computation.

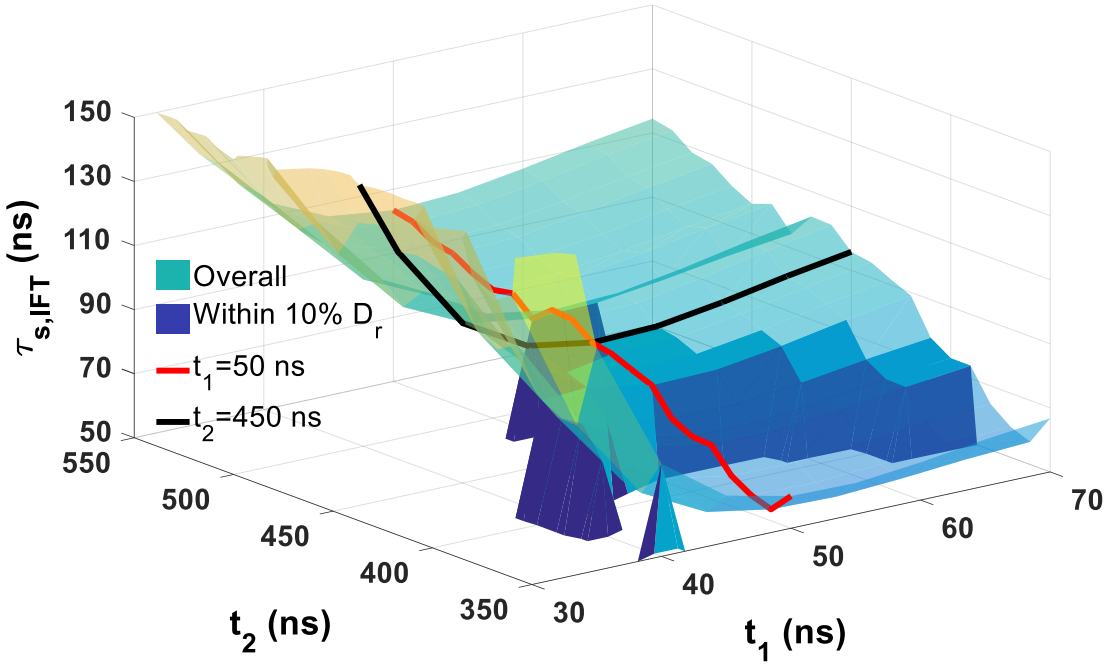

(a)

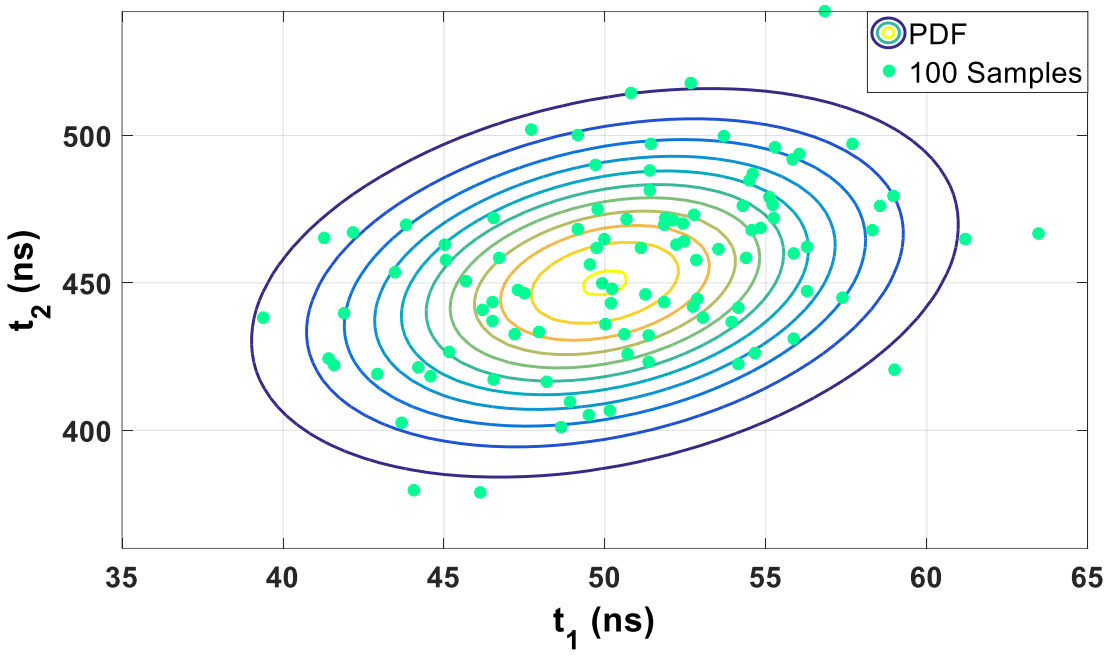

(b)

Figure 3.5: (a) $\tau_{s,IFT}$ as a function of t_1 and t_2. (b) The contour representation of the PDF of t=[t_1,t_2]^T and 100 randomly generated samples.

Next, to emulate human behavior when selecting the time region, $t=\left[t_1,t_2\right]^T$ is modeled as a random vector that follows Gaussian distribution as specified in (3.24):

$$t \sim N\left(\mu,\Sigma\right)$$
$$\mu=\left[\mu_1,\mu_2\right]^T=\left[50,450\right]^T \tag{3.24}$$
$$\Sigma=\begin{bmatrix}\sigma_1^2 & \rho\sigma_1\sigma_2\\ \rho\sigma_1\sigma_2 & \sigma_2^2\end{bmatrix}=\begin{bmatrix}25 & 45\\ 45 & 900\end{bmatrix}$$

where μ is the mean vector (with unit ns), Σ is the covariance matrix, σ_1 (5 ns) and σ_2 (30 ns) are the standard deviations of the corresponding variables, and $\rho=0.3$ is the correlation coefficient. The contour representation of the PDF of t is shown in Figure 3.5 (b) with 100 randomly generated samples. The result shows that only 34 out of these 100 samples give $\tau_{s,IFT}$ within 10% relative discrepancy to $\tau_{s,ACF}$ in value.

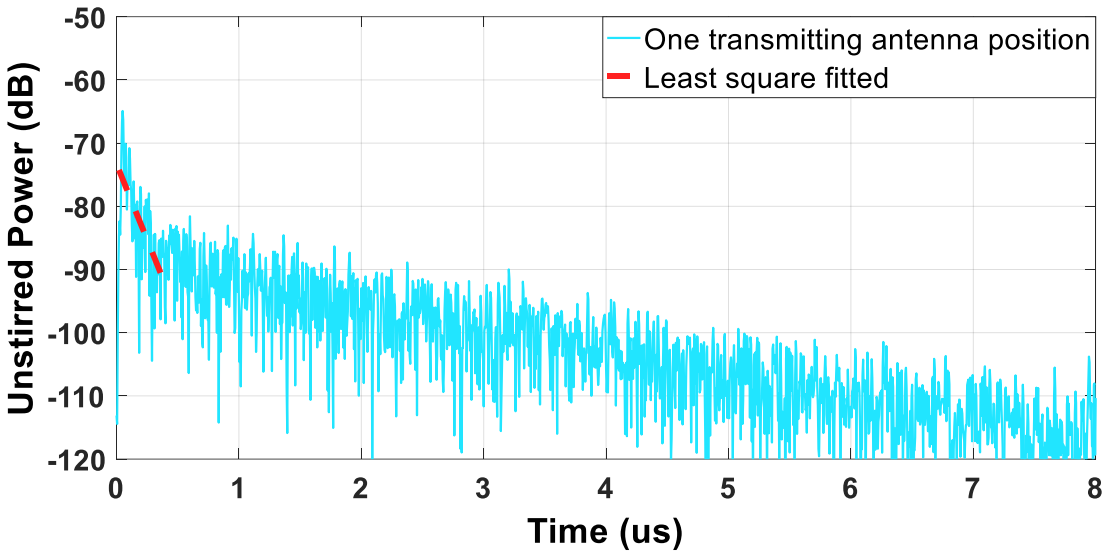

(a)

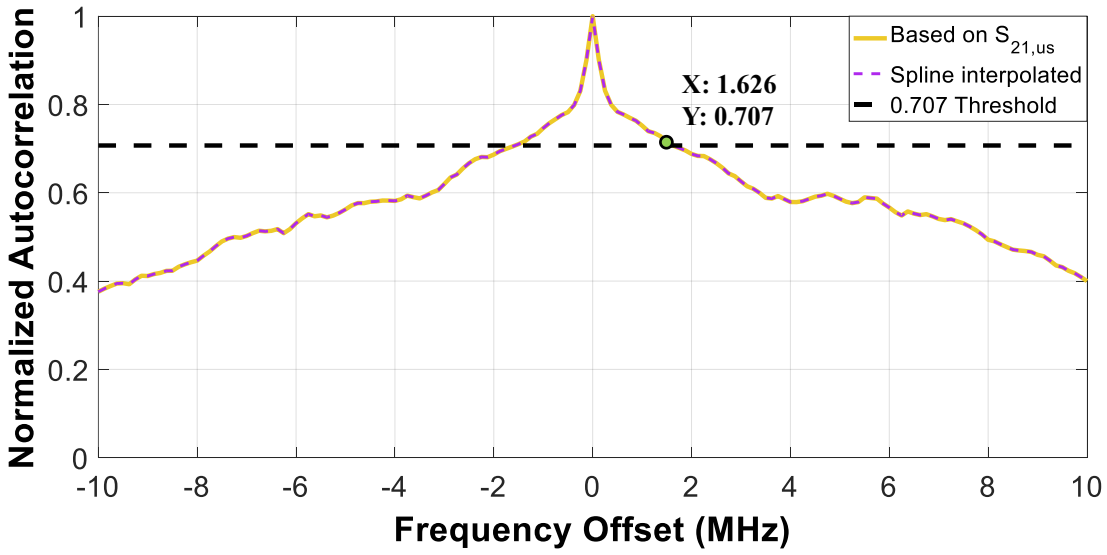

(b)

Figure 3.6: Extracting τ_s in the frequency range 5.8 GHz – 6.0 GHz: (a) IFT-based method. (b) ACF-based method.

For the 5.8 GHz – 6.0 GHz band, details for obtaining τ_{RC} are omitted for the sake of simplicity, with results listed as $\tau_{RC,IFT} = 1201$ ns and $\tau_{RC,ACF} = 1179$ ns. Figure 3.6 depicts the τ_s extraction processes. The 10 dB drop of the signal level shown in Figure 3.6 (a) compared to that in Figure 3.4 (a) is due to increased path loss for the higher frequency band. Following the same procedures as the previous measurement, it can be

obtained that $k_2 = -4.79\times10^7$ and $\partial f_{th2} = 1626$ kHz, which correspond to $\tau_{s,IFT} = 98$ ns and $\tau_{s,ACF} = 107$ ns, respectively.

According to Table 3-II, there is reasonable concordance between the measured results using two methods (relative discrepancy figures are all below 10%). Compared with Table 3-I, values of τ_s calculated at the higher band are larger than that at the lower band, leading to smaller $TSCS$ and lower η_s (below 85%).

Table 3-II: Comparison of parameters obtained using IFT and ACF methods in the frequency range 5.8 GHz – 6.0 GHz

Parameter	IFT-based	ACF-based	Relative Discrepancy
τ_s (ns)	98	107	8.4%
$\widehat{TSCS}$ (m^2)	2.84	2.60	9.2%
η_s (%)	83.2	80.5	3.4%

This finding can be validated by utilizing the enhanced backscattering coefficient [20], which is defined as

$$e_b = \frac{\sqrt{\left\langle \left|S_{11,s}(f,n)\right|^2 \right\rangle_N \left\langle \left|S_{22,s}(f,n)\right|^2 \right\rangle_N}}{\left\langle \left|S_{21,s}(f,n)\right|^2 \right\rangle_N} \tag{3.25}$$

where $S_{*,s}(f,n)$ is the stirred part of the transmission or reflection coefficients, and * can be 11, 22, and 21, respectively. Theoretically, e_b equals 2 for an RC working in the ideal homogeneous, isotropic, and polarization balanced condition. Deviation of e_b from its theoretical value manifests the degradation of spatial uniformity. According to Figure 3.7, the mean value of e_b (denote as $\overline{e}_b$) at the lower band is 2.05, which implies better spatial uniformity performance than that of the higher band case where $\overline{e}_b = 2.15$. This is consistent with the τ_s measurement results.

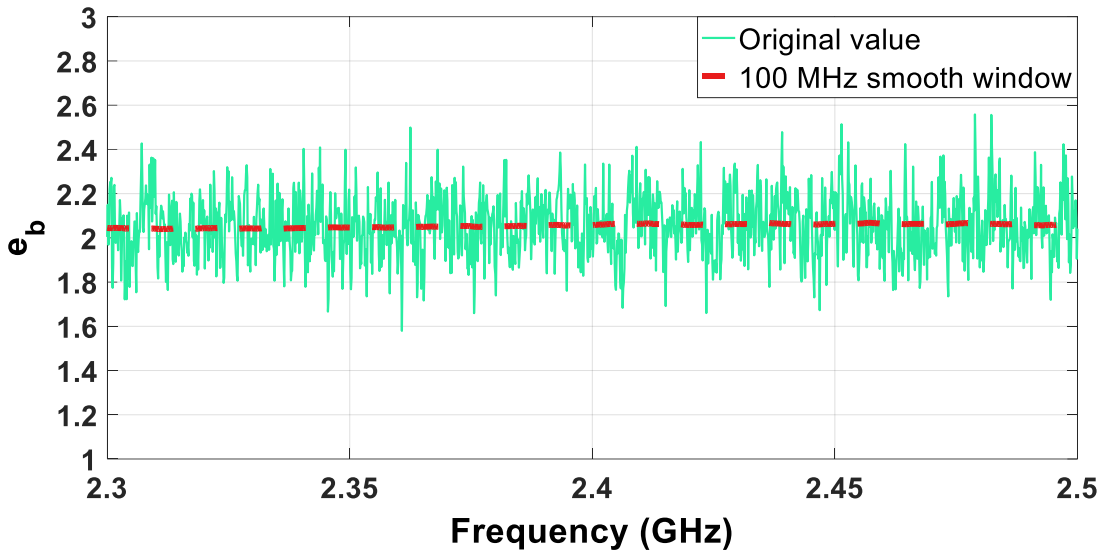

(a)

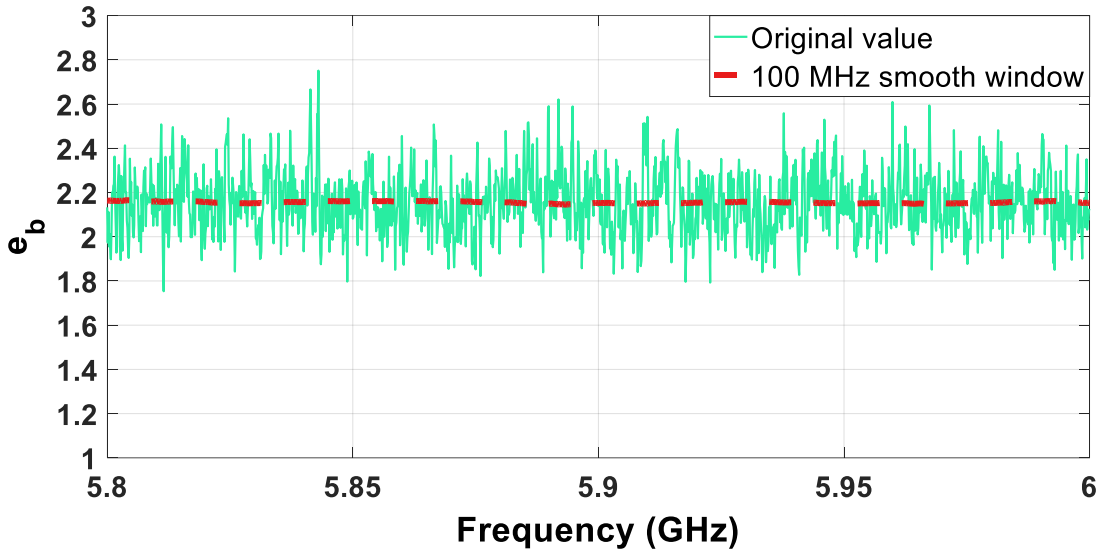

(b)

Figure 3.7: Measured e_b for RC characterization: (a) 2.3 GHz – 2.5 GHz. (b) 5.8 GHz – 6.0 GHz.

3.4.2 Three Different Stirrer Setups

The frequency band was fixed at 2.3 GHz – 2.5 GHz in this scenario. In addition to the stirrer configuration adopted in Section 3.4.1 (both the horizontal stirrer and the vertical stirrer rotating simultaneously), two more stirrer setups were implemented.

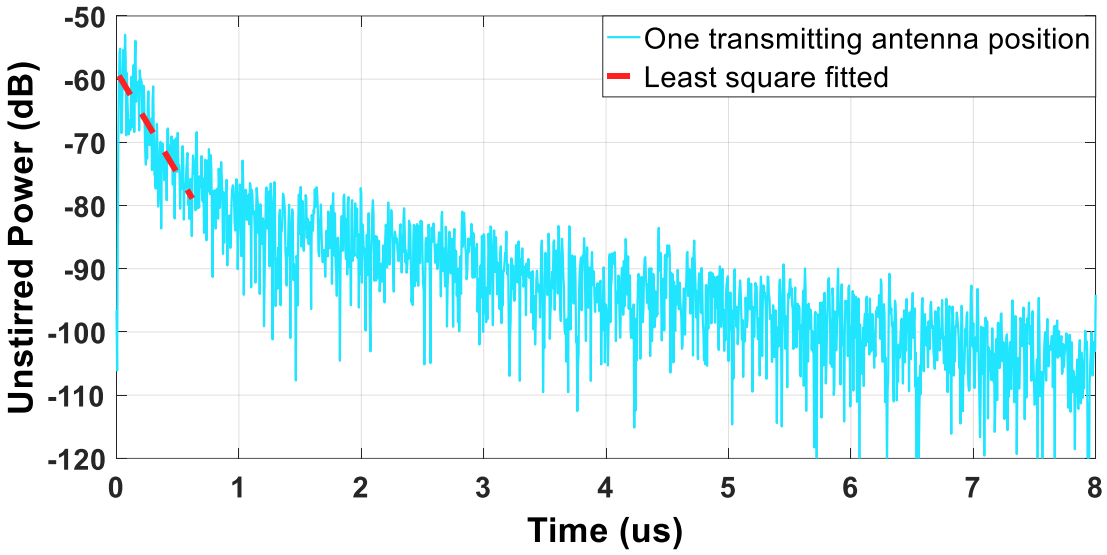

(a)

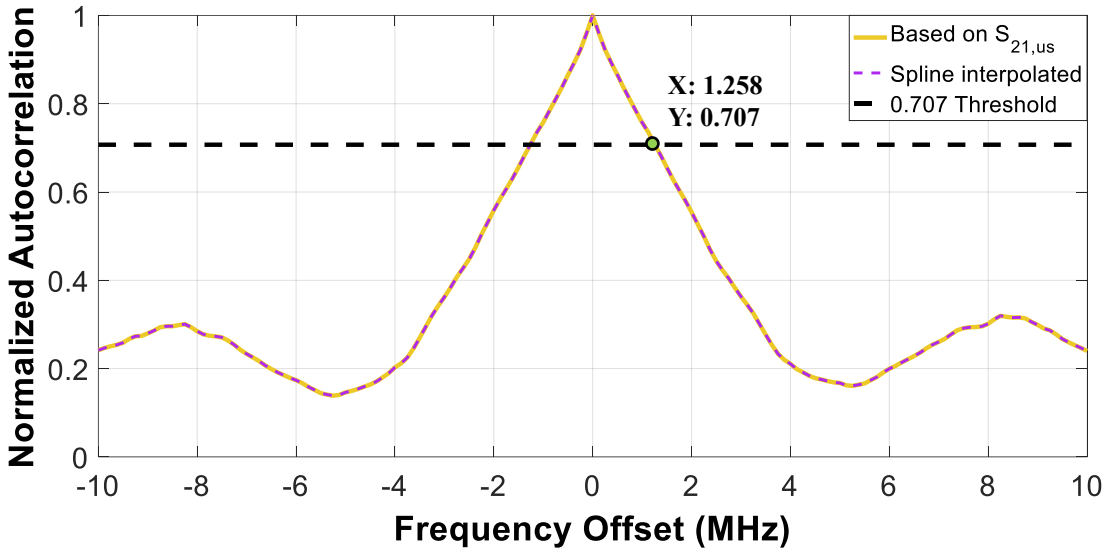

(b)

Figure 3.8： Extracting τ_s in the frequency range 2.3 GHz – 2.5 GHz with only the horizontal stirrer: (a) IFT-based method. (b) ACF-based method.

Firstly, only the horizontal stirrer was rotated while the vertical stirrer was kept still. It is apparent that the signal shown in Figure 3.8 (a) decays much slower than that of Figure 3.4 (a). Hence a longer time interval (50 ns – 600 ns) should be chosen for linear fitting. The resultant $\tau_{s,IFT}$ is 148 ns as derived from the slope value ($k_2 = -3.24\times10^7$).

The ACF-based method, in contrast, does not require any modification. $\partial f_{th2} = 1258$ kHz read from Figure 3.8 (b) gives $\tau_{s,IFT} = 139$ ns. Then we halted the horizontal stirrer and rotated the vertical stirrer instead. Details are omitted here.

Measurement scenarios are summarized in Table 3-III and Table 3-IV, respectively. Not surprisingly, the two stirrer setups provide similar $TSCS$ (around 2 m^2) because the two mechanical stirrers have a similar physical size, and they rotate in the same manner about a fixed axis. Overall, the IFT-based method and the proposed ACF method are in good agreement regarding measured parameters. It is interesting to note that the sum of the $TSCS$ of the two single-stirrer scenarios is slightly larger than that of the two-stirrers case. This is because, for the two-stirrers scenario, the horizontal stirrer and the vertical stirrer were rotated simultaneously, which further limits the freedom of movement to some extent.

Table 3-III: Comparison of parameters obtained using IFT and ACF methods with the horizontal stirrer only in the frequency range 2.3 GHz – 2.5 GHz

Parameter	IFT-based	ACF-based	Relative Discrepancy
τ_s (ns)	148	139	6.5%
$\widetilde{TSCS}$ (m^2)	1.88	2.00	6.0%
η_s (%)	69.3	71.6	3.2%

Table 3-IV: Comparison of parameters obtained using IFT and ACF methods with the vertical stirrer only in the frequency range 2.3 GHz – 2.5 GHz

Parameter	IFT-based	ACF-based	Relative Discrepancy
τ_s (ns)	133	138	3.6%
$\widetilde{TSCS}$ (m^2)	2.09	2.02	3.5%
η_s (%)	73.2	71.9	1.8%

3.5 Conclusion

In this chapter, to accurately characterize the stirrer performance of an RC, a novel frequency domain approach for extracting τ_s based on the FD-ACF and the FD-ACFUS has been presented. In this manner, the IFT operation, which is necessary for the currently widely used time domain method, can be omitted. Theoretical derivation of the proposed method has been given, and experimental validations have been performed for both the 2.3 GHz – 2.5 GHz and 5.8 GHz – 6.0 GHz bands, as well as three different stirrer configuration scenarios. While in general τ_s, $\widetilde{\mathrm{TSCS}}$ and η_s extracted by the two methods are in good agreement, it has been demonstrated the proposed frequency domain method can provide more stable and reliable results since it has a wider dynamic range and eliminates the procedure of manually selecting the fitting range.

So far, no analytical expression has been derived for calculating the ground-truth value of τ_s, except for a relatively loose lower boundary which is derived based on the upper limit of $\widetilde{\mathrm{TSCS}}$ given in [5]

$$\tau_s^{LB} = \frac{4V}{A_s c_0} \tag{3.26}$$

where the superscript ^{LB} represents the lower bound, and A_s stands for the stirring surface area. For instance, the total A_s of the two mechanical stirrers installed inside the RC at the University of Liverpool is roughly 8 m^2, which gives $\tau_s^{LB} \approx 14$ ns. It can be seen that this lower bound is significantly smaller than τ_s values calculated in this chapter. In order to obtain more credible τ_s value, the conventional IFT-based method and the proposed ACF-based method can be performed simultaneously for cross-validation.

Effective as it is, the ACF-based method also has its limitations. Firstly, it needs a relatively finer frequency step to obtain more accurate ∂f_{th} and ∂f_{th2} readings than the IFT-based method in which only the Nyquist theorem is required to be met. In practice, the interpolation technique can be used to relieve this problem. Secondly,

under heavy loading conditions, the normalized $R_{us}(\partial f)$ can be so high that its average value is quite near the threshold value (as illustrated in Figure 3.9), which might introduce significant error to τ_s estimation. However, for τ_s extraction, the OUT is the stirrer of the RC, and it should be tested in an empty RC.

Another interesting thing to note is that according to (3.18), larger ∂f_{th2} gives smaller τ_s, and thus larger $\widetilde{\text{TSCS}}$ and higher η_s. This implies that the FD-ACFUS itself could be an efficient parameter to characterize the stirrer, which also will be a future research direction.

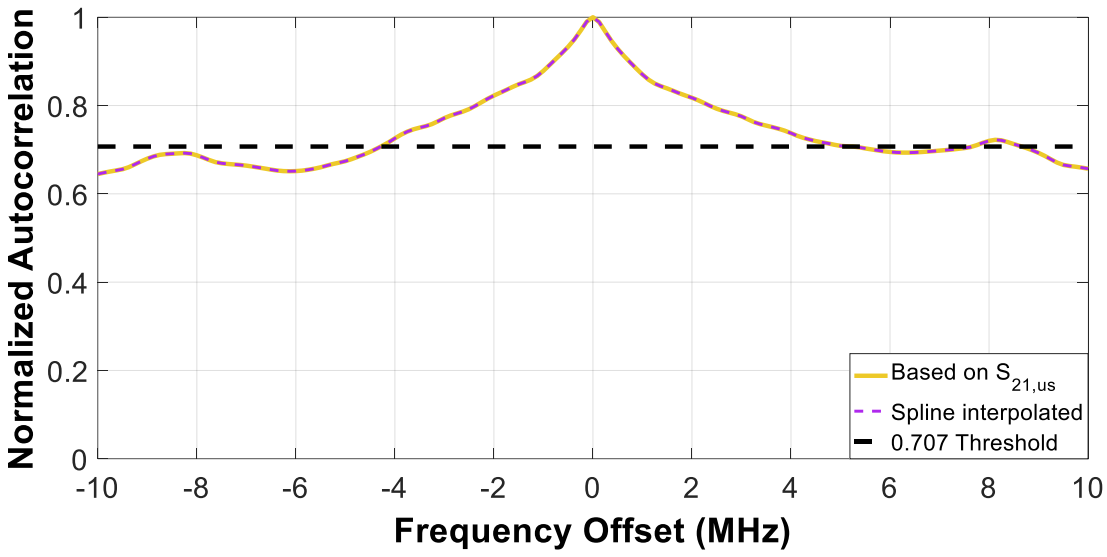

Figure 3.9: The FD-ACFUS in the frequency range 2.3 GHz – 2.5 GHz with 3 absorbers loaded into the RC.

3.6 References

[1] G. Lerosey and J. de. Rosny, "Scattering cross section measurement in reverberation chamber," *IEEE Trans. Electromagn. Compat.*, vol. 49, no. 2, pp. 280–284, May 2007.

[2] *Electromagnetic Compatibility (EMC)—Part 4–21: Testing and Measurement Techniques – Reverberation Chamber Test Methods*, IEC 61000-421, IEC Standard, Ed 2.0, Jan. 2011.

[3] S. Lallechere, I. E. Baba, P. Bonnet, and F. Paladian, "Total scattering cross section improvements from electromagnetic reverberation chambers modelling and stochastic formalism," in *Proc. 5th European Conf. Antennas Propag.*, Rome, pp. 81–85, Italy, Apr. 2011.

[4] I. E. Baba, S. Lallechere, P. Bonnet, J. Benoit, and F. Paladian, "Computing total scattering cross section from 3-D reverberation chambers time modelling," in *Proc. Asia-Pacific Symp. Electromagn. Compat.*, Singapore, May 2012.

[5] Q. Xu, Y. Huang, L. Xing, Z. Tian, C. Song, and M. Stanley, "The limit of the total scattering cross section of electrically large stirrers in a reverberation chamber," *IEEE Trans. Electromagn. Compat.*, vol. 58, no. 2, pp. 623–626, Apr. 2016.

[6] Q. Xu, L. Xing, Y. Zhao, T. Loh, T. Jia and Y. Huang, "The Noise Level of Total Scattering Cross Section Measurement in a Reverberation Chamber," *IEEE Antennas Wireless Propag. Lett.*, vol. 17, no. 10, pp. 1842-1846, Oct. 2018.

[7] Q. Xu, Y. Huang, L. Xing, Z. Tian, M. Stanley, and S. Yuan, "B-scan in a reverberation chamber," *IEEE Trans. Antennas Propag.*, vol. 64, no. 5, pp. 1740–1750, May 2016.

[8] K. A. Remley, C.-M. J. Wang, D. F. Williams, J. J. aan den Toorn, and C. L. Holloway, "A significance test for reverberation-chamber measurement uncertainty in total radiated power of wireless devices," *IEEE Trans. Electromagn. Compat.*, vol. 58, no. 1, pp. 207–219, Feb. 2016.

[9] G. Andrieu and N. Ticaud, "Performance Comparison and Critical Examination of the Most Popular Stirring Techniques in Reverberation Chambers Using the "Well-Stirred" Condition Method," *IEEE Trans. Electromagn. Compat.*, vol. 62, no. 1, pp. 3-15, Feb. 2020.

[10] X. Chen, "Experimental investigation of the number of independent samples and the measurement uncertainty in a reverberation chamber," *IEEE Trans. Electromagn. Compat.*, vol. 55, no. 5, pp. 816–824, Oct. 2013.

[11] P.-S. Kildal, X. Chen, C. Orlenius, M. Franzén, and C. S. L. Patané, "Characterization of reverberation chambers for OTA measurements of wireless devices: Physical formulations of channel matrix and new uncertainty formula," *IEEE Trans. Antennas Propag.*, vol. 60, no. 8, pp. 3875–3891, Aug. 2012.

[12] X. Chen, J. Tang, T. Li, S. Zhu, Y. Ren, Z. Zhang, and A. Zhang, "Reverberation Chambers for Over-the-Air Tests: An Overview of Two Decades of Research," *IEEE Access.*, vol. 6, pp. 49129-49143, Aug. 2018.

[13] C. L. Holloway, H. A. Shah, R. J. Pirkl, W. F. Young, D. A. Hill, and J. Ladbury, "Reverberation chamber techniques for determining the radiation and total efficiency of antennas," *IEEE Trans. Antennas Propag.*, vol. 60, no. 4, pp. 1758–1770, Apr. 2012.

[14] X. Zhang, M. P. Robinson, I. D. Flintoft, and J. F. Dawson, "Efficient determination of reverberation chamber time constant," *IEEE Trans. Electromagn. Compat.*, vol. 60, no. 5, pp. 1296–1303, Oct. 2018.

[15] E. W. Weisstein, "Wiener–Khinchin Theorem." From MathWorld— A Wolfram Web Resource. [Online]. Available: http://mathworld. wolfram.com/Wiener-KhinchinTheorem.html

[16] Q. Xu, L. Xing, Y. Zhao, Z. Tian, and Y. Huang, "Wiener–Khinchin theorem in a reverberation chamber," *IEEE Trans. Electromagn. Compat.*, vol. 61, no. 5, pp. 1399-1407, Oct. 2019.

[17] Q. Xu and Y. Huang, *Anechoic and Reverberation Chambers: Theory, Design and Measurements*, Wiley-IEEE, UK, 2019.

[18] X. Chen, P.-S. Kildal, C. Orlenius, and J. Carlsson, "Channel sounding of loaded reverberation chamber for over-the-air testing of wireless devices: Coherence bandwidth versus average mode bandwidth and delay spread," *IEEE Antennas Wireless Propag. Lett.*, vol. 8, pp. 678–681, Jul. 2009.

[19] E. W. Weisstein, „Cubic Spline." From MathWorld--A Wolfram Web Resource. [Online]. Available: http://mathworld.wolfram.com/CubicSpli ne.html

[20] J. M. Ladbury and D. A. Hill, "Enhanced backscatter in a reverberation chamber: Inside every complex problem is a simple solution struggling to get out," in *Proc. IEEE Int. Symp. Electromagn. Compat.*, pp. 1–5, Jul. 9–13, 2007.

Chapter 4 Average Rician *K*-Factor Based Analytical Uncertainty Model for Over-the-air Total Radiated Power Testing

After the stirrer performance characterization in Chapter 3, the RC is applied to the practical OTA TRP tests. It is shown in this chapter that the statistical property of the average Rician *K*-factor is of pivotal significance for the accurate characterization of an RC's anisotropy. Based on this, an improved analytical uncertainty model is established for the RC-based TRP measurement by considering the sample correlation, the statistical anisotropy, and the practical experimental procedures.

4.1 Introduction

TRP measures how much power is radiated by the antenna of an active radio source. Traditionally, the TRP is measured in an AC with a 3D spherical scanning grid, and the result is summed up over all possible angles. TRP has been widely adopted as a figure of merit (FoM) by standardization organizations for the 5G OTA conformance testing [1] – [5]. Non-directional requirements including but not restricted to output power, adjacent channel leakage ratio (ACLR), operating band unwanted emissions (OBUE), spectrum emission mask (SEM), and spurious can be quantified via TRP measurements.

Numerous researches have shown that owing to its unique attractive property, the RC-based measurement of non-directional parameters including TRP can be fast and efficient [6] – [18]. However, in order to thoroughly characterize a testing facility and evaluate the performance of its relevant measurement techniques, it is still required to quantify its measurement uncertainty. Since an RC is typically modeled and employed as a stochastic

process, the measurement uncertainty analysis should stem from its statistical characteristics. So far, Numerous studies have been conducted in this field [9], [11], [13], [14], [19] – [27]. It is commonly accepted that for a practical RC that inevitably renders non-zero unstirred power, the corresponding measurement uncertainty dependents not only on the finite number of independent samples [9], [19] but also on the imperfect spatial isotropy [11], [20] – [26]. Under certain scenarios, the latter can even dominate the uncertainty [21].

The Rician *K*-factor (*K*), which is defined as the ratio of the unstirred power to the average stirrer power, is a suitable measure of this anisotropy effect [28] – [31]. Therefore, uncertainty formulations proposed by various researchers [11], [20] – [22] adopt the explicit representation of *K* for improved model accuracy. However, there are several concerns when using *K* in uncertainty models: a) *K* has its own measurement uncertainty; b) when applying source stirring (like rotating platform stirring and polarization stirring) and frequency stirring, the value of *K* actually varies; c) it is hard, if not impossible, to acquire the value of *K* when measuring the DUT; d) the reference measurement of a single-case *K* might be quite different from that for the DUT measurement. As a result, the average Rician *K*-factor (K_{avg}), which is based on the assumption of random unstirred power [11], [32], [33], should be used instead. The definition of K_{avg} was given in [33] as the ratio of the average unstirred power to the average stirrer power when the unstirred component can be changed randomly. It was first adopted by [11] for uncertainty quantification, but the corresponding model was derived heuristically by empirical assumptions. The analytical expression in [20] was based on the components-of-variance model, and *K* appeared in the expression is equivalent to K_{avg} when source stirring is conducted. However, there was no analysis about how to estimate K_{avg} and the corresponding uncertainty. Reference [22] simply pooled multiple single-case *K* values, which is mathematically viable but lacks physical meaning and explanation.

Furthermore, until now a pure analytical uncertainty model for the TRP measurement using an RC reflecting the impacts of both stages (*i.e.*, the calibration stage and the measurement stage) as well as the statistical anisotropy is still unavailable in the literature.

The main contributions of this chapter are listed as follows:

1) K_{avg} is formulated based on the random unstirred power assumption, and the statistical distribution of the MLE of K_{avg} is obtained for the first time (Section 4.2).

2) The MLE of K_{avg} is verified by Monte Carlo simulations, and the corresponding unbiased estimator is given. The statistical anisotropy of the RC can be more accurately characterized based on the derived statistics of K_{avg} (Section 4.2).

3) An improved analytical uncertainty model for the RC-based TRP measurement is derived based on the independent sample number and K_{avg} (Section 4.3).

4) The proposed model considers both stages for the TRP measurement. It also allows different experimental configurations in each stage, making it possible to characterize the measurement dispersion without tedious and inefficient empirical estimation processes (Section 4.3).

5) Extensive measurements are performed using the 9-Point estimation procedure to validate the proposed analytical model (Section 4.4).

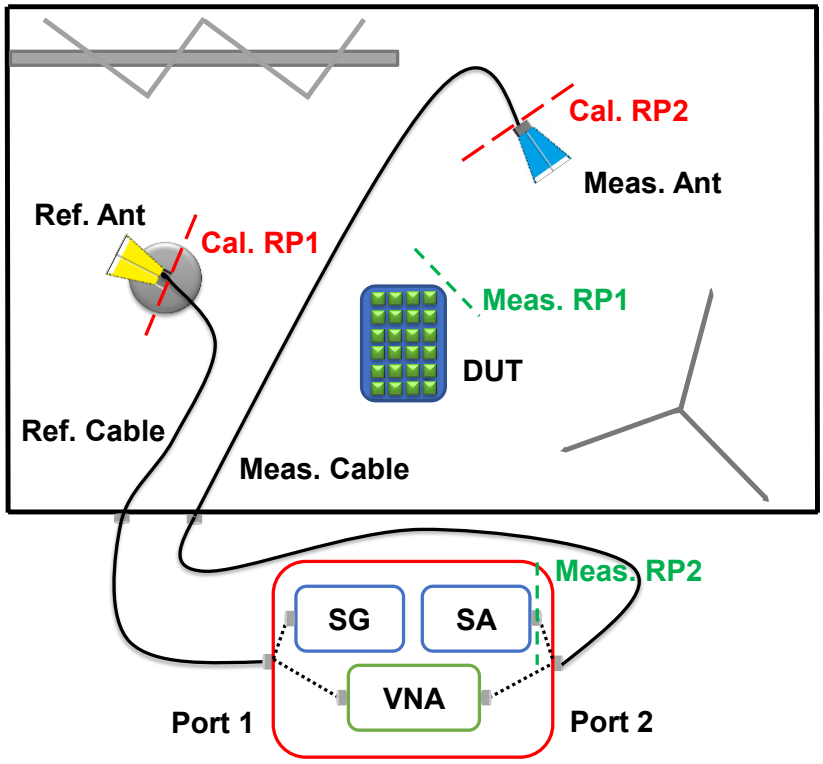

Figure 4.1: Schematic diagram of typical RC-based TRP measurement setup. The dotted lines represent virtual connections so that the VNA or SG/SA can be chosen on demand; the two dashed line pairs indicate the positions of the RPs of the relevant stages.

4.2 Formulation and Statistical Modeling for the Average Rician *K*-Factor

4.2.1 Formulation of the Average Rician *K*-Factor

Without loss of generality, the samples provided by each stirring technique are considered as independent in this section. Sample correlation and derivation of independent sample numbers for different stirring techniques will be discussed in detail in Section 4.4. A typical RC-based measurement setup is depicted in Figure 4.1. Assume that a complete mechanical stirring process generates N samples [9], and the same process is repeated $L=M\cdot F$ times at M source positions [10], [11] and F frequency points [12] – [14] for further decreasing the measurement uncertainty. Here, for frequencies separated larger than the coherent bandwidth (so that they can be considered as independent), the corresponding spatial channels that the EM signal experiences are quite different according to the wireless propagation theory. For each stirrer sequence l, the complex-valued transmission coefficient $S_{21}(l)$ measured by a VNA can be modeled as the superposition of the following two terms [11]:

$$S_{21}(l) = S_{21,s}(l) + S_{21,us}(l) \tag{4.1}$$

where $S_{21,s}(l)$ in (4.1) is the stirred component of $S_{21}(l)$ that fully interacts with the mechanical stirrers of the RC. It follows a complex circular Gaussian distribution with zero-mean and variance σ_s^2 [6]:

$$S_{21,s}(l) = S_{21,s}^{re}(l) + jS_{21,s}^{im}(l) \sim \mathcal{N}\left(0,\sigma_s^2\right) + j\mathcal{N}\left(0,\sigma_s^2\right) \tag{4.2}$$

where the superscripts re and im are the real and imaginary parts, respectively, and they are *i.i.d.*

$S_{21,us}(l)$, the unstirred component, is the residual that remains unaffected during the stirrer rotating, which is assumed to be a deterministic complex value:

$$S_{21,us}(l) = S_{21,us}^{re}(l) + jS_{21,us}^{im}(l) = \mu_{re}(l) + j\mu_{im}(l) \tag{4.3}$$

where $\mu_{re}(l)$ and $\mu_{im}(l)$ are two unknown constants (but dependent upon l). In practice, the above two components are estimated by the following estimators:

$$\hat{S}_{21,us}(l) = \left\langle S_{21}(l) \right\rangle_N = \left\langle S_{21}^{re}(l) \right\rangle_N + j\left\langle S_{21}^{im}(l) \right\rangle_N = \hat{\mu}_{re}(l) + j\hat{\mu}_{im}(l) \tag{4.4}$$

$$\hat{S}_{21,s}(l) = S_{21}(l) - \left\langle S_{21}(l) \right\rangle_N = \left(S_{21}^{re}(l) - \hat{\mu}_{re}(l)\right) + j\left(S_{21}^{im}(l) - \hat{\mu}_{im}(l)\right) \tag{4.5}$$

where < > denotes the ensemble average operation, and ^ is the estimator symbol of the relevant quantity.

For the l_{th} mechanical stirring process, the single-case K is defined as follows [28]

$$K(l) = \frac{P_{us}(l)}{P_{s,avg}(l)} = \frac{P_{us}(l)}{E\left[P_s(l)\right]} \tag{4.6}$$

where

$$P_{us}(l) = \left|S_{21,us}(l)\right|^2 = \mu_{re}^2(l) + \mu_{im}^2(l) \tag{4.7}$$

is the unstirred power, and

$$P_s(l) = \left|S_{21,s}(l)\right|^2 \sim Exp(\frac{1}{2\sigma_s^2}) \tag{4.8}$$

is the stirred power which follows an exponential distribution with mean (also standard deviation)

$$P_{s,avg}(l) = E\left[P_s(l)\right] = 2\sigma_s^2 \tag{4.9}$$

Based on equations (4.4) and (4.5), the MLEs of (4.7) and (4.9) are given as:

$$\hat{P}_{us}(l) = \left|\hat{S}_{21,us}(l)\right|^2 = \hat{\mu}_{re}^2(l) + \hat{\mu}_{im}^2(l) \tag{4.10}$$

$$\begin{aligned} \hat{P}_{s,avg}(l) &= \frac{1}{N-1}\sum_{n=1}^{N}\left|\hat{S}_{21,s}(l)\right|^2 \\ &= \frac{1}{N-1}\sum_{n=1}^{N}\left|S_{21}^{re}(l) - \hat{\mu}_{re}(l)\right|^2 + \frac{1}{N-1}\sum_{n=1}^{N}\left|S_{21}^{im}(l) - \hat{\mu}_{im}(l)\right|^2 \end{aligned} \tag{4.11}$$

Detailed statistical modeling of different estimators of $K(l)$ can be found in [29] – [31].

Furthermore, when all the L realizations are considered simultaneously (so that the dependency of l can be suppressed), the resultant unstirred part cannot be regarded as a constant anymore. If L is large enough so that the ergodic condition is fulfilled, it should be described as a stochastic process [11], [32]. According to [20], the random unstirred

component $S_{21,us}$ is modeled by a complex circular Gaussian distribution with zero-mean and variance σ_{us}^2:

$$\begin{aligned} S_{21,us} &= S_{21,us}^{re} + jS_{21,us}^{im} = \mu_{re} + j\mu_{im} \\ &\sim \mathcal{N}\left(0,\sigma_{us}^2\right) + j\mathcal{N}\left(0,\sigma_{us}^2\right) \end{aligned} \tag{4.12}$$

Compared with equation (4.3), it is now clear that $\mu_*(l)$ (and thus $S_{21,us}(l)$) is essentially a sample drawn from the corresponding random distribution μ_* ($S_{21,us}$) in (4.12). Conversely, as already implied in (4.2) and (4.8), the statistical characteristics of the stirred part remain intact throughout the L realizations (*i.e.*, independent of l).

From the above analysis, K_{avg} can be formulated as follows [33]:

$$K_{avg} = \frac{P_{us,avg}}{P_{s,avg}} = \frac{E\left[P_{us}\right]}{E\left[P_{s,avg}\left(l\right)\right]} \tag{4.13}$$

where

$$P_{us} = \left|S_{21,us}\right|^2 = \left|\mu_{re}\right|^2 + \left|\mu_{im}\right|^2 \sim Exp(\frac{1}{2\sigma_{us}^2}) \tag{4.14}$$

is the random unstirred power which follows an exponential distribution with mean (also standard deviation)

$$P_{us,avg} = E\left[P_{us}\right] = 2\sigma_{us}^2 \tag{4.15}$$

Similarly, $P_{us}(l)=\mu_{re}^2(l)+\mu_{im}^2(l)$ in (4.7) is the l_{th} sample drawn from the distribution in (4.14). With the purpose of verifying the theoretical distribution of P_{us}, 1601 frequency points (in the frequency range 3.4 GHz – 3.6 GHz) are collected as samples and the corresponding measured cumulative distribution function (CDF) is plotted and compared with the theoretical exponential CDF (as shown in Figure 4.2). Not surprisingly, good agreement is achieved between theory (dashed) and experimental result (solid). This also proves that frequency stirring can provide randomness to the unstirred NLoS component.

As for the denominator part of (4.13), regarding (4.9),

$$P_{s,avg} = E\left[P_{s,avg}\left(l\right)\right] = E\left[E\left[P_s\left(l\right)\right]\right] = 2\sigma_s^2 \tag{4.16}$$

Substituting (4.15) and (4.16) into (4.13) gives

$$\kappa_{avg} = \frac{\sigma_{us}^2}{\sigma_s^2} \tag{4.17}$$

which is the ground truth value of K_{avg}. It can be seen that (4.13) is a necessary continuation of (4.6) in order to characterize an RC when multiple stirring techniques are utilized.

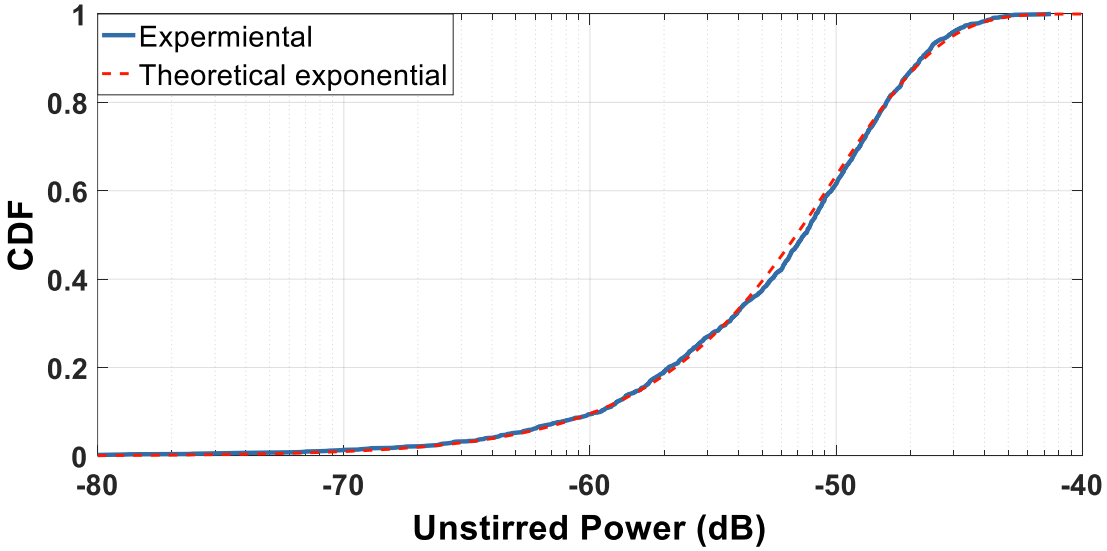

Figure 4.2: Comparisons of the theoretical and experimental CDF of P_{us} using adjacent frequency points (3.4 GHz – 3.6 GHz) as samples.

4.2.2 Estimation of the Average Rician *K*-Factor for Independently Drawn Stirred and Unstirred Parts

Assume that samples of $S_{21,s}(l)$ and $S_{21,us}$ can be drawn independently from the unknown distributions (4.2) and (4.12). Taking into consideration that the number of available samples (both N and L) are finite, a basic estimator of (4.13) is given as:

$$\hat{K}_{avg} = \frac{V}{U} = \frac{\langle P_{us} \rangle_L}{\langle P_s(l) \rangle_{N,L}} \tag{4.18}$$

the use of U and V are for notational convenience. Based on (4.8), U follows a Gamma distribution

$$U \sim Gamma\left(NL, \frac{NL}{2\sigma_s^2} \right) \tag{4.19}$$

with $E[U]=2\sigma_s^2$ and $std[U]=2\sigma_s^2/\sqrt{NL}$. Note that the shape-rate parametrization is used here.

To validate the theoretical distribution of U in (4.19), 360 mechanical stirrer positions (as N) and 401 frequency points between 3.475 GHz and 3.525 GHz (as L) are collected. Note that different antenna positions, orientations, polarizations, *etc.* can also be used. Here, an indirect approach is adopted by separately verifying $\langle P_s(l)\rangle_N \sim Gamma(N, N/2\sigma_s^2)$ and $\langle P_s(l)\rangle_L \sim Gamma(L, L/2\sigma_s^2)$. Subsequently, (4.19) can be proved by the summation and scaling properties of the gamma distribution. The benefit of doing this is that while examining one stirring technique, the other can be used for generating samples without using a third stirring technique.

The relevant CDF plots are shown in Figure 4.3. One thing should be mentioned is that the shape parameter controls the overall shape of a gamma distribution. Hence, the theoretical CDF only fit well with the measured CDF with proper shape parameter value (360 for Figure 4.3 (a) and 155 for Figure 4.3 (b)). This also implies an effective alternative method for estimating the number of independent samples in addition to the widely-used autocorrelation/autocovariance function method, as will be compared and discussed later.

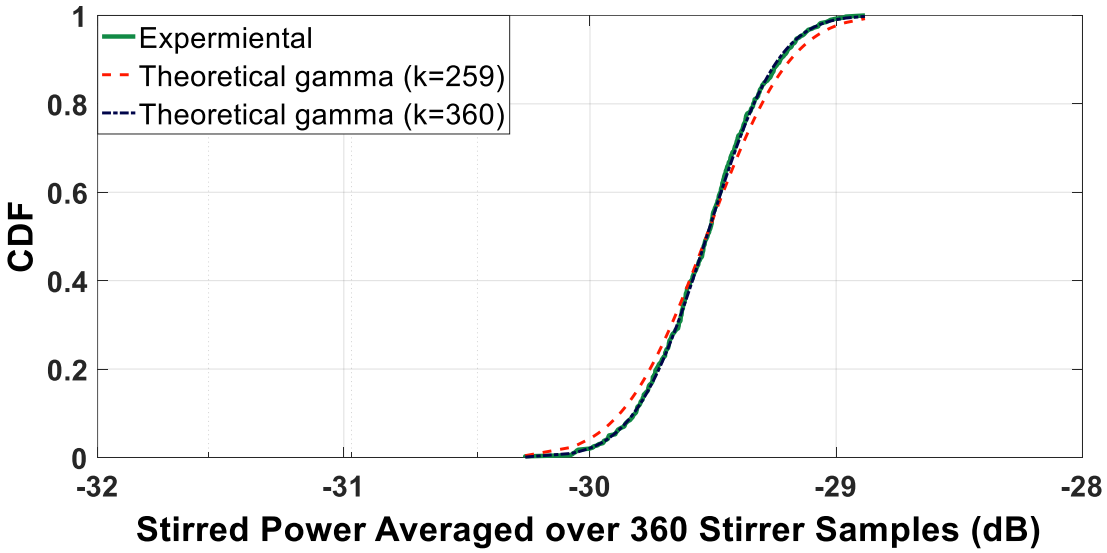

(a)

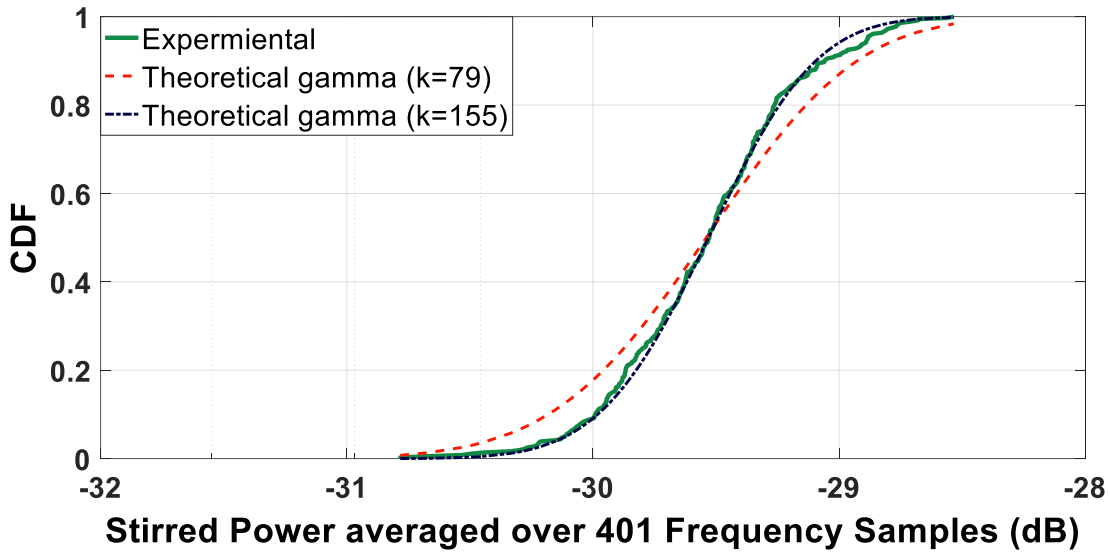

(b)

Figure 4.3: Comparisons of the theoretical and experimental CDF of (a) $\langle P_s(l)\rangle_N$ using adjacent frequency points (3.475 GHz – 3.525 GHz) as samples. (b) $\langle P_s(l)\rangle_L$ using different stirrer positions as samples. In both subplots, the black dash-dot curve is with the optimal shape parameter value, while the red dashed curve is with an arbitrary suboptimal shape parameter value for comparison.

Similarly, following (4.14), we have

$$V \sim Gamma\left(L, \frac{L}{2\sigma_{us}^2}\right) \tag{4.20}$$

with $E[V]=2\sigma_{us}^2$ and $std[V]=2\sigma_{us}^2/\sqrt{L}$.

Therefore, regarding [34], $\hat{K}_{avg}$ follows a generalized beta prime distribution with three shape parameters L, NL, and 1, and one scale parameter NK_{avg}:

$$\hat{K}_{avg} \sim \beta'\left(L, NL, 1, NK_{avg}\right) \tag{4.21}$$

Specifically,

$$\begin{aligned} E\left[\hat{K}_{avg}\right] &= \frac{NL}{NL-1}\cdot K_{avg} \\ std\left[\hat{K}_{avg}\right] &= \frac{NL}{NL-1}\sqrt{\frac{L+NL-1}{L(NL-2)}}\cdot K_{avg} \end{aligned} \tag{4.22}$$

Actually, $\widehat{K}_{avg}$ is an asymptotically unbiased estimator of K_{avg}, and its relative uncertainty (also known as the coefficient of variation) is defined as:

$$\tilde{u}\left[\hat{K}_{avg}\right]=\frac{std\left[\hat{K}_{avg}\right]}{E\left[\hat{K}_{avg}\right]}=\sqrt{\frac{L+NL-1}{L\left(NL-2\right)}} \tag{4.23}$$

Nevertheless, it is quite unlikely in practice that samples of $S_{21,us}$ can be directly acquired, and (4.23) does not reflect the uncertainty introduced by estimating $S_{21,us}$, either. Still, the formulation of (4.18) can offer insight into the distribution characteristics of each component.

4.2.3 Estimation of the Average Rician *K*-Factor Based on the MLE

Now we consider a more practical implementation in which MLEs (4.4), (4.5), (4.10), and (4.11) are used for inferring the relevant quantities. Then the estimator of K_{avg} can be formulated as

$$\hat{K}_{avg}^{'}=\frac{V^{'}}{U^{'}}=\frac{\left\langle \hat{P}_{us}\left(l\right)\right\rangle_{L}}{\left\langle \hat{P}_{s,avg}\left(l\right)\right\rangle_{L}} \tag{4.24}$$

Based on (4.4) and (4.10), we have

$$\hat{\mu}_{*}\left(l\right)\sim\mathcal{N}\left(\mu_{*}\left(l\right),\frac{\sigma_{s}^{2}}{N}\right) \tag{4.25}$$

which is a Gaussian distribution with mean $\mu_*(l)$ and variance σ_s^2/N, and

$$\frac{N}{\sigma_{s}^{2}}\hat{\mu}_{*}^{2}\left(l\right)\sim\chi_{1}^{2}\left(\frac{N\mu_{*}^{2}\left(l\right)}{\sigma_{s}^{2}}\right) \tag{4.26}$$

a noncentral chi-square distribution with 1 degree of freedom (DoF) and the noncentrality parameter $N\mu_*^2(l)/\sigma_s^2$. Thus, according to the additivity property of chi-square distribution, it is easy to derive that

$$\frac{NL}{\sigma_{s}^{2}}V^{'}\sim\chi_{2L}^{2}\left(2NLK_{avg}\right) \tag{4.27}$$

Following (4.5) and (4.11), we can get

$$\frac{1}{\sigma_s^2}\sum_{n=1}^{N}\left|S_{21}^{*}(l)-\hat{\mu}_{*}(l)\right|^2 \sim \chi_{N-1}^2(0) \tag{4.28}$$

a central chi-square distribution with N-1 DoF. Therefore,

$$\frac{L(N-1)}{\sigma_s^2}U' \sim \chi_{2L(N-1)}^2(0) \tag{4.29}$$

Combining (4.24), (4.27), and (4.29), one can conclude that

$$N\hat{K}'_{avg} = \frac{\frac{NV'}{2\sigma_s^2}}{\frac{U'}{2\sigma_s^2}} \sim F'_{2L,2L(N-1)}\left(2NLK_{avg}\right) \tag{4.30}$$

a noncentral F distribution with $2L$ and $2L(N\text{-}1)$ DoFs, and noncentrality parameter $2NLK_{avg}$ [34]. The mean and standard deviation of $\hat{K}'_{avg}$ can be obtained accordingly as:

$$E\left[\hat{K}'_{avg}\right] = \frac{L(N-1)}{NL-L-1}\left(\frac{1}{N}+K_{avg}\right) \tag{4.31}$$

$$std\left[\hat{K}'_{avg}\right] = \sqrt{\frac{L^2(N-1)^2\left(1+NK_{avg}\right)^2}{N^2(NL-L-1)^2(NL-L-2)} + \frac{L(N-1)^2\left(1+2NK_{avg}\right)}{N^2(NL-L-1)(NL-L-2)}} \tag{4.32}$$

Unsurprisingly, when L=1, (4.31) and (4.32) degenerate to (5) and (6) in [30].

In order to further investigate the statistical properties of $\hat{K}'_{avg}$, three 10000-sample Monte Carlo simulations with different value combinations of N and L are performed, with parameter settings $P_{s,avg}$=-20 dB and $P_{us,avg}$=-40 dB (K_{avg}=-20 dB). The resulting histograms and fitted PDFs are shown in Figure 4.4. In all three scenarios, the clear discrepancies between the estimated means and the ground truth value indicate that $\hat{K}'_{avg}$ is biased, tending to give overestimated results. While N dominates the bias of mean (0.0028 for Figure 4.4 (a) and Figure 4.4 (b), and 0.0100 for Figure 4.4 (c)), both N and L affect the dispersion of samples. Smaller N and L lead to larger variance. It is also interesting to note that the fitted distributions tend to be of a symmetrical bell shape since the DoFs in (4.30) are large in all three cases.

Next, we construct the unbiased estimator $\hat{K}''_{avg}$ as follows

$$\hat{K}''_{avg} = \frac{NL-L-1}{L(N-1)}\hat{K}'_{avg} - \frac{1}{N} \tag{4.33}$$

so that $E[\hat{K}''_{avg}]=K_{avg}$, and its standard deviation can be derived as

$$std\left[\hat{K}''_{avg}\right] = \sqrt{\frac{L\left(1+NK_{avg}\right)^2 + \left(NL-L-1\right)\left(1+2NK_{avg}\right)}{LN^2\left(NL-L-2\right)}} \tag{4.34}$$

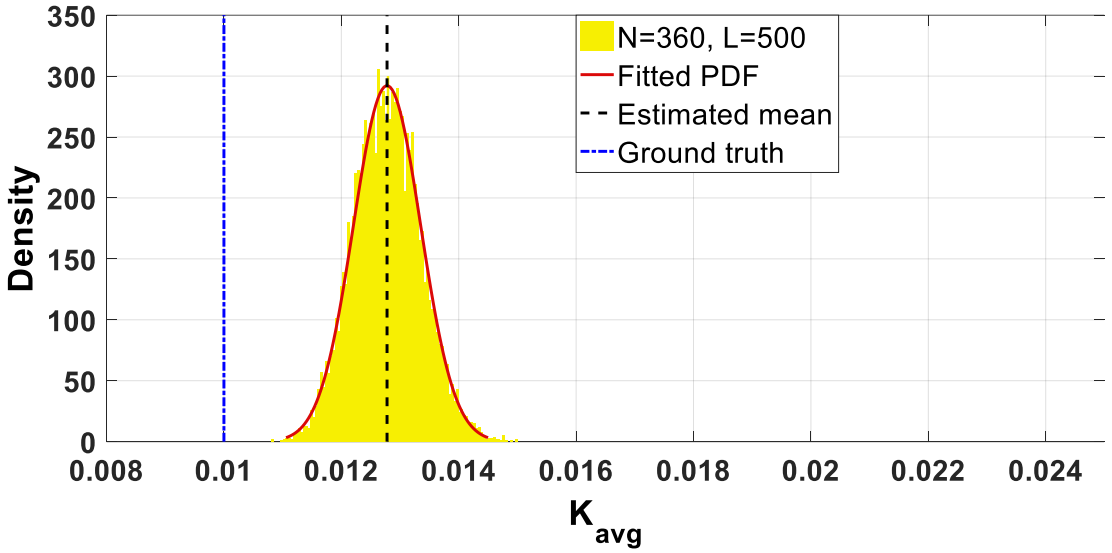

(a)

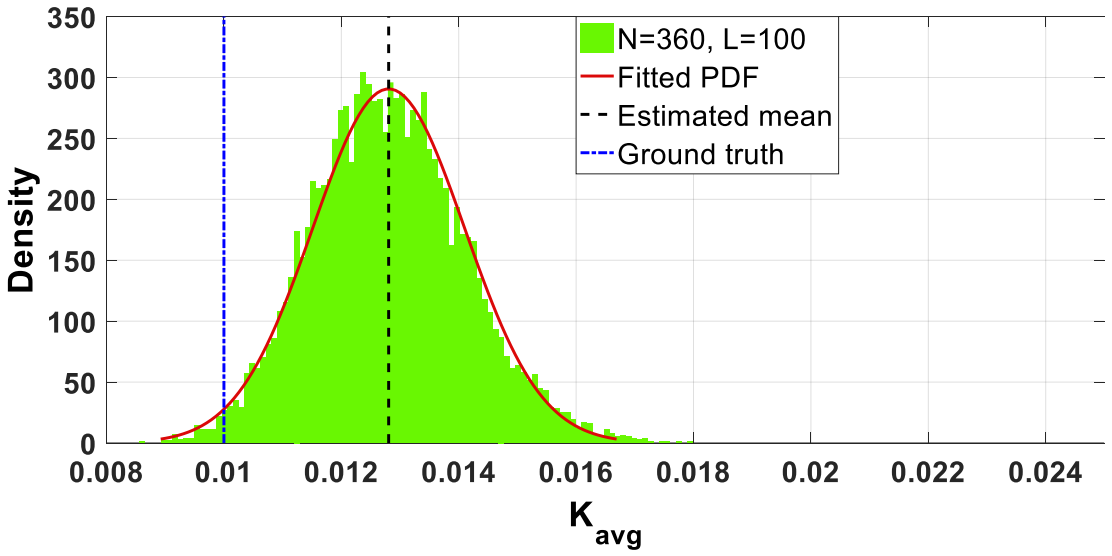

(b)

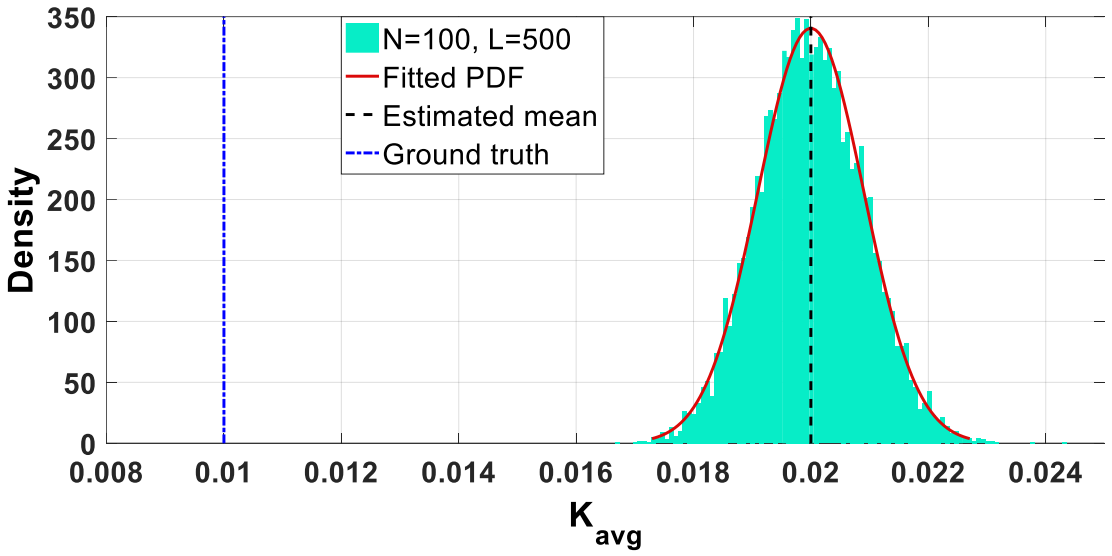

(c)

Figure 4.4: Monte Carlo simulation results of sample distributions of the MLE estimator $\hat{K}'_{avg}$ with different N and L combinations (a) N=360, L=500. (b) N=360, L=100. (c) N=100, L=500. In each subplot, the black dashed line indicates the estimated mean, while the blue dash-dot line indicates the ground truth.

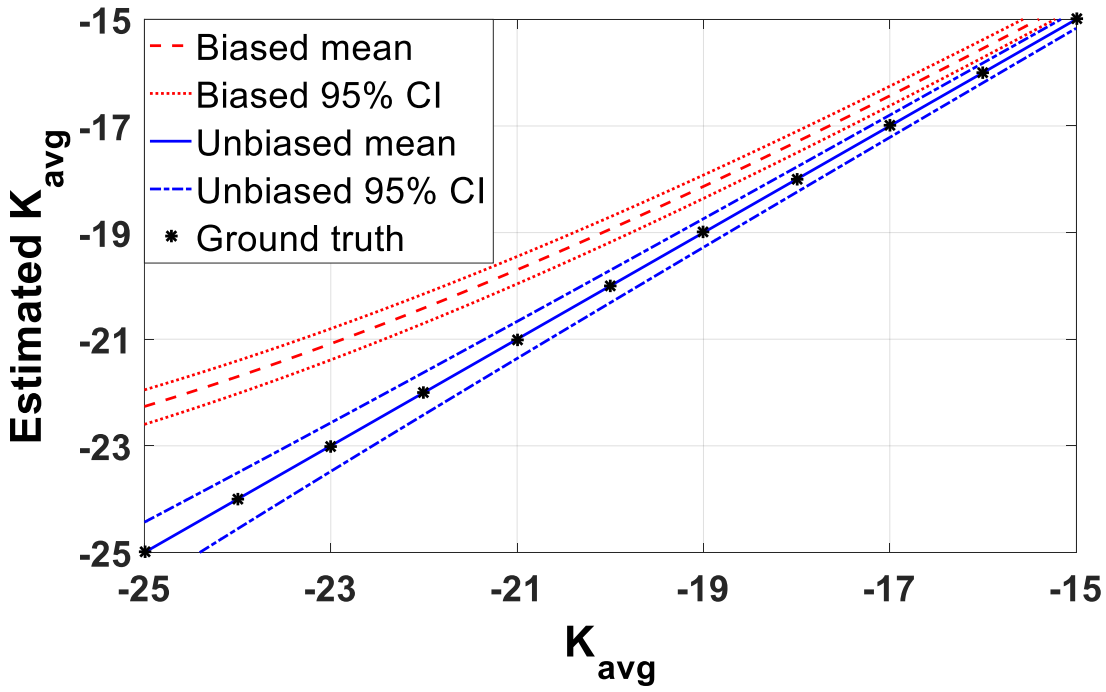

(a)

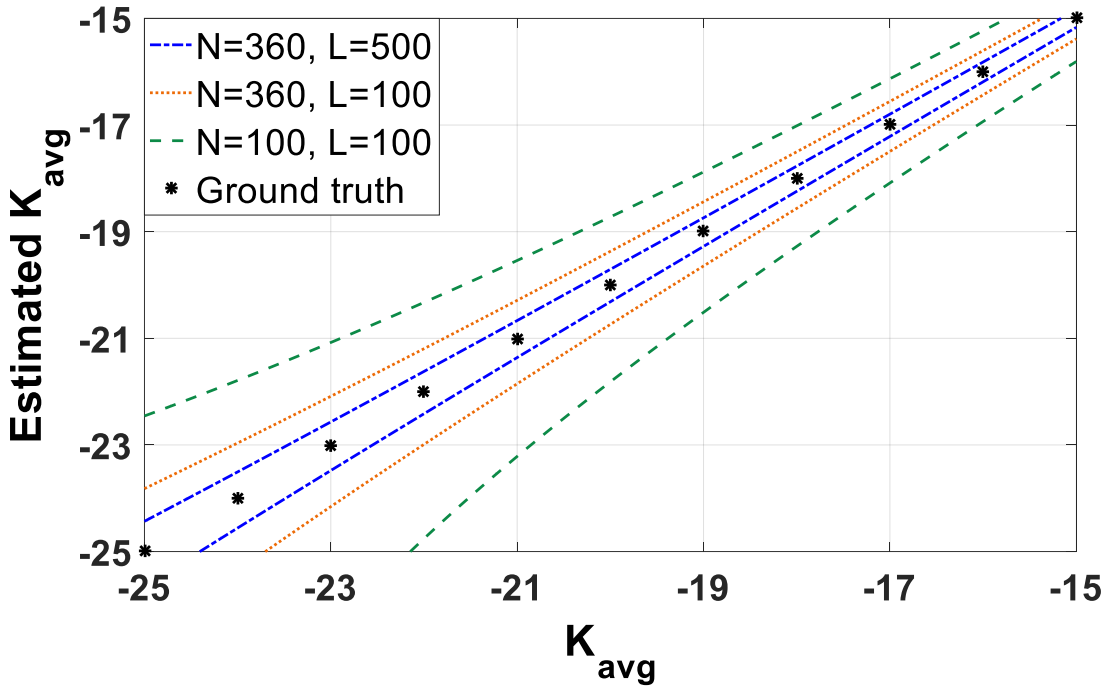

(b)

Figure 4.5: (a) Comparison of simulated results of estimators $\hat{K}'_{avg}$ and $\hat{K}''_{avg}$ in the region $K_{avg}\epsilon[-25, -15]$ dB with N=360 and L=500. (b) Comparison of expanded uncertainty intervals (95% CI) of $\hat{K}''_{avg}$ with different N and L combinations in the region $K_{avg}\epsilon[-25, -15]$ dB.

Simulated estimation results of $\hat{K}'_{avg}$ and $\hat{K}''_{avg}$, and their corresponding expanded uncertainty regions (95% confidence interval (CI)) [35] with N=360 and L=500 as a function of the ground truth value from -25 dB to -15 dB are illustrated in Figure 4.5 (a). As already pointed out in Figure 4.4, $\hat{K}'_{avg}$ results in overestimation. Moreover, this bias becomes more significant as K_{avg} decreases. For example, at -19 dB the discrepancy is less than 1 dB, while at -23 dB it increases to around 2 dB. $\hat{K}''_{avg}$, on the other hand, always makes the correct estimation, but at the expense of slightly increased uncertainty. Figure 4.5 (b) demonstrates how N and L affect the performance of $\hat{K}''_{avg}$. As expected, increasing the number of independent stirrer samples and the number of independent realizations can effectively reduce the estimation uncertainty. Another thing worth noting

is that for fixed N and L values, the estimation uncertainty of $\widehat{K}''_{avg}$ tends to become worse with declining K_{avg}.

It should be stressed that in [29] – [31] the main focus is the single-case K whose definition is given in (4.6). At adjacent uncorrelated frequency points, K can be treated as *i.i.d*. Therefore, when averaged, the new estimator (which is essentially the sample mean) has the exact same mean but the standard uncertainty is reduced to $1/\sqrt{F}$ of the original value (as shown in (14) and (15) in [30]). By contrast, this work is about K_{avg} which is defined in (4.13). The number of frequencies as well as the number of antenna positions, orientations, and polarizations are regarded as realizations that can provide randomness to the unstirred part (see (4.12) and (4.14)), and their effect on the mean and standard deviation of $\widehat{K}''_{avg}$ can be precisely and exactly reflected in (4.33) and (4.34).

4.3 Procedures of TRP Measurement and the Analytical Uncertainty Model

4.3.1 Calibration Stage

Typical RC-based TRP measurement generally comprises two stages [15], [27], [36], namely 1) the calibration stage and 2) the measurement stage. In the calibration stage, the chamber transfer function (G_{Cal}, also known as the chamber insertion loss) at the frequency band of interest is estimated between the reference antenna and the measurement antenna. The two antennas are connected to Port 1 and Port 2 of the VNA through cables. If the standard 2-Port calibration is performed, the RPs are shifted to the inputs of the two antennas (illustrated by the red dashed lines in Figure 4.1). Thus, the corrected chamber transfer function can be estimated by

$$\hat{G}_{Cal} = \frac{\left\langle \left| S_{21} \right|^2 \right\rangle_{N_1, L_1}}{\eta_{t,Ref}\eta_{t,Meas}} \tag{4.35}$$

where $\eta_{t,Ref}$ and $\eta_{t,Meas}$ are the total efficiencies of the reference antenna and the measurement antenna, respectively. We follow the convention in Section 4.2 to use $L_1=F_1 \cdot M_1$ for notational convenience, where F_1 and M_1 denote the numbers of independent frequency points and independent source locations used in the calibration stage. In addition, N_1 is the number of independent stirrer samples adopted in this stage.

4.3.2 Measurement Stage

As for the measurement stage, the RPs are indicated by the green dashed lines in Figure 4.1. The DUT is radiating at its maximum power, and the measurement antenna is connected to the SA through the measurement cable. Then the averaged receiving power read from the SA can be expressed as

$$\left\langle P_{SA} \right\rangle_{N_2} = P_{DUT} \hat{G}_{Meas} \eta_{t,Meas} L_{Meas} \tag{4.36}$$

where P_{DUT} is the unknown TRP of the DUT to be inferred, $\widehat{G}_{Meas}$ is the equivalent estimated chamber transfer function in the measurement stage (which cannot be directly obtained), L_{Meas} is the loss of the measurement cable, and N_2 is the number of independent stirrer samples used in this stage. Note that frequency stirring is not applicable in the measurement stage (F_2=1) since the radiating property of the wireless device might be quite different at different frequencies (depending upon the specific protocol) [37]. Based on (4.35), (4.36), and the assumption that $\widehat{G}_{Cal}=\widehat{G}_{Meas}$, the TRP estimator of the DUT can be formulated as

$$\hat{P}_{DUT} = \frac{\eta_{t,Ref}}{L_{Meas}} \cdot \frac{\left\langle P_{SA} \right\rangle_{N_2}}{\left\langle \left| S_{21} \right|^2 \right\rangle_{N_1,L_1}} = \alpha \cdot \frac{Y}{X} \tag{4.37}$$

α can be treated as a constant if datasheets of the corresponding quantities are available. In contrast, X and Y are two independent random variables, and individual relative uncertainties should be combined in quadrature and propagated to $\widehat{P}_{DUT}$ [38] as

$$\tilde{u}\left[\hat{P}_{DUT} \right] = \sqrt{\tilde{u}^2\left[X\right] + \tilde{u}^2\left[Y\right]} \tag{4.38}$$

4.3.3 Analytical Uncertainty Model Based on the Average Rician *K*-Factor

As already indicated in (4.37), when measuring the TRP of a wireless device, only scalar information (the receiving power measured by the SA, or equivalently $|S_{21}|^2$) is obtainable. As a result, the anisotropy issue cannot be directly compensated [24]. To overcome this problem, various uncertainty models adopt the explicit representation of K so as to quantify the effect of the lacking of isotropy [11], [20] – [22]. Based on (17) in [20] which utilizes a components-of-variance model and by doing the following: 1) extend the model from K to K_{avg}; 2) neglect the effect of measurement perturbation (*e.g.*, noise, imperfection of calibration, and cable movement); 3) correct sample correlations by estimating the independent sample number for each stirring technique utilized; and 4) combine uncertainties in both the calibration stage and the measurement stage using (4.38), we can derive the overall analytical uncertainty model for TRP measurement in an RC as:

$$\tilde{u}_{ana}\left[\hat{P}_{DUT}\right]=\sqrt{\frac{\frac{1}{N_1L_1}+\frac{2}{N_1L_1}K_{avg}+\frac{1}{M_1}K_{avg}^2}{\left(1+K_{avg}\right)^2}+\frac{\frac{1}{N_2}+\frac{2}{N_2}K_{avg}+K_{avg}^2}{\left(1+K_{avg}\right)^2}} \tag{4.39}$$

In reality, K_{avg} should be replaced by the corrected MLE estimator $\hat{K}''_{avg}$. Regarding (4.39) it is clear that, with the intention of achieving low measurement uncertainty, the number of independent samples used in each stage should be large, and K_{avg} should be kept small. Specifically, when K_{avg} is so small that it is negligible, (4.39) reduces to a baseline model:

$$\tilde{u}_{BL}=\sqrt{\frac{1}{N_1L_1}+\frac{1}{N_2}} \tag{4.40}$$

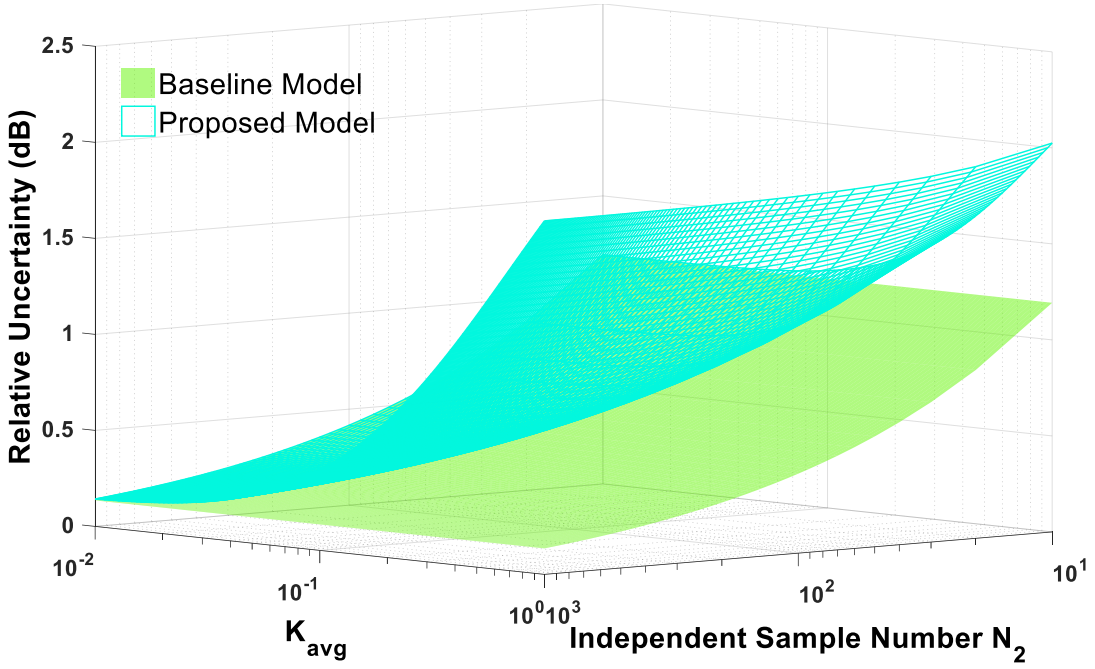

Figure 4.6: Comparison of analytical models (4.39) and (4.40) as a function of $K_{avg}\epsilon[-20, 0]$ dB and $N_2\epsilon[10, 1000]$ with N_1=360, F_1=158 and M_1=9.

Figure 4.6 illustrates the comparison result of the proposed analytical model (4.39) and the baseline model (4.40) with N_1=360 and L_1=1422 (F_1=158 and M_1=9) as a function of the K_{avg} (-20 dB – 0 dB) and N_2 (10 – 1000). As K_{avg} increases, its adverse effect on the measurement uncertainty becomes more prominent. Consequently, the baseline model (4.40) tends to significantly underestimate the uncertainty and renders overly optimistic predictions. In addition, using a larger N_2 value during the measurement stage seems to magnify this impact.

4.4 Measurements

In this section, the TRP of the DUT is measured following the procedures described in Section 4.3. The relative measurement uncertainty is then empirically estimated using the 9-Point approach [15], [21], [23], and the results are compared to that directly predicted by the analytical uncertainty model (4.39) for assessment. Methods for the derivation of relevant parameters present in (4.39) are also explained.

4.4.1 Experimental Setup and Preparations

(a)

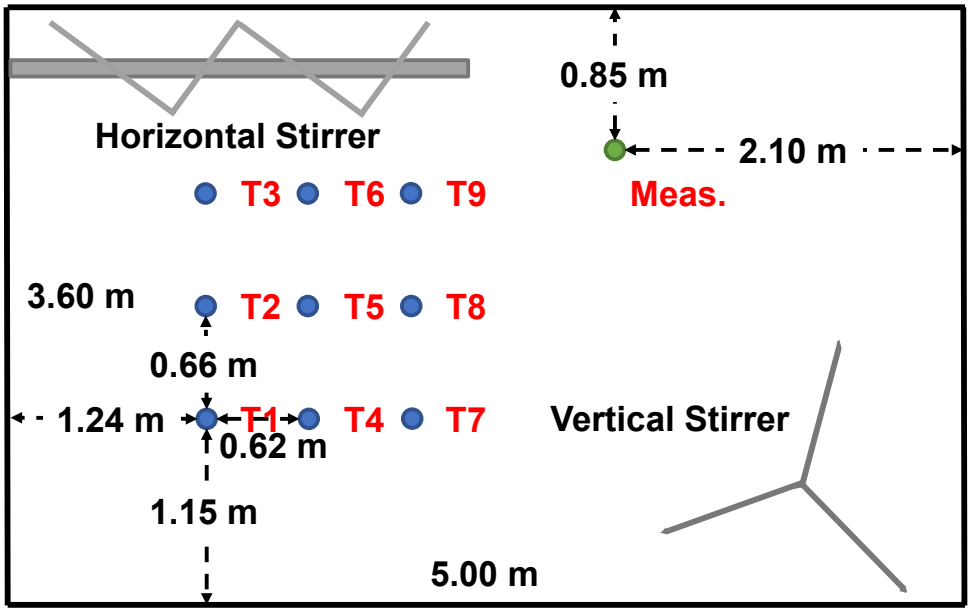

(b)

Figure 4.7: Experimental setup for TRP measurement and uncertainty assessment procedures: (a) Measurement scenario inside the RC at the University of Liverpool. (b) Schematic diagram of the top view showing the 9 locations for the reference antenna/DUT and the fixed position for the measurement antenna.

Measurements are conducted using the RC at the University of Liverpool, which has a size of 3.60 m (w) × 5.80 m (l) × 4.00 m (h). Figure 4.7 (a) shows the interior of the RC and the typical measurement setup. One horizontal stirrer (with rotating radius 0.50 m) and one vertical stirrer (with rotating radius 0.70 m) with asymmetrical paddles are installed at the opposite corners inside the RC. During the mechanical stirring process, the two stirrers are synchronized by the motor controller to rotate simultaneously in mode-tuning mode. A rotating platform (1.52 m high) is used to mount the reference antenna/DUT, and a tripod with 1.40 m in height is utilized to support the measurement antenna. To minimize the LoS and the unstirred NLoS components, the reference antenna/DUT and the measurement antenna should be directed away from each other and towards different stirrers. As depicted in Figure 4.7 (b), T1 through T9 represent the 9 locations of the reference antenna/DUT for applying source stirring or 9-Point uncertainty estimation. The measurement antenna, by contrast, is fixed at the point labeled "Meas.". Useful distance information is also available in Figure 4.7 (b). Throughout the whole measurement process, the reference antenna, the DUT, and the measurement antenna should all be placed inside the RC so that the loading condition of the RC (and thus the composite Q factor) remains unchanged. The reference antenna or the DUT, which is in idle mode, should be terminated with a 50 Ω load.

Detailed configuration information and parameter specification for the calibration stage and the measurement stage is summarized in Table 4-I. The n78 band, which belongs to the 5G frequency range 1 (FR1) [39] with 3.5 GHz carrier frequency, is selected for the experiment. A 50 MHz frequency sweeping (3.475 GHz – 3.525 GHz with 125 kHz frequency resolution) is performed using an Agilent N9917A FieldFox VNA in the calibration stage. In contrast, in the measurement stage, only the single carrier point is measured by a Keithley 2820 SA. A Rohde & Schwarz HF 906 antenna is used as the reference antenna, and the measurement antenna is of type SATIMO SH 2000. An SG (Keithley 2920, used as the power source), an MVG SH1000 dual-ridge horn antenna (used as the radiator), and the cable (the Ref. cable as sketched in Figure 4.1) connecting them are considered as a "combined" DUT. The output power of the SG is set to 3 dBm (3.5 GHz single tone), and the total efficiency of the radiating antenna and the insertion loss of the Ref. cable are -0.44 dB and -6.71 dB, respectively at 3.5 GHz. Therefore, the nominal TRP of this DUT is -4.15 dBm (this also ensures the consistency of the RP "Meas. RP1" as shown in Figure 4.1). Multiple configurations of stirrer positions and step angles

are used to repeat the measurement stage so that the relative uncertainty as a function of N_2 can be illustrated and examined.

Table 4-I: Configuration information and parameter specification for the TRP measurement and estimation of the relative uncertainty

Stage	Parameter	Value
Calibration	Frequency range	3.475 GHz – 3.525 GHz
	Number of frequency points	401
	Frequency domain resolution	125 kHz
	Number of stirrer positions	360
	Stirrer step size	1°
	Number of source locations	9
	Equipment	VNA
	Ref. antenna bandwidth	2 GHz – 32 GHz
	Ref. antenna efficiency	-0.46 dB (89.95%)
Measurement	Carrier frequency	3.5 GHz
	Number of stirrer positions	10, 20, 30, 60, 90, 120, 180, 360
	Stirrer step size	36°, 18°, 12°, 6°, 4°, 3°, 2°, 1°
	Equipment	SG & SA
	DUT antenna bandwidth	1 GHz – 18 GHz
	DUT antenna efficiency	-0.44 dB (90.36%)
	Output power of the SG	3 dBm
	Ref. cable loss at 3.5 GHz	-6.71 dB
	Nominal TRP of the DUT	-4.15 dBm
Common settings	IF bandwidth	10 kHz
	Meas. antenna bandwidth	1 GHz – 18 GHz
	Meas. cable loss at 3.5 GHz	-6.29 dB
	Idle mode termination	50 Ω

4.4.2 Calibration Stage

A. Estimation of the number of independent stirrer position, frequency, and source location samples

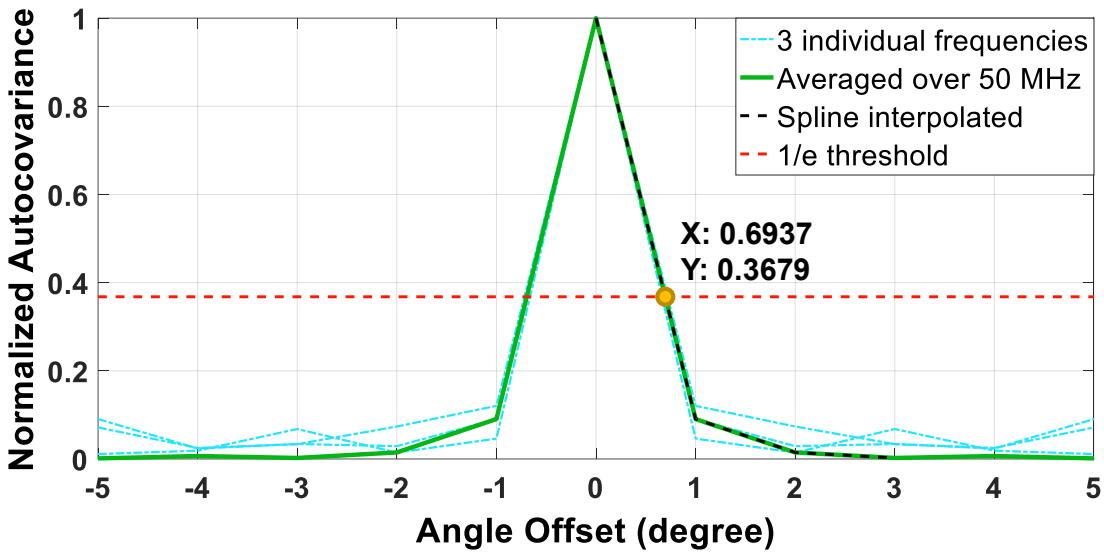

(a)

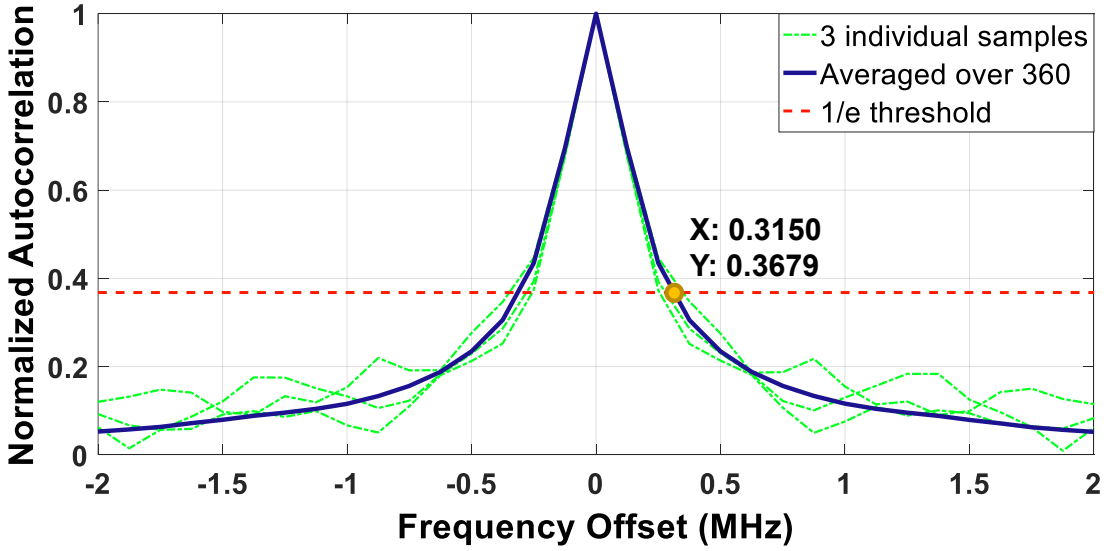

(b)

Figure 4.8: (a) Estimation of the number of independent stirrer samples using the normalized autocovariance function averaged over 50 MHz bandwidth. (b) Estimation of the number of independent frequency points using the normalized ACF averaged over 360 stirrer positions. In both figures, arbitrarily picked individual samples, as well as the averaged result, are plotted for comparison.

The autocovariance of the transmission coefficient S_{21} as a function of the offset angle $\partial\theta$ of the stirrer positions is defined as:

$$C(\partial\theta, f) = \int_{-\Theta}^{+\Theta} \left(S_{21}(\theta, f) - \langle S_{21}(\theta, f) \rangle_{\Theta} \right) \left(S_{21}^{*}(\theta + \partial\theta, f) - \langle S_{21}^{*}(\theta, f) \rangle_{\Theta} \right) d\theta \quad (4.41)$$

where the superscript * is the complex conjugate notation, and f denotes frequency (3.5 GHz in this case). A whole stirrer revolution (Θ=360°) is considered with 1° step size, and $\theta+\partial\theta$ is processed by the modulo 360 operation. Then (4.41) is normalized by its maximum value and averaged over the frequency region 3.475 GHz – 3.525 GHz.

The result is illustrated in Figure 4.8 (a). Note that the cubic spline interpolation is applied around the region of interest to increase the density of points (the black dashed curve). Following the IEC standard [15] with a $1/e$ threshold, the coherence angle is approximately 0.69°, less than the step size between adjacent stirrer positions, which means that all the 360 samples provided by mechanical stirring can be considered as uncorrelated (and equivalently, independent). Therefore, we have N_1=360.

Similarly, the ACF in terms of the frequency offset ∂f at a certain stirrer position n is given as:

$$R(\partial f, n) = \int_{f_{start}}^{f_{end}} S_{21}(f, n) S_{21}^{*}(f + \partial f, n)\, df \quad (4.42)$$

where f_{start}=3.475 GHz, and f_{start}=3.525 GHz. Figure 4.8 (b) plots 3 individual stirrer positions as well as the averaged result over 360 stirrer positions. For the $1/e$ threshold, the coherence bandwidth is 315 kHz, which corresponds to F_1=158 independent frequency points across a 50 MHz band. It should be pointed out that Figure 4.8 is obtained with the Ref. antenna placed at T1. The same process is also repeated for the other eight locations, and highly close results can be obtained.

Recall Figure 4.3, as aforementioned, the task of independent sample number estimation can be converted into a parameter optimization problem aiming at finding the optimum shape factor k that minimizes the sum of square error (SSE) between the relevant theoretical CDF of the gamma distribution and the measured CDF (we name it the CDF fitting method):

$$\arg\min_{k} SSE(k) = \arg\min_{k} \left[CDF_{meas} - CDF_{theo}(k) \right]^2 \quad (4.43)$$

where the subscript *meas* means "measured", and *theo* means "theoretical". Due to its physical meaning, k should be a positive integer. The measured CDF is available from experimental results (by using one stirring technique as sample average, and the other stirring technique as sample realization), while multiple theoretical CDFs are swept in

terms of multiple integer values of k (with sample mean and sample standard deviation estimated using the MLE). After the optimum k is determined, the rate factor β can be obtained accordingly. The numbers of independent stirrer positions and frequency points derived by the CDF fitting method are N_1=360 and F_1=155 (as shown in Figure 4.3). It can be seen that the two methods give similar results, so they can be used for cross-validation for improved estimation accuracy. For consistency's sake, in the following calculations we still adopt the results derived by the autocovariance/autocorrelation method.

As demonstrated in Figure 4.7 (b), the minimum separation distance between two adjacent source locations is 0.62 m, which corresponds to approximately 7.23 λ at 3.5 GHz. Therefore, it is reasonable to assume that all the 9 source positions are spatially uncorrelated, *i.e.*, M_1=9.

B. Derivation of K_{avg} value

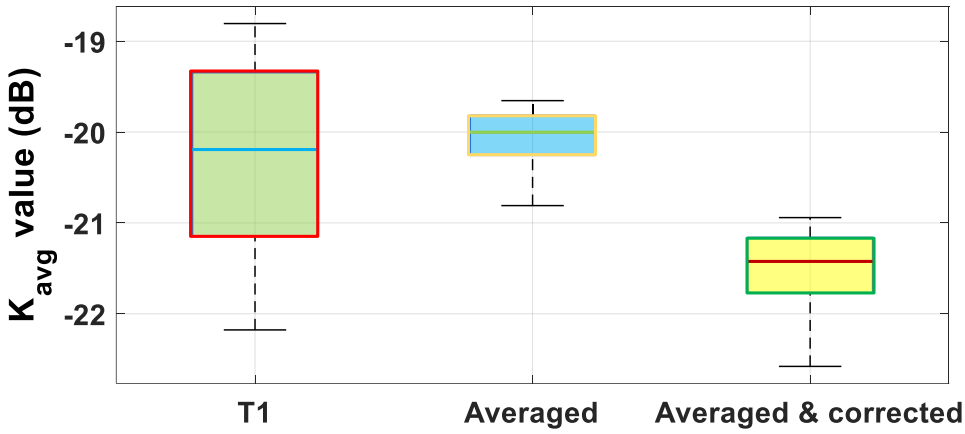

Figure 4.9: Derivation of K_{avg} with N_1=360, F_1=158 and M_1=9 using the MLE estimator (4.24) and then the result is corrected by (4.33). Adjacent frequency points are treated as samples for the boxplot. The K-factor estimated at a single source position T1 is also shown for comparison.

As explained in Section 4.2.3, K_{avg} is estimated using the MLE estimator (4.24) and then corrected by the unbiasing operation (4.33). With the aim of showing the dispersion

of measurement, K_{avg} at adjacent frequency points are used as *i.i.d* samples. The resultant boxplots are shown in Figure 4.9. It can be found that by utilizing source stirring (so that the unstirred part is considered as random), the uncertainty can be further improved compared with the individual source position case (T1). After the unbiasing operation, the median value of K_{avg} is decreased (also the mean value), but a slight increase in terms of the uncertainty is observed, which is consistent with the simulated results shown in Figure 4.5 (a). It can be derived that $\widehat{K}''_{avg}$=-21.49 dB at 3.5 GHz, and this value will be used in subsequent calculations.

C. Uncertainty comparison

In the calibration stage, the transfer function $\widehat{G}_{Cal}$ (or equivalently X) is calculated using 360 stirrer positions (N_1=360), a 50 MHz band with a frequency step of 125 kHz (F_1=158) and 9 reference antenna locations (M_1=9). The uncertainty is first directly estimated by the 9-Point method, and then analytically calculated using the proposed model (4.39) and the baseline model (4.40) for comparison. Note that up to now we only consider the calibration stage, so only the first term of (4.39) and (4.40) in the square root is used.

To select the appropriate equation for the 9-Point uncertainty estimation procedure, the one-way analysis of variance (ANOVA) test, which examines whether the means of multiple sample groups are equal or not by comparing the between and within variances [21], [38], is performed. Details of how to form the sum of squares between (SSB), the sum of squares within (SSW), and the relevant F statistic are omitted here. The test result is listed in Table 4-II. Since the P-value (6.06×10^{-7}) is much smaller than the 0.05 significance level, the impact of lacking isotropy dominates the uncertainty, and the null hypothesis that "all sample groups (transfer functions calculated at each of the nine locations T1–T9) have identical mean value" should be rejected. Consequently, (4.44) should be used for assessing the relative uncertainty [21].

$$\tilde{u}_{est}\left[X\right]=\frac{\sqrt{\sum_{m=1}^{M_1}\left(\left\langle\left|S_{21}\left(m\right)\right|^2\right\rangle_{N_1,F_1}-X\right)^2}}{\sqrt{M_1\left(M_1-1\right)}X} \tag{4.44}$$

where M_1 is the number of source positions used for sample realization in order to estimate the relative uncertainty. For the widely used 9-point estimation method, M_1=9.

It should be stressed that the M_1 source positions are also used as source stirring samples for calculating X. That is why there is a $\sqrt{M_1}$ term in the denominator of (44).

Comparison between the estimated and analytical models is shown in Table 4-III. Since a very large set of independent samples is utilized (511920 as derived in Section 4.4.2 A)), all three methods give low relative uncertainty values. The baseline model (4.40) leads to an underestimated result, while the proposed model (4.39) can make effective improvement even in an environment with extremely low K_{avg} value (-21.49 dB). Apart from the finite number of independent samples and the limited isotropy, there might be other sources of uncertainty.

Table 4-II: ANOVA table

Source	Sum of Squares	DoF	Mean Square	F-value	P-value
Between	3.96×10^{-7}	8	4.95×10^{-8}	5.51	6.06×10^{-7}
Within	2.90×10^{-5}	3231	8.98×10^{-9}		
Total	2.94×10^{-5}	3239	—		

Table 4-III: Table of comparison between estimated and analytical relative uncertainties in the calibration stage

N_1=360, F_1=158, and M_1=9	Relative Uncertainty
9-Point estimation	0.37%
Proposed model (39) (calibration stage only)	0.27%
Baseline model (40) (calibration stage only)	0.14%

4.4.3 Measurement Stage

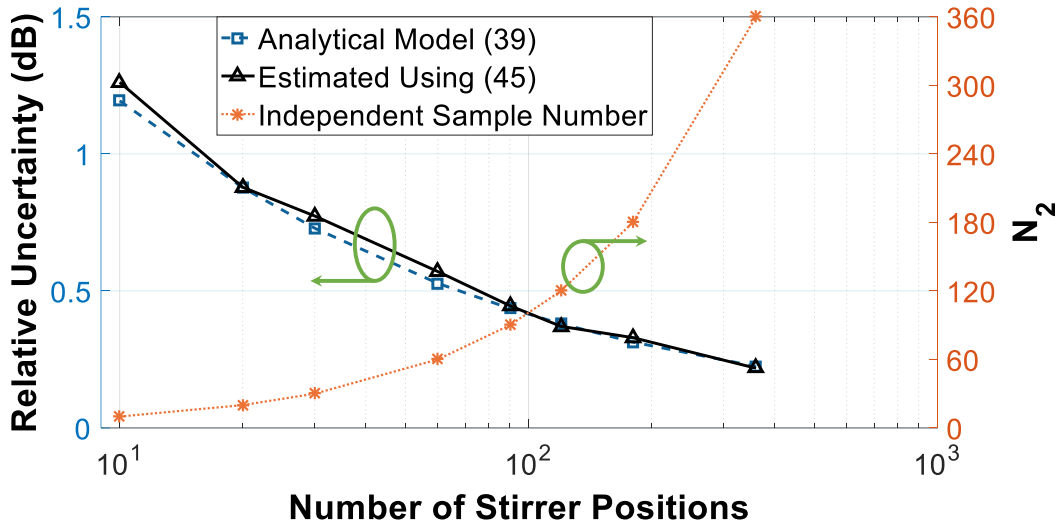

Figure 4.10: Comparison of the overall estimated and proposed analytical relative uncertainties as a function of N_2 at 3.5 GHz.

In this stage, the TRP of the DUT is measured, and the overall relative uncertainty considering both stages is estimated and compared with that theoretically calculated using the proposed model (4.39). After N_2 samples of P_{SA} are collected by the SA, its sample mean Y can be derived, and (4.37) is utilized to calculate $\hat{P}_{DUT}$. This procedure is performed nine times with the DUT placed at T1–T9. At each source location, the orientation of the DUT is intentionally configured to be different from that of the reference antenna during the calibration stage. The empirical relative uncertainty is calculated according to the following equation:

$$\tilde{u}_{est}\left[\hat{P}_{DUT}\right]=\frac{\sqrt{\sum_{m=1}^{M_1}\left(\hat{P}_{DUT}(m)-\left\langle\hat{P}_{DUT}\right\rangle_{M_1}\right)^2}}{\sqrt{(M_1-1)}\left\langle\hat{P}_{DUT}\right\rangle_{M_1}} \tag{4.45}$$

Then the measurement stage is repeated with various N_2 values (as specified in Table 4-I). The result of the comparison as a function of N_2 is demonstrated in Figure 4.10. The linear to decibel transformation defined in [15]

$$\tilde{u}_{dB}=10\log_{10}(1+\tilde{u}) \tag{4.46}$$

is adopted for illustration purposes. It can be found that both $\tilde{u}_{est}[\hat{P}_{DUT}]$ and $\tilde{u}_{ana}[\hat{P}_{DUT}]$ monotonically decrease with increasing N_2. Generally speaking, the two uncertainty

curves are in good agreement with each other, although the estimated one is slightly higher. The reason is similar to that in the calibration stage. The measurement process is also repeated with the DUT located at nine positions different from T1–T9 (but still within the working volume), and the result is comparable with that shown in Figure 4.10.

Next, the whole process is redone at two additional carrier frequencies (3.45 GHz and 3.55 GHz) within the n78 band. The 50 MHz offset from the original 3.5 GHz carrier frequency guarantees that it is large enough to be considered independent, but small enough to assume that the values of $\eta_{t,Ref}$, L_{Meas}, and L_{Ref} are similar. Typical variations of individual $\widehat{P}_{DUT}$ measurements at the three frequencies are shown in Figure 4.11 with two measurement stage configurations: N_2=360 and N_2=60. The expanded relative uncertainty regions derived analytically using (4.39) with a scaling factor of 1.96 are also plotted (centered at the corresponding sample means). By comparing the two subplots, it is easy to see that the larger the value of N_2, the smaller the measurement dispersion, and the smaller the fluctuation of the sample means. However, if more independent samples are used, the measurement time will be longer. That is to say, there is a clear trade-off between measurement accuracy and measurement efficiency. Another thing worth mentioning is that the 95% CIs calculated using (4.39) fit individual measurements quite well, which verifies that the proposed analytical model is reasonably accurate.

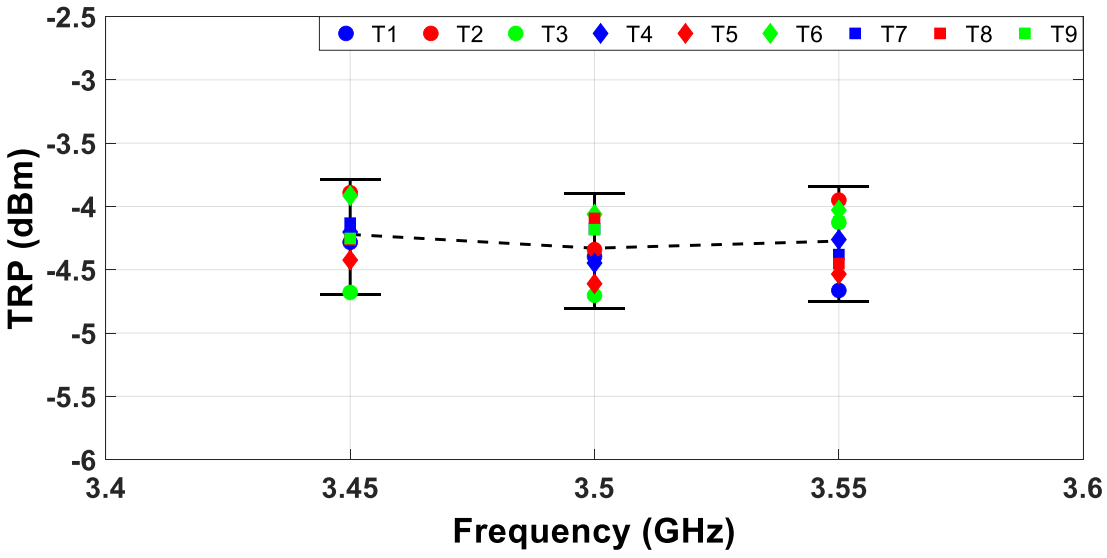

(a)

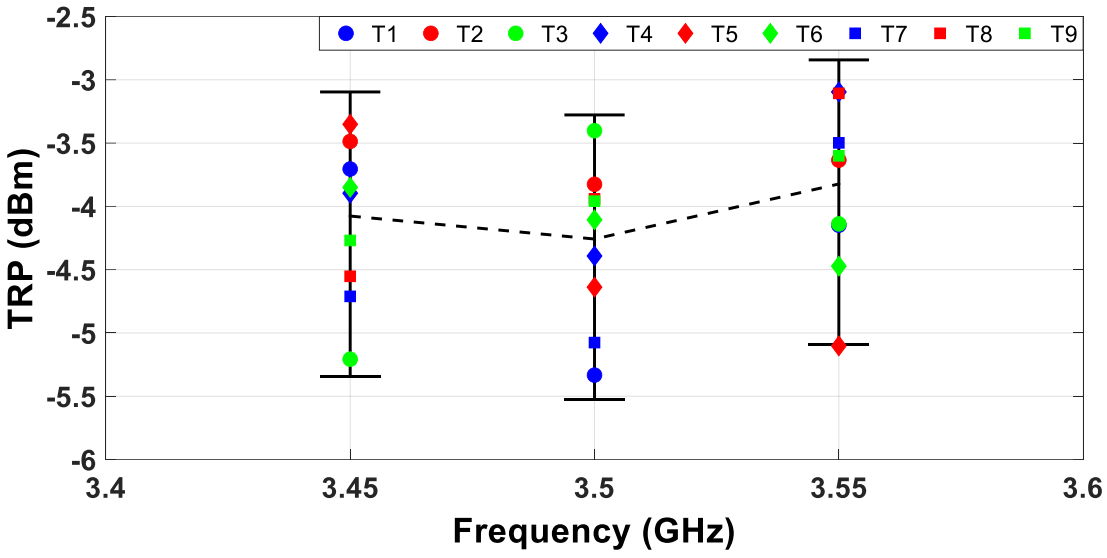

(b)

Figure 4.11: Individual $\widehat{P}_{DUT}$ measurements at nine source locations T1–T9 at three different carrier frequencies (3.45 GHz, 3.5 GHz, and 3.55 GHz) with corresponding expanded relative uncertainties (95% CI) calculated using the proposed analytical model (39): (a) N_2=360. (b) N_2=60.

4.5 Conclusion

In this chapter, the RC was applied to the practical OTA TRP tests. It was demonstrated that by using K_{avg} instead of single-case K, the statistical anisotropy of an RC can be more accurately characterized. A thorough statistical analysis for K_{avg} was conducted, including the formulation of its MLE estimator and the corresponding unbiased correction. Monte Carlo simulations were also performed to verify the derived statistics. Then an improved analytical uncertainty model for the RC-based OTA TRP measurement was derived by considering both the sample correlation and the anisotropy issues. Good agreement between the proposed analytical model and the 9-Point estimation process demonstrated that the proposed model is reasonably accurate.

The proposed model dramatically simplifies the work needed for characterizing the measurement uncertainty and guides the best practice for TRP measurement using an RC. It aims at providing satisfactory measurement accuracy while maintaining fast measurement speed. Since the calibration stage is conducted "offline", it is recommended

that a large number of independent samples is used with multiple stirring techniques. By contrast, for the measurement stage performed "online", there is a trade-off between the number of independent samples provided and the measurement efficiency. Therefore, the value of N_2 should be carefully set on demand. In all cases, K_{avg} should be kept small so that good isotropy can be achieved.

Another thing worth mentioning is that during the experiment, the reference antenna and DUT are both directional and have similar radiation patterns at the frequency band of interest. In practice, for a DUT whose radiation property could be quite different from the reference antenna used in the calibration stage, a slightly higher uncertainty might be observed. How to effectively solve this problem might be a future research direction.

4.6 References

[1] T. S. Rappaport, S. Sun, R. Mayzus, H. Zhao, Y. Azar, K. Wang, *et al*., "Millimeter-wave mobile communications for 5G cellular: It will work!," *IEEE access.*, vol. 1, pp. 335–349, 2013.

[2] F. Boccardi, R. W. Heath, A. Lozano, T. L. Marzetta, and P. Popovski, "Five disruptive technology directions for 5G," *IEEE Commun. Mag.*, vol. 52, no. 2, pp. 74–80, Feb. 2014.

[3] W. Fan *et al*., "A step toward 5G in 2020: Low-cost OTA performance evaluation of massive MIMO base stations.," *IEEE Antennas Propag. Mag.*, vol. 59, no. 1, pp. 38–47, 2017.

[4] Y. Qi *et al*., "5G over-the-air measurement challenges: Overview," *IEEE Trans. Electromagn. Compat.*, vol. 59, no. 6, pp. 1661–1670, Dec. 2017.

[5] K. A. Remley *et al*., "Measurement challenges for 5G and beyond: An update from the National Institute of standards and technology," *IEEE Microw. Mag.*, vol. 18, no. 5, pp. 41–56, Jul./Aug. 2017.

[6] D. A. Hill, *Electromagnetic Fields in Cavities,* Piscataway, NJ, USA: IEEE Press, 2009.

[7] X. Chen, J. Tang, T. Li, S. Zhu, Y. Ren, Z. Zhang, and A. Zhang, "Reverberation Chambers for Over-the-Air Tests: An Overview of Two Decades of Research," *IEEE Access.*, vol. 6, pp. 49129–49143, Aug. 2018.

[8] Q. Xu and Y. Huang, *Anechoic and Reverberation Chambers: Theory, Design and Measurements*, Wiley-IEEE, UK, 2019.

[9] L. R. Arnaut, "Measurement uncertainty in reverberation chambers – I. Sample statistics," NPL, London, U.K., NPL Rep. TQE2, pp. 1–136, Dec. 2008.

[10] Y. Huang and D. J. Edwards, "A novel reverberating chamber: Source stirred chamber," in *Proc. Int. Conf. Electromagn. Compat.*, Edinburgh, U.K., pp. 120–124, Sep. 1992.

[11] P.-S. Kildal, X. Chen, C. Orlenius, M. Franzén, and C. S. L. Patané, "Characterization of reverberation chambers for OTA measurements of wireless devices: Physical formulations of channel matrix and new uncertainty formula," *IEEE Trans. Antennas Propag.*, vol. 60, no. 8, pp. 3875–3891, Aug. 2012.

[12] D. A. Hill, "Electronic mode stirring for reverberation chambers," *IEEE Trans. Electromagn. Compat.*, vol. 36, pp. 294–299, 1994.

[13] A. Gifuni, L. Bastianelli, F. Moglie, V. M. Primiani, and G. Gradoni, "Base-case model for measurement uncertainty in a reverberation chamber including frequency stirring," *IEEE Trans. Electromagn. Compat.*, vol. 60, no. 6, pp. 1695–1703, Dec. 2018.

[14] Gifuni, A., Bastianelli, L., Migliaccio, M., *et al.*: "On the estimated measurement uncertainty of the insertion loss in a reverberation chamber including frequency stirring," *IEEE Trans. Electromagn. Compat.*, vol. 61, no. 5, pp. 1414-1422, Oct. 2019.

[15] *Electromagnetic Compatibility (EMC)—Part 4–21: Testing and Measurement Techniques – Reverberation Chamber Test Methods*, IEC 61000-421, IEC Standard, Ed 2.0, Jan. 2011.

[16] *User Equipment (UE) / Mobile Station (MS) Over The Air (OTA) antenna performance; Conformance testing*, 3GPP Std. TS 34.114, Rev. V12.2.0, Sep. 2016.

[17] *Test Plan for Wireless Large-Form-Factor Device Over-the-Air Performance*, CTIA, ver. 1.2.1, Feb. 2019.

[18] *Radio Frequency (RF) conformance testing background for radiated Base Station (BS) requirements*, 3GPP Std. TR 37.941, Rev. V16.0.1, Jun. 2020.

[19] R. J. Pirkl, K. A. Remley, and C. S. L. Patane, "Reverberation chamber measurement correlation," *IEEE Trans. Electromagn. Compat.*, vol. 54, no. 3, pp. 533–545, Jun. 2012.

[20] K. A Remley, R. J Pirkl, H. A Shah, and C.-M. Wang, "Uncertainty from choice of mode-stirring technique in reverberation-chamber measurements," *IEEE Trans. Electromagn. Compat.*, vol. 55, no. 6, pp. 1022– 1030, Dec. 2013.

[21] K. A. Remley, C.-M. J. Wang, D. F. Williams, J. J. aan den Toorn, and C. L. Holloway, "A significance test for reverberation-chamber measurement uncertainty in total radiated power of wireless devices," *IEEE Trans. Electromagn. Compat.*, vol. 58, no. 1, pp. 207–219, Feb. 2016.

[22] D. Senic *et al*., "Estimating and reducing uncertainty in reverberation chamber characterization at millimeter-wave frequencies," *IEEE Trans. Antennas Propag.*, vol. 64, no. 7, pp. 3130–3140, Jul. 2016.

[23] K. A. Remley *et al*., "Configuring and verifying reverberation chambers for testing cellular wireless devices," *IEEE Trans. Electromagn. Compat.*, vol. 58, no. 3, pp. 661–672, Jun. 2016.

[24] K. A. Remley *et al*., "Estimating and correcting the device-under-test transfer function in loaded reverberation chambers for over-the-air-tests," *IEEE Trans. Electromagn. Compat.*, vol. 59, no. 6, pp. 1724–1734, Dec. 2017.

[25] M. G. Becker, M. Frey, S. Streett, K. A. Remley, R. D. Horansky and D. Senic, "Correlation-based uncertainty in loaded reverberation chambers," *IEEE Trans. Antennas Propag.*, vol. 66, no. 10, pp. 5453-5463, Oct. 2018.

[26] X. Chen, "Measurement uncertainty of RC and its reduction techniques for OTA tests: a review," *IET Microw. Antennas Propag.*, vol. 13, no. 15, pp. 2598-2604, Dec. 2019.

[27] W. Xue, F. Li, X. Chen and T. Svensson, "Statistical analysis of measurement uncertainty in total radiated power of wireless devices in reverberation chamber," *IET Microw. Antennas Propag.*, vol. 14, no. 11, pp. 1241-1245, Sep. 2020.

[28] C. L. Holloway, D. A. Hill, J.M. Ladbury, P. F. Wilson, G. Koepke, and J. Coder, "On the use of reverberation chamber to simulate a Rician radio environment for the testing of wireless devices," *IEEE Trans. Antennas Propag.*, vol. 54, no. 11, pp. 3167–3177, Nov. 2006.

[29] C. Lemoine, E. Amador, and P. Besnier, "On the *K*-factor estimation for Rician channel simulated in reverberation chamber," *IEEE Trans. Antennas Propag.*, vol. 59, no. 3, pp. 1003–1012, Mar. 2011.

[30] C. M. J. Wang *et al*., "Parameter estimation and uncertainty evaluation in a low Rician *K*-factor reverberation-chamber environment," *IEEE Trans. Electromagn. Compat.*, vol. 56, no. 5, pp. 1002–1012, Oct. 2014.

[31] A. Gifuni and S. Perna, "*K*-Factor Estimate: Statistical Behavior of Its Distribution for Large Sample Sizes," *IEEE Trans. Electromagn. Compat.*, vol. 61, no. 6, pp. 1896-1899, Dec. 2019.

[32] X. Chen, P.-S. Kildal, and J. Carlsson, "Investigation of the distribution of the random LOS component in a reverberation chamber," *Proc. Eur. Conf. Antennas Propag. (EuCAP)*, Gothenburg, Sweden, pp. 8-12, Apr. 2013.

[33] X. Chen, P. S. Kildal, and S. H. Lai, "Estimation of average Rician *K*-factor and average mode bandwidth in loaded reverberation chamber," *IEEE Antennas Wireless Propag. Lett.*, vol. 10, pp. 1437–1440, 2011.

[34] N. L. Johnson and S. Kotz, *Continuous Univariate Distributions, Volume 2 (2nd Edition)*. New York, NY, USA: Wiley, 1995.

[35] A. Papoulis, *Probability, Random Variables, and Stochastic Processes*. New York: McGraw-Hill, 1965.

[36] Q. Xu, Y. Huang, S. Yuan, L. Xing, and Z. Tian, "Two alternative methods to measure the radiated emission in a reverberation chamber," *International Journal of Antennas and Propagation*, Article ID 5291072, pp. 1-7, 2016.

[37] J. C. West and C. F. Bunting, "Effects of frequency stirring on reverberation chamber testing: An analysis as a radiation problem," *IEEE Trans. Electromagn. Compat*., vol. 61, no. 4, pp. 1345–1352, Aug. 2019.

[38] B. N. Taylor and C. E. Kuyatt, "Guidelines for Evaluating and Expressing the Uncertainty of NIST Measurement Results," NIST Tech. Note 1297, Sep. 1994.

[39] *NR; User Equipment (UE) radio transmission and reception; Part 1: Range 1 Standalone*, 3GPP Std. TS 38.101-1, Rev. V16.4.0, Jun. 2020.

Chapter 5 Investigation of the Enhanced Backscattering Effect and Modeling of the Highest Usable Frequency

In Chapter 3 and Chapter 4, the stirrer performance and the statistical anisotropy of an RC were characterized. Another factor that potentially affects the RC's statistical property is the system SNR, which becomes more prominent at a higher frequency of operation. In this chapter, the enhanced backscattering effect is first investigated in an RC in different domains. Based on the experimental evidence, a HUF model for the RC-based measurement system is derived. Essentially, this HUF describes the system SNR, and it provides a fast characterization of the RC in terms of the frequency of operation and the output power of the source.

5.1 Introduction

As already demonstrated in previous chapters, the statistical performance of an RC is determined by the stirrer efficiency [1] – [3], the number of modes excited [4], and the statistical anisotropy [5], [6]. According to the cavity mode theory [4], to ensure good statistical uniformity and isotropy, the stirrers should be able to interact with a sufficient number of modes. Since the number of modes excited inside an RC monotonically increases with the frequency, an RC should only have a LUF in theory. Therefore, the RC is usually designed to be large to extend its LUF and increase its working volume. The nominal wide operating frequency range and spacious working volume of the RC make it an increasingly popular candidate facility for various OTA tests in the wireless industry [5] – [10], and the relevant measurement technologies are continuously

evolving with new testing requirements [11] – [16].

For a practical RC-based measurement system, the measured signal actually consists of two parts: the desired signal and the undesired noise. The statistical property of the measured signal should be the superposition of these two random variables. Conventionally, the noise is assumed to be negligible, which is reasonable at the widely used ultra-high frequency (UHF) band. A consensus has recently been reached for the emerging 5G cellular networks that the frequency spectra beyond the sub-6 bands, especially the mm-wave band, will be extensively utilized [17]. While drastically improving the carrier bandwidth, spectral efficiency, and data capacity, it has the drawback of much more severe signal attenuation [18]. As the frequency of operation increases, the signal strength at the receiving end continues to drop. Eventually, it can become even comparable to the system noise. In this case, the statistical property of the actual measured signal could be changed entirely, making the RC virtually unusable.

The enhanced backscattering effect is recognized as a general natural phenomenon of various wave types despite their specific physical characteristics [19]. Inside an RC, this effect can be well described by the enhanced backscatter coefficient (e_b), which should be equal to 2 in value for the RC to operate in the ideal condition [20]. So far, this feature has been widely applied in various EM measurements [21] – [25]. Furthermore, due to its simplicity of implementation, e_b has been widely accepted as an effective parameter to characterize the RC's statistical performance [26], [27].

In Section 5.2, a thorough investigation of e_b in terms of the frequency, power, and spatial domains is first conducted to characterize the RC. Experimental evidence indicates that as frequency increases, e_b will drop drastically from its theoretical value, which implies a frequency upper limit, above which the RC cannot work at its optimum condition anymore. We name this frequency the highest usable frequency, or HUF for short. It is also shown that the HUF is actually dependent upon the power level of the transmitting signal (more precisely, the SNR of the RC-based measurement system).

In order to analytically quantify the HUF of an RC, an explicit theoretical model that includes all influencing parameters is desired. The HUF model should not only provide a fast characterization of the RC-based measurement system at a certain operating frequency and output power level, but also shed light on how to optimize the system

setup for improved HUF.

In Section 5.3, we derive this HUF model based on the statistical distributions of the average power of the desired received signal and the corresponding average noise power [28], [29]. In essence, the HUF should be a function of the chamber volume, chamber decay constant, cable losses, the power level of the transmitting signal, sensitivity of the equipment, *etc*. Then, a detailed analysis and discussion of each term in the HUF expression are given. The physical meaning of the proposed HUF model is also explained, and an iterative algorithm is provided for efficiently calculating the theoretical HUF. Finally, experimental validation of the HUF model is performed for different transmitting power levels.

5.2 Investigation of the Enhanced Backscattering Effect in Different Domains

5.2.1 The Enhanced Backscatter Coefficient

According to [21], e_b is formulated as the geometric mean of the enhanced backscatter coefficients at the transmitting antenna (e_{b1}) and the receiving antenna (e_{b2}):

$$e_b = \sqrt{e_{b1}e_{b2}} = \frac{\sqrt{\left\langle \left|S_{11,s}\right|^2 \right\rangle \left\langle \left|S_{22,s}\right|^2 \right\rangle}}{\left\langle \left|S_{21,s}\right|^2 \right\rangle} \tag{5.1}$$

$$e_{b1} = \frac{\left\langle \left|S_{11,s}\right|^2 \right\rangle}{\left\langle \left|S_{21,s}\right|^2 \right\rangle} \cdot \frac{\eta_2\left(1-\left|\left\langle S_{22}\right\rangle\right|^2\right)}{\eta_1\left(1-\left|\left\langle S_{11}\right\rangle\right|^2\right)} \tag{5.2}$$

$$e_{b2} = \frac{\left\langle \left|S_{22,s}\right|^2 \right\rangle}{\left\langle \left|S_{12,s}\right|^2 \right\rangle} \cdot \frac{\eta_1\left(1-\left|\left\langle S_{11}\right\rangle\right|^2\right)}{\eta_2\left(1-\left|\left\langle S_{22}\right\rangle\right|^2\right)} \tag{5.3}$$

where η_1 and η_2 are the radiation efficiencies of the transmitting antenna and the

receiving antenna, respectively. $\langle\ \rangle$ is the ensemble average operator which is performed frequency-wise over all stirrer positions. $S_{*,s}$ is the stirred part of the corresponding transmission or reflection coefficients derived by the following vector average subtraction equation [5]:

$$S_{*,s} = S_* - \langle S_* \rangle \tag{5.4}$$

It is easy to see that by this definition, the influence caused by radiation efficiencies of the two antennas can be effectively removed in the calculation of e_b [30].

It was found in [20] that for a well-stirred RC, the average amount of stirred power that is reflected back to the transmitting antenna should be equal to twice that coupled to the receiving antenna. Based on this, e_b has been recognized as an important parameter to characterize the performance of an RC. Nonetheless, due to the finite number of independent samples, the e_b value directly calculated by using equation (5.1) is actually biased. According to [30], an unbiased estimator of e_b was derived on the basis of the analytical expression of its statistical distribution:

$$e_{b,unbias} \approx e_{b,bias} \frac{N-1}{N} \tag{5.5}$$

where N is the number of independent samples. As can be seen from (5.5), e_b derived from (5.1) tends to overestimate the true value, especially when N is small. Therefore, for the measurement in which a very limited number of independent samples can be provided, it is necessary to use (5.5) for correction.

5.2.2 Experimental Setup

The RC at the University of Liverpool, which has a size of $3.60\,m$ (w) × $5.80\,m$ (l) × $4.00\,m$ (h), is used for enhanced backscattering effect investigation [31]. In Figure 5.1 (a), an example measurement setup is shown. Two mechanical stirrers are installed inside the RC: the horizontal one (with a rotating radius of $0.50\,m$) is mounted near the ceiling, while the vertical one (with a rotating radius of $0.70\,m$) is placed close to a corner. The paddles of the two stirrers are intentionally designed to be of asymmetric shape to provide as many uncorrelated samples as possible per revolution. When

performing mechanical stirring, the two stirrers rotate simultaneously about fixed axes (denoted by the yellow bars in Figure 5.1 (b)) in a stepwise manner.

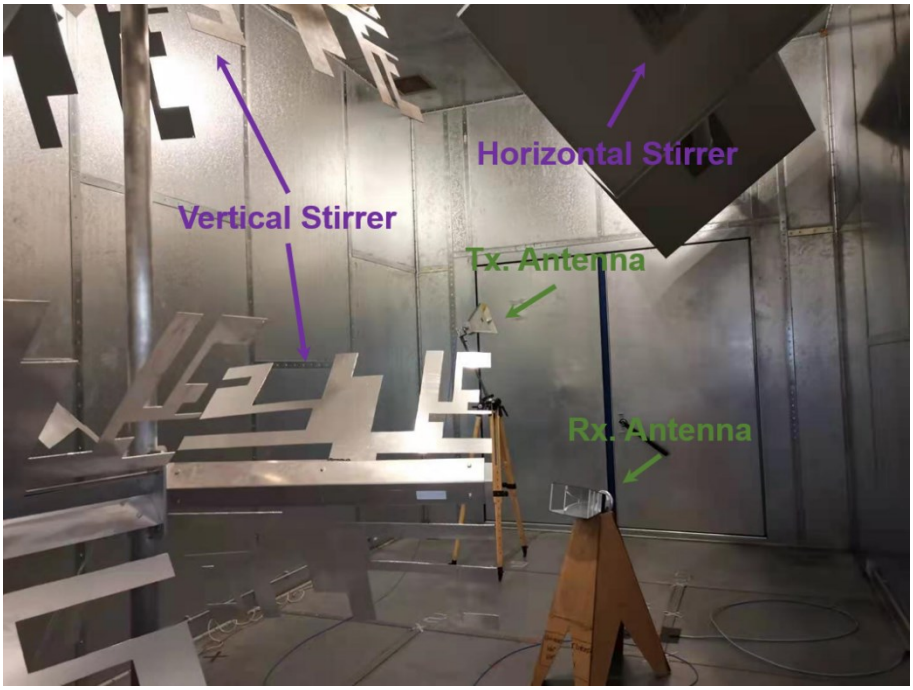

(a)

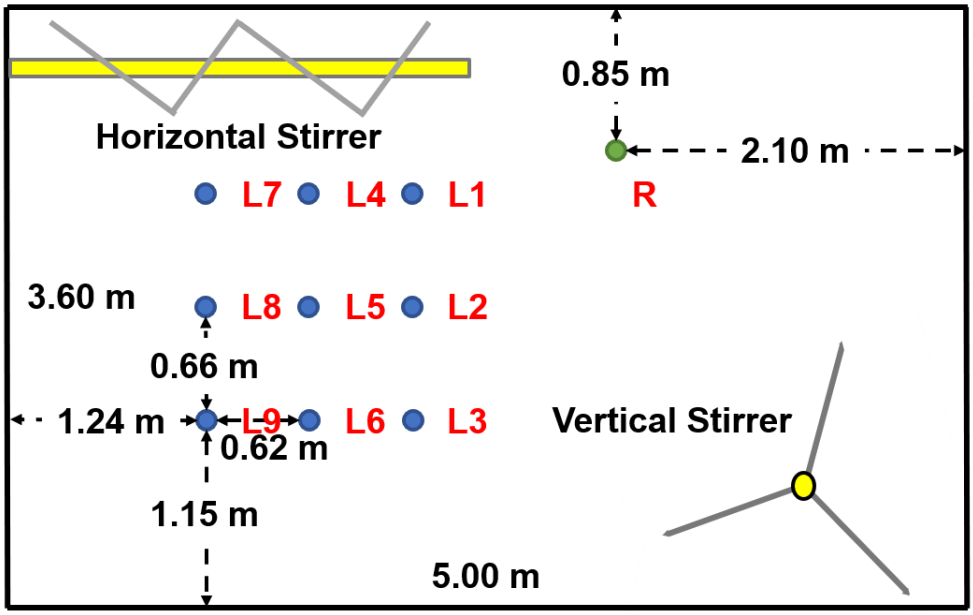

(b)

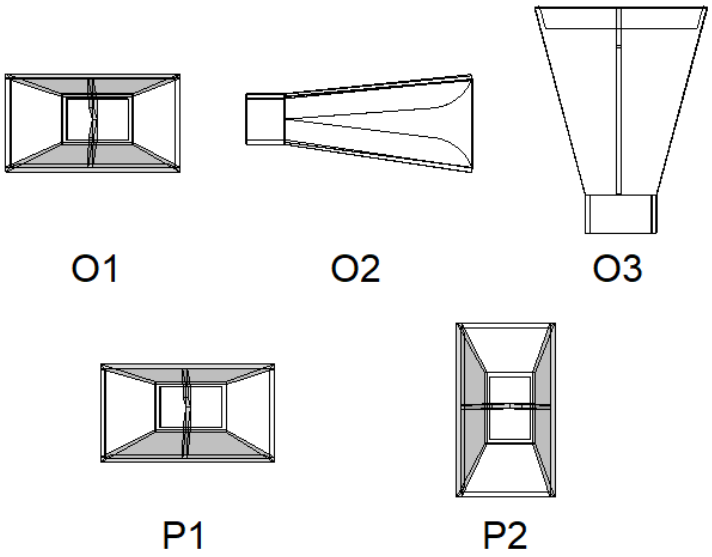

(c)

Figure 5.1: Typical experimental setup: (a) Measurement scenario. (b) Schematic diagram showing locations of the transmitting antenna and the receiving antenna. (c) Orientations and polarizations of the transmitting antenna.

Two double-rigid waveguide horn antennas are used as the transmitting antenna (Rohde & Schwarz HF 906) and receiving antenna (SATIMO SH 2000), respectively. Throughout the whole measurement procedure, the transmitting antenna (with 1.40 m in height) is moved successively to three different locations (L1, L5, and L9 in Figure 5.1 (b)), three orthogonal orientations (O1, O2, and O3 in Figure 5.1 (c)), and two crossed polarizations (P1 and P2 Figure 5.1 (c)). In contrast, the receiving antenna is fixed at location "R" as marked in Figure 5.1 (b) with unchanged orientation (towards the vertical stirrer), polarization (vertical polarization), and height (0.77 m).

One 3.5 mm cable is used to connect the transmitting antenna and port 1 of the VNA, while one N-type cable was used to link the receiving antenna and port 2 of the VNA. In order to compensate for the cable loss, standard 2-port calibration should be performed. The same calibration result is maintained at the same frequency band, while at a different frequency band, a new calibration is required. The IF bandwidth is chosen to be 10 kHz as a compromise between reasonable noise level and measurement time. During each set of experiments, the stirrers are first rotated by 6 degrees. After the paddles are stabilized, the VNA conducts a complete sweep in the frequency domain,

and 1001 points are collected by the computer correspondingly. Then this procedure is repeated 60 times until the stirrers completed a whole circle. This guarantees that each experiment set has the identical 60 stirrer positions, or equivalently, boundary conditions. The measurement time for each set of experiments is approximately 18 minutes.

5.2.3 Frequency Domain Results

As for the frequency domain investigation, S-parameters from 2.8 GHz to 12.2 GHz are measured and recorded for e_b calculation. The transmitting antenna is fixed at location 9 (L9), orientation 1 (O1), and polarization 1 (P1), as indicated in Figure 5.1 (b) and Figure 5.1 (c). In order to obtain finer frequency granularity, the entire frequency range is further divided into nine narrower subbands (see the horizontal bars in Figure 5.2), each with 1.4 GHz bandwidth. Note that there is a 400 MHz overlap between consecutive subbands for smoothing. Therefore, nine sets of experiments with independent calibration operations should be performed. Subsequently, the whole process is repeated with four different VNA output power settings (0 dBm, -3 dBm, -6 dBm, and -27 dBm) for comparison.

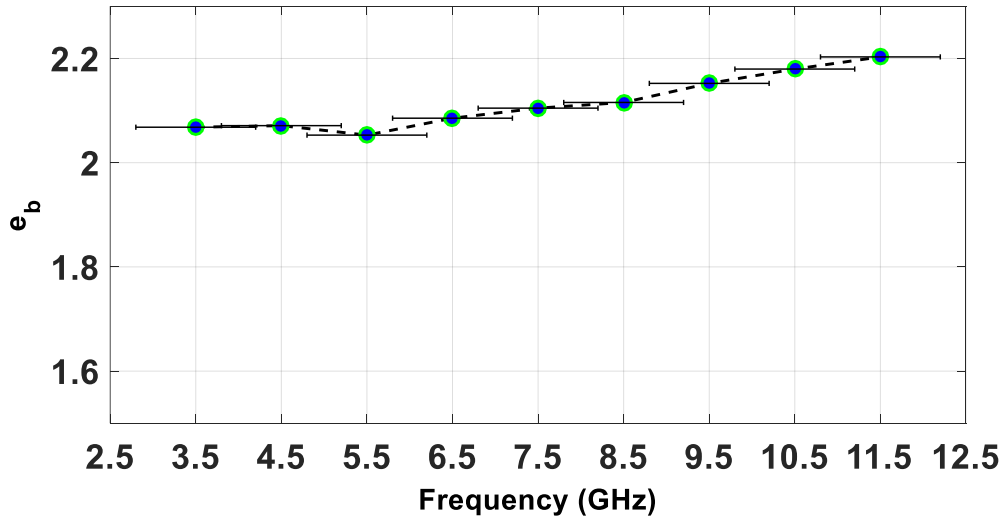

(a)

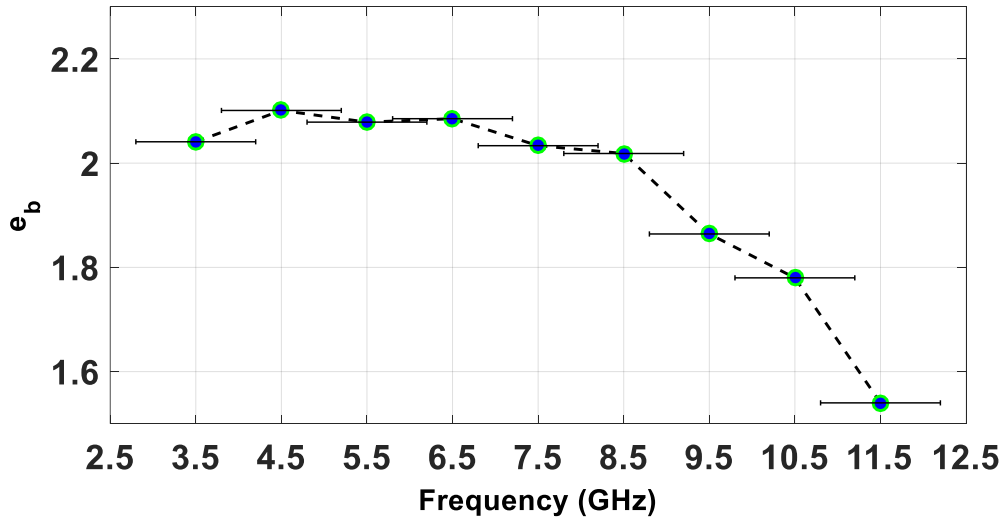

(b)

Figure 5.2: Enhanced backscattering effect investigation in terms of the frequency domain: (a) with -3 dBm VNA output power. (b) with -27 dBm VNA output power.

The measurement results are illustrated in Figure 5.2. Values of e_b are the mean values of each subband, respectively (denoted as $\overline{e}_b$). According to Figure 5.2 (a), when the output power of the VNA is set to -3 dBm, $\overline{e}_b$ remains relatively stable across the entire 2.8 GHz - 12.2 GHz frequency range, despite a slight upward trend (from about 2.10 to 2.20) with fluctuations. Adjusting the VNA power to 0 dBm and -6 dBm also gives similar results as Figure 5.2 (a). In contrast, when the VNA output power is reduced to -27 dBm (see Figure 5.2 (b)), an abnormal pattern can be clearly observed from somewhere between 8.5 GHz and 9.5 GHz onwards – the value of e_b begins to drop rapidly below its theoretical value 2. At around 11.5 GHz, $\overline{e}_b$ is already below 1.6. This implies that the RC-based measurement system has already been malfunctioning under the corresponding frequency band. A reasonable assumption can also be made here that there exists a HUF for the RC given a specific excitation power, only below which the RC can work at its ideal condition.

5.2.4 Power Domain Results

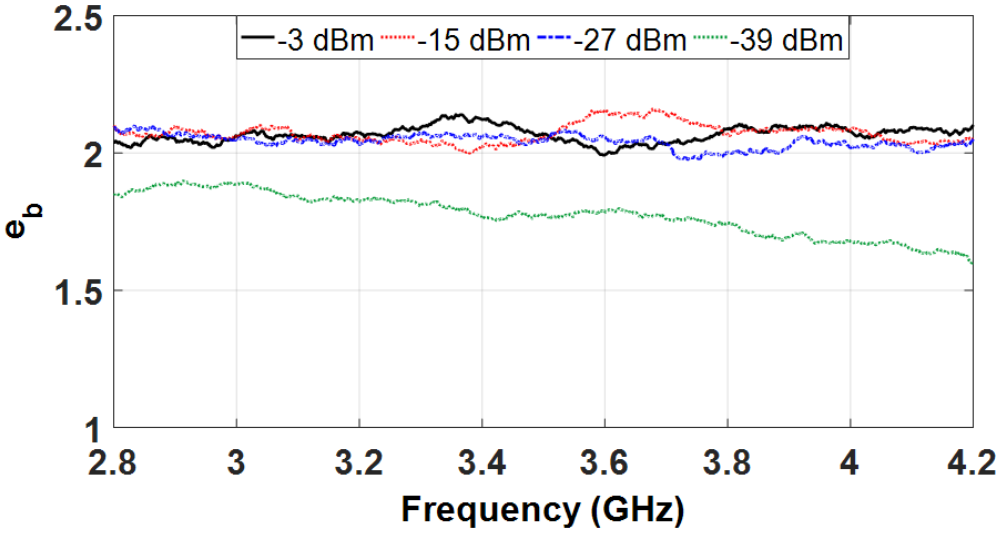

(a)

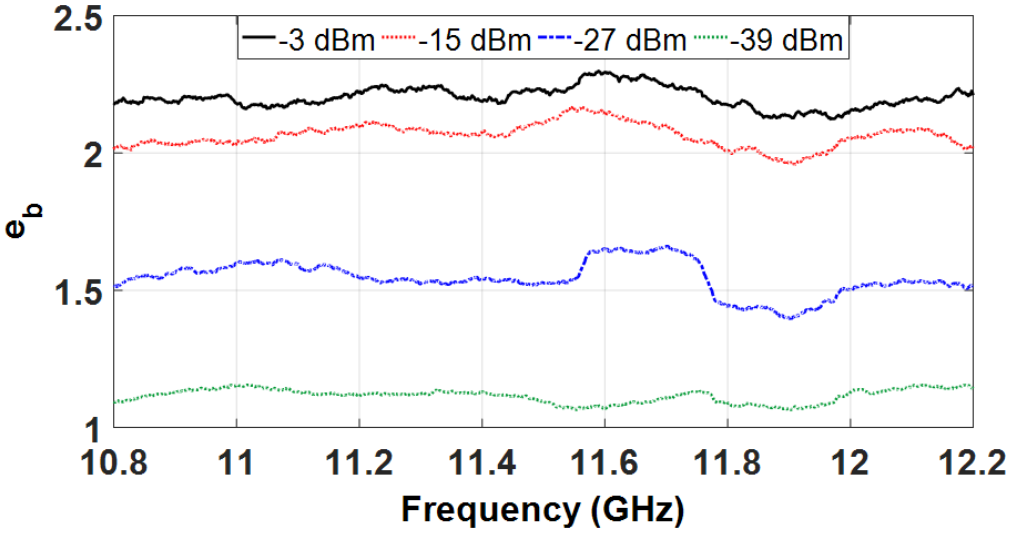

(b)

Figure 5.3: Enhanced backscattering effect investigation in terms of the power domain: (a) in2.8 GHz – 4.2 GHz band. (b) in 10.8 GHz – 12.2 GHz band.

Based on the investigation results in Section 5.2.3, e_b is further investigated in terms of the power domain. The output power of the VNA is successively changed to four different levels while maintaining the default transmitting antenna settings (the same as

that in Section 5.2.3). In addition, two frequency bands (2.8 GHz – 4.2 GHz and 10.8 GHz – 12.2 GHz) are used for comparison. The e_b curves are corrected using equation (5.5) and then smoothed with a 100 MHz window for ease of illustration. According to Table 5-I, at the 2.8 GHz – 4.2 GHz band, $\overline{e}_b$ does not change much when the excitation power is reduced from -3 dBm to -27 dBm. However, when it is further reduced to -39 dBm, $\overline{e}_b$ already plunges to 1.78 (also refer to Figure 5.3 (a)). As for the 10.8 GHz – 12.2 GHz band, $\overline{e}_b$ continuously drops and asymptotically approaches 1 as the output power decreases from -3 dBm to -39 dBm (see Figure 5.3 (b)).

Table 5-I: Average value of the enhanced backscatter coefficient at the corresponding frequency bands for different power levels

	Different Power Levels			
	2.8 GHz – 4.2 GHz			
Metrics	-3 dBm	-15 dBm	-27 dBm	-39 dBm
$\overline{e}_b$	2.07	2.07	2.04	1.78
	10.8 GHz – 12.2 GHz			
Metrics	-3 dBm	-15 dBm	-27 dBm	-39 dBm
$\overline{e}_b$	2.20	2.06	1.54	1.11

To find the possible reason for this pattern of $\overline{e}_b$ shown in the power domain, the corresponding average power of the stirred parts of transmission coefficients are also checked and illustrated in Figure 5.4. Ideally, if all the other experimental conditions are identical, $\left\langle \left| S_{21,s} \right|^2 \right\rangle$ should be the same irrespective of the change of the excitation power (since it is a normalized value). However, in practice, the measurement system has limited sensitivity. If the received signal is so weak that it can be disturbed by the system noise, an increase of $\left\langle \left| S_{21,s} \right|^2 \right\rangle$ can be observed. In Figure 5.4 (a), the increase is detected at -39 dBm output power level, whereas in Figure 5.4 (b), the increase can be vaguely spotted at -15 dBm (but not as apparent as that in Figure 5.3 (b)). Thus, there exists a lower threshold for the excitation power at a given operating frequency, below which the signal at the receiving end will exceed the system noise floor. This is consistent with the findings in Section 5.2.3.

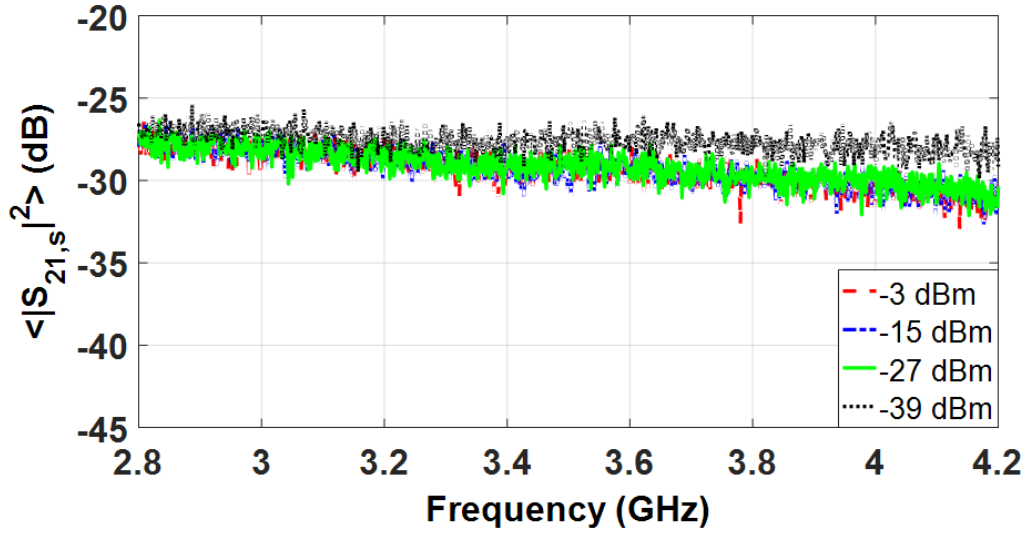

(a)

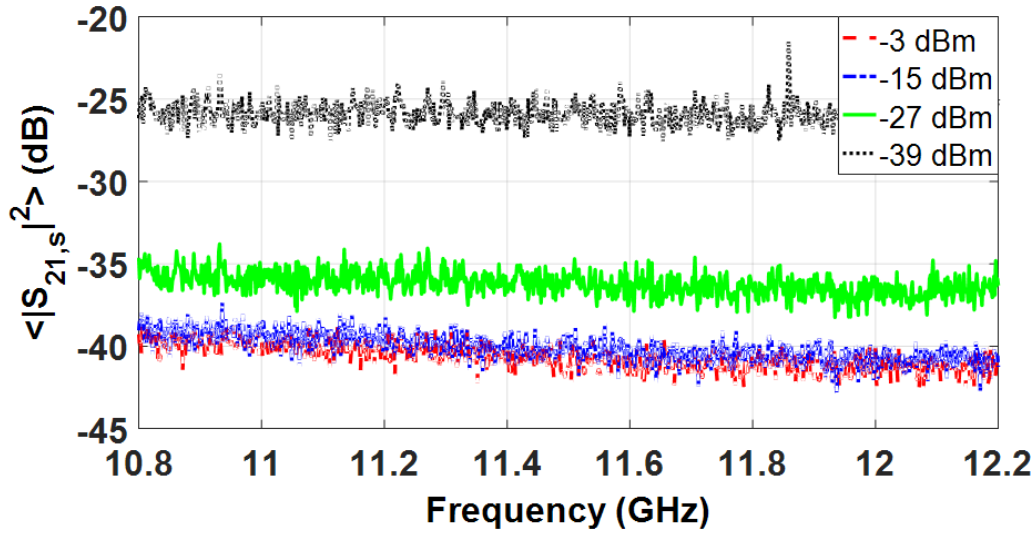

(b)

Figure 5.4: The measured stirred parts of transmission coefficients for different power levels: (a) with 2.8 GHz – 4.2 GHz band. (b) with 10.8 GHz – 12.2 GHz band.

5.2.5 Spatial Domain Results

Three sets of spatial domain experiments are conducted in this section to investigate whether and to what extent the measured values of e_b can be affected by the location, orientation, and polarization of the transmitting/receiving antenna while keeping all the

other experimental conditions unchanged. Besides, these experiments are repeated with two different frequency bands (lower band: 2.8 GHz – 4.2 GHz, higher band: 10.8 GHz – 12.2 GHz). The output power of VNA is set to -3 dBm to make sure the recorded S parameters are well above the noise floor. The following equation is used to quantify the relative discrepancy of e_b:

$$D_x = \frac{\frac{1}{C_A^2}\sum_i \sum_{j>i} \left| \bar{e}_{b,i} - \bar{e}_{b,j} \right|}{e_{b,th}} \times 100\% \tag{5.6}$$

where the subscript x can be L, O or P. C_A^2 denotes the combination operation, and A is the cardinality of the set that i and j belong to. For instance, if x=L, then $A = 3$ since $j > i \in \{1,5,9\}$.

Firstly, the transmitting antenna is moved to three different locations (L1, L5, and L9 in Figure 5.1 (b)) with fixed orientation and polarization (O1 and P1 in Figure 5.1 (c)). Then the transmitting antenna is altered to three mutually orthogonal orientations (O1, O2, and O3) with a fixed location (L9) and polarization (P1). Finally, two crossed polarizations (P1 and P2) of the transmitting antenna are examined while other settings are maintained. Measurement results are illustrated in Figure 5.5. Without loss of generality, only the results at the lower band are shown.

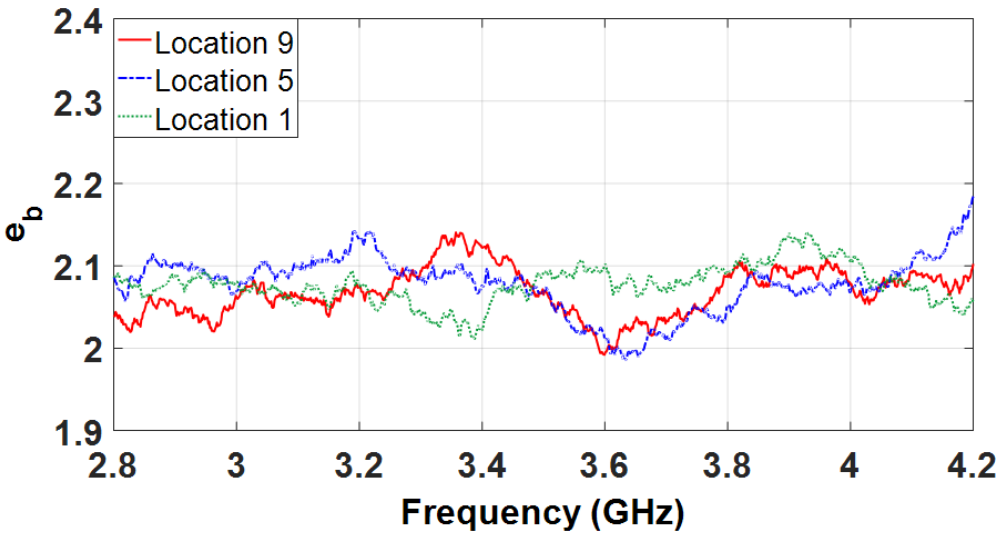

(a)

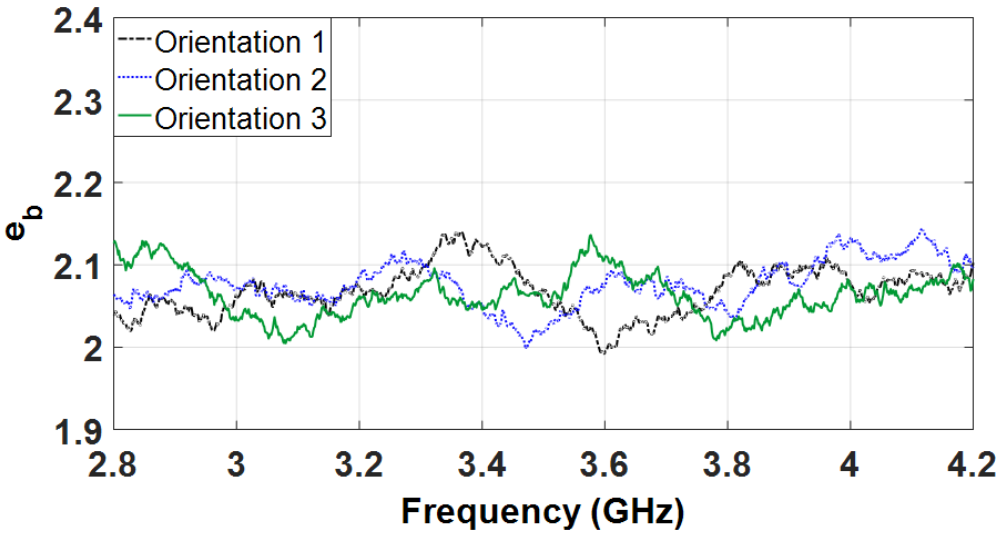

(b)

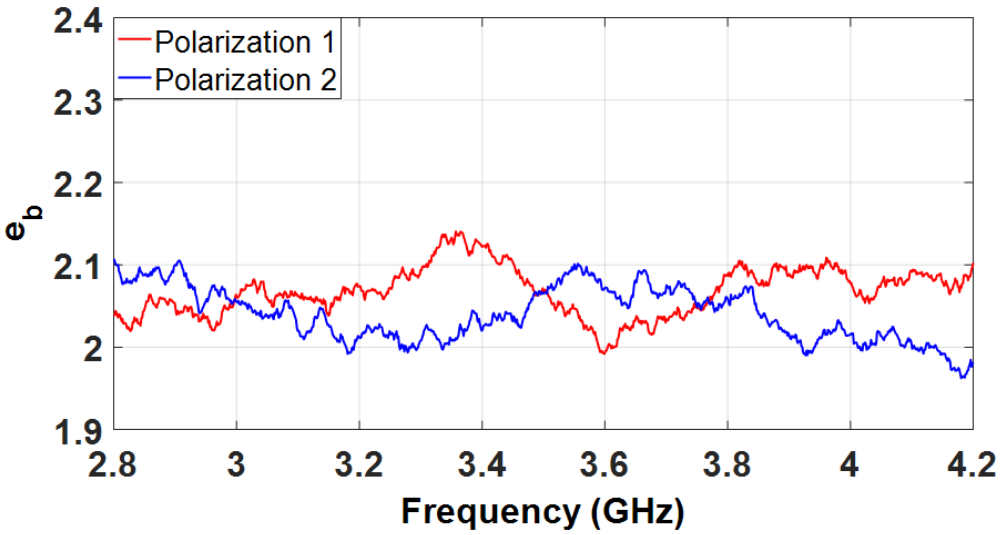

(c)

Figure 5.5: Enhanced backscattering effect investigation in terms of the spatial domain: (a) different transmitting antenna locations. (b) different transmitting antenna orientations. (c) different transmitting antenna polarizations.

The e_b curves are corrected using equation (5.5) and then smoothed with a 100 MHz window. Detailed statistics are listed in Table 5-II, Table 5-III, and Table 5-IV, respectively. It can be seen that for both frequency bands, notwithstanding the change of the antenna location, orientation, and polarization, values of $\overline{e}_b$ remain relatively stable. This proves that the investigation findings in Section 5.2.3 and Section 5.2.4 are

robust against the spatial domain.

Table 5-II: Statistics of the enhanced backscatter coefficient at the corresponding frequency bands for different transmitting antenna locations

Different Locations						
	2.8 GHz – 4.2 GHz			10.8 GHz – 12.2 GHz		
Metrics	L1	L5	L9	L1	L5	L9
$\bar{e}_b$	2.08	2.08	2.07	2.21	2.21	2.20
D_L	0.32%			0.25%		

Table 5-III: Statistics of the enhanced backscatter coefficient at the corresponding frequency bands for different transmitting antenna orientations

Different Orientations						
	2.8 GHz – 4.2 GHz			10.8 GHz – 12.2 GHz		
Metrics	O1	O2	O3	O1	O2	O3
$\bar{e}_b$	2.07	2.08	2.06	2.20	2.25	2.18
D_O	0.42%			2.37%		

Table 5-IV: Statistics of the enhanced backscatter coefficient at the corresponding frequency bands for different transmitting antenna polarizations

Different Polarizations				
	2.8 GHz – 4.2 GHz		10.8 GHz – 12.2 GHz	
Metrics	P1	P2	P1	P2
$\bar{e}_b$	2.07	2.04	2.20	2.15
D_P	1.42%		2.31%	

5.3 The HUF Model of an RC

In Section 5.2, extensive investigations of the enhanced backscattering effect have been conducted for RC performance characterization. Experimental evidence shows that there exists a HUF above which the performance degradation of the RC-based

measurement system can be observed. Moreover, the HUF is closely related to the power of the excitation source (more precisely, the system SNR), but is insusceptible to antenna location, orientation, and polarization. In this section, the deduction procedures for the HUF model will be elaborated based on statistical theories [4], [28], [29], [32].

5.3.1 Statistical Modeling of the Received Signal

Considering practical situations, the transmission coefficient measured by the VNA (denoted as R_{21}) actually consists of two parts, namely the desired signal S_{21} and the noise N_{21} [28]:

$$R_{21} = S_{21} + N_{21} \tag{5.7}$$

where the real and imaginary parts of N_{21} are *i.i.d* random variables following a Gaussian distribution with 0 mean and standard deviation σ_{noise}. *i.i.d* stands for "independent and identically distributed". If multiple random variables are considered as *i.i.d*, then they are mutually independent and have the same probability distribution with identical mean and variance values. Note that N_{21} here is assumed to be after perfect calibration operation (cable losses are compensated), so it is not additive wight Gaussian noise (AWGN) in terms of the frequency domain. In other words, σ_{noise} is frequency-dependent (since cable losses and other losses are frequency-dependent), and it is hard to be directly estimated. Procedures for estimating the parameters of corresponding noise distributions will be detailed in Section 5.3.2.

The estimator of the unstirred part of the received signal is:

$$\langle R_{21} \rangle_N = \langle S_{21} \rangle_N + \langle N_{21} \rangle_N \tag{5.8}$$

where N without a subscript is the number of independent samples. It can be derived that $\langle N_{21} \rangle_N$ is complex Normal distributed with 0 mean and standard deviation $\frac{\sigma_{noise}}{\sqrt{N}}$ [32].

Then, by taking the vector average subtraction [5] and combining (5.7) and (5.8), the estimator of the stirred part of the received signal is:

$$R_{21,s} = R_{21} - \langle R_{21} \rangle_N = S_{21} - \langle S_{21} \rangle_N + N_{21} - \langle N_{21} \rangle_N = S_{21,s} + V \tag{5.9}$$

here we define $V=N_{21}-\langle N_{21}\rangle_N=V_1-V_2$ for notational convenience, with $V_1=\frac{N-1}{N}N_{21}$ and $V_2=\frac{N-1}{N}\langle N_{21}\rangle_{N-1}$. By doing this, it is ensured that V_1 and V_2 are two independent random variables (see Appendix I for detailed statistics of V_1 and V_2). $S_{21,s}=S_{21,s}-\langle S_{21,s}\rangle_N$ is the stirred part of the desired signal, whose two quadrature components follow *i.i.d* Gaussian distribution with 0 mean and standard deviation $\sqrt{\frac{G_{ref}}{2}}$, with G_{ref} the transfer function of the RC which is defined as [4], [31]:

$$G_{ref}=\frac{\lambda^3}{16\pi^2 V}Q \tag{5.10}$$

where Q is the quality factor, λ is the wavelength, and V is the volume of the RC. Then the power of the actual measured stirred part is:

$$\left|R_{21,s}\right|^2=\left(S_{21,s}+V\right)\left(S_{21,s}^*+V^*\right)=\left|S_{21,s}\right|^2+\left|V\right|^2+S_{21,s}V^*+S_{21,s}^*V \tag{5.11}$$

where the superscript $*$ denotes the complex conjugation operation. The desired stirred power $\left|S_{21,s}\right|^2$ follows an Exponential distribution with mean G_{ref} and standard deviation G_{ref} [32]. Similarly, $|V|^2$ is also exponentially distributed with both mean and standard deviation $2\sigma^2=2\frac{N-1}{N}\sigma_{\text{noise}}^2$ (see Appendix I for detailed statistics of V) [32].

Taking the ensemble average on both sides of equation (5.11) gives:

$$\left\langle\left|R_{21,s}\right|^2\right\rangle_N=\left\langle\left|S_{21,s}\right|^2\right\rangle_N+\left\langle\left|V\right|^2\right\rangle_N+\left\langle S_{21,s}V^*\right\rangle_N+\left\langle S_{21,s}^*V\right\rangle_N \tag{5.12}$$

Since $S_{21,s}$ and V are independent, if N is large, we have $\langle S_{21,s}V^*\rangle_N+\langle S_{21,s}^*V\rangle_N=0$ (see Appendix II). Therefore, the following relationship can be derived:

$$\left\langle\left|R_{21,s}\right|^2\right\rangle_N=\left\langle\left|S_{21,s}\right|^2\right\rangle_N+\left\langle\left|V\right|^2\right\rangle_N \tag{5.13}$$

Let $x=\left\langle\left|S_{21,s}\right|^2\right\rangle_N$, then x follows a Gamma distribution with shape factor N and scale factor $\frac{G_{ref}}{N}$. The PDF and corresponding statistics of x are shown below [29]:

$$f(x)=\frac{N^N x^{N-1}\exp\left(-\frac{Nx}{G_{ref}}\right)}{G_{ref}^N\Gamma(N)},\mu_x=G_{ref},\sigma_x=\frac{G_{ref}}{\sqrt{N}} \tag{5.14}$$

where $\Gamma(*)$ is the gamma function, which is the analytical continuation of the factorial function to complex numbers.

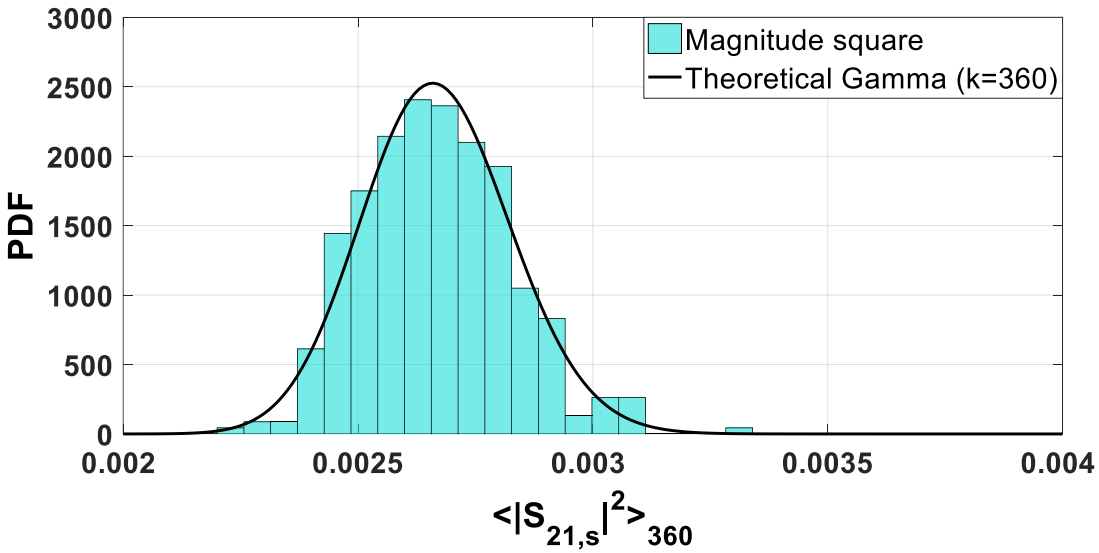

(a)

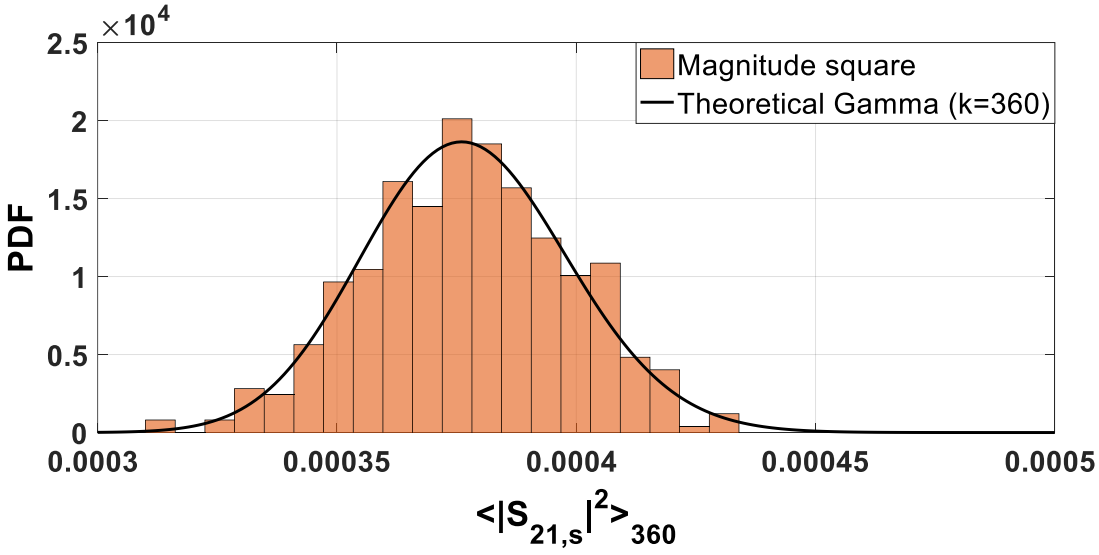

(b)

Figure 5.6: Distributions of the desired average stirred power *x* and the corresponding theoretical Gamma PDF at: (a) 2.45 GHz. (b) 5.8 GHz.

To validate the distribution in (5.14), samples of the average stirred power calculated over 360 mechanical stirrer positions are collected at two standard Wi-Fi bands (2.45 GHz and 5.8 GHz). The output power of the VNA is set to "High" to minimize the interference of the noise. Adjacent frequency points (within 100 MHz) are utilized for sample realization. The histograms of the measured samples and the theoretical Gamma PDFs directly calculated using (5.14) with shape factor N=360 are illustrated in Figure 5.6. It can be seen that, although the average power level at 5.8 GHz (around -34.2 dB) is much lower than that at 2.45 GHz (about -25.7 dB), the empirical distributions are in good agreement with the corresponding theoretical Gamma distributions in both cases.

Similarly, $y=\langle |V|^2 \rangle_N$ is also Gamma distributed with shape factor N, scale factor $\frac{2\sigma^2}{N}$, and the following statistics [29]:

$$f(y)=\frac{N^N y^{N-1}\exp\left(-\frac{Ny}{2\sigma^2}\right)}{2^N\sigma^{2N}\Gamma(N)},\mu_y=2\sigma^2,\sigma_y=\frac{2\sigma^2}{\sqrt{N}} \tag{5.15}$$

However, it is hard to directly verify the distribution in (5.15) since σ is frequency-dependent and is unknown up to this point. According to the CLT, it is reasonable to assume that both x and y follow Gaussian distributions when N is large [32]. The random variables x and y are the core for the establishment of the HUF model. Hence, all relevant parameters that determine the distributions in (5.14) and (5.15) should be known. In the next section, an explicit expression for σ will be given.

5.3.2 The Explicit Expression for σ

For a VNA, the noise floor level (which is a relative value in dB) is related to its output power level. If a reference output power level P_{ref} (usually, a high value is preferable so that it is well above the noise floor) is chosen with the corresponding average power level of the noise floor $2\sigma_{ref}^2$, and later the output power is changed to P_{out} with the average power level of the noise floor $2\sigma_{out}^2$, then the following equation holds:

$$C=P_{ref}\cdot 2\sigma_{ref}^2=P_{out}\cdot 2\sigma_{out}^2 \tag{5.16}$$

where C stands for "constant", which is fixed for a given VNA. In the following, an efficient approach for estimating σ is given:

I. Without cable calibration, set the output power level to P_{ref} (P_{ref}=-3 dBm in this case). Connect the ends of both cables with the load ports of the calibration kits. Then the transmission coefficient readings should solely reflect the noise. Denote this noise as $N_{21,ref}$ (different from N_{21} which is after perfect cable calibration). Then the real and imaginary parts of $N_{21,ref}$ are *i.i.d* AWGN with 0 mean and standard deviation σ_{ref}. Equivalently, the relative power $|N_{21,ref}|^2$ follows an Exponential distribution with mean and standard deviation $2\sigma_{ref}^2$.

II. An unbiased MLE is established to estimate σ_{ref}:

$$\hat{\sigma}_{ref} = \sqrt{\frac{\sum_{n=1}^{N}\left(\mathrm{Re}\left\{N_{21,ref}\right\}-\mathrm{Re}\left\{\bar{N}_{21,ref}\right\}\right)^2+\sum_{n=1}^{N}\left(\mathrm{Im}\left\{N_{21,ref}\right\}-\mathrm{Im}\left\{\bar{N}_{21,ref}\right\}\right)^2}{2(N-1)}} \tag{5.17}$$

where $\hat{}$ means "estimated", and $\bar{}$ stands for the sample mean with $\bar{N}_{21,ref}=\frac{1}{N}\sum_{n=1}^{N} N_{21,ref}$. Due to the property of AWGN, all frequency samples collected can be utilized, which drastically increases the number of samples. The samples used for σ_{ref} estimation and the corresponding result using (5.17) are shown in Figure 5.7 (a). The distribution of $|N_{21,ref}|^2$ is also examined by comparing its empirical CDF with the theoretical Exponential CDF with scale parameter $2\hat{\sigma}_{ref}^2$. As illustrated in Figure 5.7 (b), good agreement is achieved.

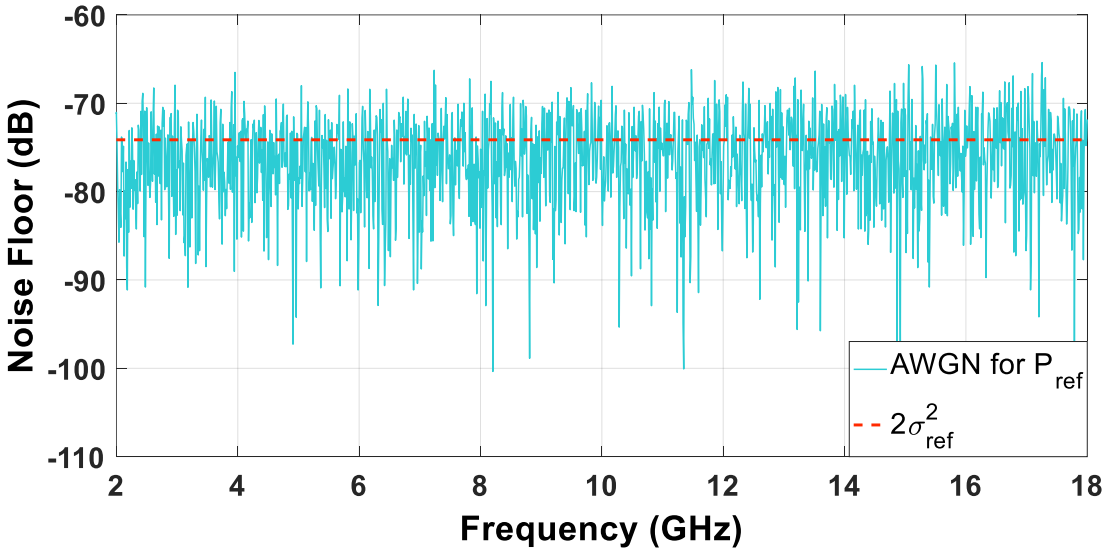

(a)

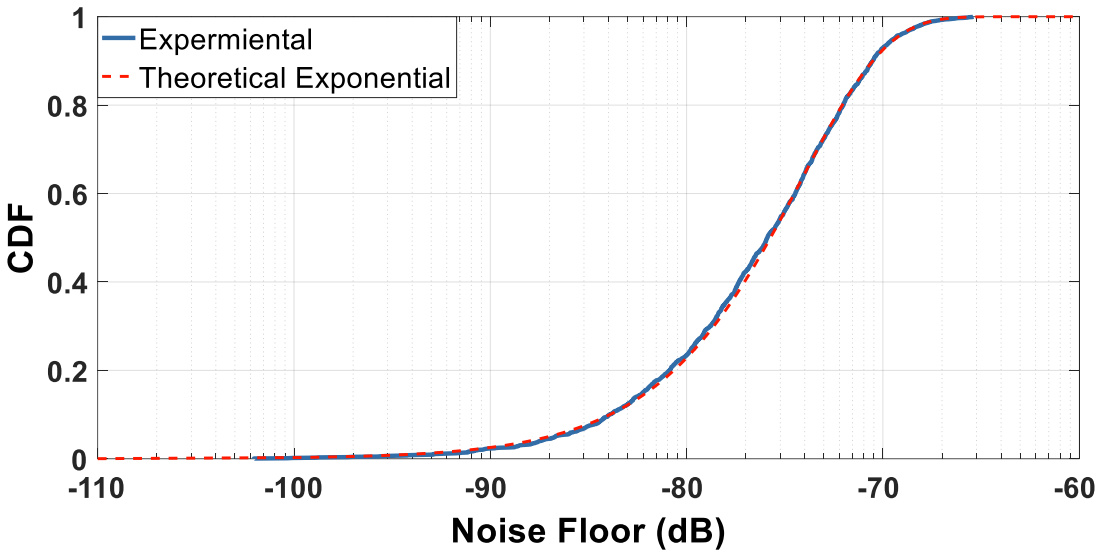

(b)

Figure 5.7: (a) Estimation result of σ_{ref} from AWGN samples in the range 2 GHz – 18 GHz using (5.17) with P_{ref}=-3 dBm. (b) Validation of the distribution of $|N_{21,ref}|^2$ by comparing the empirical and theoretical CDFs.

III. For an arbitrary output power level P_{out}, according to equation (5.16), we have

$$\sigma_{out} = \sqrt{\frac{P_{ref}}{P_{out}}}\sigma_{ref} \tag{5.18}$$

IV. Compensate the cable losses to obtain σ_{noise} for N_{21}:

$$\sigma_{noise} = \frac{\sigma_{out}}{\sqrt{L_1 L_2}} = \sqrt{\frac{P_{ref}}{L_1 L_2 P_{out}}}\sigma_{ref} \tag{5.19}$$

where L_1 and L_2 are the losses of the two cables which are frequency dependent. As a result, σ_{noise} should also be frequency-dependent.

V. Finally based on (5.19) and (5.A4) in Appendix I, σ can be expressed as:

$$\sigma = \sqrt{\frac{N-1}{N}}\sigma_{noise} = \sqrt{\frac{N-1}{N}\frac{P_{ref}}{L_1 L_2 P_{out}}}\sigma_{ref} \tag{5.20}$$

According to equation (5.20), N, P_{ref}, P_{out}, and σ_{ref} are available for arbitrary measurement system configurations.

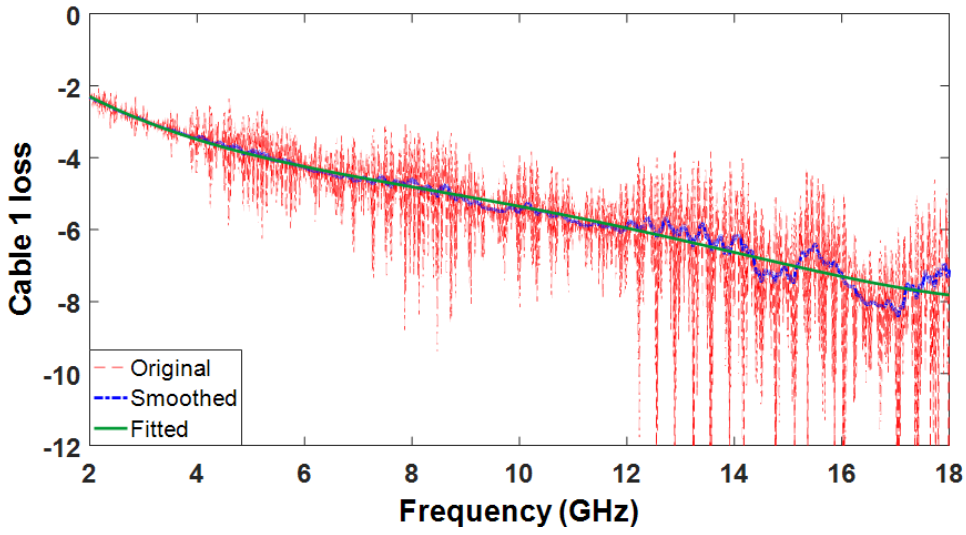

(a)

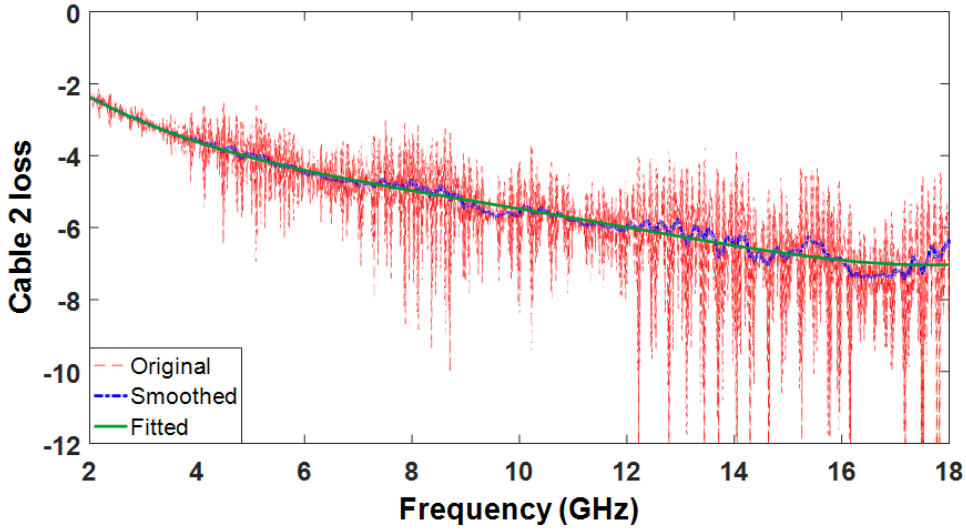

(b)

Figure 5.8: Cable loss modeling in the frequency range 2 GHz – 18 GHz: (a) Cable 1. (b) Cable 2.

L_1 and L_2 can be measured and estimated by adopting the following procedures:

1. Without calibration, set the output power level of the VNA to P_{ref}. Connect the ends of both cables with short ports.
2. Calculate the round-trip cable loss for each cable.
3. Calculate the corresponding single-trip cable loss by taking the square root of the

round-trip cable loss.

4. Smooth the cable loss curves with a 100 MHz window.
5. Perform polynomial curve fitting for the smoothed cable loss curves.

Cable loss modeling results for Cable 1 and Cable 2 are shown in Figure 5.8. It should be stressed that especially at higher frequency bands, the original measurement results for both cables suffer from large fluctuation (more than 5 dB). One possible reason is that the cables are very long (around 5 m), and they are bent multiple times which causes phase offset and unexpected resonance. If both cables are terminated with open ports, the results can be even worse. However, since L_1 and L_2 are modeled as deterministic values (rather than random variables) in this chapter, the degraded cable performance will only affect the system bias (but not the system variance). Future work can focus on how the cable performance will affect the HUF, and different cables can be used for comparison and validation.

5.3.3 HUF Model Establishment and Physical Explanation

In this section, an explicit model for the HUF of an RC-based measurement system will be established based on the statistical theory, and the physical meaning of the derived model will be explained. For RC-based measurement tasks, the main quantity of interest is the average stirred power measured at the receiving end as shown in equation (5.13), rather than the raw signal in (5.7). Begin with the following:

$$\mu_x - k\sigma_x > \mu_y + k\sigma_y \tag{5.21}$$

where k is a positive integer which determines the corresponding CI. The larger the value of k, the more stringent the boundary, and the lower the value of HUF (see Appendix III). A typical value is k=3. Then based on (5.10), (5.14), (5.15), and (5.20), the following can be obtained:

$$\mu_x - k\sigma_x = \left(1 - \frac{k}{\sqrt{N}}\right)\frac{\lambda^3}{16\pi^2 V}Q \tag{5.22}$$

$$\mu_y + k\sigma_y = 2\left(1+\frac{k}{\sqrt{N}}\right)\frac{N-1}{N}\frac{P_{ref}}{L_1 L_2 P_{out}}\sigma_{ref}^2 \tag{5.23}$$

It should be stressed that $\left(1-\frac{k}{\sqrt{N}}\right)$ should be positive. For instance, if k=3, N should be greater than 9, which is a reasonable requirement. Substituting (5.22) and (5.23) into (5.21) with $\lambda=\frac{c}{f}$ and $Q=\omega\tau_{RC}=2\pi f\tau_{RC}$ [21] gives

$$f < \sqrt{\frac{c^3}{16\pi}\cdot\frac{N\left(1-\frac{k}{\sqrt{N}}\right)}{(N-1)\left(1+\frac{k}{\sqrt{N}}\right)}\cdot\frac{P_{out}}{VP_{ref}\sigma_{ref}^2}\cdot\tau_{RC}L_1L_2} \tag{5.24}$$

Then we define the right side of (5.24) as

$$f_{HUF} = \sqrt{\frac{c^3}{16\pi}\cdot\frac{N\left(1-\frac{k}{\sqrt{N}}\right)}{(N-1)\left(1+\frac{k}{\sqrt{N}}\right)}\cdot\frac{P_{out}}{VP_{ref}\sigma_{ref}^2}\cdot\tau_{RC}L_1L_2} \tag{5.25}$$

Equation (5.25) is the explicit expression for the HUF showing all influencing factors. Rearranging (5.24) and transforming into dB scale gives

$$P_{re,dBm} - P_{re,dBm} > GB_{dB}$$

$$\left(P_{out,dBm} + L_{1,dB} + G_{ref,dB} + L_{2,dB}\right) - \left(\mathrm{P}_{ref,dBm} + 10\log_{10}\left(2\frac{N-1}{N}\sigma_{ref}^2\right)\right) \tag{5.26}$$

$$> 10\log_{10}\left(\frac{\left(1+\frac{k}{\sqrt{N}}\right)}{\left(1-\frac{k}{\sqrt{N}}\right)}\right)$$

where

$P_{re,\mathrm{dBm}}=P_{out,\mathrm{dBm}}+L_{1,\mathrm{dB}}+G_{ref,\mathrm{dB}}+L_{2,\mathrm{dB}}$ is the ground truth power value of the desired signal before entering Port 2 of the VNA, as depicted in Figure 5.9;

$P_{sen,\mathrm{dBm}} = P_{ref,\mathrm{dBm}} + 10\log_{10}\left(2\frac{N-1}{N}\sigma_{ref}^2\right)$ is the absolute noise floor level of the VNA in dBm in terms of the average stirred power;

$\mathrm{GB_{dB}}=10\log_{10}\left(\frac{\left(1+\frac{k}{\sqrt{N}}\right)}{\left(1-\frac{k}{\sqrt{N}}\right)}\right)$ is an adaptive guard band from the statistical point of view.

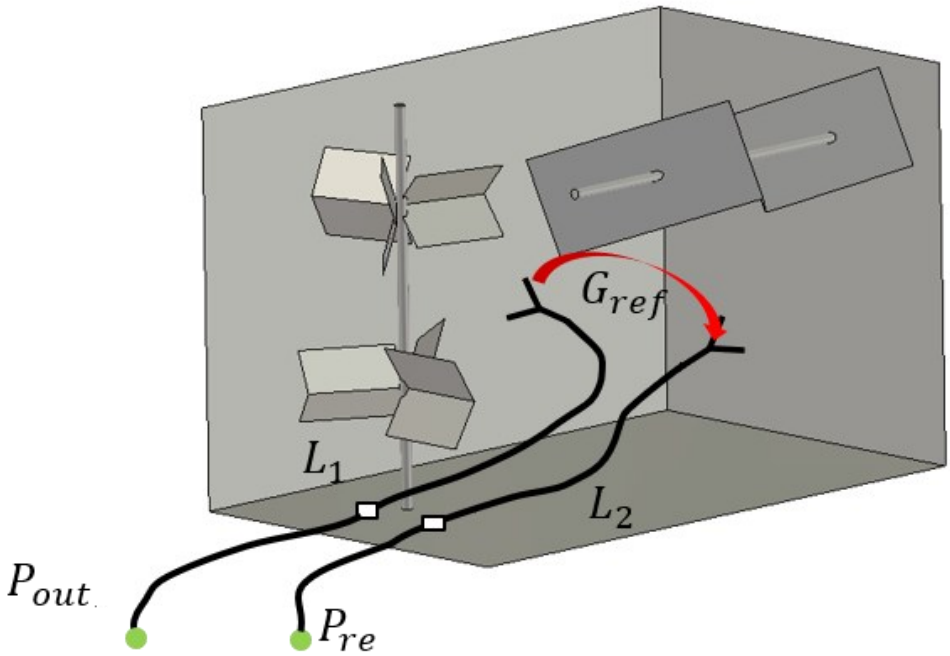

Figure 5.9: Schematic plot of the path loss model for an RC-based measurement system.

Consequently, it can be found from (5.26) that the physical meaning of the HUF model is straight forward: the average power level of the desired signal at the receiving end should be well above the corresponding noise floor level of the measurement equipment at frequencies below f_{HUF}.

5.3.4 HUF Model Analysis and an Iterative Method for HUF Estimation

In this section, a detailed analysis of the proposed HUF model (5.25) is performed. The methodology is to classify all the parameters under the square root into four terms and analyze each term independently:

I. $\frac{c^3}{16\pi}$: a constant value that can be treated as a scaling factor.

II. $\frac{N\left(1-\frac{k}{\sqrt{N}}\right)}{(N-1)\left(1+\frac{k}{\sqrt{N}}\right)}$: the term that includes the effect of the independent sample number N and the CI selector k which collaboratively determine the guard band. We name this term the *N*-*k* function. The simulated result of the *N*-*k* function is demonstrated in Figure 5.10. It can be seen that the *N*-*k* function monotonically increases with N and monotonically decreases with k, as expected. Note that the negative simulated result for small N should be discarded since the condition $\left(1-\frac{k}{\sqrt{N}}\right)>0$ is not fulfilled. By applying the L'Hôpital's rule, it can be derived that:

$$\lim_{N\to+\infty}\frac{N\left(1-\frac{k}{\sqrt{N}}\right)}{(N-1)\left(1+\frac{k}{\sqrt{N}}\right)}=1 \tag{5.27}$$

According to Figure 5.10, especially for higher k value, there is an obvious gap from its limit 1 even when N=360. This implies that f_{HUF} can be further improved by increasing the number of independent samples, at the cost of increased measurement time. Source stir (including position, orientation, and polarization) and frequency stir are recommended in addition to the mechanical stir method to increase the independent sample number.

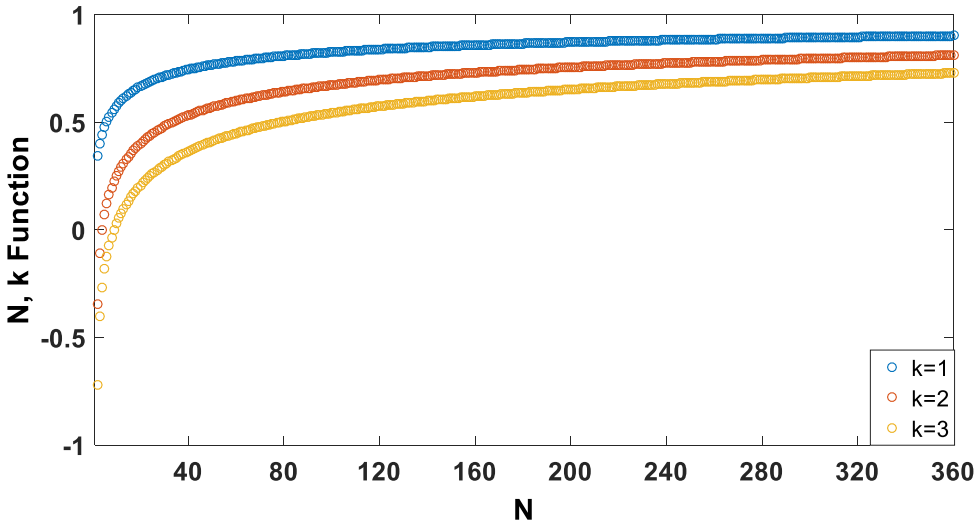

Figure 5.10: Simulation result of the *N*-*k* function.

III. $\frac{P_{out}}{VP_{ref}\sigma_{ref}^2}$: a system-wise fixed term. The f_{HUF} for different measurement system setups is mainly affected by this term. Higher DUT radiated power P_{out} results in higher f_{HUF}; RC with larger volume V results in higher insertion loss at the same frequency, which leads to lower f_{HUF}; measurement equipment with better sensitivity (lower $P_{ref}\sigma_{ref}^2$ value) gives higher f_{HUF}.

IV. $\tau_{RC}L_1L_2$: a combination of all the components that are frequency dependent. Both L_1 and L_2 decrease with frequency. A cable with poor quality or longer in size has higher loss at the same frequency, which leads to lower f_{HUF}. τ_{RC} tends to decrease first and then slightly fluctuate as frequency increases. Overall, the change in τ_{RC} is within 1.2 dB in the frequency range 2 GHz – 18 GHz. Loading the RC can drastically reduce τ_{RC}, or equivalently the Q factor, which also results in the reduction of f_{HUF}. Let $\mathrm{F}(f) = \tau_{RC}L_1L_2$, then it is reasonable to assume that $\mathrm{F}(f)$ decreases with frequency. It is counterintuitive that there is a frequency-dependent term inside the HUF expression. This is why it is hard to define the HUF. In this case, an iterative procedure can be used to calculate the theoretical value of f_{HUF}. Due to the computational complexity for calculating τ_{RC} (usually, IFT is needed and the number of frequency samples should be large enough to fulfill the Nyquist theorem), τ_{RC} cannot have the same granularity as L_1 and L_2. The interpolation method should be used.

The abovementioned iterative method for calculating f_{HUF} is summarized in Algorithm 5:1. The corresponding flow chart is visualized in Figure 5.11. Note that in order to avoid the risk of infinite loop, a second termination condition is set to force the program to terminate automatically if it has been running for over 1000 loops. However, this does not ensure the convergence of the algorithm, which might result in bigger error. Therefore, the termination condition is also a necessary output in addition to the theoretical HUF by the proposed algorithm.

Algorithm 5:1 Iterative algorithm for HUF calculation

1. Choose a start frequency f_1 (empirically a relatively large value is preferred).
2. Calculate $F(f_1)$.
3. Calculate f_{HUF}^1, where the superscript denotes that it is the first iteration:

$$f_{HUF}^1 = \sqrt{\frac{c^3}{16\pi} \cdot \frac{N\left(1-\frac{k}{\sqrt{N}}\right)}{(N-1)\left(1+\frac{k}{\sqrt{N}}\right)} \cdot \frac{P_{out}}{VP_{ref}\sigma_{ref}^2} \cdot F(f_1)} \tag{5.28}$$

4. While iteration number $i \geq 1$:

   if $f_{HUF}^i < f_i$:

   then $f_{i+1} = f_i - \left(f_i - f_{HUF}^i\right) \times 50\%$

   else if $f_{HUF}^i > f_i$:

   then $f_{i+1} = f_i + \left(f_{HUF}^i - f_i\right) \times 50\%$

Then calculate $F(f_{i+1})$ and f_{HUF}^{i+1} for the next iteration step

5. Repeat step 4 until the termination condition reaches.

Termination conditions:

either Con 1

$$\frac{\left|f_{HUF}^i - f_i\right|}{f_{HUF}^i} \times 100\% < 1\%$$

or Con 2

$$i > 1000$$

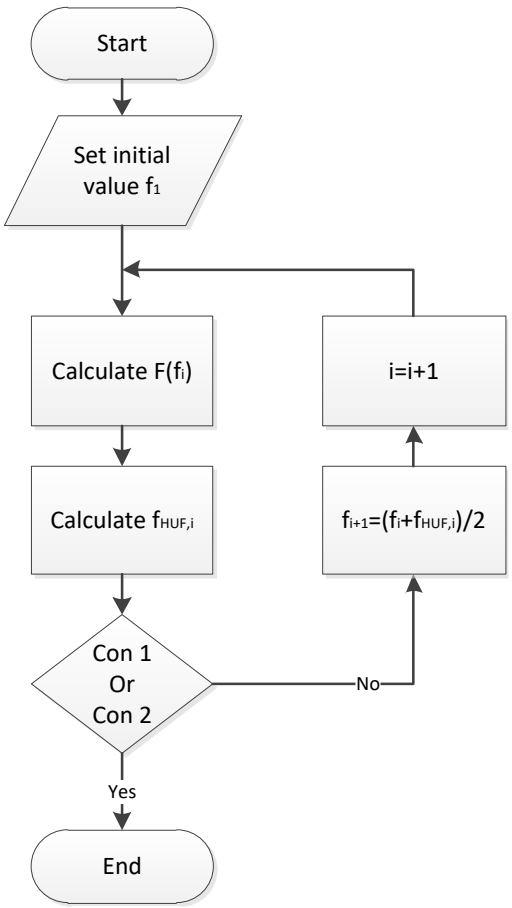

Figure 5.11: Flow chart diagram of the iterative approach for calculating the HUF.

5.3.5 Experimental Validation of the HUF Model

In this section, the HUF of the RC-based measurement system at the University of Liverpool (see Figure 5.1) for different P_{out} settings are theoretically derived based on the proposed model (5.25). The iterative algorithm described in Figure 5.11 is adopted for calculation. Then the results are validated by the experimental estimation procedure described by (5.26). The RC configuration and measurement setup are similar to that elaborated in Section 5.2.2 and are thus omitted here. Key parameters and their specifications are summarized in Table 5-V.

Table 5-V: Parameter specifications for HUF measurement and estimation

Parameter	Value
Chamber size	83.52 m^3
IF bandwidth	10 kHz
Frequency range	2 GHz – 18 GHz
Number of frequency points	1601
Number of stirrer positions	180
Number of independent samples	180
Stirrer step size	2°
VNA	Agilent N9917A
VNA measurement range	10 MHz – 18 GHz
Transmitting antenna	Rohde & Schwarz HF 906
Transmitting antenna bandwidth	1 GHz – 18 GHz
Receiving antenna	SATIMO SH 2000
Receiving antenna bandwidth	2 GHz – 32 GHz
Cable 1 type	3.5 mm
Cable 1 frequency range	DC – 26.5 GHz
Cable 2 type	N type
Cable 2 frequency range	DC – 18 GHz
P_{ref}	-3 dBm
P_{out}	-21 dBm, -24 dBm, -27 dBm, -30 dBm, -33 dBm, -36 dBm
CI selector	3

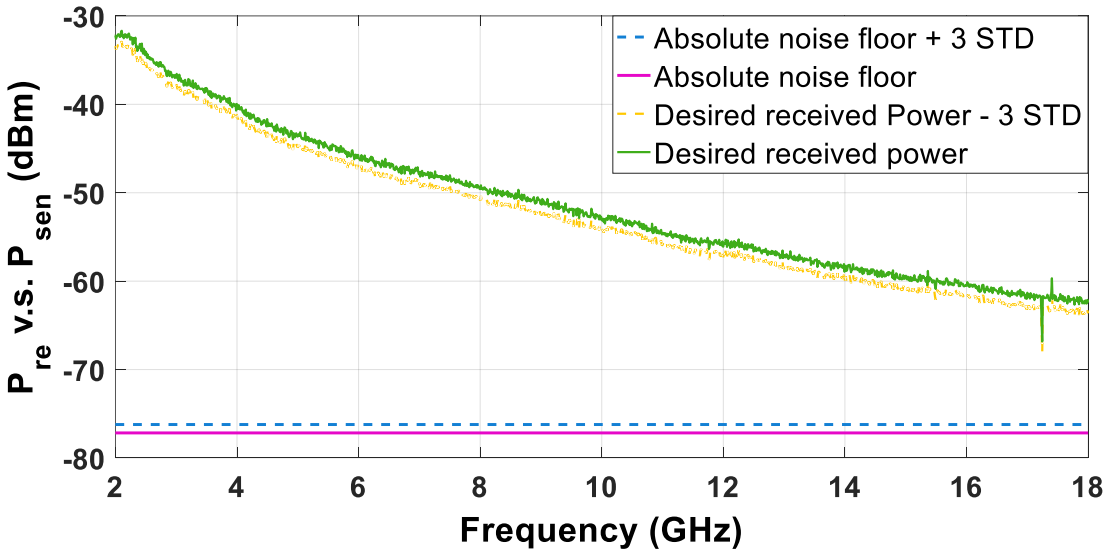

(a)

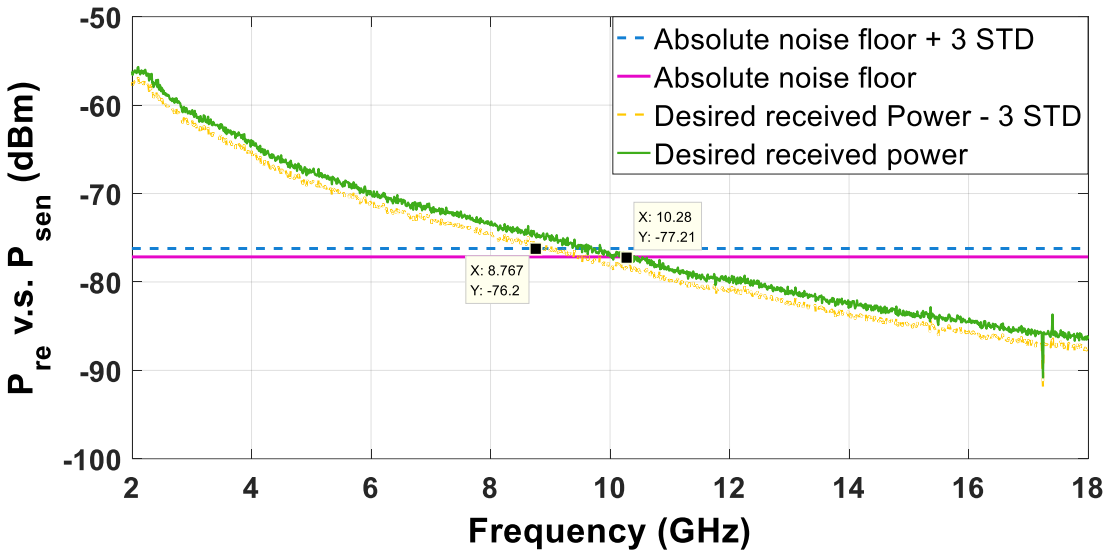

(b)

Figure 5.12: Experimental HUF estimation procedure based on (5.26): (a) Examination for P_{ref}= -3 dBm. (b) Example HUF derivation for P_{out}= -27 dBm.

The experimental process for HUF derivation is illustrated in Figure 5.12. The green solid curve represents the desired received power $P_{re,\mathrm{dBm}}=P_{out,\mathrm{dBm}}+L_{1,\mathrm{dB}}+G_{ref,\mathrm{dB}}+L_{2,\mathrm{dB}}$ in (5.26). The magenta solid line indicates the absolute noise floor level $P_{sen,\mathrm{dBm}} = P_{ref,\mathrm{dBm}} + 10\log_{10}\left(2\frac{N\text{-}1}{N}\sigma_{ref}^2\right)$ in (5.26), which is fixed system-wise irrespective of the output power P_{out}. After considering the 3-standard deviation shift, the corresponding results are denoted by the dashed curves. By doing this, the guard band in (5.26) is already incorporated in the two dashed curves. The frequency point at which the two dashed lines intersect with each other denotes the HUF.

In Figure 5.12 (a), it can be seen that for $P_{out}=P_{ref}$= -3 dBm, the measured received power is well beyond the noise floor for the frequency range of interest (2 GHz – 18 GHz), which guarantees that the measured G_{ref} remains intact from the system noise. As a result, P_{re} can be considered as "desired". Figure 5.12 (b) shows an example of experimental HUF derivation for P_{out}= -27 dBm. By looking up the intersection point of the two dashed lines, we have that f_{HUF}=8.77 GHz.

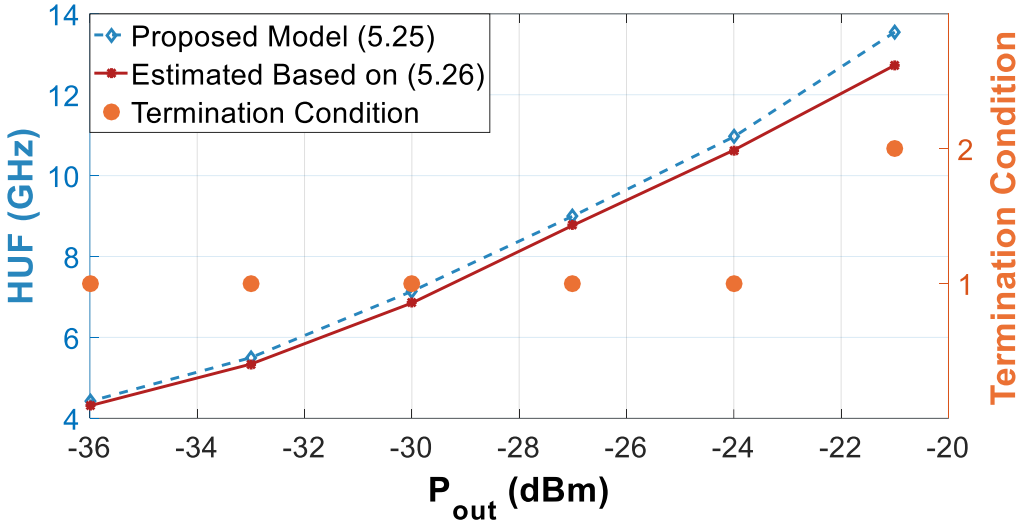

Figure 5.13: HUF calculated by the proposed model (5.25) and estimated by the experimental process (5.26) as a function of P_{out}.

Table 5-VI: Table of Comparison between the theoretically calculated HUF (5.25) and the experimentally estimated HUF (5.26) for different P_{out} values

P_{out}	Experimental Estimation (5.26)	Iterative Algorithm (5.25)	Termination Condition	Relative Discrepancy
-21 dBm	12.73 GHz	13.55 GHz	Con 2	6.44%
-24 dBm	10.63 GHz	10.96 GHz	Con 1	3.10%
-27 dBm	8.77 GHz	9.00 GHz	Con 1	2.62%
-30 dBm	6.85 GHz	7.14 GHz	Con 1	4.23%
-33 dBm	5.34 GHz	5.50 GHz	Con 1	3.00%
-36 dBm	4.31 GHz	4.42 GHz	Con 1	2.55%

The comparison result of f_{HUF} calculated by the proposed model (5.25) and estimated by the experimental process (5.26) is demonstrated in Figure 5.13. Detailed figures as well the relative discrepancies are listed in Table 5-VI. Not surprisingly, for both cases, f_{HUF} monotonically increases with increasing P_{out} values. Overall, the two curves are in good agreement with each other, which verifies the proposed model. However, there

exists a systematic bias that f_{HUF} calculated by (5.25) is always slightly higher than that by (5.26) at the same P_{out} values. This is due to the difference of the Q factor calculated in the frequency domain and in the time domain, as explained in [21]. Including the losses of the transmitting antenna and the receiving antenna may relieve this problem. One thing should be mentioned is that when P_{out}=-21 dBm, the termination condition of the iterative algorithm is "Con 2", which implies that the resultant f_{HUF} might not be convergent. Consequently, a relatively large discrepancy is observed (6.44%). One possible reason is that as frequency increases, the reduced dynamic range in the time domain may introduce error to τ_{RC} estimation.

5.4 Conclusion

In this chapter, firstly in Section 5.2, the enhanced backscattering effect inside an RC with volume 83.52 m^3 was investigated in terms of the frequency, spatial, and power domains by calculating and comparing e_b with its theoretical value. As the experimental results indicated, a HUF should be defined for the RC-based measurement system, above which the statistical characteristics of the measured received signal will be severely disturbed by the system noise due to increased attenuation.

On the one hand, the HUF of the RC depends upon the system SNR, which is different from the LUF defined based on the mode density and mode bandwidth. On the other hand, the HUF is in accordance with the LUF in that it is not sensitive to the spatial domain characteristics such as location, orientation, and polarization within the working volume of the RC.

Then, in Section 5.3, detailed deduction procedures for an explicit HUF model were elaborated based on the statistical distributions of $\langle|S_{21,s}|^2\rangle_N$ and $\langle|V|^2\rangle_N$. Physical explanation verified that the proposed HUF model essentially describes the change of the system SNR as a function of frequency. Analysis and discussion of each term in (5.25) and their effects on the HUF were also performed. To tackle the problem that there are frequency-dependent terms inside the HUF expression, an iterative algorithm was developed for efficient calculation. Finally, experimental validation of the proposed HUF model was conducted with different output power levels, and good agreement

between the experimental estimation described in (5.26) and the proposed model (5.25) was achieved.

With the aid of the proposed HUF model, fast characterization and evaluation of the RC-based measurement system at a certain frequency band and output power level becomes possible, and the system setup can be optimized accordingly so that the HUF of the existing RC can be improved.

So far, the proposed HUF model has been validated for different P_{out} values. Future works should primarily concentrate on further validation of the HUF model in terms of other influencing factors. Specifically, the validation in a second RC with different design characteristics like chamber volume, Q factor, and stirrer configuration is preferred. It is also possible to further modify the proposed HUF model to fulfill different test requirements. For instance, an additional term that represents a deterministic guard band (*e.g.*, 10 dB) can be added in (5.25) to guarantee certain system SNR.

5.5 References

[1] X. Chen, "Experimental investigation of the number of independent samples and the measurement uncertainty in a reverberation chamber," *IEEE Trans. Electromagn. Compat.*, vol. 55, pp. 816-824, 2013.

[2] Q. Xu, Y. Huang, L. Xing, Z. Tian, M. Stanley, and S. Yuan, "B-scan in a reverberation chamber," *IEEE Trans. Antennas Propag.*, vol. 64, no. 5, pp. 1740–1750, May 2016.

[3] T. Jia, Y. Huang, Q. Xu, Z. Tian, J. Jiang, and Q. Hua, "Frequency Domain Method for Scattering Damping Time Extraction of a Reverberation Chamber Based on Autocorrelation Functions," *IEEE Trans. Electromagn. Compat.*, vol. 62, no. 6, pp. 2349-2357, Dec. 2020.

[4] D. A. Hill, *Electromagnetic Fields in Cavities*, Piscataway, NJ, USA: IEEE Press, 2009.

[5] P.-S. Kildal, X. Chen, C. Orlenius, M. Franzén, and C. Lötbäck Patané, "Characterization of reverberation chambers for OTA measurements of wireless

devices: Physical formulations of channel matrix and new uncertainty formula," *IEEE Trans. Antennas Propag.*, vol. 60, no. 8, pp. 3875–3891, 2012.

[6] T. Jia, Y. Huang, Q. Xu, Q. Hua, and L. Chen, "Average Rician K-Factor Based Analytical Uncertainty Model for Total Radiated Power Measurement in a Reverberation Chamber," *IEEE Access*, vol. 8, pp. 198078-198090, Oct. 2020.

[7] M. G. Becker, M. Frey, S. Streett, K. A. Remley, R. D. Horansky and D. Senic, "Correlation-based uncertainty in loaded reverberation chambers," *IEEE Trans. Antennas Propag.*, vol. 66, no. 10, pp. 5453-5463, Oct. 2018.

[8] *User Equipment (UE) / Mobile Station (MS) Over The Air (OTA) antenna performance; Conformance testing*, 3GPP Std. TS 34.114, Rev. V12.2.0, Sep. 2016.

[9] *Study on radiated metrics and test methodology for the verification of multi-antenna reception performance of NR User Equipment (UE)*, 3GPP Std. TR 38.827, Rev. V16.1.0, Jan. 2021.

[10] *Radio Frequency (RF) conformance testing background for radiated Base Station (BS) requirements*, 3GPP Std. TR 37.941, Rev. V16.0.1, Jun. 2020.

[11] M. Gustafsson, T. Jämsä, and M. Högberg, "OTA methods for 5G BTS testing—Survey of potential approaches," *in Proc. 32nd URSI GASS*, Montreal, QC, Canada, pp. 1–4, Aug. 2017.

[12] W. Fan, I. Carton, P. Kyosti, A. Karstensen, T. Jamsa, M. Gustafsson, *et al*., "A step toward 5G in 2020: Low-cost OTA performance evaluation of massive MIMO base stations," *IEEE Antennas Propag. Mag.*, vol. 59, no. 1, pp. 38–47, Feb. 2017.

[13] K. A. Remley *et al*., "Measurement challenges for 5G and beyond: An update from the National Institute of Standards and Technology," *IEEE Microw. Mag.*, vol. 18, no. 5, pp. 41–56, Jul./Aug. 2017.

[14] X. Chen, J. Tang, T. Li, S. Zhu, Y. Ren, Z. Zhang, and A. Zhang, "Reverberation Chambers for Over-the-Air Tests: An Overview of Two Decades of Research," *IEEE Access.*, vol. 6, pp. 49129–49143, Aug. 2018.

[15] P. Zhang, X. Yang, J. Chen, and Y. Huang, "A survey of testing for 5g: Solutions, opportunities, and challenges," *China Communications.*, vol. 16, no. 1, pp. 69–85, Jan 2019.

[16] X. Chen, "Measurement uncertainty of RC and its reduction techniques for OTA tests: a review," *IET Microw. Antennas Propag.*, vol. 13, no. 15, pp. 2598-2604, Dec. 2019.

[17] T. S. Rappaport, S. Sun, R. Mayzus, H. Zhao, Y. Azar, K. Wang, *et al*., "Millimeter-wave mobile communications for 5G cellular: It will work!," *IEEE Access*, vol. 1, pp. 335–349, 2013.

[18] T. S. Rappaport, G. R. MacCartney, M. K. Samimi, and S. Sun, "Wideband millimeter-wave propagation measurements and channel models for future wireless communication system design," *IEEE Trans. Commun.*, vol. 63, no. 9, pp. 3029–3056, Sep. 2015.

[19] Y. Barabanenkov, Y. Kravtsov, V. Ozrin, and A. Saichev, "Enhanced backscattering: The universal wave phenomenon," *Proc. IEEE*, vol. 79, pp. 1367–1370, Oct. 1991.

[20] J. M. Ladbury and D. A. Hill, "Enhanced backscatter in a reverberation chamber: Inside every complex problem is a simple solution struggling to get out," *in Proc. IEEE Int. Symp. on Electromagnetic Compatibility*, pp. 1–5, Jul. 2007.

[21] C. L. Holloway, H. Shah, R. J. Pirkl, W. Young, J. Ladbury, and D. A. Hill, "Reverberation chamber techniques for determining the radiation and total efficiency of antennas," *IEEE Trans. Antennas Propag.*, vol. 60, no. 4, pp. 1758–1770, Apr. 2012.

[22] C. Li, T.-H. Loh, Z. Tian, Q. Xu, and Y. Huang, "Evaluation of chamber effects on antenna efficiency measurements using non-reference antenna methods in two reverberation chambers," *IET Microw. Antennas Propag.*, vol. 11, pp. 1536-1541, Aug. 2017.

[23] Q. Xu, Y. Huang, X. Zhu, L. Xing, Z. Tian, and C. Song, "A modified two-antenna method to measure the radiation efficiency of antennas in a reverberation chamber," *IEEE Antennas Wireless Propag. Lett.*, vol. 15, pp. 336–339, 2016.

[24] Z. Tian, Y. Huang, Y. Shen, and Q. Xu, "Efficient and accurate measurement of absorption cross section of a lossy object in reverberation chamber using two one-antenna methods," *IEEE Trans. Electromagn. Compat.*, vol. 58, no. 3, pp. 686–693, Jun. 2016.

[25] Q. Xu, Y. Huang, X. Zhu, L. Xing, Z. Tian, and C Song, "Shielding effectiveness measurement of an electrically large enclosure using one antenna," *IEEE Trans. Electromagn. Compat.*, vol. 57, no. 6, pp. 1476– 1471, Dec. 2015.

[26] C. Dunlap C. Holloway, R. Pirkl, J. Ladbury, E. Kuester, D. Hill, *et al*., "Characterizing reverberation chambers by measurements of the enhanced backscatter coefficient," *in Proc. IEEE Int. Symp. Electromagn. Compat.*, pp. 210–215, Aug. 2012.

[27] G. Andrieu, N. Ticaud, F. Lescoat, and L. Trougnou, "Fast and accurate assessment of the "well stirred condition" of a reverberation chamber from s11 measurements," *IEEE Trans. Electromagn. Compat.*, pp. 1–9, 2019.

[28] K. A Remley, R. J Pirkl, H. A Shah, and C.-M. Wang, "Uncertainty from choice of mode-stirring technique in reverberation-chamber measurements," *IEEE Trans. Electromagn. Compat.*, vol. 55, no. 6, pp. 1022– 1030, Dec. 2013.

[29] N. L. Johnson and S. Kotz, *Continuous Univariate Distributions, Volume 2 (2nd Edition)*. New York, NY, USA: Wiley, 1995.

[30] Q. Xu, L. Xing, Z. Tian, Y. Zhao, X. Chen, L. Shi, and Y. Huang, "Statistical distribution of the enhanced backscatter coefficient in reverberation chamber," *IEEE Trans. Antennas Propag.*, vol. 66, no. 4, pp. 2161–2164, Apr. 2018.

[31] Q. Xu and Y. Huang, Anechoic and Reverberation Chambers: Theory, Design and Measurements, Wiley-IEEE, UK, 2019.

[32] A. Papoulis, *Probability, Random Variables, and Stochastic Processes*. New York: McGraw-Hill, 1965.

Chapter 6 Conclusion & Future Work

6.1 Key Contributions

In this thesis, accurate, reliable, and fast RC characterization processes regarding different stirrer configurations, practical TRP measurement setups, and different frequencies & transmitting power levels have been researched, developed, analyzed, and validated [1] – [3]. Key contributions in each chapter are briefly summarized as follows:

Chapter 3: A novel method for scattering damping time extraction and stirrer performance characterization

A novel frequency domain approach has been proposed in this chapter for calculating the scattering damping time, thereby providing a more reliable and efficient way for stirrer performance characterization of an RC [1]. Similar to the definition of the FD-ACF, the FD-ACFUS, which describes how the unstirred components are correlated with respect to frequency offset, was defined for the first time in this work. Then, by constructing these two ACFs, we showed that the scattering damping time can be directly obtained in the frequency domain without performing the IFT. Detailed mathematical proof of the proposed method was given based on the Wiener-Khinchin theorem, and its advantages over the conventional IFT-based approach were discussed and analyzed by simulation. Experimental validations were performed for both the 2.3 GHz – 2.5 GHz and 5.8 GHz – 6.0 GHz bands and three different stirrer configurations to verify the proposed method.

Summary about the importance and impact:

1) Compared with the traditional IFT-based method, the proposed frequency domain method can provide more stable and reliable results since it has a wider dynamic range and eliminates the procedure of manually selecting the fitting range.
2) The mathematical relationship between the FD-ACFUS and the scattering damping time is established for the first time in this work.

3) Based on the proposed method, the reliable stirrer performance characterization of an RC can be achieved.

Chapter 4: Statistical Modelling of the average Rician *K*-factor

An unbiased MLE of the average Rician *K*-factor has been given for accurate characterization of the statistical anisotropy of the RC [2]. Firstly, the average Rician *K*-factor was formulated based on the random unstirred power assumption. Secondly, the statistical distribution of the MLE of the average Rician *K*-factor was obtained, and Monte Carlo simulations showed that the MLE is actually biased. An improved unbiased MLE for the average Rician *K*-factor was then given, and its statistical properties were theoretically analyzed. Experimental comparison for the MLEs was also performed.

Summary about the importance and impact:

1) This is the first work that derives the statistical distribution of the MLE of the average Rician *K*-factor.
2) The statistical anisotropy of the RC can be more accurately characterized based on the derived statistics of the average Rician *K*-factor.

Chapter 4: An improved analytical uncertainty model for the RC-based OTA TRP measurement

After accurately characterizing its statistical anisotropy, the RC was applied to OTA TRP measurement. It was shown that sample correlation and statistical anisotropy played a vital role in the relative measurement uncertainty. Consequently, an improved analytical uncertainty model was derived based on the number of independent samples and the average Rician *K*-factor [2]. The statistical properties of the average Rician *K*-factor have already been derived, and two approaches for independent sample number estimation were introduced for cross-checking. The RC-based TRP measurement process was divided into two stages: the calibration stage and the measurement stage. Sources of uncertainty in each stage were analyzed and propagated to the overall uncertainty formula. Extensive 9-Point estimation measurements were also conducted for performance evaluation.

Summary about the importance and impact:

1) The proposed analytical uncertainty model is more accurate than the traditional

model since it takes both the sample correlation and the statistical anisotropy into consideration.

2) The proposed model is the first analytical model that includes the uncertainties from both the calibration stage and the measurement stage during the TRP measurement. It also allows different experimental configurations for these two stages.

3) The proposed model makes it possible to characterize the uncertainty of the RC-based OTA TRP measurement without tedious and time-consuming empirical estimation processes.

Chapter 5: Investigation of the enhanced backscattering effect in different domains

Thorough enhanced backscattering effect investigations were performed for RC characterization in terms of the frequency, spatial, and power domains. According to the experimental results, it was inferred that in addition to the well-known LUF, there should be a HUF for the RC-based measurement system, above which its statistical behavior will be severely disturbed by the system noise due to increased attenuation. It was also found that the HUF should be insensitive to the spatial domain characteristics like location, orientation, and polarization within the working volume of the RC.

Summary about the importance and impact:

1) The investigation indicates that there exists a HUF for an RC, and it is related to the output power of the source.

2) The investigation also shows that the HUF is not sensitive to the excitation source's location, orientation, and antenna polarization.

Chapter 5: Modelling of the HUF of the RC-based measurement system

A HUF model was derived based on the statistical distributions of the average power of the desired received signal and the corresponding average noise power [3]. Detailed deduction procedures were elaborated. According to its explicit expression, the HUF should be a function of parameters like chamber volume, chamber decay constant, cable losses, the power level of the transmitting signal, sensitivity of the measurement equipment, and their influences on the HUF were also analyzed and discussed. We also gave a physical explanation for the proposed HUF model. In order to deal with the problem that frequency-dependent terms are included in the HUF expression, an

iterative algorithm was developed. Experimental evaluation of the proposed HUF model was conducted with different output power levels, and good agreement between the empirical estimation and the proposed HUF model was achieved.

Summary about the importance and impact:

1) To the best of the author's knowledge, this is the first comprehensive study of the HUF of an RC.
2) Fast characterization of the RC-based measurement system in terms of the frequency of operation and the output power level becomes possible with the help of the proposed HUF model.
3) The proposed HUF model guides how to optimize the existing system setup for improved HUF.

6.2 Future Work

Chapter 3

Until now, there is only a relatively loose theoretical lower boundary for the scattering damping time [4]:

$$\tau_s^{LB} = \frac{4V}{A_s c_0} \tag{6.1}$$

where the superscript ^{LB} stands for the lower bound, and A_s is the stirring surface area. For example, the total stirring surface area of the two mechanical stirrers installed inside the RC at the University of Liverpool is around 8 m^2, which gives $\tau_s^{LB} \approx 14$ ns. Nevertheless, the measured values of the scattering damping time in this work are much larger than this lower bound. If an analytical expression for calculating the ground-truth value of the scattering damping time can be derived, it will help for fast RC stirrer performance characterization.

It has been pointed out that, under heavy loading conditions, the proposed frequency domain method may lose its effectiveness. While this situation might be rare in practice (for the scattering damping time extraction, the OUT is the stirrer of the RC, and there

is no reason to test it in a heavily loaded setup), analyzing and solving this problem is still of research value.

Chapter 4

The DUT used for the TRP measurement in this thesis was an "equivalent" DUT comprises an SG, a dual-ridge horn antenna, and the cable connecting them. This is actually different from the real DUT (*e.g.*, user terminal, BS) in radiation pattern, loading effect, emitted signal, *etc*. Therefore, a real DUT can be used for further evaluating the proposed analytical uncertainty model in the future.

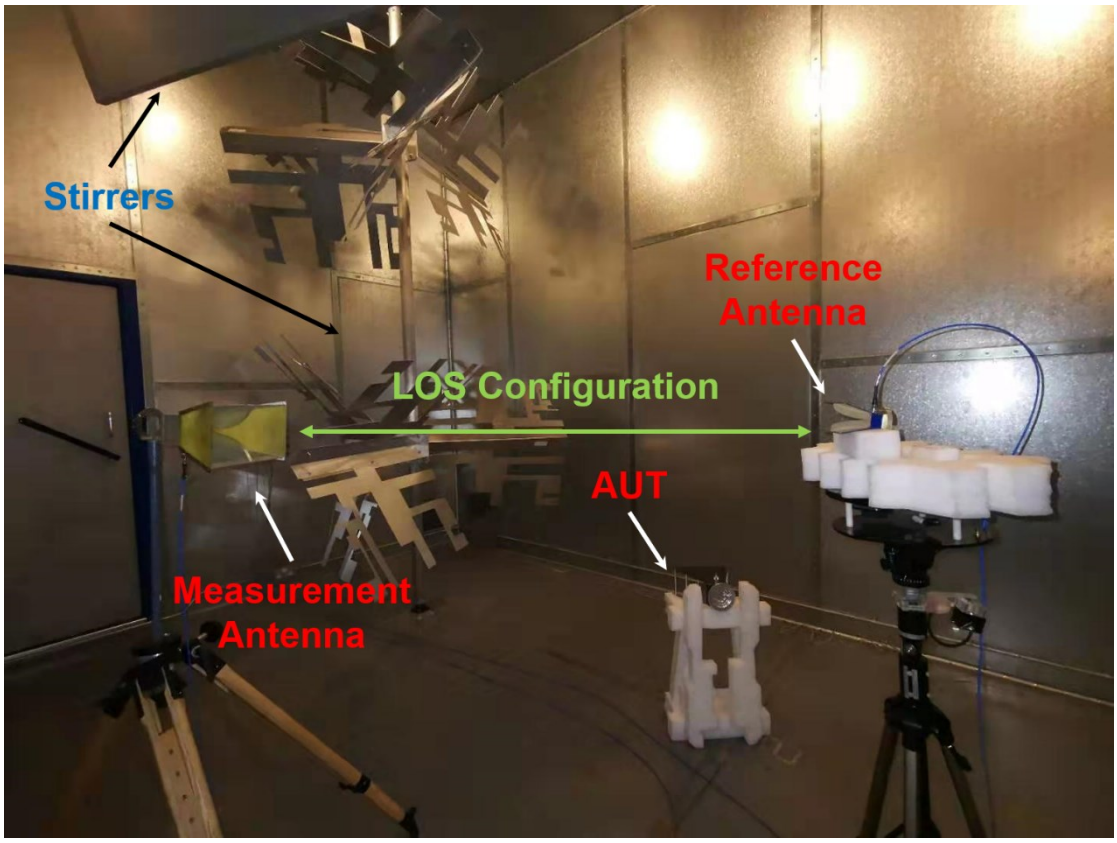

Figure 6.1: Experimental setup for measuring the directivity of the AUT using an RC.

In addition to the TRP, the effective isotropic radiated power (EIRP) is another critical FoM for the OTA tests [5]. EIRP can be represented as:

$$EIRP = TRP + D \tag{6.2}$$

where D denotes the directivity of the DUT antenna. In [6], it was demonstrated that

the directivity can be measured in an RC using a two-stage reference substitution method with the LOS configuration. A typical experimental setup for measuring the directivity using an RC is depicted in Figure 6.1. Accurate characterization of the RC under this measurement setup and quantification of the corresponding measurement uncertainty can provide meaningful reference to standard bodies and institutions, making the RC an economical and efficient alternative to the AC for OTA EIRP testing.

Chapter 5

So far, the proposed HUF model has been verified in terms of different output power levels. In the future, further validation should primarily concentrate on other parameters. Specifically, the validation in a second RC with different characteristics is preferred.

It is also possible to further improve the proposed HUF model. For instance, an additional term representing a deterministic guard band (*e.g.*, 10 dB) can be added to guarantee certain system SNR.

With the aid of the proposed HUF model, it is possible to further optimize the HUF of the existing RC-based measurement system. Therefore, future research can focus on the design and optimization of the RC, and our ultimate goal is to design an RC which has a much wider frequency band that covers the requirements of mainstream standards, with smaller dimensions and lower measurement uncertainty.

6.3 References

[1] T. Jia, Y. Huang, Q. Xu, Z. Tian, J. Jiang, and Q. Hua, "Frequency Domain Method for Scattering Damping Time Extraction of a Reverberation Chamber Based on Autocorrelation Functions," *IEEE Trans. Electromagn. Compat.*, vol. 62, no. 6, pp. 2349-2357, Dec. 2020.

[2] T. Jia, Y. Huang, Q. Xu, Q. Hua, and L. Chen, "Average Rician K-Factor Based Analytical Uncertainty Model for Total Radiated Power Measurement in a Reverberation Chamber," *IEEE Access*, vol. 8, pp. 198078-198090, Oct. 2020.

[3] T. Jia, Y. Huang, Q. Xu, and Q. Hua, "Highest Usable Frequency Model for a Reverberation Chamber," *IEEE Antennas Wireless Propag. Lett.*, to be submitted.

[4] Q. Xu, Y. Huang, L. Xing, Z. Tian, C. Song, and M. Stanley, "The limit of the total scattering cross section of electrically large stirrers in a reverberation chamber," *IEEE Trans. Electromagn. Compat.*, vol. 58, no. 2, pp. 623–626, Apr. 2016.

[5] *Radio Frequency (RF) conformance testing background for radiated Base Station (BS) requirements*, 3GPP Std. TR 37.941, Rev. V16.0.1, Jun. 2020.

[6] C. Lemoine, E. Amador, P. Besnier, J. Floc'h, and A. Laisné, "Antenna directivity measurement in reverberation chamber from Rician *K*-factor estimation," *IEEE Trans. Antennas Propag.,* vol. 61, no. 10, pp. 5307– 5310, Oct. 2013.

Appendix I

$$V_1 = \frac{N-1}{N} N_{21} \tag{A.1}$$

Based on the statistics of N_{21}, we have that $\mathrm{Re}\{V_1\}$ and $\mathrm{Im}\{V_1\}$ are *i.i.d* variables following a Gaussian distribution with mean 0 and standard deviation $\frac{N\text{-}1}{N}\sigma_{\mathrm{noise}}$, where Re and Im are operations that taking the real and imaginary part of the corresponding quantity, respectively.

$$V_2 = \frac{N-1}{N} \langle N_{21} \rangle_{N-1} \tag{A.2}$$

It is also easy to obtain that $\mathrm{Re}\{V_2\}$ and $\mathrm{Im}\{V_2\}$ are also *i.i.d* Gaussian distributed with 0 mean and standard deviation $\frac{\sqrt{N\text{-}1}}{N}\sigma_{\mathrm{noise}}$. Recall the equation

$$V = N_{21} - \langle N_{21} \rangle_N = V_1 - V_2 \tag{A.3}$$

Since V_1 and V_2 are independent, V also follows a complex Normal distribution with 0 mean and standard deviation σ [1]:

$$\sigma = \sqrt{\left(\frac{N-1}{N}\sigma_{noise}\right)^2 + \left(\frac{\sqrt{N-1}}{N}\sigma_{noise}\right)^2} = \sqrt{\frac{N-1}{N}}\sigma_{noise} \tag{A.4}$$

Appendix II

$$\left\langle \left|R_{21,s}\right|^2 \right\rangle_N = \left\langle \left|S_{21,s}\right|^2 \right\rangle_N + \left\langle \left|V\right|^2 \right\rangle_N + \left\langle S_{21,s}V^* \right\rangle_N + \left\langle S_{21,s}^* V \right\rangle_N \tag{A.5}$$

$$\begin{aligned} S_{21,s}V^* = {} & \mathrm{Re}\left\{S_{21,s}\right\}\mathrm{Re}\left\{V\right\} + \mathrm{Im}\left\{S_{21,s}\right\}\mathrm{Im}\left\{V\right\} \\ & + j\,\mathrm{Im}\left\{S_{21,s}\right\}\mathrm{Re}\left\{V\right\} - j\,\mathrm{Re}\left\{S_{21,s}\right\}\mathrm{Im}\left\{V\right\} \end{aligned} \tag{A.6}$$

$$\begin{aligned} S_{21,s}^* V = {} & \mathrm{Re}\left\{S_{21,s}\right\}\mathrm{Re}\left\{V\right\} + \mathrm{Im}\left\{S_{21,s}\right\}\mathrm{Im}\left\{V\right\} \\ & - j\,\mathrm{Im}\left\{S_{21,s}\right\}\mathrm{Re}\left\{V\right\} + j\,\mathrm{Re}\left\{S_{21,s}\right\}\mathrm{Im}\left\{V\right\} \end{aligned} \tag{A.7}$$

Based on (A.6) and (A.7), we can get

$$\left\langle S_{21,s}V^* \right\rangle_N + \left\langle S_{21,s}^* V \right\rangle_N = 2\left\langle \mathrm{Re}\left\{S_{21,s}\right\}\mathrm{Re}\left\{V\right\} \right\rangle_N + 2\left\langle \mathrm{Im}\left\{S_{21,s}\right\}\mathrm{Im}\left\{V\right\} \right\rangle_N \tag{A.8}$$

The two random variables $\mathrm{Re}\{S_{21,s}\}$ and $\mathrm{Re}\{V\}$ are independent and of 0 mean. Similarly, $\mathrm{Im}\{S_{21,s}\}$ and $\mathrm{Im}\{V\}$ are independent and of 0 mean [2]. Therefore, if N is large, $\langle S_{21,s}V^* \rangle_N + \langle S_{21,s}^* V \rangle_N = 0$.

Appendix III

According to the CLT [2], it is reasonable to assume that both x and y in Section 5.3.1 follow Gaussian distributions for large N. The probability that x does not exceed k stand deviations (only the lower bound) is given as:

$$P\left(x > \mu_x - k\sigma_x\right) = 1 - \Phi\left(-k\right) = \Phi\left(k\right) \tag{A.9}$$

where $\Phi(*)$ denotes the CDF of the standard normal distribution. Similarly, the probability that y does not exceed k stand deviations (only the upper bound) is:

$$P\left(y < \mu_y + k\sigma_y\right) = \Phi\left(k\right) \tag{A.10}$$

Table A-I: Statistical data for different *k* values

k	$\Phi(k)$	ER=1-$\Phi^2(k)$
1	0.8413	29.22%
2	0.9772	4.51%
3	0.9987	0.26%

Then the overall excess rate can be defined accordingly as:

$$ER = 1 - P\left(x > \mu_x - k\sigma_x\right)P\left(y < \mu_y + k\sigma_y\right) = 1 - \Phi^2\left(k\right) \tag{A.11}$$

Statistical figures are available in Table A-I.

References

[1] B. N. Taylor and C. E. Kuyatt, “Guidelines for Evaluating and Expressing the Uncertainty of NIST Measurement Results,” NIST Tech. Note 1297, Sep. 1994.

[2] A. Papoulis, *Probability, Random Variables, and Stochastic Processes*. New York: McGraw-Hill, 1965.

END